

**Characterisation of cement microstructure  
and pore – water interaction by  
<sup>1</sup>H Nuclear Magnetic Resonance Relaxometry**

---

by

Agata M. Gajewicz

Submitted for the degree of Doctor of Philosophy

Department of Physics  
Faculty of Engineering and Physical Sciences  
University of Surrey

2014

© Agata M. Gajewicz 2014

# Abstract

$^1\text{H}$  nuclear magnetic resonance (NMR) relaxometry is used to characterise cement paste microstructure from the stand point of the pore water. Attention focuses primarily on pore-water interactions and the morphology of calcium-silicate-hydrate (C-S-H), the active phase of cement paste. The method is non-destructive and non-invasive.

NMR allows the quantitative separation of water by confinement. The first pore-type resolved sorption isotherm of any cementitious material is measured. This provides insight into water location during drying and wetting. The C-S-H interlayer and gel pore sizes are estimated based on  $T_2$  relaxation times ( $0.94 \pm 0.04$  and  $3.1 \pm 0.2$  nm) and amplitudes of relaxation components during drying ( $1.5 \pm 0.3$  and  $4.5 \pm 1.6$  nm). The specific surface areas are also evaluated.

The evolution of nanoscale porosity for underwater cured white cement pastes, with and without silica fume addition, are determined during hydration and as a function of temperature in the range  $10^\circ\text{C}$  to  $60^\circ\text{C}$ .

The C-S-H density and chemical composition are evaluated using NMR supported by X-ray diffraction and thermogravimetric analysis. The calculated C-S-H ‘solid’ density and composition, excluding gel pore water, in never-dried 28 days old white cement paste are  $2.64 \pm 0.03$  g/cm<sup>3</sup> and  $\text{Ca}_{1.53 \pm 0.02}(\text{Si}_{0.96 \pm 0.01}, \text{Al}_{0.04 \mp 0.01})\text{O}_{3.51 \pm 0.02}(\text{H}_2\text{O})_{1.92 \pm 0.05}$ . The C-S-H ‘bulk’ density, including gel pore water, is  $1.90 \pm 0.02$  g/cm<sup>3</sup>. Increase of curing temperature does not alter the Ca/(Si+Al) ratio. However, a significant decrease in C-S-H water content and increase in density is observed and attributed to the fewer locally stacked C-S-H layers.

NMR relaxation activation energies are estimated.

Insight into the mechanism of water-isopropanol exchange, used for arresting cement hydration, is provided. NMR shows that the exchange occurs in a selective manner with no C-S-H interlayer water alteration. The connectivity of the C-S-H interlayer and gel pores with interhydrate-capillary pores is evidenced.

## **Declaration of originality**

This thesis and the work to which it refers are the results of my own efforts. Any ideas, data, images or text resulting from the work of others (whether published or unpublished) are fully identified as such within the work and attributed to their originator in the text, bibliography or in footnotes. This thesis has not been submitted in whole or in part for any other academic degree or professional qualification.

I agree that the University has the right to submit my work to the plagiarism detection service TurnitinUK for originality checks. Whether or not drafts have been so-assessed, the University reserves the right to require an electronic version of the final document (as submitted) for assessment as above.

# Acknowledgements

The completion of this thesis would not be possible without help and support of several people to whom I am extremely grateful.

Foremost I extend my gratitude to my supervisor Professor Peter McDonald for his important guidance throughout this thesis, continuous support, thoughtful advice, enthusiasm and warm encouragement.

My warmest thanks also go to Doctor Radoslaw Kowalczyk for his insightful suggestions, interesting, very often exciting, discussions and sharing NMR experience with me. I am also grateful to Mr Bob Derham for his helpful hand in NMR laboratories and to Mrs Violeta Doukova for her kind support with thermogravimetric analysis. Thank you all for sharing time with me and friendly words.

I am truly grateful for the opportunity to meet the professors, researches, fellows and PhD students in the Nanocem consortium who were kind enough to share the expertise and knowledge with me.

I would also like to thank my PhD friends from Transcend project for many good times when we discussed science and when we had fun. It was great to be surrounded during the course of the project by people whose company I enjoyed very much and as such made the whole experience very positive and pleasurable.

The very special thanks go to Doctor Marek Petri and my friends, Kasia and Mikolaj; without them this journey would never have started. Thank you for your support and encouragement.

I also wish to express my gratitude to my family for love, support and care. They always believed in me even when I doubted myself.

The last, but certainly not least, I owe by loving thanks to my boyfriend Borys who was always supportive, motivating and patient. He helped me to persist through the hardest times of the PhD.

I would like to acknowledge the sponsorship from European Commission for Marie-Curie Initial Training Network Transcend 'The Understanding TRANSport for Concrete which is Eco friendly, iNnovative and Durable' (EP7/2007-2013).

# Contents

---

<i>Contents</i> .....	iv
<i>Abbreviations and symbols</i> .....	viii
<i>List of tables</i> .....	ix
<i>List of figures</i> .....	x
<b>1. Introduction</b> .....	1
1.1. Motivation to study cement.....	1
1.2. Transcend Project.....	3
1.3. NMR Relaxometry as characterisation technique.....	4
1.4. Thesis objectives and overview of conducted work.....	5
<b>2. Introduction to cementitious materials</b> .....	7
2.1. Cement .....	7
2.1.1. Composition and chemical nomenclature.....	7
2.1.2. Hydration.....	7
2.2. Microstructure models.....	9
2.2.1. Powers and Brownyard's model of cement paste.....	9
2.2.2. C-S-H models .....	11
2.2.2.1. Powers model.....	11
2.2.2.2. Feldman-Sereda model .....	11
2.2.2.3. Colloidal models by Jennings and Tennis (CM-I) and Jennings (CM-II) .....	12
2.2.2.4. Relation to crystalline phases.....	14
2.3. Porosity and methods to characterise pore structure.....	15
2.3.1. Mercury intrusion porosimetry .....	16
2.3.2. Scanning Electron Microscopy.....	17
2.3.3. Gas sorption.....	19
2.3.4. Low temperature Calorimetry .....	21
2.3.5. Small Angle Neutron Scattering and X-rays Scattering.....	22
2.3.6. Nuclear Magnetic Resonance Relaxometry .....	23
2.4. Characteristics of C-S-H .....	23
2.4.1. C/S ratio.....	24
2.4.2. H <sub>2</sub> O content .....	25
2.4.3. Density.....	26
<b>3. NMR relaxometry</b> .....	29
3.1. Excitation and relaxation.....	29
3.2. NMR Relaxometry measurement techniques.....	33
3.2.1. Free induction decay.....	33
3.2.2. CPMG pulse sequence.....	34

3.2.3. Quadrature echo sequence .....	37
3.2.4. $T_1$ measurements.....	38
3.2.4.1. Saturation recovery .....	38
3.2.4.2. Inversion recovery .....	38
3.3. Theory of relaxation.....	39
3.3.1. BBP theory .....	39
3.3.2. Fast exchange model of relaxation for liquids in pores and for pore size analysis	41
3.3.3. Korb model.....	42
3.4. NMR application to cement based materials.....	43
3.4.1. Evolution of relaxation component over hydration time.....	43
3.4.2. 2D exchange experiments.....	45
3.4.3. Pore size distribution .....	46
3.4.3.1. Fast Exchange Model for pore size analysis.....	46
3.4.3.2. Amplitude Model.....	47
3.4.4. Specific surface area.....	49
<b>4. Experimental methods .....</b>	<b>50</b>
4.1. Sample preparation.....	50
4.1.1. Cement composition .....	50
4.1.2. Mixing and curing .....	51
4.1.3. Samples casting and specific preparation for experiments.....	51
4.1.3.1. Samples for sorption isotherm measurements .....	51
4.1.3.2. Samples for temperature dependent curing studies .....	52
4.1.3.3. Samples for activation energy analysis.....	52
4.1.3.4. Samples for water-isopropanol exchange experiments.....	52
4.2. NMR measurements.....	53
4.2.1. Spectrometers .....	53
4.2.2. Quad Echo parameters.....	53
4.2.3. CPMG parameters .....	54
4.2.4. $T_1$ recovery parameters .....	54
4.3. Analysis of NMR data.....	55
4.3.1. Quad echo analysis .....	55
4.3.2. CPMG and $T_1$ recovery analysis.....	56
4.3.2.1. Multi exponential fitting .....	56
4.3.2.2. Inverse Laplace Transform .....	57
4.3.2.3. Exponential stripping .....	58
4.4. Thermogravimetric analysis.....	59
4.5. X-Ray diffraction .....	59
4.6. Sorption Analyser.....	60
4.7. Temperature control .....	61
<b>5. Sorption hysteresis.....</b>	<b>63</b>
5.1. Calibration and assignment of signals.....	63

5.1.1. Is all the water detected by NMR? .....	63
5.1.2. Origin of the solid signal .....	65
5.1.3. Differentiation of the mobile water component .....	66
5.2. Total intensity hysteresis loop.....	68
5.3. Pore-type resolved desorption isotherm.....	69
5.4. Isotherm loops for particular water reservoirs .....	71
5.5. $T_2$ distribution.....	74
5.6. Adsorption mechanism.....	75
5.7. Pore size and specific surface area calculations.....	76
5.7.1. Specific surface area based on adsorption isotherm.....	76
5.7.2. Surface relaxation model .....	77
5.7.2.1. Pore size calculation .....	77
5.7.2.2. Specific surface area calculation.....	78
5.7.3. Amplitude model for calculation of pore size .....	79
5.7.3.1. Modification to the Amplitude model.....	79
5.7.3.2. Pore size calculation .....	82
5.7.3.3. Specific surface area calculation.....	83
<b>6. Influence of curing temperature on cement microstructure .....</b>	<b>85</b>
6.1. C-S-H density and composition calculation model.....	85
6.1.1. C-S-H density .....	85
6.1.2. C-S-H composition .....	86
6.1.3. C-S-H ‘solid’ and ‘bulk’ density .....	87
6.2. Microstructure, C-S-H density and composition at 20°C.....	88
6.2.1. Evolution of different water populations.....	88
6.2.2. Density and C-S-H composition.....	88
6.2.3. C-S-H water content at different humidities.....	94
6.3. Evolution of water population for white cement paste at different temperature.....	95
6.3.1. Uptake of water during hydration.....	95
6.3.2. ‘Free’ water evolution .....	96
6.3.3. Chemically combined water evolution .....	97
6.3.4. C-S-H interlayer and gel water evolution.....	100
6.3.5. $T_2$ relaxation times .....	100
6.4. Density and composition vs temperature .....	101
6.4.1. Input data .....	101
6.4.2. Density of C-S-H at various temperature .....	103
6.4.3. Composition of C-S-H at various temperature .....	104
6.4.4. Mass and volume composition of cement paste at various temperature .....	105
6.4.5. Sensitivity analysis of C-S-H density and composition model .....	106
6.5. Evolution of water population for white cement paste with 10% of silica fume.....	111
6.5.1. Uptake of water during hydration.....	111
6.5.2. ‘Free’ water evolution .....	112
6.5.3. Chemically combined water evolution .....	113

6.5.4. C-S-H interlayer and gel water evolution.....	114
6.5.5. $T_2$ relaxation times .....	115
6.6. Comparison: white cement paste vs white cement paste with silica fume.....	116
6.6.1. Evolution of water populations at 20°C.....	116
6.6.2. The comparison for the full range of temperature .....	117
<b>7. Other experimental insight .....</b>	<b>119</b>
7.1. Activation energy of water dynamic .....	119
7.1.1. Verification of experiments integrity .....	119
7.1.1.1. Water $T_1$ relaxation time as a function of temperature .....	119
7.1.1.2. The total signal intensity as a function of temperature .....	119
7.1.2. Activation energy .....	120
7.1.2.1. The analysis of $T_1$ relaxation measurements.....	120
7.1.2.2. Activation energy .....	121
7.1.2.3. The activation energy calculation for cement paste.....	122
7.2. Water - isopropanol exchange.....	124
7.2.1. Protonated cement paste .....	124
7.2.2. Deuterated cement paste .....	126
7.2.3. Time dependency of exchange .....	127
<b>8. Summary / Conclusion .....</b>	<b>128</b>
8.1. Sorption isotherm .....	128
8.2. Influence of curing temperature on cement microstructure .....	129
8.3. Activation energy of water dynamic .....	130
8.4. Water - isopropanol exchange.....	130
8.5. Future work .....	131
<b>Appendixes.....</b>	<b>132</b>
<b>Bibliography .....</b>	<b>155</b>

# Abbreviations and symbols

<i>AFt</i>	Ettringite – calcium sulfoaluminate	$d_{wat}$	Size of water molecule
<i>AFm</i>	Calcium monosulfoaluminate	$D$	Diffusion coefficient
<i>AMU</i>	Atomic mass unit	$E$	Energy
<i>BPP</i>	Bloembergen, Purcell, Pound	$E_A$	Activation energy
<i>BSE</i>	Backscattered Electrons	$f$	Mass fraction of particular phase
<i>CH</i>	Calcium Hydroxide (Portlandite)	$G$	Magnetic field gradient strength
<i>CPMG</i>	Carr-Purcell-Meiboom-Gill	$G^{(m)}$	Autocorrelation functions
<i>C-S-H</i>	Calcium – Silicate – Hydrate	$\hbar$	Planck constant divided by $2\pi$
<i>FID</i>	Free Induction Decay	$I$	NMR Intensity
<i>Hyd</i>	Hydrogen	$I$	Spin quantum number
<i>Hz</i>	Hertz	$I_{SAS}$	Small Angle Scattering Intensity
<i>ILT</i>	Inverse Laplace Transform	$J$	Spectral density function
<i>LTC</i>	Low Temperature Calorimetry	$k_B$	Boltzmann constant
<i>MIP</i>	Mercury Intrusion Porosimetry	$m$	Mass
<i>NMR</i>	Nuclear Magnetic Resonance	$M$	Magnetization
<i>QE</i>	Quadrature (Quad, Solid) Echo	$M^o$	Magnetisation at equilibrium state
$P_{90}$	90 degree pulse	$n$	Molar content
$P_{180}$	180 degree pulse	$p$	Pressure
$RH, \varphi$	Relative humidity	$Q$	Scattering vector
<i>SANS</i>	Small Angle Neutron Scattering	$r$	Radius
<i>SAXS</i>	Small Angle X-ray Scattering	$r_K$	Kelvin radius
<i>SEM</i>	Scanning Electron Microscopy	$R$	Universal gas constant
<i>SF</i>	Silica Fume	$S$	Surface area
<i>SSA</i>	Specific surface area	$S/N$	Signal to noise ratio
<i>TEM</i>	Transmission Electron Microscopy	$t$	Time
<i>TGA</i>	Thermogravimetric Analysis	$t_\theta$	Duration of excitation pulse
<i>XRD</i>	X-ray diffraction	$t_{nf}$	Thickness of non-freezable layer of adsorbed water
$A_{CSH}$	Specific surface area of C-S-H interlayer pores per unit volume of paste	$T$	Temperature
$A_{gel}$	Specific surface area of C-S-H gel pores per unit volume of paste	$T_1$	Spin-lattice relaxation time
$A_m$	Cross section area of gas molecule	$T_2$	Spin-spin relaxation time
$B_o$	Static magnetic field	$u_m$	Gas amount corresponding to monolayer coverage of surface
$B_I$	Oscillating magnetic field	$V$	Volume
$c$	Cement mass	$V_p$	Volume of paste
$d$	Pore size	$V_{wp}$	Volume of water in unit volume of paste
		$w$	Water mass

$w/b$	Water to binder mass ratio	$\varepsilon$	Surface layer thickness
$w/c$	Water to cement mass ratio	$\theta$	Angle of magnetization rotation
$w/c_{mix}$	Water to cement mass ratio at mixing time	$\theta_c$	Contact angle
$x$	Water fraction of C-S-H	$\theta_i$	Angle of incidence
$x'$	Water fraction for fully saturated C-S-H gel (C-S-H and gel water)	$\theta_{SAS}$	Angle of small angle scattering
$y$	Silicon fraction of C-S-H	$\lambda$	Wavelength / Surface relaxivity
$z$	Calcium fraction of C-S-H	$\mu$	Magnetic moment
		$\mu_o$	Vacuum permeability
		$\nu$	Frequency
$\alpha$	Degree of hydration	$\rho$	Density
$\alpha'$	Mass of reacted $C_3S$ and $C_2S$ divided by mass of anhydrous cement	$\sigma$	Gaussian width
$\alpha_R$	Regularisation parameter for ILT	$\sigma_S$	Surface density of paramagnetic impurities
$\beta_{CH, Et}$	Reciprocal water mass fraction of Portlandite and ettringite	$\tau$	Pulse gap
$\gamma$	Gyromagnetic ratio	$\tau_c$	Correlation time
$\gamma_{CSH}$	Reciprocal water mass fraction of C-S-H		Correlation time associated with molecule's jumps across the surface (hopping time)
$\gamma_S$	Surface tension	$\tau_m$	
$\delta$	Minimum distance for water molecule to approach impurity	$\tau_{rd}$	Repetition time
$\delta_w$	Reciprocal water mass fraction of pore fluid	$\tau_s$	Surface residency time
$\Delta H_{fus}$	Heat of fusion	$\varphi$	Relative humidity
$ \Delta\rho_{SAS} ^2$	Scattering contrast	$\omega$	Circular angular frequency
		$\omega_o$	Larmor frequency

## List of tables

Table 2.1	Chemical notation in cement science.....	7
Table 2.2	Summary of C-S-H density values from literature; additionally the values of C/S and H/S are listed where possible.....	28
Table 4.1	Mineralogical composition of used cements.....	50
Table 4.2	Chemical composition of used cements.....	50
Table 4.3	Characteristic of samples casting.....	53
Table 4.4	Characteristic of experimental analysis.....	58
Table 5.1	Specific surface area of C-S-H interlayer pores, gel pores and both together.....	78
Table 5.2	Gradients and intercepts of fitting lines for (ii) and (iv) stage of drying.....	82
Table 5.3	Calculated size of C-S-H interlayer and gel pores. ....	83

Table 5.4	Calculated specific surface area of C-S-H interlayer and gel pores.....	84
Table 6.1	Parameters for application of the C-S-H density and composition model for white cement paste at 20°C.....	92
Table 6.2	The intensities used to calculate C-S-H density and composition at 20°C. The error in intensities is around $\pm 0.010$ based on standard deviation of the data for multiple samples.....	92
Table 6.3	The C-S-H density and composition for white cement paste at 20°C.....	93
Table 6.4	CH and ettringite mass fractions measured by TGA and XRD, their water mass fractions calculated from mass fractions and measured solid NMR signals for white cement pastes mixed at $w/c_{mix}$ ratio 0.4 and cured underwater at different temperature. The fraction of CH water at 90 days was calculated based on TGA measured at Surrey, while at 28 days on average XRD and TGA results obtained at EPFL.....	99
Table 6.5	Water uptake and degree of hydration for white cement pastes mixed at $w/c_{mix}$ ratio 0.4 and cured underwater at different temperature.....	102
Table 6.6	The intensities used to calculate C-S-H density and composition at 28 and 90 days of hydration. The error in intensities is around $\pm 0.010$ .....	102
Table 6.7	Sensitivity analysis of C-S-H density and composition calculation based on 28 days old paste cured at 20°C with initial parameters $\rho_{CSH} = 2.60 \text{ g/cm}^3$ , $\rho_{CSH}' = 1.91 \text{ g/cm}^3$ , $x = 1.51$ , $x' = 4.58$ , $z = 1.78$ and $y = 0.98$ . The parameters were changed by +5% ( $\uparrow$ ) or -5% ( $\downarrow$ ). Presented are the percentage changes in densities and elements contents. ('c' means that this is the parameter which compensate the 5% change of the given parameter so that $I_{sol} + I_{CSH} + I_{gel} + I_{cap} = 1$ or $I_{Et} = I_{sol} - I_{CH}$ ).....	109
Table 6.8	Extension of the sensitivity analysis of C-S-H density and composition presented in table 6.7. Presented are the percentage changes in densities and elements contents caused by simultaneous changes of two input parameters.....	109
Table 6.9	The mass and water content of CH measured by TGA; the NMR solid signal; ettringite water content calculated as the difference of solid signal and CH water content; and ettringite content based on its water content; at 90 days of hydration for white cement pastes with addition of 10% silica fume mixed at $w/b_{mix}$ ratio 0.4 and cured underwater at different temperature.....	113
Table 7.1	The gradients of the fitting lines of $\ln(1/T_1)$ as a function of temperature for cement paste at 28 (fig 7.3 a) and 90 (fig. 7.3 b) days of hydration and activation energy of water transport in associated pores calculated based on these gradients.....	122
Table 7.2	Signal intensities of different water populations in as prepared and isopropanol exchanged pastes normalised to ignited paste mass and 'as prepared' paste with $H_2O$ .....	125

## List of figures

Figure 1.1	Price of materials and their annual production (adapted from [3]; quoted in [2]).....	1
Figure 1.2	Left – Energy required for production of 1 tonne of material. Right – $CO_2$ emission per tonne of produced material (adapted from [1]).....	2
Figure 1.3	Various length scale of concrete / cement porosity [8].....	3
Figure 1.4	The relationship between the projects. Theme A – blue boxes, Theme B – pink, Theme C - green. Arrows show the links between projects. For project 9, the blue arrows represent the	

	data provision, green arrows - the places of secondment and the pink arrow – collaboration on NMR method.....	4
Figure 2.1	Heat evolution over time for Portland cement (adopted from [30]). A – Initial reaction, B – Induction period, C – Acceleration period, D – Deceleration period.....	9
Figure 2.2	Volume phase composition diagrams by Powers for sealed cured cement paste as reworked by Jensen [37]. The dashed line in the graph for $w/c < 0.42$ indicates the degree of hydration at which hydration stops due to insufficient amount of capillary water.....	10
Figure 2.3	Simplified structure of hydrated paste based on electron micrograph, the zoom area (circle) presents the model of C–S–H structure by Powers (adopted from [36, 37]). .....	11
Figure 2.4	Schematic model of C-S-H morphology proposed by Feldman and Sereda (adapted from [38])	12
Figure 2.5	a) and b): Graphical representation of Low Density (a) and High Density (b) C–S–H as presented in colloidal model of Tennis and Jennings (adopted from [40], [41]); c) Schematic representation of CM-II C-S-H Jennings model (adapted from [6]).....	13
Figure 2.6	The XRD patterns (left) and $^{29}\text{Si}$ NMR spectra (right) for tobermorite $14\text{\AA}$ and C-S-H [44]-[46].....	14
Figure 2.7	Schematic of three layers of tobermorite 1.4 nm nanostructure [29].....	14
Figure 2.8	The pore nomenclature variations for cement porosity (adapted from Geiker [48]). .....	15
Figure 2.9	Range of pore's sizes that can be measured by specific methods – thickness of t-layer not included (adapted from Geiker [51]).....	16
Figure 2.10	Schematic of liquid interaction with the surface. Left: surface wetted; right: surface not wetted [52] .....	16
Figure 2.11	The effect of hydration time for pastes with $w/c = 0.5$ (left) and effect of water to cement ratio at 7 days of hydration (right) on MIP results [55] .....	17
Figure 2.12	a) Exemplary BSE SEM image of the Portland cement mortar; b) Grey level histogram of cement paste; AM refers to anhydrous material [31, 58].....	18
Figure 2.13	Exemplary adsorption isotherms of water vapour for cement pastes mixed at different $w/c$ ratios and cured for 180 days [32].....	20
Figure 2.14	The exemplary heat flow (given as apparent heat capacity) as a function of temperature for cement paste, $w/c = 0.5$ , after 75 days of hydration [63].....	22
Figure 2.15	The exemplary SANS data plotted as $I(Q) \cdot Q^4$ for ordinary Portland cement mixed at $w/c$ ratio 0.4, with and without addition of $\text{CaCl}_2$ , and hydrated for 28 days [66].....	23
Figure 2.16	a) C/S ratio in C–S–H as a function of $\text{Ca}^{2+}$ concentration in solution (adapted from [68]). b) Histogram of Ca/Si frequency for C-S-H in cement pastes 1 day to 3.5 year old as measured by X-ray microanalysis in the TEM (adapted from [47]).....	25
Figure 2.17	TEM micrographs of fine ‘inner’ C-S-H (a) and ‘outer’ CSH: fibrillar (b) and foil-like (c) (adapted from [71]).....	25
Figure 2.18	C–S–H water content ( $\text{H}_2\text{O}/\text{Si}$ ) as a function of Ca/Si ratio. Data obtained after: oven drying at $110^\circ\text{C}$ of $\text{CaO-SiO}_2$ ( $\circ$ ) and $\beta\text{-Ca}_2\text{SiO}_4$ ( $\square$ ) [43]; D-drying of $\text{CaO-SiO}_2$ ( $\Delta$ ) (reported in [74]) and $\text{Ca}_3\text{SiO}_5$ ( $\bullet$ ) [74] .....	26
Figure 3.1	The macroscopic, net magnetization vector ( $M_z^0$ ) of nuclear magnetic moments ( $I = 1/2$ ) in external magnetic field.....	30
Figure 3.2	Main: Pulse sequence diagram for FID experiment – Free Induction Decay; grey region is	

	spectrometer dead time. Inset: a) $P_{90}^x$ along $x'$ -axis rotates $M$ from the equilibrium position to $y'$ -axis, b) Magnetisation decreases as spins dephase.....	33
Figure 3.3	The Hahn spin-echo pulse sequence diagram. The red dash line shows the decay of transverse magnetisation.....	34
Figure 3.4	The Hahn spin-echo experiment: a) application of $P_{90}^x$ along $x'$ -axis, b) de-phasing of spins, c) application of $P_{180}^x$ along $x'$ -axis at time $\tau$ , d) re-phasing of spins, e) refocused magnetisation at time $2\tau$ .....	35
Figure 3.5	The spin-echoes pulse sequence diagram by Carr-Purcell method. The red dash line shows the decay of transverse magnetisation.....	35
Figure 3.6	De-phasing and re-phasing of spins during the CPMG pulse sequence: a) application of $P_{90}^x$ along $x'$ -axis, b) de-phasing of spins, c) application of $P_{180}^y$ along $y'$ -axis, d) re-phasing of spins, e) refocus of magnetisation at time $2\tau$ .....	36
Figure 3.7	Pulse sequence diagram for CPMG sequence. The red dash line shows the decay of transverse magnetisation.....	36
Figure 3.8	Pulse sequence diagram for Quadrature Echo sequence. The solid line presents the observable signal. Dash line shows the sum of solid and liquid signals as it would look only after $P_{90}^x$ . Dash – dot line shows the liquid signal. Grey region is spectrometer dead time.....	37
Figure 3.9	Left: Pulse sequence diagrams for $T_1$ saturation recovery at variable $\tau_{rec}$ . The red dash line shows the recovery of longitudinal magnetisation. Right: a) Magnetisation is saturated, $M = 0$ ; b) Recovery of magnetisation during $\tau_{rec}$ ; c) application of $P_{90}^x$ ; d) reverse magnetisation in transverse plane.....	38
Figure 3.10	Left: Pulse sequence diagrams for $T_1$ inversion recovery. The red dash line shows the recovery of longitudinal magnetisation. Right: a) magnetisation is reversed by $P_{180}^x$ , $M = -M_z$ ; b) recovery of magnetisation during $\tau_{rec}$ ; c) application of $P_{90}^x$ ; d) reverse magnetisation in transverse plane. ....	39
Figure 3.11	$T_1$ and $T_2$ relaxation times for hydrogen spins as a function of correlation time $\tau_c$ [82].....	41
Figure 3.12	Scheme of two-dimensional diffusion process of water molecules on the pore surface containing paramagnetic impurities – $Fe^{3+}$ . $\tau_s$ is the surface residency time, $\tau_m$ is the correlation time associated with molecule's jumps across the surface [92].....	42
Figure 3.13	The $T_1$ - $T_2$ correlation spectra of white cement paste (left) and white cement paste with addition of silica fume (right) cured for 7 days (adapted from [92]).....	45
Figure 3.14	The scheme of pore drying: a) pore full of mobile water, b) two possible ways of pore drying, c) surface water layer staying, d) an empty pore [26]. Circles represent mobile water molecules, crosses are immobile, surface water molecules.....	48
Figure 4.1	The range of temperature at which different phases lose mass (adopted from [108], [109]).....	59
Figure 4.2	Schematic diagram of the system to calibrate the temperature: the copper – constantan thermocouple is merged into the cement sample and allows calculation of actual sample temperature, while the controlling unit displays the temperature recorded by sensor.....	61
Figure 4.3	Temperature of thermocouple merged in cement sample and placed in spectrometer against the sensor display temperature of controlling system. Temperature of sample in spectrometer is controlled in three different ways: by using liquid nitrogen (blue circles), ice (red triangles) and heaters (green squares) combined with gas nitrogen flow. Dashed line is $y = x$ plot.....	62

Figure 5.1	Quad echo signals recorded for white cement paste cure underwater ( $w/c_{mix} = 0.4$ ) for 28 days and equilibrated at 23% relative humidity (black circles). Pulse gap ( $\tau$ ) was: a: 12 $\mu$ s, b: 15 $\mu$ s, c: 19 $\mu$ s, d: 24 $\mu$ s, e: 30 $\mu$ s, f: 37 $\mu$ s, g: 45 $\mu$ s. The lines present fitting for solid (blue) and mobile (red) components; the green line is the total intensity fit. The zero time is taken as the end of first 90° pulse of the sequence.....	63
Figure 5.2	Solid (black squares) and mobile (red circle) signal intensity as a function of pulse gap ( $\tau$ ). The lines are the fits to the data: exponential for solid and linear for mobile signals.....	64
Figure 5.3	Changes in total NMR signal intensity as a function of normalised sample mass during drying of white cement paste.....	65
Figure 5.4	Stack plot of the Quad echo signals recorded for dried Ca(OH) <sub>2</sub> . Pulse gap, $\tau$ , from bottom to top was: 12, 15, 19, 24, 30, 37, 45 and 54 $\mu$ s.....	65
Figure 5.5	The CPMG signal recorded for white cement paste cure underwater ( $w/c_{mix} = 0.4$ ) and equilibrated at 90% RH. The echoes decay data (circles) are presented in form of linear-linear (a) and log-linear (b) plots. Green lines are the fits based on $T_2$ and intensity values obtained from ILT. The inverse Laplace transform of the CPMG decay is presented in (c). In (b) negative baseline points are not shown.....	67
Figure 5.6	The normalised sample mass (left) and total NMR intensity (right) against relative humidity in progressively dried (black squares), wetted (red circles) and re-dried (green triangles) white cement paste.....	68
Figure 5.7	The normalised total signal intensity (black circle) as a function of relative humidity (left) and relative water mass (right). Total signal is further de-composed into chemically combined water (orange diamonds), C–S–H interlayer pore water (red squares), C–S–H gel pore water (green triangles) and ‘free’ water (blue inverted triangles).....	70
Figure 5.8	The schematic morphology of the C–S–H phase at 100, ~25 and ~3% RH. Black lines are Ca–O layers with SiO <sub>4</sub> tetrahedra on both sides. The C–S–H gel water molecules are presented by green triangles. Red squares are the water molecules filling C–S–H interlayer spaces and surface molecules in C–S–H gel pores at lower humidity. At the lowest humidity water molecules in interlayer spaces appear as solid-like and are shown as orange diamonds. ....	71
Figure 5.9	Signal intensity isotherm loops for chemically bound water (a), water in C–S–H interlayer (b) and gel (c) pores and ‘free’ water (d) during desorption (black squares), adsorption (red circles) and re-desorption (green triangles) as a function of relative humidity.....	72
Figure 5.10	Signal intensity isotherm loops for chemically bound water (a), water in C–S–H interlayer (b) and gel (c) pores and ‘free’ water (d) during desorption (black squares), adsorption (red circles) and re-desorption (green triangles) as a function of relative water mass.....	73
Figure 5.11	The $T_2$ relaxation time distribution as a function of relative water mass – lower axis, and RH – upper axis, during desorption (a), adsorption (b) and re-desorption (c) for C–S–H interlayer pore water (green triangles) and gel pore water (blue circles). The light blue boxes span the width of $T_2$ peaks of primary desorption and are provided as a guide to the eye.....	74
Figure 5.12	The fitting lines (thick dashed lines) of the interlayer signal for adsorption. Orange diamonds represent chemically combined water signal, red squares – the C–S–H interlayer pore water, green triangles – the C–S–H gel pore water and blue inverted triangles – the ‘free’ water signals. The black circles show the total water signal.....	76
Figure 5.13	The schematic mechanism of desorption (a) and adsorption (b) processes. Circles represent mobile water molecules, crosses are immobile, surface water molecules.....	76
Figure 5.14	The adsorption isotherm in form of total NMR intensity sample mass (left) and sample mass (right). The green line presents the fitting according to BET equation.....	77
Figure 5.15	The parameters $p$ and $q$ are the gel and interlayer pore sizes respectively, without counting the surface water layer, expressed in number of water molecules; $s_p$ and $s_q$ are the fraction of	

	specific surface area of gel and interlayer pores still filled with water during drying, $g_p$ and $g_q$ are the fraction of surface area covered by water layer.....	79
Figure 5.16	The scheme of five stages of cement paste drying according to NMR, description in text. Orange lines represent chemically combined water signal, red – the C–S–H interlayer pore water, green – the C–S–H gel pore water and blue– the ‘free’ water signals. The black line shows the total water signal.....	80
Figure 5.17	The fitting lines (solid lines) used to calculate the pore sizes from primary (a) and secondary desorption (b). Orange diamonds represent chemically combined water signal, red squares – the C–S–H interlayer pore water, green triangles – the C–S–H gel pore water and blue inverted triangles – the ‘free’ water signals. The black circles show the total water signal.....	81
Figure 6.1	A scheme of water location inside C-S-H at 100% humidity for C–S–H ‘solid’ (left) and ‘bulk’ (right) density calculation. It shows that for C–S–H ‘solid’ density only water molecules in interlayer spaces (red squares) are included in calculation. While for C–S–H ‘bulk’ density water in interlayer and gel pores (green triangles) is considered.....	88
Figure 6.2	Quad echo signals recorded for 28 days old white cement paste (black circles) at eight values of $\tau$ : a: 12 $\mu$ s, b: 15 $\mu$ s, c: 19 $\mu$ s, d: 24 $\mu$ s, e: 30 $\mu$ s, f: 37 $\mu$ s, g: 45 $\mu$ s, h: 54 $\mu$ s. The lines present fitting for solid (blue) and mobile (red) components; the green line is the total intensity fit. The zero time is taken as the end of first 90° pulse of the sequence.....	89
Figure 6.3	Solid echo (black squares) and mobile decay (red circle) signal amplitudes as a function of pulse gap ( $\tau$ ). The lines are the fits to the data: exponential for solid and linear for mobile signals.....	89
Figure 6.4	Graph presents the exponential stripping procedure for CPMG decay (black circles) of 28 days old white cement paste cure underwater ( $w/c_{mix} = 0.4$ ). The grey line is the ‘free’ water fit and blue triangles are the data after subtraction of that fit from CPMG decay. Blue line presents the fit of gel water intensity which further was subtracted, leaving red diamonds. Red line shows the fit for interlayer water signal. The green line is the total fit make as sum of the capillary, gel and interlayer fits.....	90
Figure 6.5	The evolution of different water population for white cement paste mixed at $w/c_{mix}$ ratio 0.4 and cured underwater at 20°C. Orange diamonds represent chemically combined water signal, red squares – the C–S–H interlayer pore water, green triangles – the C–S–H gel pore water and blue inverted triangles – the ‘free’ water signals. The black circles show the total water signal normalized to the initial mass of water at the mixing point. Lines are guide for eyes.....	91
Figure 6.6	The evolution of $T_2$ relaxation time for water populations of white cement paste mixed at $w/c_{mix}$ ratio 0.4 and cured underwater at 20°C. Red squares represent the $T_2$ relaxation time for C–S–H interlayer pore water, green triangles for C–S–H gel pore water and blue inverted triangles for ‘free’ water.....	91
Figure 6.7	The C-S-H water content isotherm as a function of C-S-H water mass (left) and relative humidity (right). The black circles represent the C-S-H water content $x'$ , including gel pores, which is divided into interlayer ‘solid’ water content $x$ (red squares), gel water content (green triangles) and solid-like surface water (orange diamonds).....	94
Figure 6.8	Uptake of water mass as a function of hydration time for white cement pastes mixed at $w/c_{mix}$ ratio 0.4 and cured underwater at different temperature: blue inverted triangles: 10°C; black circles: 20°C; cyan diamonds: 30°C; red squares: 40°C; orange left-triangles: 50°C; and green triangles: 60°C.....	96
Figure 6.9	Consumption of ‘free’ water for white cement pastes mixed at $w/c_{mix}$ ratio 0.4 and cured underwater at different temperature. The hydration time of sample at which the initial fraction of ‘free’ water is consumed by 50% is shown as blue squares, by 80% as red circles and by 90% as green triangles. The black lines are exponential fits to the data. (The consumption of	

	‘free’ water by 90% at 60°C is obtained by extrapolation as it was not achieved within experimental time).....	97
Figure 6.10	Evolution of ‘free’ water as a function of hydration time for white cement pastes mixed at $w/c_{mix}$ ratio 0.4 and cured underwater at different temperature: blue inverted triangles: 10°C; black circles: 20°C; cyan diamonds: 30°C; red squares: 40°C; orange left-triangles: 50°C; and green triangles: 60°C. Lines are guides for eyes.....	97
Figure 6.11	Evolution of chemically combined water as a function of hydration time for white cement pastes mixed at $w/c_{mix}$ ratio 0.4 and cured underwater at different temperature: blue inverted triangles: 10°C; black circles: 20°C; cyan diamonds: 30°C; red squares: 40°C; orange left-triangles: 50°C; and green triangles: 60°C. Lines are guides for eyes.....	98
Figure 6.12	Evolution of C-S-H interlayer (left) and gel (right) pore water as a function of hydration time for white cement pastes mixed at $w/c_{mix}$ ratio 0.4 and cured underwater at different temperature: blue inverted triangles: 10°C; black circles: 20°C; cyan diamonds: 30°C; red squares: 40°C; orange left-triangles: 50°C; and green triangles: 60°C.....	100
Figure 6.13	The evolution of $T_2$ relaxation time for water populations of white cement pastes mixed at $w/c_{mix}$ ratio 0.4 and cured underwater at different temperature. The upper graph shows the $T_2$ of ‘free’ water, the middle graph - $T_2$ of C-S-H gel pore water and the lower graph - $T_2$ of C-S-H interlayer space water. Blue inverted triangles: 10°C; black circles: 20°C; cyan diamonds: 30°C; red squares: 40°C; orange left-triangles: 50°C; and green triangles: 60°C. Lines are guides for eyes.....	101
Figure 6.14	C-S-H density as a function of the curing temperature for 28 days (triangles and diamonds) and 90 days old (squares and circles) white cement pastes mixed at $w/c_{mix}$ ratio 0.4 and cured underwater. The blue diamonds and red circles represent the C-S-H bulk density, inclusive of the gel water; green triangles and black squares represent the C-S-H ‘solid’ density, exclusive of the gel pore water.....	103
Figure 6.15	An arrangement of calcium silicate layers ( $l$ ) –black strips, and water ( $l-1$ ) layers – blue dotted strips presenting the increase of the $l/(l-1)$ ratio.....	103
Figure 6.16	Water content in the C-S-H as a function of the curing temperature for 28 days (left) and 90 days old (right) white cement pastes mixed at $w/c_{mix}$ ratio 0.4 and cured underwater. The red circles represent the water in the C-S-H, including the gel water ( $x'$ ); black squares represent water in the C-S-H excluding the gel pore water ( $x$ ).....	104
Figure 6.17	Ca/(Si+Al) ratio (left) and Si content (right) in the C-S-H as a function of the curing temperature for 28 days (red circle) and 90 days old (black squares) white cement pastes mixed at $w/c_{mix}$ ratio 0.4 and cured underwater.....	105
Figure 6.18	Mass and volume composition for 28 days (a and c) and 90 days old (b and d) white cement pastes mixed at $w/c_{mix}$ ratio 0.4 and cured underwater. From bottom: the orange region corresponds to Portlandite, yellow to ettringite, red to the C-S-H, green to gel pore water, blue to joined ‘free’ and voids water and dark cyan to unreacted cement.....	106
Figure 6.19	Uptake of water mass as a function of hydration time for white cement pastes with addition of 10% silica fume mixed at $w/b_{mix}$ ratio 0.4 and cured underwater at different temperature: blue inverted triangles: 10°C; black circles: 20°C; cyan diamonds: 30°C; red squares: 40°C; orange left-triangles: 50°C; and green triangles: 60°C.....	111
Figure 6.20	Evolution of ‘free’ water as a function of hydration time for white cement pastes with addition of 10% silica fume mixed at $w/b_{mix}$ ratio 0.4 and cured underwater at different temperature: black circles: 20°C; cyan diamonds: 30°C; red squares: 40°C and green triangles: 60°C. The upper plot shows the evolution of total signal intensity. Lines are guides for eyes.....	112
Figure 6.21	Evolution of chemically combined water as a function of hydration time for white cement pastes with addition of 10% silica fume mixed at $w/b_{mix}$ ratio 0.4 and cured underwater at different temperature: blue inverted triangles: 10°C; black circles: 20°C; cyan diamonds:	

	30°C; red squares: 40°C; orange left-triangles: 50°C; and green triangles: 60°C. Lines are guides for eyes.....	113
Figure 6.22	Evolution of C-S-H interlayer (left) and gel (right) pore water as a function of hydration time for white cement pastes with addition of 10% silica fume mixed at $w/b_{mix}$ ratio 0.4 and cured underwater at different temperature: black circles: 20°C; cyan diamonds: 30°C; red squares: 40°C and green triangles: 60°C.....	114
Figure 6.23	The evolution of $T_2$ relaxation time for water populations of white cement pastes with addition of 10% silica fume mixed at $w/b_{mix}$ ratio 0.4 and cured underwater at different temperature. The upper graph shows the $T_2$ of 'free' water, the middle graph - $T_2$ of C-S-H gel pore water and the lower graph - $T_2$ of C-S-H interlayer space water. Black circles: 20°C; cyan diamonds: 30°C; red squares: 40°C; and green triangles: 60°C. Lines are guides for eyes.....	115
Figure 6.24	The evolution of different water population for white cement paste with 10% addition of silica fume mixed at $w/b_{mix}$ ratio 0.4 and cured underwater at 20°C. Orange diamonds represent chemically combined water signal, red squares - the C-S-H interlayer pore water, green triangles - the C-S-H gel pore water and blue inverted triangles - the 'free' water signals. The black circles show the total water signal normalized to the initial mass of water at the mixing point. Open black symbols are corresponding signals for reference white cement paste cured at 20°C.....	116
Figure 6.25	The evolution of $T_2$ relaxation time for white cement paste with 10% addition of silica fume mixed at $w/b_{mix}$ ratio 0.4 and cured underwater at 20°C. Red squares represent the C-S-H interlayer pore water, green triangles - the C-S-H gel pore water and blue inverted triangles - the 'free' water $T_2$ relaxation times. Open black symbols are corresponding times for reference white cement paste cured at 20°C.....	117
Figure 6.26	The evolution of different water population for white cement paste (top) and white cement paste with silica fume (bottom) over the time of hydration for samples cured underwater at various temperature. Total signal is de-composed into chemically combined water (orange), water in C-S-H interlayer spaces (red), C-S-H gel pores (green) and 'free' water (blue). The total signal fractions go above 1 indicating the underwater curing.....	118
Figure 7.1	The changes in the $T_1$ relaxation time of water as a function of temperature. Red circles are the author experimental data, black squares are the data reported by Krynicki [125].....	119
Figure 7.2	Total signal intensity for white cement paste cured underwater ( $w/c_{mix} = 0.4$ ) for 28 (a) and 90 (b) days of hydration as a function of temperature at which measurements were performed.....	120
Figure 7.3	The changes in $\ln(1/T_1)$ as a function of temperature for white cement paste at 28 (a) and 90 (b) days of hydration based on multi-exponential analysis with constrained intensities. Lines are the linear fit to the data.....	121
Figure 7.4	The activation energy dependence on $T_1$ relaxation time for white cement paste 28 (red circles) and 90 (green triangles) days of hydration. The blue diamond represents the approximated water activation energy based on fitting line of $\ln(1/T_1)$ of experimental data presented in figure 7.1.....	123
Figure 7.5	The $T_2$ relaxation times distribution of as prepared paste with H <sub>2</sub> O (top), exchanged with isopropanol (middle) and exchanged back with H <sub>2</sub> O (bottom) - analysis performed by Dr R. Kowalczyk.....	125
Figure 7.6	The increase of sum interhydrate and capillary pore water intensity (blue triangles) and decrease of sum C-S-H interlayer and gel pore water intensity (red squares) for isopropanol exchange of large paste sample. The lines are the exponential fits - solid with one and dashed with two components.....	127

*“People need not fear the unknown because they are capable of achieving what they need and want”*

Paulo Coelho

Challenges have accompanied science and technology for millennia. Without them it would not be possible to achieve any progress. It is thanks to the will of learning and the perseverance in understanding the rules and laws responsible for various processes, that the enormous progress in building materials technology have been possible.

However, as time passes new questions, concerns and tasks appear, driving scientists to face them and resolve.

# 1. Introduction

## 1.1. MOTIVATION TO STUDY CEMENT

Concrete is a building material. Nowadays it is the most manufactured man-made material world wide with almost three tons used for each human annually [1]. It has become a crucial part of our everyday life as it is used in the majority of buildings and in many other infrastructural applications. The reasons for the large, and still increasing, consumption of concrete are various. First, concrete is unrivalled in terms of price per ton (fig. 1.1). It benefits as it is easy to make and can be formed in nearly any shape [2]. The energy consumed to produce one tonne of concrete is much less than for other building material – fig. 1.2 left. Other significant properties factors in favour of concrete are durability, strength and water-tightness [1].

Concrete is composed of anhydrous cement powder, aggregates, sand, and water. Cement, the most important component, reacts with water causing concrete setting and hardening. The formed paste bonds all the other concrete components together. Cement paste comprises of hydrates, porosity and unreacted cement grains. The main hydrate created is calcium silicate hydrate (C-S-H) that provides the binding properties.

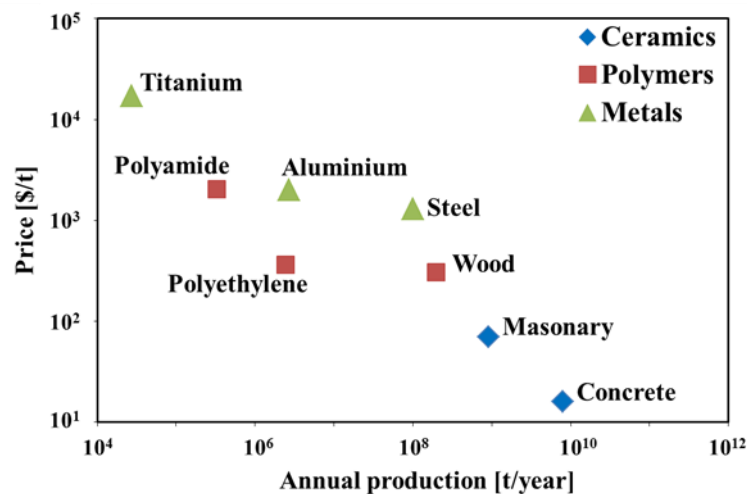


Figure 1.1 Price of materials and their annual production (adapted from [3]; quoted in [2]).

Despite all the above positive features of concrete, an important aspect to consider is the emission of carbon dioxide (CO<sub>2</sub>) during cement production. CO<sub>2</sub> emissions result primarily from the burning of fuel to heat limestone to make anhydrous cement powder (~40%) and from the breakdown of the limestone itself during that process (~50%). The remaining 10% comes from electricity use and transportation.

CO<sub>2</sub> emission from cement production is relatively small compared to other materials on a tonne for tonne basis (fig. 1.2 right). However, the enormous amount of cement produced each year worldwide (4.0 billion tonnes in 2013 [4]) results in 5% of global non-natural CO<sub>2</sub>

emission. [1]. Given this fact, the cement industry places high importance on the reduction of CO<sub>2</sub> emissions.

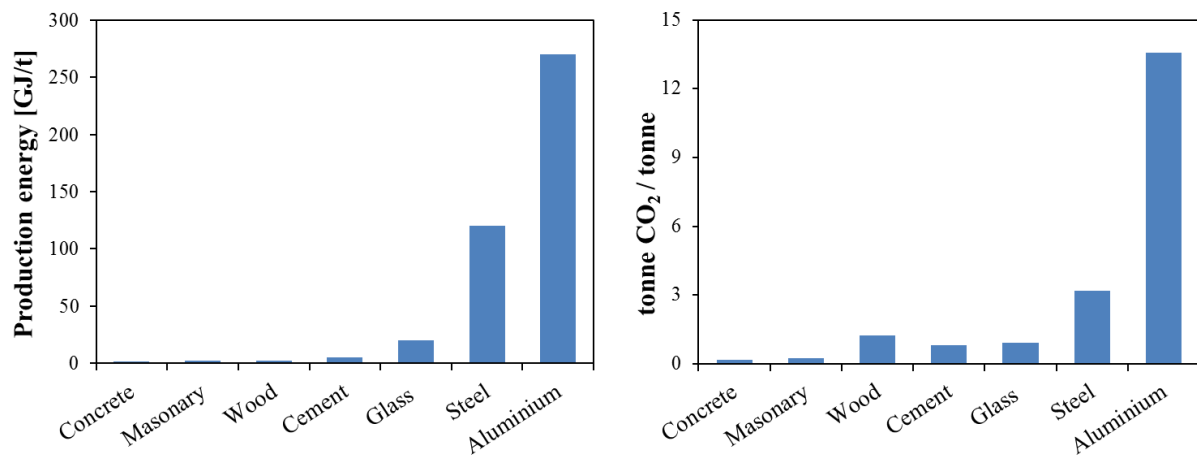


Figure 1.2 Left – Energy required for production of 1 tonne of material. Right – CO<sub>2</sub> emission per tonne of produced material (adapted from [1]).

Improvements have been made to cement manufacturing plant technology increasing energy efficiency to nearly 80%. Only small progress can now be made in the combustion process. Therefore, one of the biggest and the most serious challenges ahead for the cement industry is to reduce demand for cement clinker<sup>1</sup> production. The route to achieve that goal is production of alternative, blended cements where clinker is partially substituted by so-called Supplementary Cementitious Materials (SCMs). In a group of SCMs are by-products of different industries, like fly ash, slag and silica fume as well as the other raw materials like raw-limestone and natural pozzolans. Exploiting SCMs would facilitate making and designing cementitious materials that have as good as, or better, performance than traditional materials: rate of reaction, service life, strength, permeability and durability.

The internal porous microstructure of cement paste and the dynamics of water within it are linked to all forms of degradation as well as to mechanical properties of hydrated cementitious materials. Porosity and the state of water within it are an innate characteristic of cementitious materials. They depend hugely on the materials' water to cement ratio, age, curing conditions and degree of saturation. The porosity of cementitious materials spans over a wide range of lengths (fig. 1.3) with millimetre size air voids and micrometre capillary pores enclosed between hydrates. At the lowest nano-level there are pores within C-S-H: interlayer pores between tetrahedral silica layers and gel pores enclosed between locally aggregated stacks of layers.

A better understanding of the microstructure and pore-water interaction within cementitious materials is required to make alternative materials more commonly used and to improve durability of concrete constructions. A better understanding would also bring insight

<sup>1</sup> product of sintering limestone with silica, alumina and iron oxide containing materials

into hydration process, allow characterisation of materials and prediction of their properties. The establishment of rapid and non-invasive / non-destructive mean to characterise cement microstructure, with emphasis on C-S-H gel, will contribute to the great progress in cement industry and allow controlling and improving long-term performance by enabling study of the relationship between evolving microstructure and performance. The study of micro and nano structure of C-S-H and mobility of water within it is very important but, at the same time, challenging as it is a fragile, heterogeneous and nano-porous material with a lack of long range order. Moreover, the changes in its structure, morphology, density and composition occur for different cement chemistry, water to cement ratios, at various ages and curing conditions (humidity, temperature, saturation). For all of these reasons, despite ongoing extensive research in cement society [5]–[7], that C-S-H structure has been not unambiguously characterised and several alternate models have been proposed.

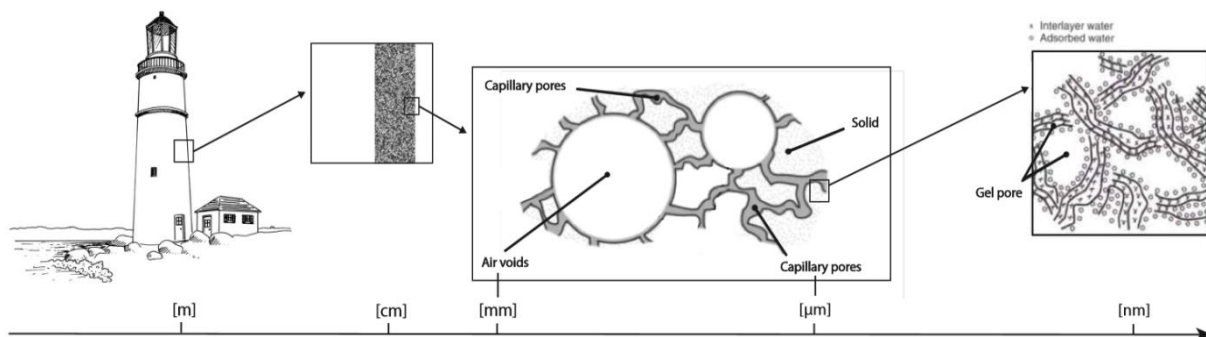


Figure 1.3 Various length scale of concrete / cement porosity [8].

## 1.2. TRANSCEND PROJECT

The work performed in the framework of this thesis is the part of the Marie – Curie Initial Training Network TRANSCEND; a scientific programme funded by European Commission. The programme name stands for ‘The Understanding **TRAN**Sport for **CON**crete which is **Eco** friendly, **iN**novative and **DUR**able’ [9].

The main aim of the programme is to describe and predict water transport in cements and concretes. The unique characteristic of the programme is the bottom-up approach. The knowledge is gained by understanding first the transport at the lowest level and then by climbing up the hierarchy of length scales. Modelling of water dynamics is directly connected with experimental and validation studies.

The TRANSCEND programme has been divided into three specific themes.

Theme A comprises five projects on the computer modelling of water dynamics in cement. The study starts at the sub-nanometre and nanosecond level (P1) with molecular dynamics modelling of transport within C-S-H layered structure. It goes on the level of the C-S-H gel pores and paste structure with Lattice Boltzmann modelling (P2,3) and reaches the level of concrete structures measured in meters with finite elements simulations (P4,5).

Theme B concerns experimental work to provide data-base required as the input for modelling. The first group of projects is concentrated on characterisation of C-S-H



The signal which follows the excitation pulse sequence in experiments provides valuable information. The signal amplitude or more accurately magnetization of relaxation time components is directly proportional to the number of spins which create a particular environmental group of protons. Therefore, NMR relaxometry can quantify those populations. NMR allows to differentiate between states of water and pore sizes as different mobility is manifested by different signal lifetimes, known as  $T_2$  relaxation time. According to fast exchange model the observed rate of relaxation ( $1/T_2$ ) is proportional to surface to volume ratio of the pore [10]. A second relaxation time  $T_1$  may also be used. NMR is sensitive to the mobility of hydrogens over the wide range of time and length scale starting from nanometres level. Therefore, NMR ‘sees’ and responds to all water hydrogens.

NMR relaxometry is the method successfully applied to characterise microstructure and liquid dynamics in porous media. It provides valuable information for broad range of systems and material sciences: mesoporous zeolites (*e.g.* [11]); clays (*e.g.* [12]); soils and earth science (*e.g.* [13]); reservoir rocks and fluids within them for petroleum engineering (*e.g.* [14]); polymers film formation and water interactions (*e.g.* [15]); food (*e.g.* [16]); pharmaceutical and biological systems (*e.g.* [17]).

The NMR technique has the advantage for studying porous media including relevant for this thesis cementitious materials as it is non-destructive and non-invasive. It measures virgin samples - does not require drying or vacuum procedure for preparation. The delicate structure of C-S-H gel stays intact by the NMR measurement. It also benefits as samples can be study continuously during hydration.

NMR relaxation time analysis has been extensively used to investigate the microstructure of cementitious materials. The early NMR studies to follow the hydration of Portland cement and tricalcium silicate pastes were conducted by Blinc *et al* [18] in the late 1970s. Later on, in the 1990s, the first attempts to evaluate the pore size distribution in cement pastes based on NMR data were made by Halperin *et al* [10] using fast exchange model of relaxation based on the concept that water relaxes at pore surface giving an observed relaxation rate proportional to the surface to volume ratio. There followed several extensive studies of  $^1\text{H}$  relaxation during cement paste hydration [19]–[24] which revealed a hierarchy of relaxation times and calculated pore sizes. However, for various reasons including variability in sample preparation, subtle differences in the measurement methods, a lack of signal intensity calibration and differences of opinion and understanding led to a broad spectrum of interpretations and assignments of  $T_2$  to water reservoirs. The study by Holly *et al* [25] was the first to propose an assignment that essentially reflects current understanding of cement paste microstructure. Further applications and extensions of the NMR technique have been introduced and allowed to extend the knowledge on cement. They will be broadly described in this thesis.

#### **1.4. THESIS OBJECTIVES AND OVERVIEW OF CONDUCTED WORK**

The purpose of this thesis is to obtain better insight into the development of cement microstructure and pore-water interaction in cementitious materials by using  $^1\text{H}$  Nuclear Magnetic Resonance Relaxometry.

The aim of this work is to demonstrate that NMR experiments are fully quantitative and deliver more detailed information about cement microstructure than other methods.

$^1\text{H}$  NMR relaxometry is used to measure the first pore-type resolved sorption isotherm. In that way it is possible to assess how changes in humidity and specific processes: desorption, adsorption and secondary desorption, affect amplitude and  $T_2$  relaxation time of water components and hence nano and microstructure of cement paste. Relaxation analysis of water in white cement paste during progressive drying and rewetting in a controlled relative humidity environment is performed. To identify and quantify all water within samples two NMR pulse sequences are applied: Quadrature echo and Carr-Purcell-Meiboom-Gill (CPMG) sequences. The signal is decomposed into chemically combined water, water in C-S-H interlayer spaces, gel and interhydrate/capillary pores. In this way a pore specific desorption / adsorption isotherm is generated. The experiments also give opportunity to compare C-S-H interlayer and gel pore sizes measured by both signal amplitude [26] and  $T_2$  relaxation time [27]. The specific surface areas of those pores are also evaluated.

The thesis shows how quantitative data obtained by NMR relaxometry technique can provide a complete description of cement paste, C-S-H chemical composition and density. The presented calculation model is the result of collaborative work with Arnaud Muller – Transcend student placed at École Polytechnique Fédérale de Lausanne in Switzerland (P8).

The influence of curing temperature on nano and microstructure of cement pastes is of great interest.  $T_2$  relaxation experiments are used in order to follow the evolution of particular water components – evolution of cement nanoporosity, during hydration at different temperatures (10 to 60°C) up to 90 days. The C-S-H density and composition within white cement paste are assessed at various curing temperature. The influence of cement composition is also investigated by examining white cement paste with and without addition of 10% of silica fume. Quadrature Echo and CPMG measurements are utilised in this part of thesis.

NMR relaxometry is used to evaluate the impact of solvent (isopropanol) replacement on cement paste, method used for arresting hydration. The mechanism of water – isopropanol exchange is evaluated through the observation of changes in amplitude and  $T_2$  relaxation time of hydrogen populations. This part of thesis is the outcome of joint research between the author and Dr Radoslaw Kowalczyk. The NMR measurements are performed on cement pastes prepared with protonated and deuterated water, before and after exchange with regular and partially deuterated isopropanol. The reversibility of the exchange process and connectivity of C-S-H interlayer and gel pores with interhydrate and capillary pore network are shown.

To support computer modelling of water dynamics in cement, the activation energy for relaxation processes in associated pore types is determinate. NMR  $T_1$  relaxation measurements of white cement paste are made as a function of temperature at which the relaxation parameters are measured.

## 2. Introduction to cementitious materials

### 2.1. CEMENT

#### 2.1.1. Composition and chemical nomenclature

Calcium, silicon, aluminium, iron and oxygen are the five essential elements for making anhydrous cement powder. The most typical combination of raw materials to create Portland cement clinker is limestone as a source of calcium oxide and smaller amounts of clay or shale for silicon, aluminium and iron oxides [28]. Table 2.1 lists the relevant oxides in standard chemical and abbreviated cement science notation.

Table 2.1 Chemical notation in cement science.

<i>Cement science notation</i>	<i>Chemical composition</i>	<i>Oxide</i>
C	CaO	Calcium oxide
S	SiO <sub>2</sub>	Silicon oxide
A	Al <sub>2</sub> O <sub>3</sub>	Aluminium oxide
F	Fe <sub>2</sub> O <sub>3</sub>	Iron (III) oxide
$\bar{S}$ / \$	SO <sub>3</sub>	Sulphur trioxide
$\bar{C}$	CO <sub>2</sub>	Carbon dioxide
H	H <sub>2</sub> O	Dihydrogen oxide / Water

In cement manufacture the raw materials are blended together and ground in accurate proportions. The mix is then put in a kiln where it is heated to the temperature of 1450°C. As a result of heating, chemical and physical changes occur. The four main clinker phases are created: tricalcium silicate – C<sub>3</sub>S called alite (50-70% of normal Portland cement clinker), dicalcium silicate – C<sub>2</sub>S called belite (15-30%), an aluminate phase – C<sub>3</sub>A (5-10%) and a ferrite phase – C<sub>4</sub>AF (5-15%). In the final stage of production clinker is ground with typically five percent of gypsum to produce anhydrous cement powder. The gypsum, or an alternate source of calcium sulphate, controls the rate of cement setting by slowing-down the aluminate and ferrite reactions with water [28].

#### 2.1.2. Hydration

Mixing cement powder with water triggers a series of dissolution-precipitation reactions which transform these solid and liquid phases into a rigid solid material with water-filled porosity. The processes which occur during hydration include: dissolution, diffusion,

nucleation, growth, complexation<sup>2</sup> and adsorption. The hydration process is complex as different cement phases react simultaneously with water, interact with each other and modify the chemistry of the pore liquid phase. Nevertheless, there are characteristic reactions [29], [30].

The calcium silicates,  $C_3S$  and  $C_2S$ , reactions with water result in formation of Calcium – Silicate – Hydrates (C-S-H) and Calcium Hydroxide (CH also called Portlandite) [29]:



The exact stoichiometry of these reactions is not defined as the C/S and H/S ratios in C-S-H are not constrained and depend on the condition at which reactions occur. C-S-H is the main product of cement hydration occupying approximately 50-65% of hydrated paste. It forms mostly around cement grains. The second primary product of hydration (CH) is crystalline and has defined formula -  $Ca(OH)_2$ . CH constitutes about 20-25% of paste [29], [31].

The hydration of calcium aluminate,  $C_3A$ , in presence of calcium sulphate results in the creation of calcium trisulphoaluminate hydrate called ettringite (AFt). When sulphate is consumed  $C_3A$  reacts with ettringite and water to produce calcium monosulphoaluminate hydrate (AFm) [29]:



Most of hydration reactions exhibit the volume changes contributing to the chemical shrinkage of the paste and creation of porosity. It is attributed to lower specific volume of bound water in hydrates in comparison with free water [29].

In general the hydration process can be divided into four stages - figure 2.1. The first stage – initial reaction, is characterised by intensive release of heat due to wetting and dissolution of cement grains. Then heat flow decreases and reaches minimum as water becomes supersaturated. This indicates the induction - slow reaction, period. Following that, during acceleration period, the rapid increase in heat flow is observed. It is caused by rapid nucleation and growth of C-S-H and CH. The maximum level of heat flow indicates the beginning of deceleration stage. During that period the growth of C-S-H and CH is slow and believed to be controlled by diffusion of reactants through already formed hydrates. At that stage, in presence of calcium sulphate, the secondary formation of ettringite, followed by creation of AFm phase, also occurs [30].

---

<sup>2</sup> chemical reactions between ions that lead to formation of ion or molecular complexes [30]

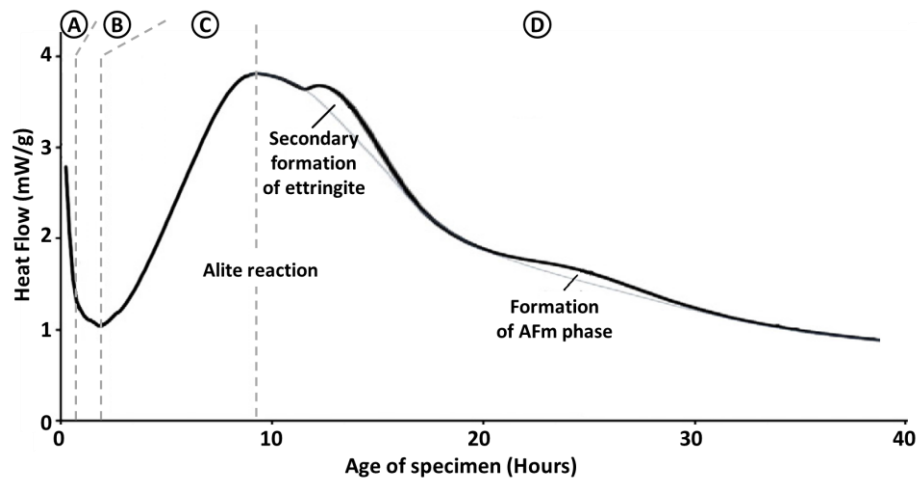


Figure 2.1 Heat evolution over time for Portland cement (adapted from [30]). A – Initial reaction, B – Induction period, C – Acceleration period, D – Deceleration period.

## 2.2. MICROSTRUCTURE MODELS

### 2.2.1. Powers and Brownayrd's model of cement paste

The most widely used model of cement microstructure was developed by Powers and Brownayrd in the 40's [32], [33]. This model was based on measurements of water vapour adsorption and of the non-evaporable water content. The model allows quantitative calculation of the volume composition of cement paste.

Powers and Brownayrd divided the water within cement paste into non-evaporable and evaporable. Non-evaporable water is considered as that persists in paste at the pressure below  $5 \cdot 10^{-5}$  mmHg at  $23^{\circ}\text{C}$ . It represents water within both non-colloidal ( $\text{OH}^-$  groups in  $\text{Ca}(\text{OH})_2$  and crystallization water in calcium sulfoaluminates) and colloidal materials (calcium silicate hydrate gel). All non-evaporable water in the model is treated as one entity. The colloidal and non-colloidal hydrates are generally called cement gel and no division into particular hydrates is made within model. The volume of non-evaporable water and cement powder is hence the absolute volume of cement gel - solid phase.

The evaporable water exists in paste at higher pressure. It is divided into gel and capillary water. The gel water is that contained in the pores of cement gel. Its amount is defined as  $4 \cdot V_m$  where  $V_m$  is the volume of water required for monolayer coverage of solid phase obtained through BET theory. That value derives from two observations. First, the adsorption curves<sup>3</sup> for all pastes are the same at lower pressure ( $RH < 0.45$ ). Second, they are the same in whole range of pressure for all mature pastes mix at lower water to cement ratio,  $w/c < 0.32$ . When the evaporable water content of saturated paste equals to  $4 \cdot V_m$ , the porous cement gel fills all the originally water filled space and the paste porosity is that of cement gel.

When the evaporable water content exceeds  $4 \cdot V_m$  the excess water occupies the space outside of the cement gel and is called capillary water. The capillary water, if present in the

<sup>3</sup>  $w/V_m$  as a function of relative humidity,  $RH$ , where  $w$  is the quantity of vapour adsorbed

microstructure, fills pores at higher pressure ( $RH > 0.45$ ). Its amount is higher for paste with bigger  $w/c$  ratio and decreases with hydration time.

As the rate of capillary water consumption is faster than the rate of filling the capillary pores with cement gel, a contraction in the volume appears called chemical shrinkage. In the case when the exterior water is available that volume becomes filled with water. However, for sealed cured paste the pores becomes partially empty.

In general Powers and Brownyard found that the content of non-evaporable water ( $w_n$ ) is between 0 and  $\sim 0.25$  g/g of anhydrous cement. The widely quoted value of gel porosity in cement gel, based on Powers and Brownyard model, is about 0.28 [29], [34], [35].

The cement paste as presented in original work of Powers and Brownyard's [32], [33] consists of hydration products considered together as cement gel, gel and capillary pore water as well as pores due to chemical shrinkage. In further work Powers introduced the unreacted cement as a part of the microstructure [36]. The calculations of volume composition based on the model have been repeated, used and slightly refined in further publications [28], [34], [37]. The diagrams of paste volume composition evaluated by Jensen [37] based on extended Powers and Brownyard model are presented in figure 2.2. They presents the general tendency during hydration as cement and capillary water are consumed at the expense of created cement gel with gel porosity embedment into it. Additionally, due to chemical shrinkage part of the pores becomes empty.

The important factor affecting the course of hydration is the sufficient quantity of water and space available for all hydration products and hydration to proceed. The critical, minimal, amount of water,  $w/c^*$  ratio, required for complete hydration to occur is given by Taylor [28] to be typically about 0.38. The minimum value is also determinate by Hansen [34] depending

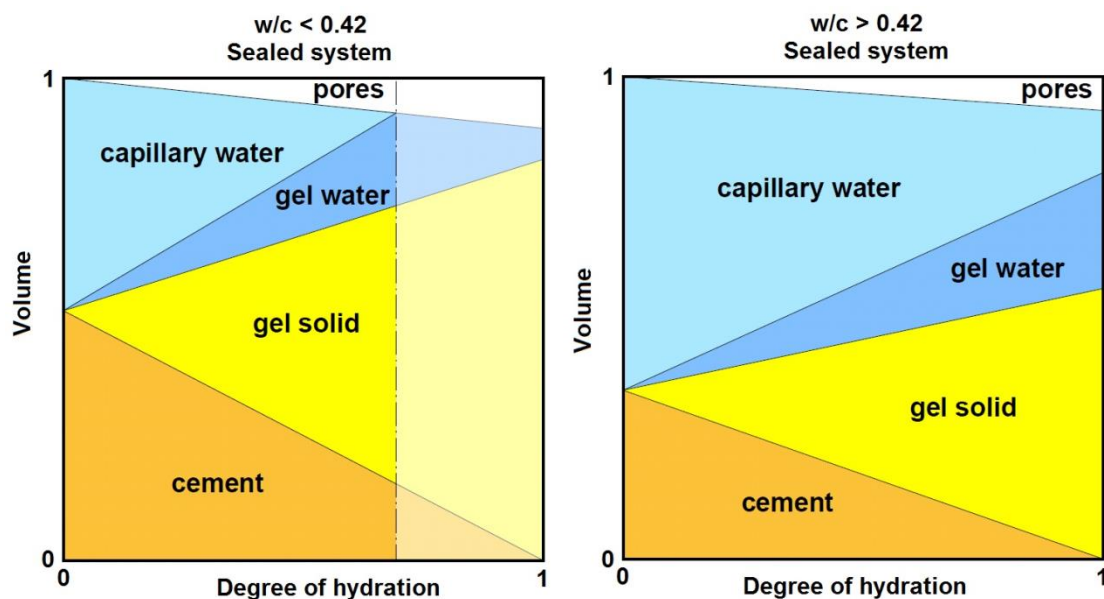


Figure 2.2. Volume phase composition diagrams by Powers for sealed cured cement paste as reworked by Jensen [37]. The dashed line in the graph for  $w/c < 0.4$  indicates the degree of hydration at which hydration stops due to insufficient amount of capillary water.

on the availability of external source water. If there is supply of water from outside, underwater curing,  $w/c^* = 0.36$ . When no extra water is available, sealed curing, critical  $w/c^* = 0.42$ . As shown in fig. 2.2 above that value the paste reaches the full hydration (right graph) whereas below the hydration stops when all capillary water is used up, all capillary space is filled by cement gel, as indicated by shadow part on left graph.

## 2.2.2. C-S-H models

### 2.2.2.1. Powers model

The first C-S-H model was proposed by Powers [36]. Its origin is based on the water adsorption results obtained by Powers and Brownyard [32], [33]. Considering the high specific surface area of gel pores ( $\sim 200 \text{ m}^2/\text{g}$  of cement for mature pastes), the small gel pore (2-4 nm) and the solid unit sizes ( $< 14 \text{ nm}$ ) Powers suggested that the solid hydrate is finely subdivided, colloidal material containing the non-evaporable water [32], [33]. Powers further defined, based on electron microscopy, the C-S-H gel particles as fibrous with straight edges. The regions of parallel particles with gel pore water between them are arranged in rigid independent blocks (figure 2.3 circle). These blocks create the cross-linked network with the amorphous material in between them. Even though the C-S-H structure is disordered it is closely similar to the crystalline mineral – tobermorite, structure [36].

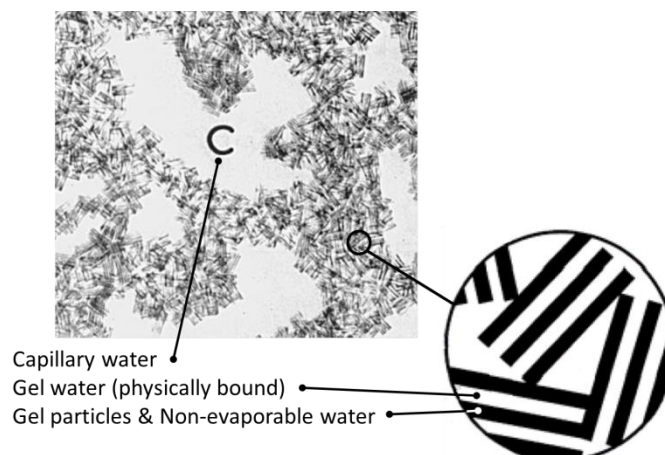


Figure 2.3 Simplified structure of hydrated paste based on electron micrograph, the zoom area (circle) presents the model of C-S-H structure by Powers (adapted from [36], [37])

### 2.2.2.2. Feldman-Sereda model

The next model of C-S-H has been presented by Feldman and Sereda in late 60's [38], [39]. It was based on the examination of sorption and length changes as a function of relative humidity as well as relation of mechanical properties (strength and Young' modulus) to relative humidity, porosity and method of sample preparation.

This model also considers that C-S-H is a layered structure composed of tetrahedral silica sheets with alternating layers of water and calcium ions. Nevertheless, the C-S-H layers are more connected and disorganized (figure 2.4) in comparison with Powers' model. The state of

water within C-S-H in this model has been differentiated based on reversible and irreversible behaviour of water upon scanning isotherm loops. The water between layers is inferred as the structural and chemical component of C-S-H, not as ‘pore’ water. This water is equivalent of the gel pore water in Powers model. It is considered irreversible water as its removal during desorption process (slow but progressive, with the biggest change at lower humidities) differs from adsorption path (gradual uptake over whole range of humidity). The reversible water is that physically held on the outer surfaces of the C-S-H layers.

The schematic representation of C-S-H proposed by Feldman and Sereda – figure 2.4, comprises also the spaces between disordered layers of C-S-H. There is no distinction regarding these spaces in the original descriptions of the model [38], [39]. In terms of current understanding and interpretation of Feldman and Sereda model the C-S-H forms stacks of quasi continuous sheets and gel pores are between imperfections in the stacking order.

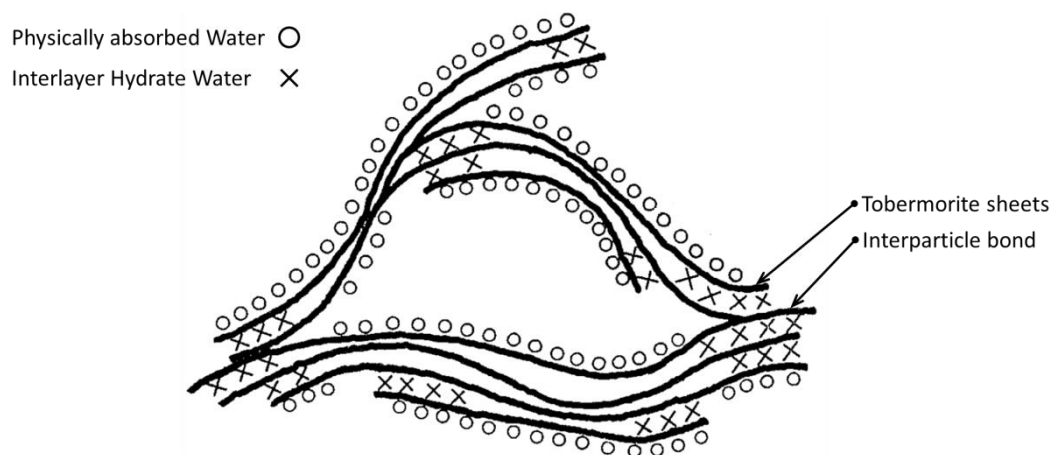


Figure 2.4 Schematic model of C-S-H morphology proposed by Feldman and Sereda (adapted from [38]).

### 2.2.2.3. Colloidal models by Jennings and Tennis (CM-I) and Jennings (CM-II)

#### *Jennings and Tennis colloidal model – CM-I*

The development of Jennings and Tennis colloidal model [40], [41] of C-S-H was triggered by discrepancies between different values of specific surface area (SSA) of C-S-H reported in the literature (reviewed [42]). The modelling of SSA, as measured by nitrogen sorption, led to the conclusion that there are two types of C-S-H created which are differentiated by densities. The low density (LD) C-S-H can be penetrated by nitrogen and the high density (HD) C-S-H cannot. The various SSA values obtained by different methods were also explained by not detecting HD type C-S-H.

The pictorial model presented in figure 2.5 a and b is simplified representation of the LD and HD C-S-H microstructure. In the model C-S-H units (layers) are represented by basic building blocks pictured as spheres. These units precipitate within capillary pores and flocculate to form globules. Depending on the packing arrangement of these globules, LD (fig. 2.5a) and HD (fig. 2.5b) C-S-H is created.

It is worth emphasising that Tennis and Jennings work [41] also provides a means to compute the quantitative cement phase composition. The model is based on known cement composition,  $w/c$  ratio and hydration equations of cement phases. Additionally, the optimized values of SSA of LD CSH and densities of LD and HD C-S-H are acquired by fits between measured and predicted values of SSA, porosity (by  $N_2$  adsorption) and capillary porosity.

### *Jennings colloidal model CM-II*

The C-S-H model presented in previous section was further developed by Jennings [6] based on the interpretation of water sorption isotherm, C-S-H density and small angle neutron scattering (SANS) results.

The model implies that the nature of C-S-H is particular or granular (figure 2.5c) as suggested by block C-S-H model of Powers and Brownyard [32], [33]. It consists of C-S-H layered globules (called in CM-I basic C-S-H units but not the same from structural point of view) with a thickness of about 4.2 nm [7]. The state of the water inside the C-S-H globules was inferred based on interpretation of the low pressure water isotherm hysteresis and changes of the density below 11% RH. CM-II defines two location of water within globules: interlayer space and intraglobular pores (IGP) of about 1 nm size enclosed through disordered layers. The hysteresis behaviour at the lower humidity, in the context of the model, is explained as in this range the interlayer water leaves but does not reenter globules until higher pressure is apply.

The C-S-H globules pack together into clusters and entrap the small gel pores (SGP) that are less than 3 nm wide. The water within SGP dries below 40% RH. The clusters arrange together to form the globule floc (fig 2.5 c) with the larger gel pores (LGP) in between. The LGP dry progressively between 85 and 40% RH. The volume of LGP pores reduces with time

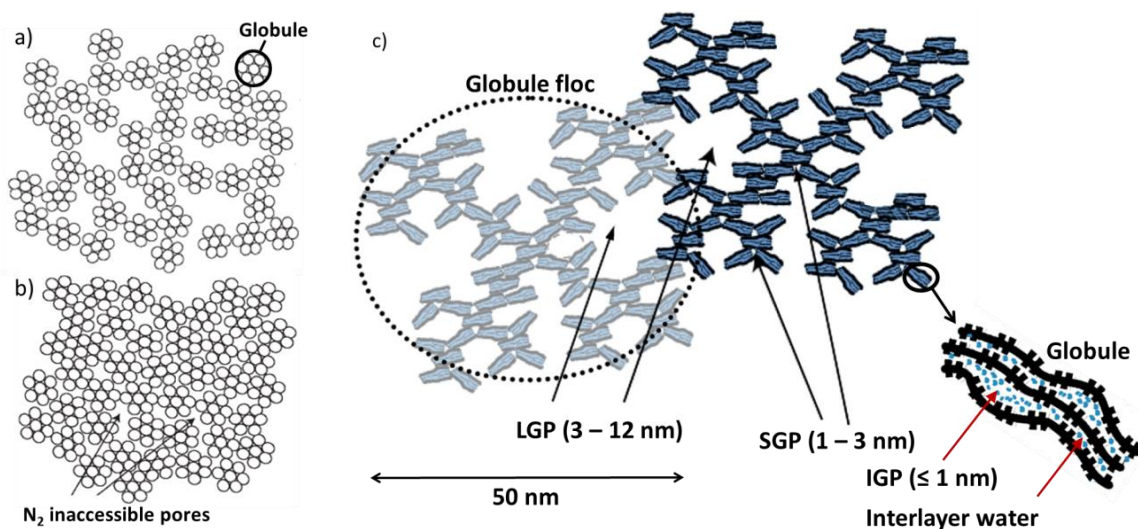


Figure 2.5 a) and b): Graphical representation of Low Density (a) and High Density (b) C-S-H as presented in colloidal model of Tennis and Jennings (adapted from [40], [41]); c) Schematic representation of CM-II C-S-H Jennings model (adapted from [6]).

by interpenetration of globule flocs - an ageing process. This process causes the formation of higher density C-S-H. The LPG pores, with the size of 3-12 nm, are considered as the intrinsic to the C-S-H gel in CM-II [6].

#### 2.2.2.4. Relation to crystalline phases

The models of C-S-H described in the previous sections are concerned with microstructure. C-S-H has also been investigated from the composition point of view by the mean of X-ray diffraction, NMR spectroscopy and microscopic techniques. Models regarding the molecular structure, characterised by structure of silicon anion (chain length), chemical formulation and Ca/Si ratio, has been evaluated with the attempt to relate short range of C-S-H with crystalline calcium silicate hydrates.

Most of the models have been based on the structure of the 1.4 nm tobermorite [5], [43] due to similarities to C-S-H in hydrated cementitious materials in the XRD patterns, MAS NMR spectra and TEM images [29], [44] – figure 2.6.

Tobermorite (1.4 nm) consists of central Ca-O layers with silicate chains on both sides for which every third tetrahedron is bridging. The repeat distance of the layers is 1.4 nm. The

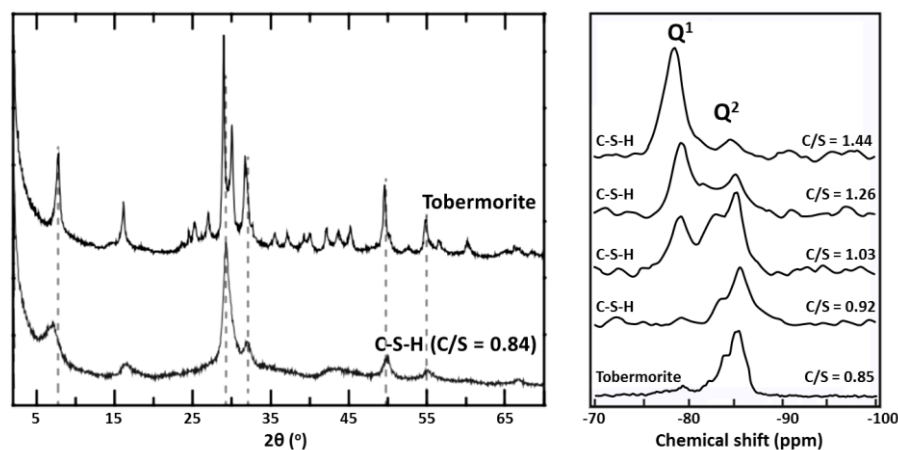


Figure 2.6 The XRD patterns (left) and  $^{29}\text{Si}$  NMR spectra (right) for 1.4 nm tobermorite and C-S-H (adapted from [44]–[46]).

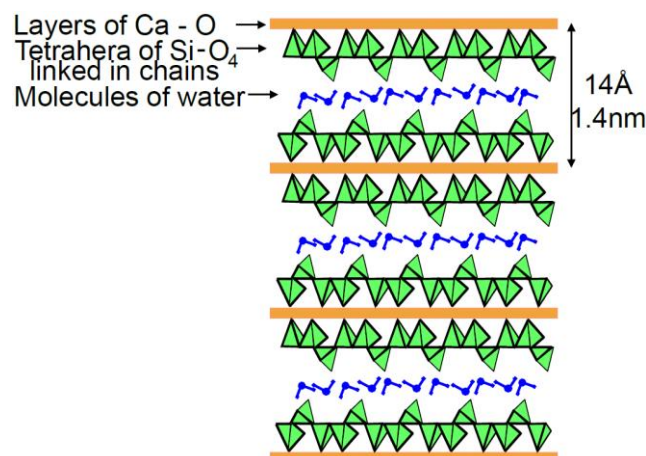


Figure 2.7 Schematic of three layers of tobermorite 1.4 nm nanostructure [29].

space between layers is filled by water and calcium ions (figure 2.7). The length of silicate chains is very long as shown by domination of  $Q^2$  groups in NMR spectrum (fig 2.6 b) [5].

Tobermorite has well defined chemical formula:  $Ca_5Si_6O_{16}(OH)_2 \cdot 7H_2O$ , with the Ca to Si ratio of 0.83 [5]. The equivalent ratio in the C-S-H present in hardened cementitious material is higher, with a mean of about 1.75 [47]. Therefore, some models incorporate the intermixing of tobermorite and jennite ( $Ca_9Si_6O_{18}(OH)_6 \cdot 8H_2O$ ) which has higher Ca/Si ratio of 1.50 and similar silicate chains [5]. Different mechanisms of changing the Ca/Si ratio have been proposed: removal of bridging tetrahedra; substitution of protons by  $Ca^{2+}$ ; incorporation of Ca-OH regions [5], [29].

### 2.3. POROSITY AND METHODS TO CHARACTERISE PORE STRUCTURE

Porosity is most often defined as the volume of air and/or water filled space within the total volume of material. In that sense the total porosity as well as the porosity of particular pore population can be characterised. Nevertheless, in wider aspect it is the quality of being porous. A number of parameters describing porosity can be identified: specific surface area, pore size distribution, threshold pore size, connectivity and tortuosity.

Pore sizes span a wide range of sizes as is presented in figure 2.8. However, among different models and researches the divisions and nomenclature of pores varies [48].

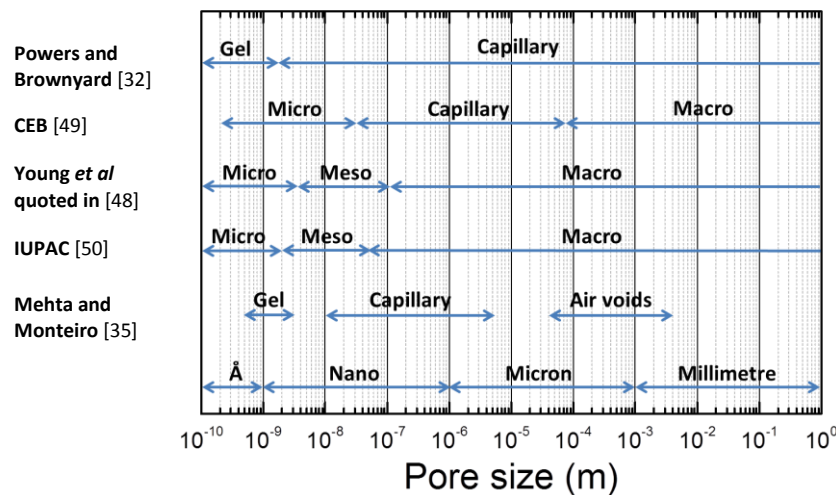


Figure 2.8 The pore nomenclature variations for cement porosity (adapted from Geiker [48]).

There are several techniques applied to characterise the porosity of cementitious materials. A brief description of selected methods follows. Different techniques are sensitive to different range of pore sizes and none can encompass the full range of pores present in cementitious materials (figure 2.8).

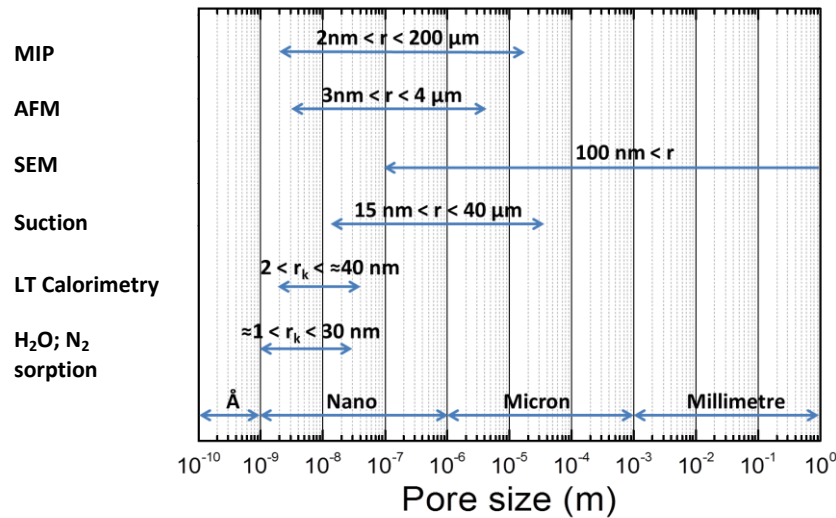


Figure 2.9 Range of pore's sizes that can be measured by specific methods – thickness of  $t$ -layer not included (adapted from Geiker [51]).

### 2.3.1. Mercury intrusion porosimetry

Liquids can interact with the surface of a solid body in two ways depending on wetting properties. If the contact angle is less than  $90^\circ$  then the surface is wetted (fig. 2.10 left), hence the liquid exhibits capillary rise. If it is more than  $90^\circ$  it does not wet surface (fig. 2.10 right) and capillary rise is not seen.

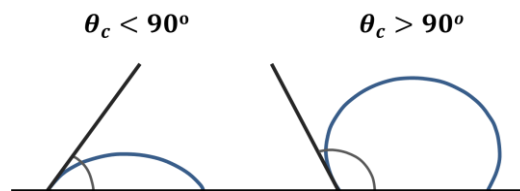


Figure 2.10 Schematic of liquid interaction with the surface. Left: surface wetted; right: surface not wetted [52].

Mercury is a liquid that does not wet the surface of cementitious material as its contact angle, at room temperature, is about  $140^\circ$  [52]. The procedure of using pressure to force mercury into empty pores and to define the pore size distribution is called Mercury Intrusion Porosimetry (MIP).

The procedure involves drying and then weighing of the sample, evacuation of gas from a chamber in which the sample is placed, introducing mercury to the chamber, applying a gradually increased pressure and monitoring the mercury intrusion [53]. The correlation between the size of pores ( $d$ ) mercury invaded and the applied, exterior pressure ( $p$ ) is expressed by the Washburn equation [54]:

$$d = \frac{2\gamma_S \cdot \cos(\theta_c)}{p} \quad (2.3)$$

where  $\gamma_S$  is the mercury surface tension and  $\theta_c$  is the contact angle between mercury and pore surface.

The volume of the mercury that enters pores at specific pressure corresponds to the volume of pores – porosity, with the pore size defined by that pressure.

MIP has been extensively used to evaluate pore size distribution and porosity of cement based materials. Exemplary data from Cook and Hover [55] are presented in figure 2.11. The results show, as expected, the decrease of the total paste porosity with passing time and smaller  $w/c$  ratio. The so-called equivalent pore width also declines. The measured pore width is the pore entry – threshold, size. The paste may contain ‘ink-bottle’ pores as well as larger pores which are connected with outside through the network of smaller pores. These can lead to erroneous conclusion about the pore size distribution and suggests that MIP data may be of limited value for small pores and actual pore sizes [53].

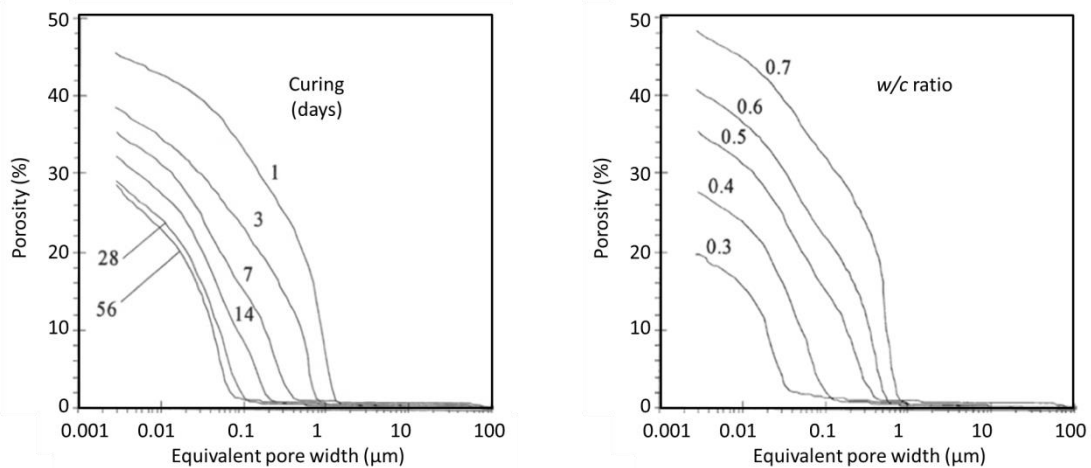


Figure 2.11 The effect of hydration time for pastes with  $w/c = 0.5$  (left) and of water to cement ratio at 7 days of hydration (right) on MIP results [55].

There are other factors and assumptions that are the source of experimental errors [52], [53]. First, the Washburn model assumes that pores are cylindrical and entirely and equally accessible from the outside surface. The cement structure can be altered due to sample drying preparation and applied pressure [56]. Additionally the method itself provides limitation as samples may be not evacuated properly and contact angle differs for different material but also for different drying methods [57].

### 2.3.2. Scanning Electron Microscopy

Scanning Electron Microscopy (SEM) is a technique providing high resolution images of material structure. Prior to experiment, the cementitious sample is dried, impregnated with epoxy resin and polished. It is then scanned with the high energy electrons beam. As a

response of interaction between sample and incident beam different signals are emitted: secondary electrons, backscatter electrons and characteristic X-rays; with the decreasing resolution respectively [31], [58].

The secondary electrons are emitted from a region close to sample surface. They are independent of the nature of elements releasing them. This imaging of cementitious materials provides topological and morphological information about the hydration products.

The backscatter electrons (BSE) originate from higher depth than secondary electrons. The intensity - brightness, of the BSE SEM signal is strongly dependent on the average atomic number of the sample local areas. Therefore, BSE provides the reproducible phase contrast. Figure 2.12a shows the typical BSE SEM image of cement mortar where the pores filled with resin are presented as black pixels; the unreacted cement grains have the highest brightness; CH is brighter than the other hydrates.

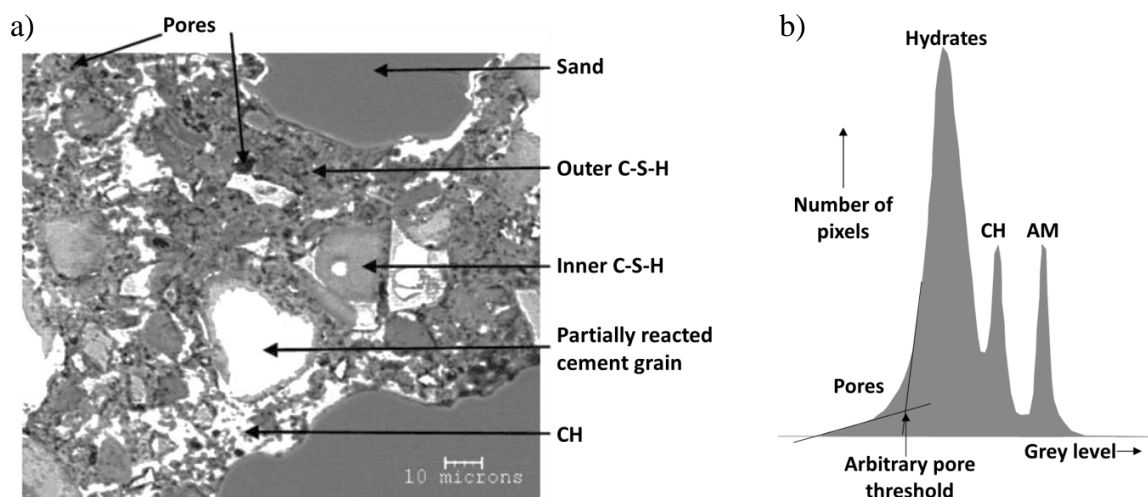


Figure 2.12 a) Exemplary BSE SEM image of the Portland cement mortar; b) Grey level histogram of cement paste; AM refers to anhydrous material (adapted from [31], [58]).

The BSE SEM allows representative visualisation of the cement paste structure and observation of the pore shapes (down to 100 nm). The quantitative analysis of size distribution, total area and volume of pores is facilitated by the reproducible contrasts between particular constituents of paste. This analysis is performed by segmenting / thresholding the grey level histogram to identify the boundary grey level between pores and hydrates (fig. 2.12b). The additional advantage is possibility of combining the local chemical microanalyses by e.g. energy dispersive spectroscopy (EDS)

The key limitations of the technique arise from limited spatial resolution, variations in grey level caused by variable composition, two dimensional imaging of an inherently 3D structure and sample preparation that may disturb the structure [31], [51].

### 2.3.3. Gas sorption

Gas sorption measures, in the form of sorption isotherm, the amount of gas adsorbed in the sample as a function of gas pressure [59].

In this method the dry sample is exposed to the gas with specified relative humidity ( $\varphi$ ). When sample has reached the equilibrium the humidity is step-like increased. The amount of the gas adsorbed on the sample surfaces is measured, through recorded sample mass, as a function of relative humidity. Alternative variant of the method involved measurements of changes in pressure when sample is exposed to the known volume of gas. The commonly used sorptive gases are water vapour and nitrogen [42].

The obtained sorption isotherm allows calculation of specific surface area (SSA), open porosity and pore size distribution.

The relation between adsorbed gas and humidity facilitates the calculation of its amount corresponding to monolayer coverage of surface ( $u_m$ ) and in turn of SSA. The most common, and one of the earliest, method for this calculation was developed by Brunauer, Emmet and Teller (BET) [60]. It expresses the amount of adsorbed gas ( $u$ ) as

$$u = \frac{K \cdot \varphi}{(1 - \varphi) \cdot (1 + K \cdot \varphi - \varphi)} \cdot u_m \quad (2.4)$$

where  $K$  is constant related to heat of adsorption.

The BET theory works well at the relative humidity below ~45%. In higher humidity range the other theory can be applied e.g. extended BET, Dent equation.

The evaluated  $u_m$  together with known cross section area of gas molecule ( $A_m$ ) leads to expression for specific surface area [59]:

$$A = \frac{1}{M^{AMU}} \cdot N_A \cdot A_m \cdot u_m \quad (2.5)$$

where  $N_A$  is Avogadro number,  $M^{AMU}$  –molar mass of gas.

At the higher relative humidity the capillary condensation occurs. The equality of the difference in pressure over capillary meniscus expressed as a function of relative humidity and of meniscus radius leads to Young-Laplace – Kelvin equation for so called Kelvin radius ( $r_K$ ) [51], [61]:

$$r_K = - \frac{M^{AMU}}{RT\rho \cdot \ln \varphi} \cdot 2\gamma_S \quad (2.6)$$

where  $\gamma_S$  – the surface tension,  $R$  – universal gas constant,  $T$  – temperature and  $\rho$  – density.

Exemplary water vapour adsorption isotherms of cement pastes are presented in figure 2.13. It can be seen above relative humidity of  $\sim 0.4$  that the capillary condensation is more pronounced with the increase of  $w/c$  ratio. In the lower humidity range, isotherms are independent of  $w/c$  ratio. The values of SSA measured by water sorption are in the range 130-210  $\text{m}^2/\text{g}$  of cement (equivalent to 110-175  $\text{m}^2/\text{g}$  of dry paste) increasing with sample age from 7 to 180 days [28], [32]. The reported values of SSA by using nitrogen tend to be lower in the range of 10 - 150  $\text{m}^2/\text{g}$  of dry paste [28], [42], [62]. The reasons for that are not fully understood, the proposed explanations are that: the size of water molecule is smaller than nitrogen's; vapour water can be re-adsorbed into C-S-H interlayer; carbonation<sup>4</sup> of CH and C-S-H; differences in morphology and amount between the LD and HD types of C-S-H proposed by Tennis and Jennings [42].

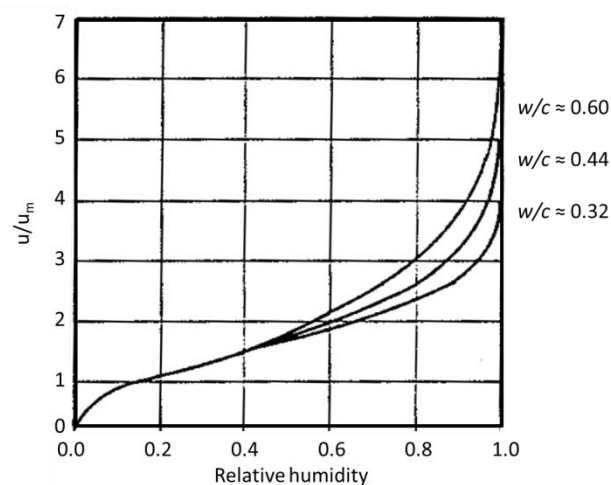


Figure 2.13 Exemplary adsorption isotherms of water vapour for cement pastes mixed at different  $w/c$  ratios and cured for 180 days [32].

Gas sorption is a well-known method. Nevertheless, it has limitations and many aspects to consider. From experimental point of view: sample preparation involves drying that may disturb the delicate structure of C-S-H; the sample equilibration is long, especially when using salt solutions to create known relative humidity. Hence there is possibility of ongoing hydration; carbonation; shrinkage; and swelling during measurement that can alter pore structure. The balance accuracy should be very high as the mass is the actual measure in the method and the mass difference can be small. The Kelvin radius calculation assumes cylindrical shape of the pores [42], [51], [62].

<sup>4</sup> reaction between carbon dioxide ( $\text{CO}_2$ ) and calcium compounds: CH and C-S-H; as a result calcium carbonate ( $\text{CaCO}_3$ ) is formed

### 2.3.4. Low temperature Calorimetry

Low Temperature Calorimetry (LTC) is based on the fact that liquid within small pores freezes at lower temperatures in comparison with bulk fluid – so-called depression of freezing point [51], [63]. The melting point depression ( $\Delta T$ ) is given by equation:

$$\Delta T = \frac{2 \cdot T_0 \cdot V_l \cdot \gamma_S}{d \cdot \Delta H_{fus}} \quad (2.7)$$

where  $T_0$  is freezing temperature of bulk liquid,  $V_l$  – molar volume of liquid,  $\gamma_S$  – the surface tension,  $d$  – the pore size and  $\Delta H_{fus}$  – the heat of fusion.

The LTC experiments are performed in the temperature range between +20°C and around -60°C and the heat flows to and from sample are measured. Plots of the heat flow present the peaks at different temperatures. The peaks' temperatures during freezing correspond to liquid freezing in pores with characteristic entry size. Melting curve peaks are correlated with actual pore sizes. It is a consequence of the freezing-melting mechanism for the structure containing 'ink-bottle' pores and bigger pores connected to surface through smaller ones [64].

The pore sizes are the sum of Kelvin radius ( $r_k$ ) and  $t$ -layer thickness (non-freezable layer of adsorbed water -  $t_{nf}$ ) [51], [63]:

$$r_k = - \frac{M^{AMU}}{\Delta H_{fus} \cdot \rho \cdot \ln(T/T_0)} \cdot 2\gamma_S \quad (2.8)$$

$$t_{nf} = 19.7 \cdot (273.2 - T)^{-1/3}$$

where  $M^{AMU}$  – liquid molar mass,  $T$  – freezing temperature of pore liquid and  $\rho$  – is the density of liquid.

The investigation of cement pastes during freezing scans typically show existence of three peaks corresponding to pore structure and occasionally additional peak due to bulk liquid [63], [65] – figure 2.14. The interpretation of heating scans for cementitious material is problematic as ice melts gradually [63].

LTC of cements is used to evaluate the pore thresholds and total volume of saturated porosity based on ice volume. The main advantage is measurement of 'as prepared' samples without need of drying. LTC is also relatively fast and young samples can be examined [51]. However, the position and width of peaks are affected by the rate of temperature changes and variable alkali concentration in pore solutions. The limitations are also: thawing that can cause cracking; the discrepancy between the reference and actual sample temperature; and supercooling. To overcome the latter nucleation agents are added to the samples [51], [63].

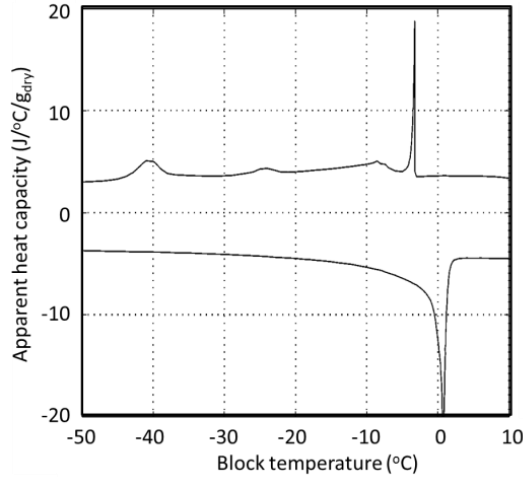


Figure 2.14 The exemplary heat flow (given as apparent heat capacity) as a function of temperature for cement paste,  $w/c = 0.5$ , after 75 days of hydration [63].

### 2.3.5. Small Angle Neutron Scattering and X-rays Scattering

Small Angle Scattering techniques are used to characterise the micro-structure of materials. The particle size distribution, total surface area and volume fractions of structural features, and fractal dimensionalities may be calculated. The porosity related characteristic is SSA.

During an experiment the intense beam of neutrons (SANS) or X-rays (SAXS) is directed at a sample. It passes through the sample and is elastically scattered out as a result of interaction with atomic nuclei (SANS) or cloud of electrons (SAXS) [42], [66]. Detailed models are required to relate scattering to structure. The forward problem – structure to scattering, is much easier and less ambiguous than inverse problem – scattering to structure.

The scattering vector ( $Q$ ) of neutrons or X-rays is defined as:

$$Q = \frac{4\pi}{\lambda} \cdot \sin\left(\frac{\theta_{SAS}}{2}\right) \quad (2.9)$$

where  $\theta_{SAS}$  is an angle of scattering and  $\lambda$  is the neutron or X-rays wavelength.

The resultant scattering profile presents a relation between the intensity of scattered neutrons or X-rays and scattering vector. In Porod's regime the calibrated scattering intensity ( $I_{SAS}$ ) is proportional to surface area ( $A$ ) per unit sample volume [42]:

$$I_{SAS} \cdot Q^4 = 2\pi \cdot |\Delta\rho_{SAS}|^2 \cdot A + C \cdot Q^4 \quad (2.10)$$

where  $|\Delta\rho_{SAS}|^2$  is scattering contrast between the voids and solid phase and  $C$  is flat background intensity.

The exemplary SANS data for ordinary Portland cement are presented in figure 2.15.

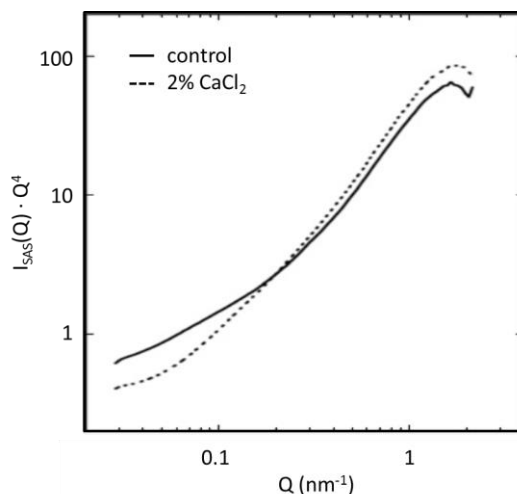


Figure 2.15 The exemplary SANS data plotted as  $I(Q) \cdot Q^4$  for ordinary Portland cement mixed at  $w/c$  ratio 0.4, with and without addition of  $\text{CaCl}_2$ , and hydrated for 28 days [66].

The surface areas of mature saturated cement pastes as measured by SANS and SAXS show the markable discrepancy. The SANS reported values are 60-150  $\text{m}^2/\text{g}$  of d-dried paste while values obtained by SAXS are significantly higher, 200-600  $\text{m}^2/\text{g}$  of d-dried paste. The probable reason is that SAXS actually probes smaller features, interlayer pores, than SANS as indicated by X-rays smaller wavelength and investigation of surface during drying [42].

The advantages of the technique are examination of saturated samples without drying and possibility of continuous study during hydration. The challenges concern primarily the strong dependence on model and analysis of data. The evolution of SSA according to presented calculation method - called the contrast method, requires the knowledge of scattering contrast for C-S-H and absolute calibration of data. The alternative analysis protocol is the scattering invariant method but brings more difficulties. The other concerns are sample preparation – the optimise thickness, and costs of equipment and its maintenance [42], [66].

### 2.3.6. Nuclear Magnetic Resonance Relaxometry

The work presented in this thesis is based on NMR relaxometry; hence chapter 3 is fully dedicated to provide a detailed description of relevant theory.

## 2.4. CHARACTERISTICS OF C-S-H

The investigation of the C-S-H stoichiometry provides valuable information about structure at molecular level. This serves as input for the modelling of water dynamics within nanostructure of C-S-H and its properties and lead to better understanding of its behaviour. In this thesis, the C-S-H composition is written as  $\text{Ca}_z (\text{Si}_y, \text{Al}_{(1-y)}) \text{O}_{(z+y/2+3/2)} (\text{H}_2\text{O})_x$  where  $x$  is the interlayer water content. Once the gel pore water is included water content is  $x'$ .

### 2.4.1. C/S ratio

A primary characteristic of interest concerning C-S-H is the molar ratio of CaO to SiO<sub>2</sub>, the so-called C/S ratio, in this thesis defined as  $z/y$ . The ratio in CaO-SiO<sub>2</sub> systems and for hydrated C<sub>3</sub>S or C<sub>2</sub>S can be calculated if the CH and amount of unreacted material is known [28]. To date, measurements of the C/S ratio has required use of complex and in some cases destructive experimental methods including e.g. the NMR spectroscopy, Electron Probe Microanalysis (EMPA), SEM and TEM with micro-analysers.

It has been reported by many researches that the C/S ratio of the C-S-H phase, in the equilibrium with Ca<sup>2+</sup> solution, increases with increase of Ca<sup>2+</sup> concentration [28], [43], [67], [68] – figure 2.16a. Based on this relation Taylor classified two types of the C-S-H: tobermorite-like C-S-H (I) with  $0.8 < C/S < 1.5$  and C-S-H (II) with  $C/S > 1.5$  corresponding to the mix of tobermorite-like and jennite-like phases [28] – region B and C in fig. 2.16a respectively. The highest values of C/S ratio for pure, synthesized C-S-H, samples free of CH, has been found to be about 1.5 [29], [43], [69]. This suggested that to reach higher values, as observed for C-S-H in cement pastes, the supersaturation of solution with respect to CH is necessary. Nonat [69] suggested the existence of three types of C-S-H:  $\alpha$ -C-S-H ( $0.66 < C/S < 1$ ) – upper part of region A in fig 2.16a;  $\beta$ -C-S-H ( $1 < C/S < 1.5$ ) – region B; and  $\gamma$ -C-S-H ( $C/S > 1.5$ ) – region C. The first,  $\alpha$ -C-S-H is typical tobermorite phase;  $\beta$ -C-S-H corresponds to Taylor's C-S-H (I);  $\gamma$ -C-S-H even though exists in the same region as C-S-H (II) shows tobermorite-like XRD pattern. The existence of single phase over whole range of C/S ratio was reported and the changes in the C/S ratio were explained by omission of bridging tetrahedra, substitution of protons by calcium ions, the presence of Ca-OH and Si-OH regions and decrease in the length of silicate chains [29], [43], [69].

Values of the C/S ratio in the C-S-H of hardened cement vary largely in the range ~1.2 to ~2.3 with the mean ~1.75 for mature pastes as measured by TEM microanalysis – figure 2.16b [47]. Recently, Allen *et al* [7] have evaluated the composition of the C-S-H by SANS analysis. They obtained the C/S ratio of 1.85 and in further analysis they assumed value of 1.70 as indicated by most studies in the cement field.

It was also noted that the C/S ratio in cement pastes changes with  $w/c$  ratio and age. The increase of paste  $w/c$  ratio lowers the C/S ratio. Additionally for younger samples the C/S present the bimodal distribution which changes to unimodal with the progress of hydration [47], [70]. This behaviour of the C/S ratio is correlated with a distinction in the C-S-H morphology (figure 2.17). The 'inner' denser C-S-H formed within the original boundary of cement grains has higher C/S ratio. The C-S-H which forms outside of these boundaries in an originally water-filled space – 'outer' C-S-H, has lower C/S. Nevertheless, with time the 'outer' C-S-H densifies, hence the single C/S ratio is reported.

The morphology of the 'outer' C-S-H is further divided into types: 'fibrillar' with intermediate C/S (fig 2.17b) and 'foil-like' with the lower values (fig 2.17c). The boundary between fibrillar and foil-like C-S-H was assigned as about 1.5 [47], [71].

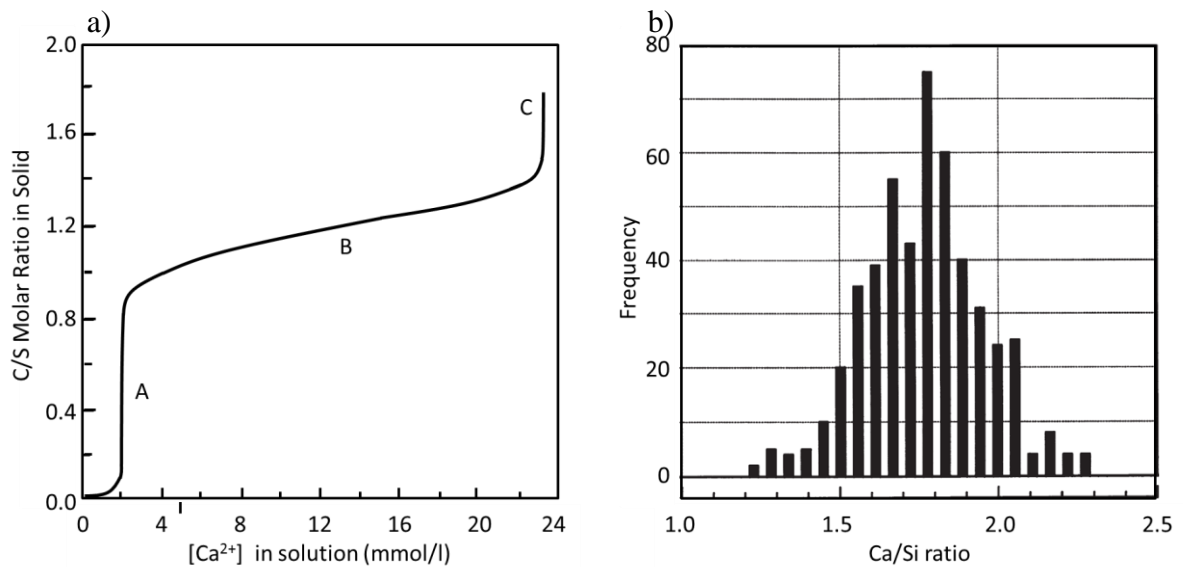


Figure 2.16 a) C/S ratio in C–S–H as a function of  $\text{Ca}^{2+}$  concentration in solution (adapted from [68]). b) Histogram of Ca/Si frequency for C-S-H in cement pastes 1 day to 3.5 year old as measured by X-ray microanalysis in the TEM (adapted from [47]).

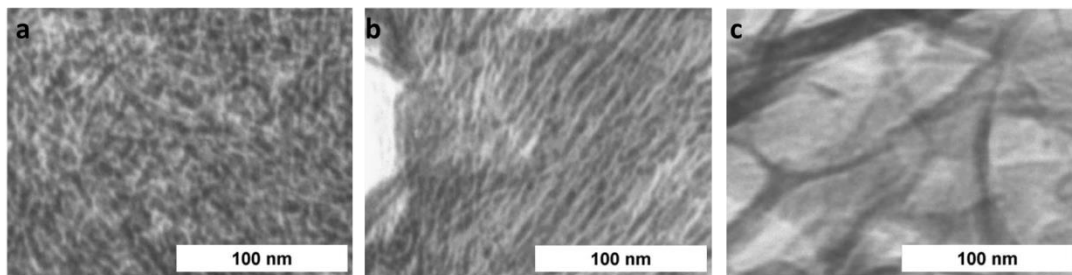


Figure 2.17 TEM micrographs of fine ‘inner’ C-S-H (a) and ‘outer’ CSH: fibrillar (b) and foil-like (c) (adapted from [71]).

#### 2.4.2. $\text{H}_2\text{O}$ content

As already described cement paste contains water in pores with a range of length scales and in various states. Water is present in the capillary, gel pores and C-S-H interlayer spaces as well as in the chemically combined, adsorbed and liquid states. Considering the molar  $\text{H}_2\text{O}$  content in the C-S-H the question arises as to what state of water it actually refers. Moreover, the  $\text{H}_2\text{O}$  content may also depend on the sample characteristic:  $w/c$  ratio, hydration time and curing conditions. When comparing the obtained values of  $\text{H}_2\text{O}$  content the types of included water or drying conditions should be clearly defined.

The water content (moles of  $\text{H}_2\text{O}$  per mole of C-S-H) for the nearly saturated C-S-H created upon hydration of  $\text{C}_3\text{S}$  (at 90% RH to not include capillary water) was defined by Hansen and Young [72]. It was 3.8 and 4.1 at  $w/c$  ratio of 0.4 and 0.6 respectively. Jennings has reviewed different studies and calculations of water in context of colloidal model CM-II. He reported the values for the C-S-H including water within large gel pores (LGP) with

packing density of globules 0.59 as 5. This value decreases with increase of packing density to e.g. 4 at packing density of 0.64. The drying of all LPG leads to H<sub>2</sub>O content of 2.7 [6].

Experiments by Hansen and Young [72] and modelling by Jennings [6] showed that the removal of water through equilibration of samples at 11% relative humidity declines the H<sub>2</sub>O content down to 2.1. At this stage it is assumed that the C-S-H globules are saturated and has water layer adsorbed on the outer surface [6], [28]. Feldman and Ramachandran measured H<sub>2</sub>O contents in hydrated C<sub>3</sub>S at that humidity and obtained slightly lower value of 1.96. They defined formula for C-S-H as  $\text{Ca}_{z=1.64}\text{Si}_{y=1}\text{O}_{(z+y/2+3/2)=3.64}(\text{H}_2\text{O})_{1.96}$  [73].

The SANS experiments shown that the water content of saturated globules alone is 1.80 assuming C/S value of 1.70 [7]. Upon application of d-drying<sup>5</sup> remaining water content in the C-S-H is 1.2-1.5 [6], [28], [73].

The other review has been performed by Chen [74]. It verified the influence of C/S ratio on the C-S-H within oven and d-dried hydrated C<sub>3</sub>S, C<sub>2</sub>S and CaO-SiO system. It is shown that the increase of C/S ratio is accompanied by the rise of the water molar content of C-S-H (figure 2.18).

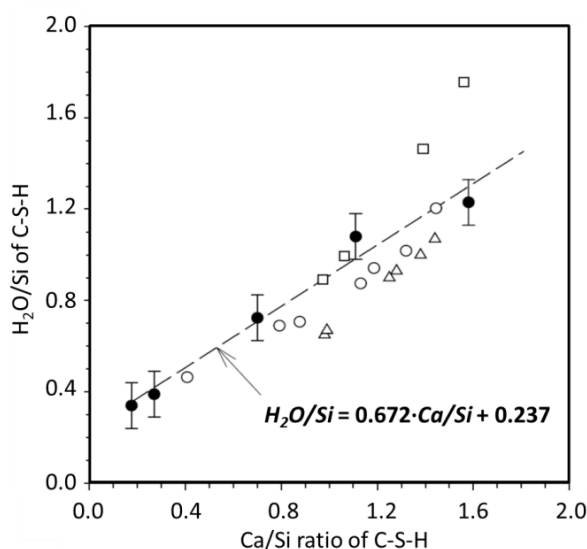


Figure 2.18 C-S-H water content ( $\text{H}_2\text{O}/\text{SiO}_2$ ) as a function of Ca/Si ratio. Data obtained after: oven drying at 110°C of CaO-SiO<sub>2</sub> (○) and  $\beta$ -Ca<sub>2</sub>SiO<sub>4</sub> (□) [43]; d-drying of CaO-SiO<sub>2</sub> (△) (reported in [74]) and Ca<sub>3</sub>SiO<sub>5</sub> (●) [74].

### 2.4.3. Density

The same consideration as for C-S-H water content to compare like-with-like has to be exercised when considering C-S-H density. Additionally, the care must be taken as to whether or not the pore volume is excluded from calculation.

<sup>5</sup> equilibration with ice at -79°C by continuous evacuation with water pressure  $5 \cdot 10^{-4}$  torr; equivalent to drying at 105°C in a CO<sub>2</sub> free atmosphere with uncontrolled humidity or 145°C with heating rate 10°C/min in dry CO<sub>2</sub>-free N<sub>2</sub> [51]

The densities of C-S-H reviewed by Jennings for corresponding states of C-S-H are also given in [6]. The density including water within large gel pores (LGP) with packing density of globules 0.59 is  $1.83 \text{ g/cm}^3$ . In the reverse manner to  $\text{H}_2\text{O}$  content, density increases with increase of packing density to e.g.  $2.03 \text{ g/cm}^3$  at packing density of 0.64. Density of saturated C-S-H based on Tennis and Jennings prediction model of high and low density C-S-H at  $20^\circ\text{C}$  was evaluated as  $1.99 \text{ g/cm}^3$  [41]. The density for nearly saturated C-S-H created upon hydration of full  $\text{C}_3\text{S}$  was defined as  $1.85\text{-}1.90 \text{ g/cm}^3$  [72].

When all LPG are dried density is  $2.31 \text{ g/cm}^3$  and at 11% relative humidity rises to  $2.47 \text{ g/cm}^3$  [6]. The helium pycnometry gives, at the same humidity, values of  $2.43\text{-}2.45 \text{ g/cm}^3$  for C-S-H in fully reacted  $\text{C}_3\text{S}$  paste [75]. While for CH leached, fully hydrated  $\text{C}_3\text{S}$  paste density is  $2.18 \text{ g/cm}^3$  as measured by gas pycnometry [72]. Progressive drying below that humidity, according to Jennings, actually causes increase of density. It is interpreted as the removal of water from interlayer spaces is accompanied by their collapse and hence both mass and volume decrease. For empty interlayer the density increases to  $2.58 \text{ g/cm}^3$ . Then water is dried from intraglobule space without change in the volume hence density declines to  $2.25\text{-}2.53 \text{ g/cm}^3$  [6].

Taylor reported the density of  $2.6\text{-}2.7 \text{ g/cm}^3$  for C-S-H dried at  $110^\circ\text{C}$  with corresponding  $\text{H}_2\text{O}$  content of 0.85 [28]. According to results of helium pycnometry the density of d-dried  $\text{C}_3\text{S}$  and cement pastes is  $2.2\text{-}2.4 \text{ g/cm}^3$ , after correction for CH and other hydrates it is  $2.4\text{-}2.5 \text{ g/cm}^3$  for C-S-H [28], [75], [76]. In the same conditions water pycnometry shows much higher values  $2.6\text{-}2.7 \text{ g/cm}^3$  (without correction). Feldman attributed the difference to the empty spaces entrapped between collapsed layers which water can easily penetrate but helium does very slowly [76]. Nevertheless, determination through the mass changes upon d-drying gave  $2.5\text{-}2.6 \text{ g/cm}^3$  [28]. Hansen in his review [34] of Powers and Brownyard model evaluated the density of  $2.51 \text{ g/cm}^3$  for C-S-H including non-evaporable water ( $0.23 \text{ g/g}$  of cement) but excluding any gel water in Powers and Brownyard's terminology<sup>6</sup>.

A recent and now widely quoted value of  $2.604 \text{ g/cm}^3$  was evaluated for saturated C-S-H globules with water content 1.8 – no adsorb surface layer, without drying of samples by SANS experiments [7].

The summary of density review is presented in table 2.2.

---

<sup>6</sup> non-evaporable water - part of total water that persists in paste at the pressure below  $5 \cdot 10^{-5} \text{ mmHg}$  at  $23^\circ\text{C}$ ; gel water - water within C-S-H gel

Table 2.2 Summary of C-S-H density values from literature; additionally the values of C/S and H/S are listed where possible.

Density [g/cm <sup>3</sup> ]	Material	Method / Model used to obtain density	C/S	H/S	Ref.
1.83	C-S-H; including water in LGP	CM-II	1.7	5	[6]
1.85-1.90	C-S-H of C <sub>3</sub> S paste; saturated at 90% RH - no capillary water	Shrinkage weight loss curve and gas pknometry at 11% RH, ‡	1.7	3.8-4.1	[72]
1.99	C-S-H of cement paste; saturated	Tennis and Jennings model	ng	ng	[41]
2.03	C-S-H; packing density of globules 0.64	CM-II	1.7	4	[6]
2.31	C-S-H; all LPG dried	CM-II	1.7	2.7	[6]
2.47	C-S-H: saturated globule with monolayer at surface at 11% RH	CM-II	1.7	2.1	[6]
2.43-2.45	C-S-H of C <sub>3</sub> S paste at 11% RH	Helium pknometry, #	ng	ng	[75]
2.18	C-S-H of C <sub>3</sub> S paste at 11% RH ‡	Gas pknometry, ‡	ng	2.1	[72]
2.58	C-S-H: globule with empty interlayer spaces and full IGP	CM-II	1.7	1.85	[6]
2.25-2.53	C-S-H: empty globule	CM-II	1.7	1.3-	[6]
2.6-2.7	C-S-H dried at 110°C	(?) using water, #	ng	0.85	[28]
2.2-2.4	d-dried C <sub>3</sub> S and cement pastes	Helium pknometry, †	–	–	[75], [76]
2.4-2.5	C-S-H of d-dried C <sub>3</sub> S and cement pastes	Helium pknometry, #	ng	ng	[28], [75]
2.6-2.7	d-dried cement paste	Water pknometry, †	–	–	[76]
2.5-2.6	d-dried cement paste	Mass changes upon d-drying, †	–	–	[28]
2.51	C-S-H solid gel particles	Evaluation of Powers and Brownyard model	ng	ng	[34]
2.604	C-S-H: saturated globules	SANS	1.85 (1.70*)	1.87 (1.80)	[7]

‡ - CH leached paste; †- without correction for CH; # - corrected for CH (and other hydrates for cement pastes); ng - not given; '–' - not applicable; '\*' - assumed;

## 3. NMR relaxometry

*“NMR is a physical phenomenon utilized to investigate molecular properties of matter by irradiating atomic nuclei in a magnetic field with radio waves”* Bernhard Blümich [77]

### 3.1. EXCITATION AND RELAXATION

The description of NMR relaxometry presented in this and the following sections is based on its presentation in several classic NMR texts [77]–[82].

Many atomic nuclei (e.g.  $^1\text{H}$ ,  $^2\text{H}$ ,  $^{31}\text{P}$ ,  $^{14}\text{N}$ ,  $^{13}\text{C}$ ,  $^{19}\text{F}$ ) possess non-zero spin angular momentum (spin,  $\vec{I}$ ). Hence, they have a nuclear magnetic moment ( $\vec{\mu}$ ) and in many ways behave like tiny magnets. The angular momentum and magnetic moment are related as  $\vec{\mu} = \gamma \cdot \vec{I}$  where  $\gamma$  is the gyromagnetic, or more correctly magnetogyric, ratio of the nuclear species. In the absence of an applied magnetic field the nuclear magnetic moments are oriented randomly. When an external, static magnetic field ( $B_0$ ) is applied the spin vectors align themselves with this field.

#### Quantum mechanics approach

The energy of a nuclear magnetic moment,  $\vec{\mu}$ , in a magnetic field,  $\vec{B}_0$ , depends on its orientation according to:

$$E = - \vec{\mu} \cdot \vec{B}_0 = - \gamma m_I \hbar B_0 \quad (3.1)$$

where  $\hbar$  is Planck constant divided by  $2\pi$ ; Here  $m_I$  defines the component of  $I$  in the direction of  $B_0$  that is universally taken as the  $z$ -direction. For  $^1\text{H}$ ,  $I = 1/2$  so  $m_I = \pm 1/2$ .

There are  $(2I+1)$  energy levels for each nucleus. The energy difference between different states is  $\Delta E = \gamma \hbar B_0$ . The parallel orientation (‘up’) is slightly energetically preferred. The populations of the parallel ( $N_{\text{parallel}}$ ) and anti-parallel ( $N_{\text{anti-parallel}}$ ) states are described by Boltzmann distribution equation:

$$\frac{N_{\text{anti-parallel}}}{N_{\text{parallel}}} = e^{-\Delta E/(k_B \cdot T)} \quad (3.2)$$

where  $k_B$  is Boltzmann constant and  $T$  is temperature.

The strength of the bulk nuclear magnetisation depends on the excess number of nuclei in the parallel population ( $\Delta N = N_{\text{parallel}} - N_{\text{anti-parallel}}$ ). If the temperature decreases the

magnetisation increases, there are more parallel spins. When temperature is increased the ratio of anti-parallel to parallel populations approaches unity and magnetisation approaches zero.

Spins can change their energy state by exchanging a photon of energy with their environment. The frequency of electromagnetic radiation that induces spin transitions ( $\nu_0$ ) is expressed by equation  $\Delta E = h\nu_0$ . By considering the energy difference between states,  $\nu_0 = \gamma B_0 / (2\pi)$ . This leads to the Larmor equation<sup>7</sup>  $\omega_0 = \gamma B_0$ , where  $\omega_0$  is angular precession frequency called the Larmor frequency.

### Classical mechanics approach

For a macroscopic sample, which contains many nuclei, it is more convenient and intuitive to consider the net magnetization using a classical approach. All similar spins in the sample are considered as a group – ‘packet’. Their magnetic momenta are added as vectors in  $x$ ,  $y$  and  $z$  direction in the presence of an external magnetic field ( $B_0$ ) oriented in  $z$ -direction, the so-called equilibrium state. The sum of magnetic moments in the  $x,y$ -plane – transverse magnetisation, is zero<sup>8</sup>:  $M_x^o = 0$  and  $M_y^o = 0$ , as their transverse magnetic components cancel out. In  $z$ -direction, as there is an excess of parallel spins, the longitudinal net magnetisation is observed:  $M_z^o = \Delta N \cdot \mu = \Delta N \cdot \gamma \cdot m_I \cdot \hbar$  (figure 3.1). Opposing spins pair up and cancel out their observable magnetisation.

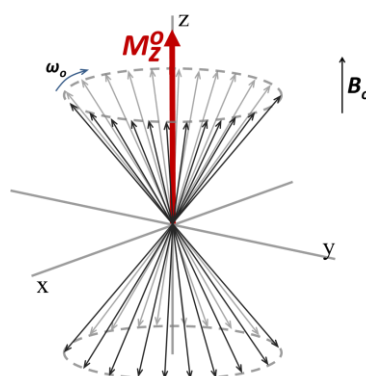


Figure 3.1 The macroscopic, net magnetization vector ( $M_z^o$ ) of nuclear magnetic moments ( $I = 1/2$ ) in external magnetic field.

### Excitation

When the net nuclear magnetization vector ( $\vec{M}$ ) is disturbed, that is tipped away from alignment with the external magnetic field, it precesses coherently around the direction of the field at the Larmor frequency<sup>7</sup>:

$$\omega_0 = \gamma B_0 \quad (3.3)$$

<sup>7</sup> note: exact Larmor equation is written with negative sign (to compensate for a negative  $\gamma$  parameter)

<sup>8</sup>  $M^o$  indicates equilibrium state magnetisation,  $M_{x,y,z}$  indicate magnetization in  $x$ ,  $y$  and  $z$  direction

The rate of change of macroscopic angular momentum ( $d(\vec{M}/\gamma)/dt$ ) depends on the torque exerted on the magnetisation by the external magnetic field,  $\vec{M} \times \vec{B}_0$ . The precession of the net magnetization is hence described by equation of motion:

$$\frac{d\vec{M}}{dt} = \gamma \vec{M} \times \vec{B}_0 \quad (3.4)$$

In NMR experiments, the tipping of magnetisation from the  $z$ -axis ‘equilibrium state’ aligned with the external magnetic field is induced by the application of a short excitation pulse. An additional oscillating magnetic field ( $B_1$ ) is applied in direction perpendicular to the external field  $B_0$ . The frequency of the  $B_1$  field is set to the Larmor frequency to achieve resonant interaction. The duration of the excitation pulse ( $t_\theta$ ) defines the angle through which net magnetization is rotated:

$$\theta = \gamma \cdot B_1 \cdot t_\theta \quad (3.5)$$

The description of magnetisation is more convenient with reference to a rotating coordinate frame<sup>9</sup>. This Cartesian frame rotates at the Larmor frequency,  $\omega_0$ , about  $B_0$ . In this frame of reference  $B_0$  is transformed to zero. The net magnetisation appears stationary in the rotating frame in contrast to laboratory frame where it precesses around external magnetic field  $B_0$ . Applied  $B_1$  is stationary and  $\vec{M}$  rotates about  $B_1$ .

Following a  $90^\circ$  pulse applied along the  $y'$ -axis of rotating frame, the precession of net magnetisation,  $\vec{M}$ , over time ( $t$ ) is given by

$$\begin{aligned} M_x(t) &= M_z^o \cdot \cos(\gamma \cdot B_0 \cdot t) \\ M_y(t) &= -M_z^o \cdot \sin(\gamma \cdot B_0 \cdot t) \\ M_z(t) &= 0 \end{aligned} \quad (3.6)$$

### **Relaxation**

Equation 3.6 implies that the longitudinal magnetisation ( $M_z$ ) is constant and both transverse magnetisations ( $M_x$  and  $M_y$ ) precess indefinitely about the magnetic field  $B_0$ . However, experimentally it is observed that the  $M_z$  increases progressively to achieve again the equilibrium while  $M_x$  and  $M_y$  both approach zero. The reason for such a discrepancy lies in the apparent assumption that all nuclei experience exactly the same magnetic field,  $B_0$ . However, in ‘real life’ each nuclei ‘sees’ a slightly different magnetic field. The difference between  $B_0$  and the actual field is called the local field.

---

<sup>9</sup> in the rotating coordinate frame axes are marked as  $x'$ ,  $y'$  and  $z'$

There are various sources of variations in the local magnetic fields. The main ones are: interactions between nuclei within the sample as each of them experiences magnetic fields produced by neighbouring nuclei; interactions of nuclei with unpaired electrons in chemical bonds; the presence of magnetic material in a form of paramagnetic species; and magnet inhomogeneity which causes a spread of  $B_0$  values over the sample volume. Additionally, local fields may change with time. Due to these conditions spins precess at different and changing frequencies. Therefore, as spins become incoherent in motion they dephase. This in turn causes relaxation.

Relaxation terms have been added to equation (3.4) by Bloch:

$$\begin{aligned}\frac{dM_x}{dt} &= \gamma |M \times B_0|_x - \frac{M_x}{T_2} \\ \frac{dM_y}{dt} &= \gamma |M \times B_0|_y - \frac{M_y}{T_2} \\ \frac{dM_z}{dt} &= \gamma |M \times B_0|_z + \frac{(M_z^o - M_z)}{T_1}\end{aligned}\tag{3.7}$$

where  $T_1$  and  $T_2$  are the longitudinal and transverse relaxation times, respectively.

Relaxation in the longitudinal direction is due to an exchange of energy between the nuclear spin system and the surrounding environment known as the ‘lattice’. The magnetisation in the  $z$ -direction realigns with the direction of external magnetic field  $B_0$ . It relaxes to  $M_z^o$ , as the equilibrium is being reached. The rate of this process is characterised by  $T_1$  known as spin-lattice or longitudinal relaxation time. The longitudinal relaxation process is described by

$$\frac{dM_z}{dt} = \frac{(M_z^o - M_z)}{T_1}\tag{3.8}$$

The equation governing magnetisation recovery following a  $90^\circ$  pulse is:

$$M_z(t) = M_z^o \left[ 1 - \exp\left(-\frac{t}{T_1}\right) \right]\tag{3.9}$$

Transverse relaxation is the process of direct interaction of nuclear spins to reach the thermal equilibrium amongst themselves. The time constant which describes the rate at which spins lose coherence – dephase, and magnetisation decay in the  $x',y'$ -plane is called the  $T_2$  relaxation time. It is also known as  $T_2$  spin-spin or transverse relaxation time. The spin relaxation process is described as

$$\frac{dM_{x,y}}{dt} = -\frac{M_{x,y}}{T_2} \quad (3.10)$$

which leads to:

$$M_{x,y}(t) = M_{x,y}(0) \cdot \exp\left(-\frac{t}{T_2}\right) \quad (3.11)$$

### 3.2. NMR RELAXOMETRY MEASUREMENT TECHNIQUES

During experiments signal is detected along the fixed axis ( $x'$  or  $y'$ ) of transverse plane.

#### 3.2.1. Free induction decay

The most basic NMR pulse sequence is free induction decay (FID) sequence. It involves application of a single  $90^\circ$  radio frequency pulse ( $P_{90}$ ) – figure 3.2. This pulse rotates the equilibrium state magnetisation ( $M$ ) along the  $z'$ -axis to the  $x',y'$ - plane. If the magnetic field  $B_1$  lies along the  $x'$ -axis of rotating frame - pulse  $P_{90}^{x'}$ , magnetisation will be rotated to  $y'$ -axis – figure 3.2 (inset a). The net magnetisation in  $y'$ -direction determines the strength of observed signal called the free induction decay (FID) signal.

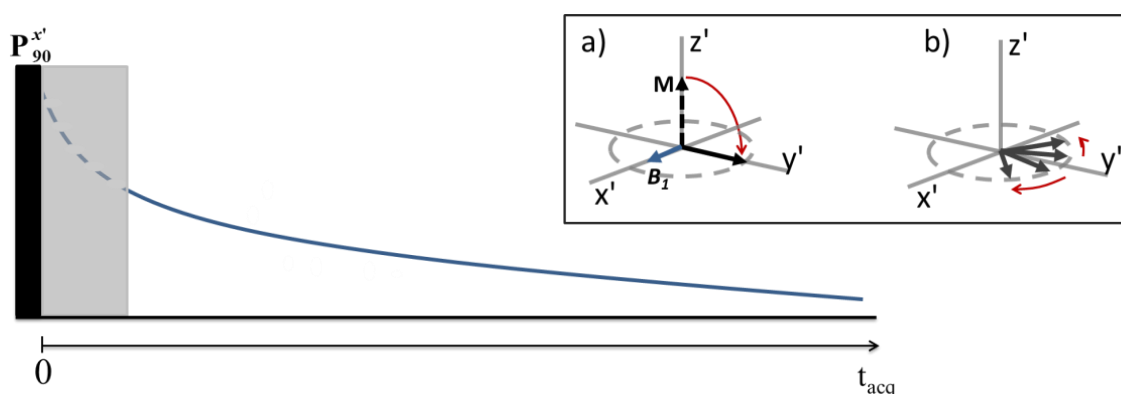


Figure 3.2 Main: Pulse sequence diagram for FID experiment – Free Induction Decay; grey region is spectrometer dead time. Inset: a)  $P_{90}^{x'}$  along  $x'$ -axis rotates  $M$  from the equilibrium position to  $y'$ -axis, b) Magnetisation decreases as spins dephase.

The transverse relaxation occurs as the magnetic moments dephase - figure 3.2 (inset b). The signal decays. In perfect experimental conditions the time constant of decay would be  $T_2$ . However, in practice the FID signal has an apparent time constant ( $T_2^*$ ) which includes contribution of molecular interaction ( $T_2$ ) and magnet field inhomogeneity ( $T_2^{\Delta B}$ ). The rate of relaxation due to FID decay is express as:

$$\frac{1}{T_2^*} = \frac{1}{T_2} + \frac{1}{T_2^{\Delta B}} \quad (3.12)$$

$$T_2^{\Delta B} \approx \frac{2}{\gamma \cdot \Delta B_0}$$

where  $\Delta B_0$  is magnet inhomogeneity.

The contribution of magnet inhomogeneity ( $T_2^{\Delta B}$ ) is of order of 0.5 to 1.0 ms for low frequency bench top spectrometers. This implies that only for a very short  $T_2$  value can the true  $T_2$  relaxation time be measured. The excitation pulse in experiments is followed by the spectrometer dead time (grey region in fig. 3.2) during which signal is not detected. This time, even though it lasts only a few microseconds, hinders the observation of the chemically bound water with the shortest relaxation time components.

### 3.2.2. CPMG pulse sequence

#### *Hahn spin-echo*

Hahn [83] was the first to suggest a method for overcoming the limitation of the external magnetic field inhomogeneity. He proposed the application of  $180^\circ$  pulse ( $P_{180}^{x'}$ ) at time  $\tau$  – known as the pulse gap, after the initial  $P_{90}^{x'}$ , as shown in figure 3.3. This reverses the loss of coherence due to field inhomogeneity - figure 3.4. The magnetisation refocuses at time  $2\tau$  along the y'-axis and a spin-echo is created. The amplitude of the echo, at time  $2\tau$ , is already attenuated due to true transverse relaxation. Hence, the maximum of the echo amplitude is a function of  $T_2$  relaxation time. It is necessary, in Hahn spin-echo experiment, to conduct separate experiments for each value of  $\tau$ . Molecular diffusion is a second source of echo attenuation if there is a magnetic field gradient present. Diffusion is most significant for big  $\tau$ . The magnetisation decay depends then on a combination of relaxation due to molecular interaction and diffusion. It is expressed as:

$$M_{y'}(2\tau) = M_0 \cdot \exp \left[ -\frac{2\tau}{T_2} - \frac{2}{3} \cdot \gamma^2 \cdot G^2 \cdot D \cdot \tau^3 \right] \quad (3.13)$$

where  $G$  is magnetic field gradient strength and  $D$  is diffusion coefficient.

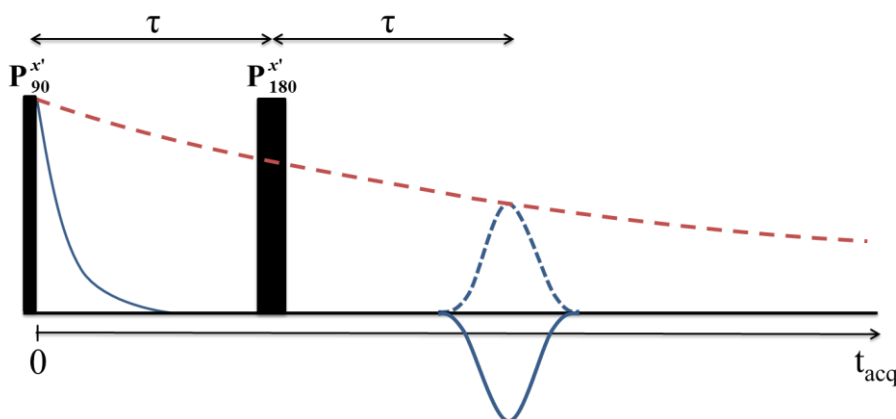


Figure 3.3 The Hahn spin-echo pulse sequence diagram. The red dash line shows the decay of transverse magnetisation.

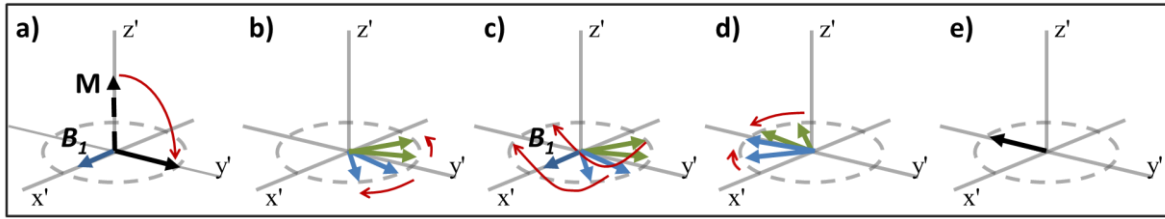


Figure 3.4 The Hahn spin-echo experiment: a) application of  $P_{90}^{x'}$  along  $x'$ -axis, b) de-phasing of spins, c) application of  $P_{180}^{x'}$  along  $x'$ -axis at time  $\tau$ , d) re-phasing of spins, e) refocused magnetisation at time  $2\tau$ .

### Carr – Purcell method

Carr and Purcell [84] provided a method that reduces the impact of diffusion on the determination of  $T_2$  relaxation time and also allows  $T_2$  to be measured in ‘one shot’. They modified the Hahn’s spin-echo pulse sequence by application of a train of  $P_{180}$  pulses as shown in figure 3.5. The Carr-Purcell sequence can be described as  $P_{90}^{x'} - \tau - [P_{180}^{x'} - 2\tau]_{N_E}$  where  $N_E$  is the number of echo acquired. It shows that subsequent  $180^\circ$  pulses are at  $\tau, 3\tau, 5\tau\dots$  whereas the amplitude of echoes appears at  $2\tau, 4\tau, 6\tau\dots$ . In Carr-Purcell method, as in Hahn spin-echo, all pulses are applied along the same axis,  $x'$  in this description. Hence, echoes are alternately positive and negative. The advantages of this technique are: a shortage of experiment time and elimination of diffusion effect. Hence, the expression for decay of magnetisation (echo amplitude at time  $2n\tau$ , where  $n$  is the echo number) is

$$M_{y'}(t) = M_0 \cdot \exp\left[-\frac{t}{T_2} - \frac{1}{3} \cdot \gamma^2 \cdot G^2 \cdot D \cdot \tau^2 \cdot t\right] \quad (3.14)$$

$$M_{y'}(t) \cong M_0 \cdot \exp\left(-\frac{t}{T_2}\right) \quad \text{for short } \tau$$

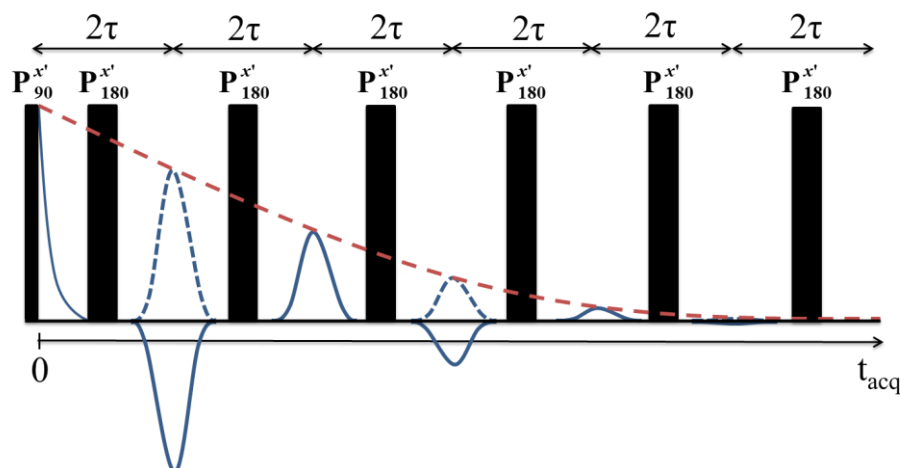


Figure 3.5 The spin-echoes pulse sequence diagram by Carr-Purcell method. The red dash line shows the decay of transverse magnetisation.

Any imperfection in the  $P_{180}$  length causes incomplete rephasing of magnetic moments. The effect is cumulative with each pulse as  $P_{180}$  is applied along  $x'$ -axis and rotates alternately the magnetisation from  $y'$  to  $-y'$  direction. It is especially important during the measurements of longer  $T_2$  as the acquisition of many  $P_{180}$  is required.

### Meiboom – Gill modification

Meiboom and Gill [85] introduce a modification to the Carr-Purcell method by shifting the phase of  $P_{180}$  by  $90^\circ$  relatively to initial  $P_{90}^{x'}$ . The  $P_{180}$  pulses are applied along  $y'$  direction as shown in figure 3.6. Hence, magnetic spins are rotated about the  $y'$ -axis and all echoes are positive. Pulse sequence is described as  $P_{90}^{x'} - \tau - [P_{180}^{y'} - 2\tau]_{NE}$ . The pulse orientation causes that only odd echoes have slightly reduced amplitudes due to pulse imperfection, but not cumulatively.

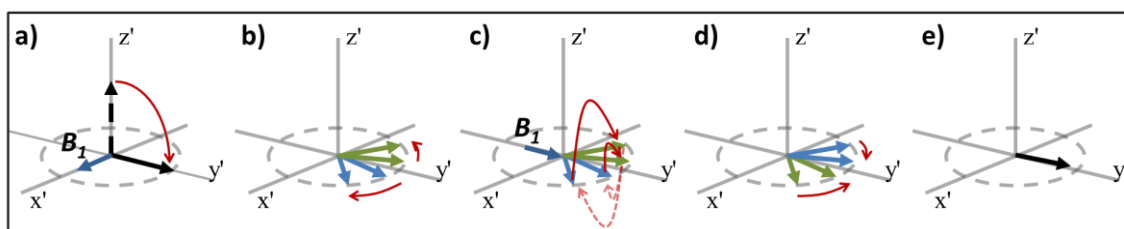


Figure 3.6 De-phasing and re-phasing of spins during the CPMG pulse sequence: a) application of  $P_{90}^{x'}$  along  $x'$ -axis, b) de-phasing of spins, c) application of  $P_{180}^{y'}$  along  $y'$ -axis, d) re-phasing of spins, e) refocus of magnetisation at time  $2\tau$ .

The Carr and Purcell NMR method with modification of Meilboon and Gill is called **CPMG pulse sequence**. The CPMG diagram is presented in figure 3.7. The CPMG sequence can be described as  $P_{90}^{x'} - \tau - [P_{180}^{y'} - 2\tau]_{NE}$ .

The common version of CPMG pulse sequence used nowadays involves application of  $P_{180}$  alternately along  $y'$  and  $-y'$ -axis and can be described as  $P_{90}^{x'} - \tau - [P_{180}^{y'} - 2\tau - P_{180}^{-y'} - 2\tau]_{NE/2}$ .

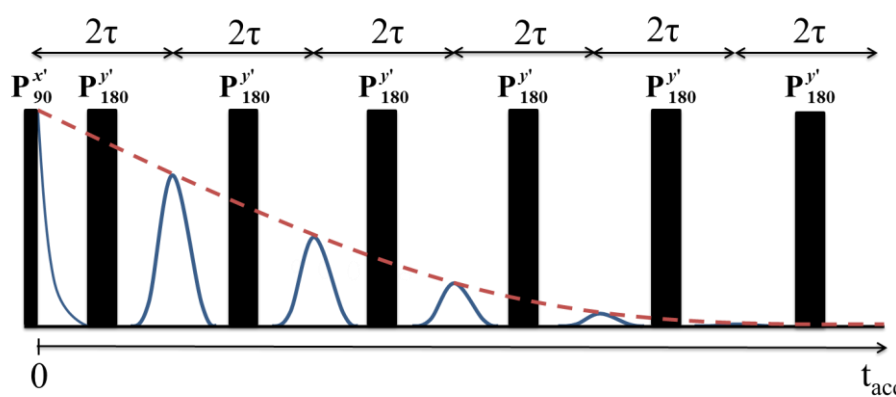


Figure 3.7 Pulse sequence diagram for CPMG sequence. The red dash line shows the decay of transverse magnetisation.

### 3.2.3. Quadrature echo sequence

The Quadrature echo experiment, also called the Quad or Solid echo experiment, has been designed to measure the static inter-nuclear magnetic dipole-dipole interaction [86].

The ‘rigid’ spins of crystalline solids coupled by such an interaction are characterised by the very short  $T_2$  relaxation time ( $\sim$ few  $\mu$ s) due to strong dipolar coupling of the spins. They are present in chemically bound and adsorbed water (solid protons). In the elementary FID experiment the relaxation due to that component is not seen or is already significantly attenuated due to the instrument dead time. While for the CPMG experiment the first echo amplitude is even further in time to ‘see’ it. The Quadrature pulse sequence overcomes that limitation by refocusing dipolar interaction.

Quadrature echo sequence (fig. 3.8) comprises two  $P_{90}$  pulses shifted relatively to each other by  $90^\circ$ . The pulses are spaced  $\tau$  pulse gap time apart:  $P_{90}^{x'} - \tau - P_{90}^{y'}$ . There are two phenomena observed. The more mobile spins (liquid) dephase continuously after first pulse due to spin-spin molecular interaction. The second  $P_{90}^{y'}$  does not alter their magnetisation [87]. Hence, the observable signal due to these spins is FID liquid signal as shown by dash - dot line extension in figure 3.8.

The application of second  $P_{90}^{y'}$  reverses the decay of solid signal - magnetic-dipolar interactions. The magnetisation of dipolar pairs of ‘rigid’ spins refocuses. It is partially recovered at time  $\tau$  from second  $P_{90}^{y'}$ . The decay due to dipolar interaction is not exponential but has an approximately Gaussian shape – echo in figure 3.8.

More details on determination of the signals intensities for ‘rigid’ and more mobile spins is presented in section 4.3.1.

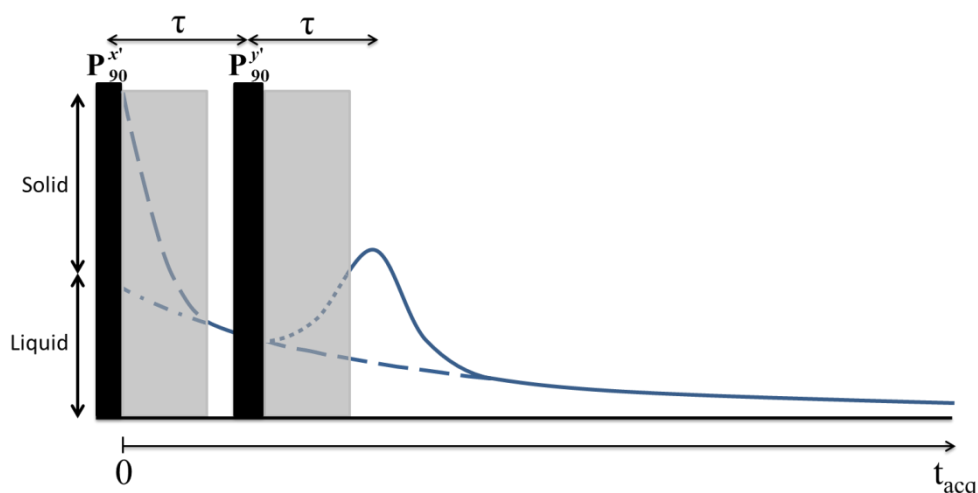


Figure 3.8 Pulse sequence diagram for Quadrature Echo sequence. The solid line presents the observable signal. Dash line shows the sum of solid and liquid signals as it would look only after  $P_{90}^{x'}$ . Dash – dot line shows the liquid signal. Grey region is spectrometer dead time.

### 3.2.4. $T_1$ measurements

There are two methods to measure  $T_1$  spin-lattice relaxation time: saturation and inversion recovery.

#### 3.2.4.1. Saturation recovery

The saturation recovery sequence (fig. 3.9) involves application of multiple  $P^{x'}$  pulses. They are used to destroy, that is bring to zero, the longitudinal magnetisation. Following that, for a variable time  $\tau_{rec}$ , the spin-lattice relaxation is allowed. Hence, the magnetisation recovers partially or fully depending on the  $\tau_{rec}$ . A single  $P_{90}^{x'}$  pulse is utilised to measure the momentary magnetisation at times  $\tau_{rec}$ . The longitudinal magnetisation as a function of  $\tau_{rec}$  is described as

$$M_z(t) = M_z^o \left[ 1 - \exp\left(-\frac{\tau_{rec}}{T_1}\right) \right] \quad (3.15)$$

where  $M_z^o$  is the equilibrium state magnetisation - aligned with the external magnetic field.

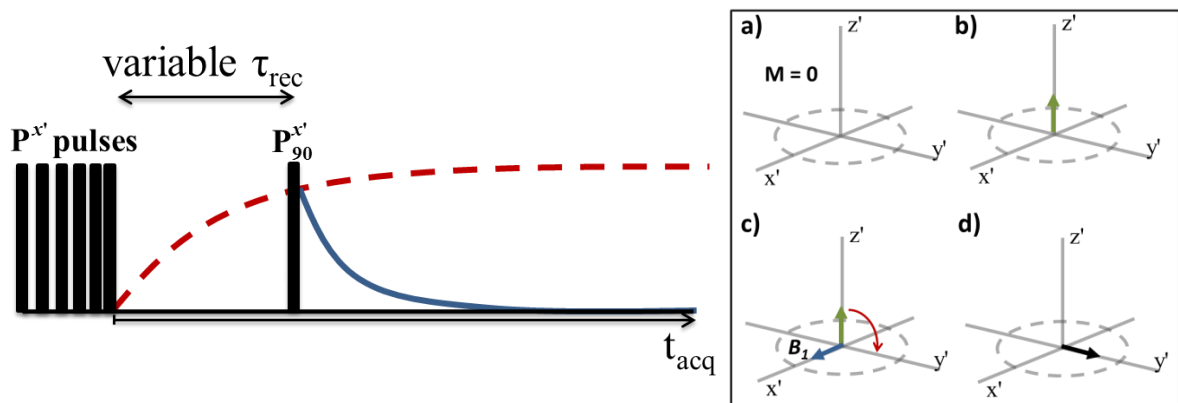


Figure 3.9 Left: Pulse sequence diagrams for  $T_1$  saturation recovery at variable  $\tau_{rec}$ . The red dash line shows the recovery of longitudinal magnetisation. Right: a) Magnetisation is saturated,  $M = 0$ ; b) Recovery of magnetisation during  $\tau_{rec}$ ; c) application of  $P_{90}^{x'}$ ; d) reverse magnetisation in transverse plane.

#### 3.2.4.2. Inversion recovery

The inversion recovery sequence is also used to determine  $T_1$ . The difference in the pulse sequence in comparison with saturation recovery is preparation of the initial magnetisation. In this case, the  $P_{180}^{x'}$  inverts the magnetisation along the  $z'$ -axis – figure 3.10. After that both sequences follow the same way. The spin-lattice relaxation process due to inversion recovery is expressed as

$$M_z(t) = M_z^o \left[ 1 - 2 \cdot \exp\left(-\frac{\tau_{rec}}{T_1}\right) \right] \quad (3.16)$$

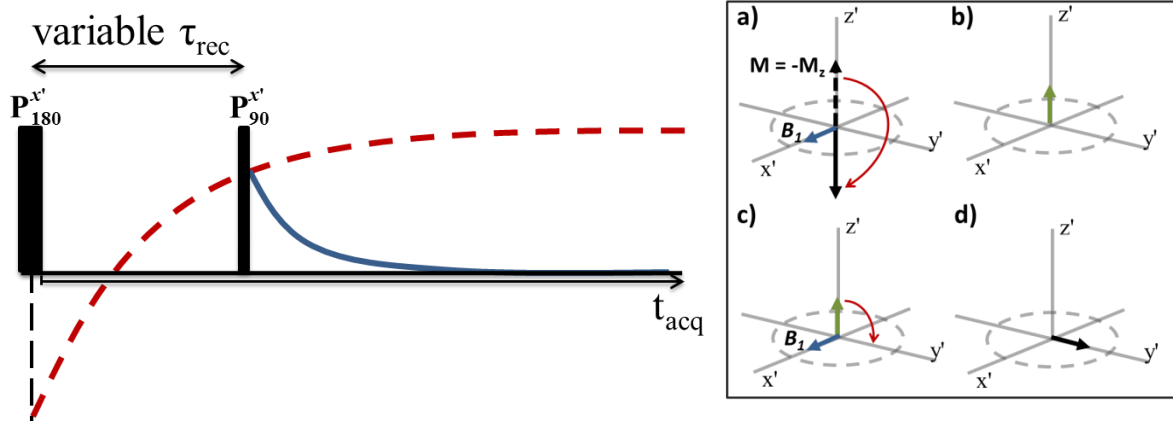


Figure 3.10 Left: Pulse sequence diagrams for  $T_1$  inversion recovery. The red dash line shows the recovery of longitudinal magnetisation. Right: a) magnetisation is reversed by  $P_{180}^{x'}$ ,  $M = -M_z$ ; b) recovery of magnetisation during  $\tau_{rec}$ ; c) application of  $P_{90}^{x'}$ ; d) reverse magnetisation in transverse plane.

Inversion recovery is the slower of two methods as the subsequent scans have to be performed after magnetisation fully recovers, for saturation recovery it saturates to zero anyway at the beginning of sequence. However, as the magnetisation is reversed to  $-M_z$  the sensitivity of method doubles.

$T_1$  measurements serve to establish the repetition time ( $\tau_{rd}$ ) of successive experiments as  $T_1$  mirrors the time when magnetisation is fully recovered. Time  $\tau_{rd}$  should be  $\sim 5 \cdot T_1$ .

### 3.3. THEORY OF RELAXATION

#### 3.3.1. BBP theory

The relaxation theory is complex and the advanced analysis based on quantum statistics is outside of the scope of this work and can be found in [88], [89]. What follows here is a brief summary.

Spins undergo rotational and translational motions that modify the magnetic dipole – dipole interactions between nuclei and the other interactions contributing to the local magnetic fields in the presence of a static magnetic field. This gives rise to the fluctuations in the local magnetic fields. The relaxation processes due to these perturbations in the dipolar field for liquids was first explained by Bloemberger, Purcell and Pound in 1948. The theory of relaxation is called after them: BPP theory [89].

Changes of the intensity and direction of the local magnetic field fluctuations with time are described by autocorrelation functions describing the relative motion of spins pairs  $G^{(m)}(t)$  [90]. The autocorrelation functions are given by:

$$G^{(m)}(t) = \alpha^{(m)} \cdot \left\langle \frac{Y_{2m}(\theta_0, \phi_0) \cdot Y_{2m}^*(\theta, \phi)}{r_0^3 \cdot r^3} \right\rangle \quad (3.17)$$

where  $Y_{2m}(\theta_o, \phi_o)$  and  $Y_{2m}^*(\theta, \phi)$  are the spherical harmonic functions of order  $m$  that has values 0, 1 and 2. The coordinates  $(r_o, \theta_o, \phi_o)$  and  $(r, \theta, \phi)$ , describe the internuclear vectors at time 0 and  $t$  respectively. The  $\alpha^{(m)}$  are constants such that  $\alpha^{(0)}=48\pi/15$ ,  $\alpha^{(1)}=8\pi/15$  and  $\alpha^{(2)}=32\pi/15$ . The \* indicates the complex conjugate. The notation  $\langle \rangle$  means the ensemble average over all pairs of the spins,  $I$ , (or, equivalently, one pair over all starting times)

In turn, the frequency dependence of intensity of fluctuation is expressed by spectral density functions  $J^{(m)}(\omega)$  that are the Fourier transform of autocorrelation functions [90]:

$$J^{(m)}(\omega) = \int_{-\infty}^{\infty} G^{(m)}(t) e^{-i\omega t} dt \quad (3.18)$$

The relaxation times are described in terms of spectral density functions  $J^{(m)}(\omega)$ . For spins  $I$  associated with the same nuclear species  $T_1$  and  $T_2$  are expressed as [90], [79]:

$$\frac{1}{T_1} = \frac{3}{2} \cdot \left(\frac{\mu_0}{4\pi}\right)^2 \cdot \gamma^4 \cdot \hbar^2 \cdot I \cdot (I + 1) \cdot [J^{(1)}(\omega_o) + J^{(2)}(2\omega_o)] \quad (3.19)$$

$$\frac{1}{T_2} = \frac{3}{2} \cdot \left(\frac{\mu_0}{4\pi}\right)^2 \cdot \gamma^4 \cdot \hbar^2 \cdot I \cdot (I + 1) \cdot \left[\frac{1}{4} \cdot J^{(0)}(0) + \frac{5}{2} \cdot J^{(1)}(\omega_o) + \frac{1}{4} \cdot J^{(2)}(2\omega_o)\right] \quad (3.20)$$

where  $\mu_0$  is the vacuum permeability.

For simple Brownian diffusion and rotations the spectral density functions are [82], [79]:

$$J^\times(\omega) = \frac{15}{12} \cdot J^{(0)}(\omega) = \frac{15}{2} \cdot J^{(1)}(\omega) = \frac{15}{8} \cdot J^{(2)}(\omega) = \frac{1}{r^6} \cdot \frac{2 \cdot \tau_c}{1 + \omega^2 \cdot \tau_c^2} \quad (3.21)$$

where  $\tau_c$  is correlation time of the motion and  $r$  is nuclear distance.

The dependence of  $T_1$  and  $T_2$  relaxation time on the correlation time  $\tau_c$  can be evaluated by substitution of spectral density functions – eq. (3.21), into the expressions for relaxation rates – eq. (3.19) and (3.20). The relation is presented in figure 3.11. At the lower values of  $\tau_c$  ( $\omega_o \cdot \tau_c < 0.62$ ) molecular motion is fast and  $T_1$  and  $T_2$  coincide. This is called the ‘extreme narrowing limit’. The  $T_1$  goes through a minimum at  $\omega_o \cdot \tau_c \approx 0.62$ . With increase of correlation time  $T_1$  and  $T_2$  diverge.  $T_1$  increases whereas  $T_2$  decreases due to  $J^{(0)}(0)$  contribution towards the ‘rigid lattice limit’ determined by the natural dipolar linewidth [82].

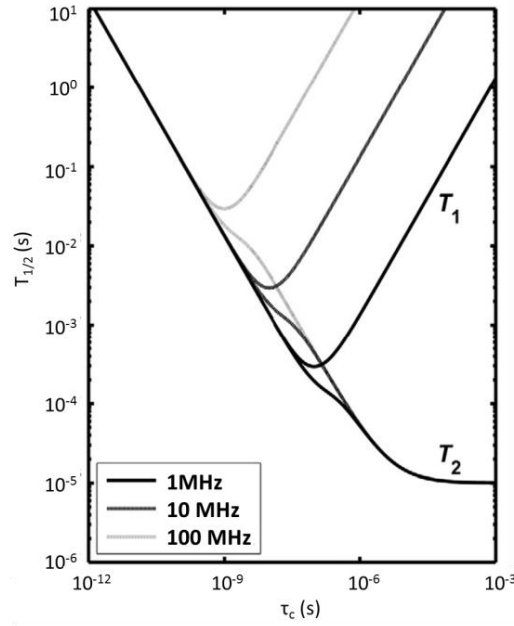


Figure 3.11  $T_1$  and  $T_2$  relaxation times for hydrogen spins as a function of correlation time  $\tau_c$  [82].

### 3.3.2. Fast exchange model of relaxation for liquids in pores and for pore size analysis

Introducing liquid to the empty space of pores in materials manifests in the increase of the relaxation rate in comparison with the bulk liquid. It implies interaction between the solid and liquid at their interface. The resulting relaxation rate of water in pores is the weighted average between slowly relaxing liquid in the pore bulk and rapidly relaxing surface water.

The equation which links the relaxation rate with the surface to volume ( $S/V$ ) ratio and hence to pore size ( $d$ ) for a system in which water molecules are in fast exchange is [27]:

$$\frac{1}{T_{1,2}} = \frac{V - \varepsilon S}{V} \cdot \frac{1}{T_{1,2}^{bulk}} + \frac{\varepsilon S}{V} \cdot \frac{1}{T_{1,2}^{surf}} \approx \frac{\varepsilon S}{V} \cdot \frac{1}{T_{1,2}^{surf}} \quad (3.22)$$

where  $T_{1,2}$  is observed  $T_1$  or  $T_2$  relaxation time,  $T_{1,2}^{surf}$  and  $T_{1,2}^{bulk}$  are the relaxation times of surface-adsorbed and bulk liquid respectively and  $\varepsilon$  is the thickness of surface layer.

The last approximation in equation (3.22) results from the facts that surface volume is  $\varepsilon S \ll V$  and surface relaxation time is  $T_{1,2}^{surf} \ll T_{1,2}^{bulk}$ . The surface layer thickness and relaxation time are related through the surface relaxivity  $\lambda = \varepsilon/T_{1,2}^{surf}$ . The pore size determination requires the knowledge of surface relaxivity. It may be established through NMR measurements of material dried to mono-layer coverage or by calculation.

An assumption of the model is the rapid exchange between molecules adsorbed on the pore surface and in the remaining part of the bulk liquid. The range of molecular diffusion should be larger than the size of measured pores:  $6 \cdot D \cdot T_{1,2}^{bulk} \gg d^2$ , where  $D$  is the liquid self-diffusion coefficient. It ensures that each molecule experiences equally the surface-layer and

bulk-pore environments. If this condition is not fulfilled then multi-exponential decay is observed [27], [82]. Application of model to cementitious materials is presented in section 3.4.3.1.

### 3.3.3. Korb model

A theoretical model of surface relaxation in proximity of a pore surface was proposed by Korb and his co-workers [91]–[93]. The mechanism of spin relaxation is explained by the modulation of the magnetic dipolar interaction between proton spins,  $I$ , diffusing on the pore surface and static paramagnetic impurities electrons,  $S$ , embedded in the pore surface. The modulation is induced by the translational diffusion of the  $I$  spins relative to fixed  $S$  spins. The dynamics of molecules at the pore surface are schematically represented in figure 3.12. The coexistence of two correlation time was proposed. The molecule undergoes a 2-dimensional diffusion across the surface encountering the impurities spins  $S$  with translational time  $\tau_m$  called the hopping time. The molecular walk across the surface lasts for characteristic surface residency time,  $\tau_s$ . Desorption of molecule from the surface occurs after a time  $\tau_s$ . The desorbed molecule has characteristics of bulk liquid. It is replaced on the surface by another molecule.

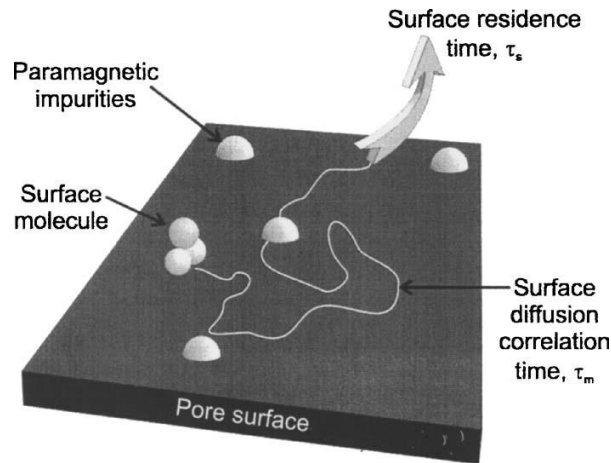


Figure 3.12 Scheme of two-dimensional diffusion process of water molecules on the pore surface containing paramagnetic impurities –  $\text{Fe}^{3+}$ .  $\tau_s$  is the surface residency time,  $\tau_m$  is the correlation time associated with molecule's jumps across the surface [92].

In the vicinity of the paramagnetic impurities (spins  $S$ ) the expressions for  $T_1$  and  $T_2$  surface relaxation times are [91], [92]:

$$\frac{1}{T_{1,surface}} = \frac{2}{9} \cdot \gamma_I^2 \cdot \gamma_S^2 \cdot \hbar^2 \cdot S \cdot (S + 1) \cdot [J^{(0)}(\omega_I - \omega_S) + 3 \cdot J^{(1)}(\omega_I) + 6 \cdot J^{(2)}(\omega_I + \omega_S)] \quad (3.23)$$

$$\frac{1}{T_{2,surface}} = \frac{4}{9} \cdot \gamma_I^2 \cdot \gamma_S^2 \cdot \hbar^2 \cdot S \cdot (S + 1) \cdot \left[ J^{(0)}(0) + \frac{1}{4} \cdot J^{(0)}(\omega_I - \omega_S) \right. \\ \left. + \frac{3}{4} \cdot J^{(1)}(\omega_I) + \frac{3}{2} \cdot J^{(1)}(\omega_S) + \frac{3}{2} \cdot J^{(2)}(\omega_I + \omega_S) \right] \quad (3.24)$$

where  $\gamma_s$  and  $\gamma_I$  are the gyromagnetic ratio for spins  $I$  and  $S$ ,  $\omega_{I,S}$  is the Larmor frequency of spin  $I$  and  $S$  respectively, and  $\omega_S = 658.21 \cdot \omega_I$

According to the Korb model, the spectral density function for the 2-dimensional walk of spins  $I$  on the pore surface is [92]:

$$J^{(0.1.2)}(\omega) = \frac{3}{40} \cdot \frac{\pi \sigma_S \tau_m}{\delta^4} \cdot \ln \left( \frac{1 + \omega^2 \tau_m^2}{\left(\frac{\tau_m}{\tau_s}\right)^2 + \omega^2 \tau_m^2} \right) \quad (3.25)$$

where  $\sigma_s$  is surface density of paramagnetic impurities,  $\delta$  is the minimum distance for water molecule to approach impurity,  $\tau_s$  is the surface residency time,  $\tau_m$  is the correlation time associated with molecule's jumps across the surface (hopping time).

### 3.4. NMR APPLICATION TO CEMENT BASED MATERIALS

#### 3.4.1. Evolution of relaxation component over hydration time

The early NMR studies of cementitious materials were conducted by Blinc *et al* [18]. The experiments were performed on cement ( $w/c = 0.42$ ) and  $C_3S$  pastes ( $w/c = 0.50$ ) prepared with distilled water and  $D_2O$ ; at frequencies 60.0 and 41.4 MHz for  $H_2O$  and  $D_2O$  respectively. The  $T_1$  and  $T_2$  relaxation times of single mobile component were measured by  $P_{90} - \tau/2$  and Carr-Purcell pulse sequences respectively [18]. The relaxation parameters were monitored from 10 minutes to 28 days of hydration. Three distinguishable stages of hydration were observed based on the changes in relaxation times: initial stage with slow decrease of  $T_1$  and  $T_2$ , intermediate stage (after about 2 and 8 hours for protonated and deuterated pastes respectively) identified by rapid decrease and final stage when decline slows down beyond ~40 and 80 h. The relaxation times of cement paste were systematically lower in comparison with  $C_3S$  paste indicating the influence of paramagnetic impurities on relaxation process.

Schreiner *et al* [19] examined Portland cement pastes prepared with  $w/c$  ratios 0.33 to 0.63 during hydration from 10 minutes to almost 1 year at 70% RH. They performed  $T_1$ ,  $T_2$  and  $T_2^*$  measurements by applying inversion recovery, Carr-Purcell and FID sequences at frequency of 38 and 19 MHz. Based on  $T_1$  results three distinct populations of hydrogens are observed in an advance stage of hydration: solid OH groups within CH,  $T_1 \sim 500$  ms at 38 MHz; water in micropores and layers,  $T_1 \sim 5$  ms; and bound water within 'solid' C-S-H gel,  $T_1 \sim 1$  ms. Four stages of hydration were identified: first, below 10 min, with a single relaxation time,  $T_1 \sim 30$  ms; dormant period when gel mobile-water is distinguished; third stage beyond 2h when the solid component begins to grow; and final stage beyond 12 h with three components clearly distinguished. The authors noted that  $T_2$  and  $T_2^*$  measurements for ordinary Portland cement

are not adequate as magnet inhomogeneity and paramagnetic impurities shorten relaxation times and prevent observation of all components. They suggested use of white cement paste to limit the influence of impurities and enhance the resolution.

In late 1980s, Lasic *et al* [20] monitored the evolution of  $T_1$  relaxation times of a synthetic white cement with  $w/c = 0.42$  at NMR frequency of 200 MHz. Initially two populations were observed with  $T_1$  of about 100 ms and between 18-25 ms corresponding to water between grains of cement and early crystalline products. After 20 hours, they evolved into five distinctive hydrogen populations: hydrogens in CH,  $T_1 \sim 1$  s; water in crystalline hydrates,  $T_1 \sim 150$  ms; pore and adsorbed water,  $T_1 \sim 30$  ms; hydrogens in C-S-H gel,  $T_1 \sim 10$  ms; and water molecules in contact with paramagnetic impurities,  $T_1 \sim 2$  ms.

The NMR experiments on white cement paste were also performed during the same year by Miljkovic *et al* [21]. The evolution of  $T_2$  relaxation times of pastes with  $w/c$  from 0.32 to 0.62 was observed by applying CPMG and FID sequences at 90 MHz. The hydrogens were divided into liquid-like,  $T_2 \sim 2$ -10 ms, and two solid-like populations,  $T_2$  of  $\sim 10$  and  $\sim 100$   $\mu$ s. The liquid-like  $T_2$  decreased beyond 8h of hydration and had shorter values at lower  $w/c$  while solid-like  $T_2$ s stayed constant despite the hydration time and  $w/c$ . The intensity of solid-like hydrogens increased with time at the expense of liquid-like. The rise was higher at lower  $w/c$ .

In 1990s the studies were focused mainly on  $T_2$  relaxation times and their correlation to pore size distribution based on fast exchange model as follows in section 3.4.3.1.

The new decade started with the study of  $T_2$  relaxation time development for sealed white cement paste,  $w/c = 0.42$ , by Greener *et al* [24]. The authors presented a new approach to analyse FID and CPMG data. FID decay was fitted to solid like components by Gaussians and to mobile like component by single exponential. The division of solid and mobile components was set at  $T_2 \sim 100$   $\mu$ s. Further the mobile signal was decomposed into particular hydrogen populations based on multi-exponential fitting of CPMG decay. Authors identified five populations: protons in solid environment (CH and ettringite) with  $T_2 \sim 20$   $\mu$ s; interlayer water with  $T_2$  below 100  $\mu$ s; C-S-H gel water with decreasing  $T_2$  from initial 3 ms to 200  $\mu$ s at 6 days (maximum measured time); capillary pore water with  $T_2$  reduction from  $\sim 30$  ms to  $\sim 800$   $\mu$ s at 6 days; and the secondary hydration water with the longest  $T_2$  of  $\sim 50$  ms attributed to the water released due to ettringite – monosulfate conversion.

The same methodology was applied by Holly *et al* [25].  $T_2$  relaxation time distributions of sealed white cement pastes,  $w/c = 0.42$ , were measured for few months at curing temperatures of 2, 20, 60 and 100°C at 30 MHz. Authors recognised the same five hydrogen populations as Greener *et al* [24]. Mature paste hydrated for  $\sim 40$  days and cured at 20°C were characterised by small quantity of capillary water, below 2%, with  $T_2 \sim 1$  ms; high fraction of protons in crystalline water and OH<sup>-</sup>, 37%,  $T_2 \sim 19$   $\mu$ s; two water reservoirs associated with C-S-H: interlayer and gel pore water with  $T_2 \sim 90$  and 200  $\mu$ s and fraction of 19 and 36%, respectively. The secondary hydration water was also detected at the hydration time of 10-20 hours. The increase of curing temperature accelerated the cement hydration process as evidenced by faster development of crystalline, interlayer and gel pore water intensities as well as supportive XRD analysis. Mature pastes ( $\sim 40$  days) cured at elevated temperatures were characterised by higher capillary and interlayer pore water intensities and lower gel pore

water intensity. No direct pattern influence of temperature rise was registered for the shortest  $T_2$  component ( $\sim 15\text{-}19\mu\text{s}$ ) as its intensity was increasing and decreasing alternately.

### 3.4.2. 2D exchange experiments

$T_1$ - $T_2$  and  $T_2$ - $T_2$  two-dimensional relaxation correlation experiments were performed on cement pastes by McDonald *et al.* [92], [94] and Monteilhet *et al* [95]. The 2D  $T_1$ - $T_2$  and  $T_2$ - $T_2$  correlation method is based on introducing an additional magnetisation storage period between encoding periods that gives hydrogens time to exchange between different environments [95]. The  $T_1$ - $T_2$  experiments have already been proposed in 80's [96] but were limited by lack of suitable tools for analysis which requires performing 2D inverse Laplace transform. The algorithm enabling that transform reliably was proposed by Venkataramanan [97].

$T_1$ - $T_2$  experiments of white cement paste ( $w/c = 0.4$ ) showed multiple discrete pore size distribution with two dominant peaks on the diagonal and one off diagonal feature – fig 3.13 left. The  $T_2$ - $T_2$  correlation spectra presented the same diagonal feature and two well-defined off-diagonal peaks. Two peaks at diagonal – water reservoirs, were assigned to gel porosity and separately resolved as inner and outer C-S-H or interlayer and gel pores. The presence of symmetrical off-diagonal peaks for  $T_2$ - $T_2$  experiment have suggested the exchange of the hydrogen or water between different pore size reservoirs [92], [95]. The alternate explanation that the exchange occurred between two reservoirs of the same size but with different  $\text{Fe}^{3+}$  concentration was investigated on synthesised C-S-H with reduced paramagnetic impurities by Valori *et al* [98]. The spectrum was shifted up the diagonal due to a decrease in paramagnetic concentration and still shown two off-diagonal peaks. It confirmed exchange between pores with different sizes occurred.

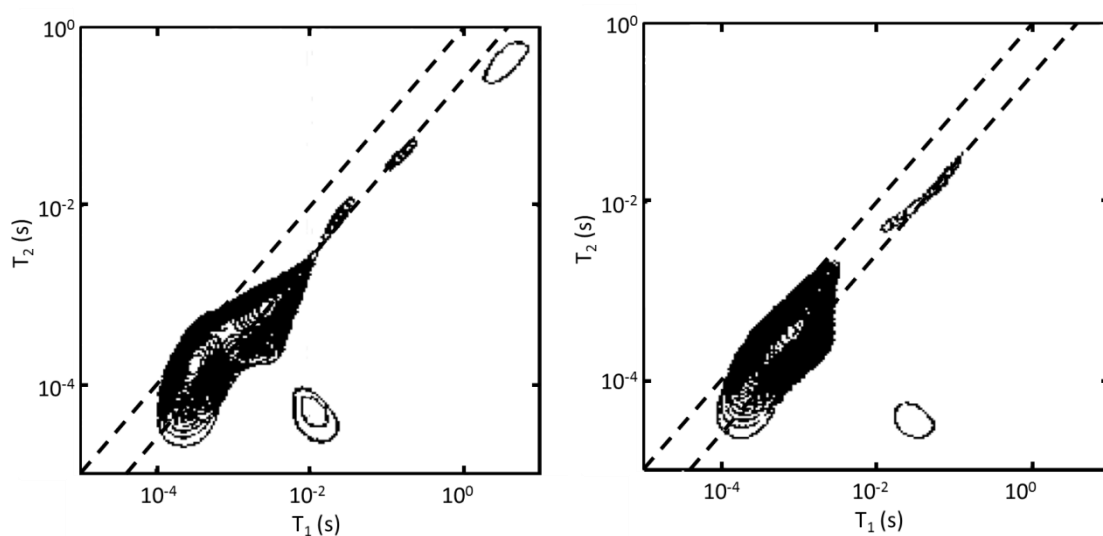


Figure 3.13 The  $T_1$ - $T_2$  correlation spectra of white cement paste (left) and white cement paste with addition of silica fume (right) cured for 7 days (adapted from [92]).

The comparison of  $T_1$ - $T_2$  spectra from paste of white cement and white cement with addition of 10% silica fume showed that diagonal peaks of silica fume paste are not as discrete as for white cement paste – fig. 3.13. The off-diagonal peak shifts towards longer  $T_1$  at the earlier age for paste with silica fume which means that the hydration of this paste progresses faster [92].

The ratio of  $T_1$  relaxation time to  $T_2$  relaxation time was determined for cement pastes by  $T_1$ - $T_2$  experiment as equal to 4 at 20 MHz - components aligned along  $T_1 = 4T_2$  as presented in figure 3.13. The result showed that the ratio of  $T_1$  to  $T_2$  is only a function of NMR Larmor frequency and two correlation times - surface resistance and hopping times -  $\tau_s$ ,  $\tau_m$  [92]. Giving the magnet frequency and hopping time of 1.3 ns [99] the surface residency time was evaluated as  $\sim 13 \mu\text{s}$  [92], [94].

Based on  $T_2$ - $T_2$  correlation the exchange time was estimated as  $\sim 5$  ms. The length scale of exchange, based on the cement grain size, was defined as  $\sim 4 \mu\text{m}$  and as between inner and outer product of hydration although it is no longer considered that exchange is between inner and outer product. The diffusion coefficient of exchange was calculated as  $5 \cdot 10^{-10} \text{ m}^2/\text{s}$ . The translation diffusion coefficient at the surface of C-S-H ( $2.3 \cdot 10^{-11} \text{ m}^2/\text{s}$ ) was calculated from the hopping time in 2D random walk on the surface – 1 ns, and mean size of jump equalled to size of water molecule – 0.3 nm [95]. The calculated NMR diffusion coefficients – for exchange and across surface, are in good agreement with diffusion coefficients obtained by molecular dynamics simulations for water diffusing in the pore space above the internal pore surface and on the internal pore surface of tobermorite,  $6 \cdot 10^{-10} \text{ m}^2/\text{s}$  and  $5.0 \cdot 10^{-11} \text{ m}^2/\text{s}$  respectively [100].

### 3.4.3. Pore size distribution

#### 3.4.3.1. Fast Exchange Model for pore size analysis

Pore size distributions in the microstructure of cement pastes can be estimated based on the fast exchange model of relaxation presented in section 3.3.2 (eq. (3.22)). The key factors in this calculation are evaluation of surface relaxation time,  $T_{1,2}^{surf}$ , and surface layer thickness,  $\varepsilon$ , that give together surface relaxivity,  $\lambda = \varepsilon/T_{1,2}^{surf}$ , and determination of the pore shape.

One approach to do so is through experiments. Bhattacharja *et al* [101] in 1993 calculated the surface relaxivity and pore size distribution of white cement paste mixed at  $w/c = 0.4$ . CPMG measurements were performed at 25 MHz during hydration from 1 to 28 days. The calculation of the surface relaxivity involved the additional study of partially filled (progressively dried) samples to correlate the observed  $T_2$  and the volume fraction of water filling pores. The surface area at each hydration time was obtained through nitrogen BET analysis. The results show that  $\lambda$  does not vary with hydration time and is  $1.6 \cdot 10^{-6} \text{ cm/ms}$ . The pore sizes of two identified populations were fairly constant over hydration with diameter of 18 and 90 nm assuming cylindrical pores.

A year later the first Laplace inversion of CPMG data to yield the  $T_2$  relaxation time and hence the pore size distribution were performed by Halperin *et al* [10]. The transverse

relaxation of water within cement paste with  $w/c = 0.43$  was measured by application of FID and CPMG sequences. The authors correlated the thickness of water monolayer,  $\varepsilon = 3 \text{ \AA}$ , with the constant relaxation time observed for pastes at saturation fraction below 0.2 when all water became the mobile surface water,  $T_2^{surf} \approx 40 \text{ \mu s}$ . The obtained surface relaxivity was  $7.5 \cdot 10^{-7} \text{ cm/ms}$ . Mobile water measured by CPMG was divided into two populations interpreted as the capillary and gel pores. The pore sizes were calculated based on spherical shape. The capillary pore size decreased from about 200 nm at 2.5 hours of hydration to 60 nm at 8 hours and 12 nm at 7 days. Beyond that time it stayed constant. The gel pore size was weakly dependent on hydration time: 3.5 nm at 2.5 hours and 2.5 nm at 59 days.

Surface relaxation time was assumed to be equalled to the relaxation time of the bound water,  $10 \text{ \mu s}$ , by Bohris *et al* [22]. Authors performed FID and CPMG measurements of cement pastes ( $w/c = 0.3$  and  $0.5$ ) at 20 MHz. Results revealed the presence of three water populations: chemically bound water, gel water with  $T_2 = 80 \text{ \mu s}$ , and capillary water,  $T_2 = 350 \text{ \mu s}$ . The pore sizes were calculated as 2.4 and 15 nm with assumption that gel pores form layers and capillary pores are spherical and partially filled.

Valckenborg *et al* [102] measured dry sample during exposure to wet air flow and assumed that the  $T_2$  relaxation time of first appearing signal is attributed to the surface layer. The obtained surface relaxation time for mortar was  $85 \text{ \mu s}$ . With monolayer of water (0.3 nm) and spherical shape of pores it led to gel and capillary pore sizes of  $\sim 6$  and  $\sim 27$  nm.

The other approach to evaluate surface relaxation time is through the calculation using the Korb model (eq. (3.24)-(3.25) in section 3.3.3). However, in that case the knowledge of other parameters is required: surface density of paramagnetic impurities ( $\sigma_s$ ), the minimum distance for water molecule to approach impurity ( $\delta$ ), surface residency time ( $\tau_s$ ) and surface hopping time ( $\tau_m$ ). Monteilhet *et al* [95] performed analysis of the pore size distribution of white cement paste based on  $T_2$ - $T_2$  correlation experiments. They inferred  $\sigma_s$  from electron spin resonance and used  $\tau_m$  and  $\tau_s$  of 1.3 nm and  $13 \text{ \mu m}$  as obtained from frequency dependence of  $T_1$  [99] and  $T_1$ - $T_2$  correlations [92] respectively. Assuming surface monolayer (0.28 nm) and value of  $\delta = 0.2 \text{ nm}$ , surface  $T_2$  relaxation time is  $100 \text{ \mu s}$ . The smallest pores had calculated thickness of 1.0-1.7 nm assuming planar shape and the larger pore size ranged between 7-30nm depending on the shape [95].

The pore size calculation according to Fast Exchange Model can bring certain level of uncertainty due to difficulty in defining the surface relaxivity.

### 3.4.3.2. Amplitude Model

An alternative method to estimate the pore sizes was developed by McDonald *et al* [26] - hereafter called Amplitude Model. The estimate of pore size distribution in that model is based on the *amplitudes* of relaxation components as a function of water content rather than on the relaxation *times*.

The Amplitude Model was developed based on the layered C-S-H microstructure. In saturated pores (fig. 3.14a) the surface water molecules are in fast exchange with those in the

bulk of pore. Hence, NMR sees all molecules as mobile with one  $T_2$  relaxation time. The drying may occur in two alternative ways. Figure 3.14b(ii) shows the scenario where no surface layer is initially created, water is removed layer by layer across the pore. All water molecules are mobile until the last layer; however the  $T_2$  relaxation time decreases as a result of increase in  $S/V$  ratio. The second possibility is that, a water layer stays on the pore surface as drying progresses (fig. 3.14b(ii)). There are two distinguished  $T_2$  water environments. One has the same relaxation time as mobile water in fully filled pore (same  $S/V$ ) and decreasing amplitude; and second – surface layer, has shorter relaxation time, since it cannot any more exchange with bulk of pore, and increasing amplitude. This scenario is typical for the drying processes that involve considerable capillary forces. Hence, it was used to perform advance quantification.

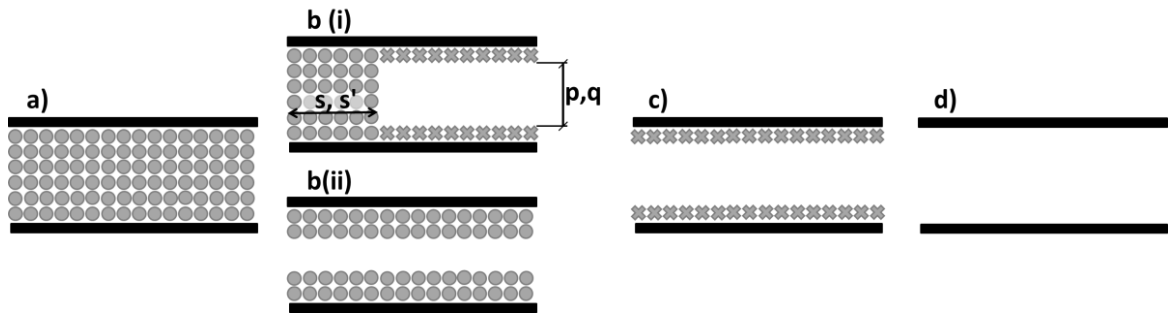


Figure 3.14 The scheme of pore drying: a) pore full of mobile water, b) two possible ways of pore drying, c) surface water layer staying, d) an empty pore [26]. Circles represent mobile water molecules, crosses are immobile, surface water molecules.

The experiments were performed for white cement paste ( $w/c = 0.4$ ) by applying Quad Echo sequence. The total signal was divided into solid ( $I_{sol}$ ) and mobile ( $I_{mob}$ ) parts. The mobile intensity decreased successively at two different rates, above and below effective water mass fraction of 0.7. The first stage was assumed to have origin in drying of C-S-H gel pores (with specific surface area,  $M$ , and thickness,  $p+2$ , both expressed in water molecules); second - of C-S-H interlayer pores (with specific surface area,  $N$ , and thickness,  $q+2$ ). During drying intensity was defined as proportional to the pore thickness and the fraction ( $s, s'$ ) of the specific surface area of pore still filled with liquid. The expression for normalised mass of water ( $m$ ) remaining along drying was stated in the same terms. The mobile intensity and mass were expressed as:

$$\begin{aligned} I_{mob} &= M \cdot (p + 2) \cdot s + N \cdot (q + 2) \cdot s' \\ m &= 1 - M \cdot p \cdot (1 - s) - N \cdot q \cdot (1 - s') \end{aligned} \quad (4.1)$$

Further, the mobile water intensity for both stages ( $I_{mob1}$  and  $I_{mob2}$ ) was characterised as a function of mass through the equations:  $I_{mob1} = a_1 \cdot m + b_1$  and  $I_{mob2} = a_2 \cdot m + b_2$ .

The equations were solved with assumption for first stage of drying that interlayer pores are full ( $s' = 1$ ) and for second stage that gel pores were empty of mobile water ( $s = 0$ ). This led to the expression for pore size parameters in function of the gradients of the fitting lines:

$$p = \frac{2}{a_1 - 1}; \quad q = \frac{2}{a_2 - 1}; \quad (4.2)$$

The calculated pore sizes are 1.5 and 4.1 nm for C-S-H interlayer and gel pores respectively.

#### 3.4.4. Specific surface area

Halperin *et al* [10] presented the changes of specific surface area of cement paste ( $w/c = 0.43$ ) over hydration time based on the evolution of  $T_2$  relaxation time and its intensity recalibrated as volume of evaporable water. Calculations were performed according to the fast exchange model of relaxation. The rapid development of the surface was observed between 6 and ~50 hours when it reached the constant value of 225 m<sup>2</sup>/g of anhydrous cement.

The surface area of cement based material was measured by application of Nuclear Magnetic Relaxation Dispersion (NMRD), so-called field cycling, experiments by Barberon *et al* [99]. This technique allows on the separation of the surface and bulk contribution towards the relaxation rate by performing measurement over the range of the nuclear Larmor frequency. Authors examined continuously the mortar sample ( $w/c = 0.38$ ) up to 12 hours of hydration at frequencies values between 0.1 and 10 MHz. The rapid increase of the specific surface area was observed after 6 hours of hydration. The calculated value at 12 hours was ~100 m<sup>2</sup>/g. The linear dependence of the area on cement degree of hydration was evidenced.

## 4. Experimental methods

### 4.1. SAMPLE PREPARATION

#### 4.1.1. Cement composition

In this study low C<sub>3</sub>A white Portland cement was used. This cement is characterised by an almost total lack of ferric impurities since there is minimal Ferrite content. Cement was delivered from Aalborg Portland in two separate batches. The mineralogical and chemical composition of the batches are presented in table 4.1 and 4.2.

Table 4.1 Mineralogical composition of used cements.

<i>Phases in anhydrous cement</i>		<i>Cement 1 [%]</i>	<i>Cement 2 [%]</i>
Alite	C <sub>3</sub> S	66.9	64.0
Belite	C <sub>2</sub> S	19.7	19.5
Aluminate	C <sub>3</sub> A	3.6	3.3
Ferrite	C <sub>4</sub> AF	0.8	0.0
Portlandite	CH	0.7	1.8
Anhydrite	C\$	2.6	–
Gypsum	C\$.2H	–	3.3
Bassanite	C\$.0.5H	2.1	2.1
Amorphous		3.6	6.0
Total		100	100

Table 4.2 Chemical composition of used cements.

<i>Oxides</i>	<i>Cement 1 [%]</i>	<i>Cement 2 [%]</i>
CaO	69.3	71.6
SiO <sub>2</sub>	24.7	21.8
Al <sub>2</sub> O <sub>3</sub>	2.2	1.5
Fe <sub>2</sub> O <sub>3</sub>	0.3	0.4
SO <sub>3</sub>	2.1	2.0
P <sub>2</sub> O <sub>5</sub>	0.3	0.4
K <sub>2</sub> O	0.1	0.1
TiO <sub>2</sub>	0.1	0.1

### 4.1.2. Mixing and curing

Cement pastes were prepared at water to binder (100% white cement or 90% white cement and 10% silica fume) ratio 0.4 by mass. This ratio was agreed across Transcend projects. The mixing of cement pastes was performed in accordance with Nanocem protocols [103], [104]. According to these protocols, to prepare each white cement paste mix, 80 grams of white cement powder and 32 grams of distilled water were weighed and the water added to the cement. This was immediately followed by 3 minutes mixing at 500 rpm, 2 minutes resting during which the paste was covered and 2 minutes mixing at 2000 rpm.

The preparation of cement paste with added silica fume involved pre-dispersion of the silica fume (8g) in distilled water (32g) with Sika ViscoCrete EH 20 superplasticizer by mixing at 2000 rpm for 5 minutes. The amount of superplasticizer was 0.1% by weight of the binder. Next, 72 grams of white cement powder was added and the three stage mixing, described above, was performed.

Pastes were placed in moulds or NMR tubes as described in next section.

In all experimental parts of this work paste samples were cured under saturated Calcium Hydroxide (CH) solution. The reasons are threefold. First, the solution fills chemical shrinkage voids during curing of small samples. Second, the solution prevents sample contact with atmospheric carbon dioxide which causes carbonation. Third, CH solution approximates the cement pore liquid and prevents leaching.

### 4.1.3. Samples casting and specific preparation for experiments

#### 4.1.3.1. Samples for sorption isotherm measurements

Freshly mixed cement paste was cast in cylindrical moulds 20 mm in height and 8 mm in diameter and covered with a small quantity of saturated CH solution. After 24 hours, they were removed from the moulds and further cured under solution in glass bottles at room temperature. The ratio of sample to solution volume was 1:1.

After 28 days of curing, samples were crushed to millimetre size grains with a pestle and mortar. Approximately 100 mg pieces were equilibrated to the desired relative humidity at room temperature in an IGA<sub>sorp</sub> Moisture Sorption Analyser (described in section 4.6).

In order to study the first desorption isotherm crushed pieces were first equilibrated at 80% relative humidity and then at different humidities in the range 80 to 3%. For the re-adsorption branch of the isotherm, samples were first equilibrated to 80% and then 5% RH and then re-equilibrated to higher relative humidity. The second desorption was studied following equilibration at 80, 5 and 80% RH and then at desired lower humidity. Three further samples were prepared. The first was an “as cured” material, taken to represent 100% RH. The second was a sample equilibrated directly to 90% RH. The third was a sample dried in a vacuum oven at 180°C, taken to represent 0% RH.

Once equilibrated, samples were removed from the IGA<sub>sorp</sub> chamber and quickly transferred to 5 mm diameter NMR tubes. Glass rods were added to reduce the free volume and the tubes sealed tightly with parafilm<sup>®</sup> to prevent changes in water content. Further, the

5 mm tubes were placed centrally in 10 mm diameter NMR tubes that fitted the NMR machine. The NMR tubes were made of borosilicate glass.

#### 4.1.3.2. Samples for temperature dependent curing studies

White cement paste and white cement paste with addition of silica fume were directly deposited into NMR tubes using a plastic pipette immediately after mixing. Sample height and diameter were around 8 mm. A few drops of CH saturated solution were added to the top of samples (2-3 mm) and tubes were closed tightly.

Six curing temperatures were chosen: 10, 20, 30, 40, 50 and 60°C. Samples were stored variously in a fridge, the laboratory or a temperature controlled water baths dependent on the desired curing temperature. The stability of the temperature was:  $10 \pm 1^\circ\text{C}$  in the fridge;  $20 \pm 0.5^\circ\text{C}$  in the laboratory; and  $30/40/50/60 \pm 0.2^\circ\text{C}$  in water baths.

Samples were periodically measured. For that purpose, the CH solution was removed by using a glass pipette, the tube walls and sample surface were touch-dried with tissue paper and the mass of sample was recorded. The glass rod was inserted to reduce the air volume and tube was sealed with parafilm<sup>®</sup>. After measurements in the temperature-controlled NMR probe (described in section 4.7), CH solution was back-added at the top of samples. The care was taken to put back as much as possible of the removed earlier solution. If it was not enough, fresh drops were added.

#### 4.1.3.3. Samples for activation energy analysis

Due to the broad temperature range to be studied (-20 to +60°C) different sample preparation methods were assessed to verify the best method of performing experiments.

The chosen method comprised samples cast in the NMR tubes to a length of 5 cm. Samples were cured under saturated CH solution. During experiments the solution was left on top of samples but outside the NMR coil. Tubes were connected by a rubber pipe to a water reservoir in order to accommodate the pressure changes during the experiments.

#### 4.1.3.4. Samples for water-isopropanol exchange experiments

Samples for collaborative research on isopropanol exchange were prepared by Dr Radoslaw Kowalczyk. Cement pastes were mixed at water to cement ratio 0.46 when prepared with H<sub>2</sub>O and 0.51 with D<sub>2</sub>O to introduce the same amount of hydrogen and deuterium moles. The pastes were cast as described in section 4.1.3.1. After 50 days of curing samples were crushed into millimetre size pieces to increase the surface area and accelerate ingress of solvent. The isopropanol, (CH<sub>3</sub>)<sub>2</sub>CHOH, and partially deuterated isopropanol, (CH<sub>3</sub>)<sub>2</sub>CDOD, were used as solvents. The exchange using deionised water was also performed to test reversibility. Exchange was carried out by 3 wash cycles of 24 hours each. Each cycle was performed with fresh solvent in solvent to sample volume ratio at least 20:1. More details on the sample preparation are presented in [105] (Appendix 2).

Sample casting for specific experiments is summarised in table 4.3.

Table 4.3 Characteristic of samples casting.

<i>Experiment</i>	<i>Cast</i>	<i>Cement</i>	<i>Sample dimension</i>		<i>Curing Temperature</i>
Sorption isotherm	Mould	1	$\phi = 8\text{mm}$	$L = 20\text{mm}$	20°C (laboratory)
Temperature dependence	Tubes	2	$\phi = 8\text{mm}$	$L = \sim 8\text{mm}$	10°C (fridge)
					20°C (laboratory)
					30-60°C (water baths)
Activation energy	Tubes	1	$\phi = 8\text{mm}$	$L = 50\text{mm}$	20°C (laboratory)
Isopropanol	Mould	2	$\phi = 8\text{mm}$	$L = 20\text{mm}$	20°C (laboratory)

## 4.2. NMR MEASUREMENTS

### 4.2.1. Spectrometers

$^1\text{H}$  NMR Quad echo, CPMG and  $T_1$  recovery measurements, described in the following sections, were made on a bench top spectrometer operating at 20 MHz. Early measurements (sorption and activation energy experiments) were performed on Resonance Instruments ‘‘Maran’’ spectrometer (Oxford Instruments, UK). Later work (the curing temperature and solvent exchange) used a Kea<sup>2</sup> spectrometer (Magritek, New Zealand).

### 4.2.2. Quad Echo parameters

The Quad Echo (QE) signals were acquired as a function of pulse gap ( $\tau$ ) between 90° radio frequency pulses. Typically eight QE experiments were performed with pulse gaps in the range 12-54  $\mu\text{s}$ . The 90° excitation pulse length was 2-2.5  $\mu\text{s}$  (Maran) and 4-5  $\mu\text{s}$  (Kea<sup>2</sup>). Following the second 90° pulse the spectrometer dead time was 10  $\mu\text{s}$  for most experiments. However, in the case of the sorption experiment it was much longer (over 20  $\mu\text{s}$ ) due to the incorporation of an additional amplifier in the system required as the sample was very small. Various 512 to 4096 points per decay were acquired with a dwell time of 1  $\mu\text{s}$  and repetition time<sup>10</sup> ( $\tau_{rd}$ ) of 1 s. The number of averages depended on the sample size. For the sorption experiment 1000 scans were recorded due to the very small quantity. In temperature dependent investigations, 32 scans were sufficient.

The isopropanol exchange experiments<sup>11</sup> were performed with pulse gap in the range 10-35  $\mu\text{s}$  and 256 scans.

<sup>10</sup> repetition time in entire thesis is treated as the time from the start of one sequence to the start of the next one

<sup>11</sup> measured by R. Kowalczyk

### 4.2.3. CPMG parameters

The NMR Carr-Purcell-Meiboom-Gill (CPMG) pulse sequence was applied to record the train of logarithmically spaced echoes.

The duration of the  $90^\circ$  radio frequency pulse was the same as for QE experiments. The  $180^\circ$  pulse was twice as long as  $90^\circ$  pulse for experiments performed on Maran spectrometer and twice as intense as  $90^\circ$  pulse for Kea<sup>2</sup> experiments.

The  $180^\circ$  pulse gaps ( $2\tau$ ) were increment logarithmically according to

$$2\tau_i = 2\tau_0 \cdot \alpha^i, \quad i = 0 \dots (N_E - 1) \quad (4.1)$$

where  $N_E$  is the number of echoes and  $\alpha$  is a constant.

In the case of sorption experiments the 256 echoes with  $\tau$  spaced from 30 to 100,000  $\mu\text{s}$  were used. Typically, 1600 averages were acquired with a repetition time of 6.5 s. Each echo counted 32 data points with a dwell time of 1  $\mu\text{s}$ . The curing temperature dependence measurements were performed by spacing  $\tau$  from 26  $\mu\text{s}$  to 22,000 or 5,000  $\mu\text{s}$ . Typically, 420 echoes with 32 data points per echo were acquired. The repetition time was decreased from 4 to 2 s. The number of scans was increased from 128 to 320. The isopropanol exchange experiments<sup>12</sup> were performed by acquiring 512 echoes with  $\tau$  spaced from 26  $\mu\text{s}$  to 5,000  $\mu\text{s}$ , repetition time of 2.5 s and up to 1024 scans.

### 4.2.4. $T_1$ recovery parameters

The activation energy at 28 and 90 days of cement hydration was measured by applying the  $T_1$  saturation recovery pulse sequence on Maran spectrometer. In the case of 7 days old samples experiments have been performed by  $T_1$  inversion recovery sequence on Kea<sup>2</sup> spectrometer.

The pulse characteristic was the same as described in previous sections. In all cases experiments were performed in 64 steps with 16 averages and repetition time of 1 s. For each step the distance from inversion pulse / saturation pulses to  $90^\circ$  FID pulse ( $\tau_{rec}$ ) was increased logarithmically

$$\tau_{rec} = \tau_{rec}^0 \cdot \beta^i, \quad i = 0 \dots (N_{St} - 1) \quad (4.2)$$

where  $N_{St}$  is the number of applied steps and  $\tau_{rec}^0$  is the minimum duration of the distance.

The values of  $\tau_{rec}$  for 7 days old cement samples were spanned between 0.02 and 4,000 ms, while for 28 and 90 days old samples they were between 0.02 and 2,000 ms.

---

<sup>12</sup> measured by R. Kowalczyk

### 4.3. ANALYSIS OF NMR DATA

An analysis of the measured data was performed after subtraction of a residual NMR signal emanating from empty NMR tube(s). Quadrature echo signals were analysed in magnitude mode. The CPMG data were phased to minimise the imaginary signal. The  $T_1$  recovery signal at each  $\tau_{rec}$  was calculated as an average of first 10 points of FID decay.

#### 4.3.1. Quad echo analysis

The recorded Quad Echo signal comprises of two parts: an echo due to the solid and an exponential decay due to the liquid. The exponential fraction is not affected by the second  $90^\circ$  pulse and therefore has the origin at the time of the first pulse. It decays with the relaxation time  $T_2^*$  determined by the magnet inhomogeneity. This signal is attributed to the mobile hydrogens. The application of the second  $90^\circ$  pulse refocuses the magnetisation of rigid dipole – dipole pairs within solid components. The solid signal originated from that fraction has an approximately Gaussian shape centred at the time  $2\tau$  and short time constant – Gaussian width ( $\sigma_{sol}$ ) of 10 – 20  $\mu\text{s}$ .

Hence the QE signal has been fitted to:

$$I_{Tot}(t, \tau) = I_{sol}(\tau) \cdot \exp\left[-\left(\frac{t - 2\tau}{\sigma_{sol}}\right)^2\right] + I_{mob}(\tau) \cdot \exp\left(-\frac{t}{T_2^*}\right) \quad (4.3)$$

where  $I_{sol}$  and  $I_{mob}$  are the solid and mobile signal intensity,  $t$  is the time counted from the end of first  $90^\circ$  pulse,  $\tau$  is the pulse gap.

The fitting procedure was performed by using code written in Matlab<sup>®</sup>. The code was designed to fit first the tail of exponential fraction, subtract that fit from total signal and then fit the Gaussian echo. The obtained fitting parameters ( $I_{sol}$ ,  $I_{mob}$ ,  $\sigma_{sol}$ ,  $T_2^*$ ) then served as the initial parameters for a full least square fitting of QE signal. To minimise the influence of magnet inhomogeneity on mobile signal intensity the analysis was made in time range below 200  $\mu\text{s}$ . The sum of solid and mobile intensities is the total signal of all hydrogen within samples. However, the solid intensity is not totally refocused as with increasing  $\tau$  it also relaxes. Therefore back-extrapolation of the echo intensity to pulse gap  $\tau = 0$  is required. A Gaussian extrapolation was found to reflect best the content of solid and total water within sample. For completeness the mobile signal was also back extrapolated – the same results within measurement uncertainty were obtained by both the exponential and linear extrapolation.

### 4.3.2. CPMG and $T_1$ recovery analysis

#### 4.3.2.1. Multi exponential fitting

The analysis of CPMG decay and  $T_1$  recovery data is based on exponential fitting with multiple relaxation time components.

The CPMG experiments probe only the mobile water signal. The solid, chemically combined, signal is substantially relaxed by the time of the first echo ( $\sim 60 \mu\text{s}$ ) since its  $T_2$  constant is  $\sim 10\text{--}20 \mu\text{s}$ . The CPMG decay intensity ( $I_{mob}$ ) is expressed by the formula

$$I_{mob}(t) = I_o \int P(T_2) \cdot \exp\left(-\frac{t}{T_2}\right) dT_2 \quad (4.4)$$

where  $P(T_2)$  is the probability of nuclei having  $T_2$  and  $I_o$  in the overall intensity at time zero.

In the case of multi-model distribution of  $n$  specific  $T_2$  values this may be rewritten as

$$I_{mob}(t) = \sum_{i=1}^n I_i \cdot \exp\left(-\frac{t}{T_{2,i}}\right) \quad (4.5)$$

where  $t$  is the time counted from  $90^\circ$  pulse,  $I_i$  is the intensity of  $i$ -th component,  $T_{2,i}$  is the  $T_2$  relaxation time of  $i$ -th component.

The similar expression for  $T_1$  relaxation intensity ( $I_{TOT}$ ) is

$$I_{TOT}(\tau_{rec}) = \sum_{i=1}^n I_i \cdot \left[1 - k \cdot \exp\left(-\frac{\tau_{rec}}{T_{1,i}}\right)\right] \quad (4.6)$$

where  $\tau_{rec}$  is the time between inversion pulse / saturation pulses and  $90^\circ$  FID pulse,  $T_{1,i}$  is the  $T_1$  relaxation time of  $i$ -th component and  $k$  is the parameter dependent on type of recovery,  $k \approx 1$  for saturation and  $k \approx 2$  for inversion recovery.

The  $k$  parameter in this study has been calculated for each data set of  $T_1$  measurements as  $k = 1 - b_1/b_2$  where  $b_1$  is the value of  $I_{TOT}$  at  $\tau_{rec} = 0$  and  $b_2$  is the maximum value of  $I_{TOT}$  at longest time.

Origin<sup>®</sup> and Matlab<sup>®</sup> have pre-defined least square fitting procedures. However, using these procedures for analysis is difficult as the obtained intensities and relaxation times depend hugely on the pre-defined number of components and their initial guess values. Hence, the use of straight exponential fittings was minimised in this study. The exception was made for activation energy experiments where the number of components is determined from prior knowledge. The alternate methods used are Laplace transform analysis and exponential stripping.

### 4.3.2.2. Inverse Laplace Transform

Multi-exponential relaxation signal intensity for  $T_2$  can be expressed as [106]

$$I(t) = \int P(T_2) \exp\left(-\frac{t}{T_2}\right) dT_2 + \epsilon(t) \quad (4.7)$$

where  $I$  is measured signal as a function of decay time  $t$ ,  $P$  is relaxation time ( $T_2$ ) distribution function – probability density of hydrogen with specific relaxation time, and  $\epsilon$  is the noise contribution (additive, zero mean and white Gaussian noise).

To solve equation 4.7 knowing the signal intensity and obtain the relaxation time ( $T_2$ ) distribution function,  $P$ , the Inverse Laplace Transform (ILT) is used. However, the Laplace inversion is known to be ill-posed problem. Numerous algorithms have been put forward to solve the problem. That adopted here is due to Venkataramanan [97]. This algorithm makes the assumption that  $P(T_2)$  is non-negative. Moreover, it introduces a regularisation parameter,  $\alpha_R$ , which defines the smoothing of the distribution [107]. ‘Similar arguments’ apply to  $T_1$  recovery analysis.

The outcome of ILT analysis depends on the  $\alpha_R$  to a limited extend. In this thesis two Laplace Inversion programs run in Matlab<sup>®</sup> were used. Analysis of the sorption and activation energy experiments data was performed by using program supplied by Schlumberger-Doll Research. In the case of that program, if the  $\alpha_R$  parameter is too big the spectrum is broad and peaks are not separated - they merge. If  $\alpha_R$  is too small then the spectrum consists of many individual peaks which become very narrow. The solvent exchange experiments were analysed by program written at Victoria University of Wellington. Here, the smoothing parameter draws a distinction from former program: small  $\alpha_R$  gives broad spectrum, big  $\alpha_R$  – narrow spectrum. The maximum amplitude and the width of the peaks in the  $T_1$  or  $T_2$  spectrum are highly dependent on the  $\alpha_R$  parameter. However the area of peaks shows much lower dependence on  $\alpha_R$ . Therefore the intensities of the relaxation time components in this work were determined as the area – integral intensity, of each peak. An inaccuracy in  $\alpha_R$  also leads to a pearling effect described as a tendency of the closely neighbouring peaks to move toward each other. This may introduces a systematic error in obtained  $T_2$  values.

The uncertainty in the obtained spectrum may also arise from the measured echo data. In order to use the ILT analysis the signal to noise ( $S/N$ ) ratio of acquired data should at least exceed the value of 500. Based on the personal experience of the author, it also is important to record the baseline of sufficient length.

The analysis of sorption and activation energy experiments were performed with  $\alpha_R$  equalled to  $10^{-5}$  and  $10^{-4}$ , respectively (Schlumberger code). The range of  $T_2$  relaxation time was  $10^{-5} - 1$  s, while for  $T_1$  it was  $10^{-5} - 10$  s with 1000 steps distribution. The solvent exchange experiment analysis was performed in the same  $T_2$  range as sorption experiments with  $\alpha_R \sim 10^{11} - 10^{12}$  (Victoria code).

### 4.3.2.3. Exponential stripping

The exponential stripping method of analysis was used for temperature dependence and isopropanol exchange experiments where the signal to noise ratio of the data is not adequate for ILT analysis. However, the number of relaxation components was established by the results obtained earlier using ILT of similar cement paste samples.

The method is based on fitting the CPMG decay in steps. The procedure starts with fitting the tail of the decay,  $I_{TOT}$  ( $t \geq t_{long}$ ), to the longest relaxation component only with a baseline. The fitting line calculated from the best fit parameters,  $I_{long}$ ,  $T_{2,long}$  and  $I_{baseline}$ , is then subtracted from the original data. The tail of residual data after subtraction is fitted to the next longest relaxation component (without baseline). This in turn is subtracted and procedure repeats iteratively until the shortest component has been fit.

Two sets of boundaries need to be considered and their choice is critical to the analysis.

The first are the lower limits of  $T_2$  relaxation times for each component. They are selected based on experience gained from examination of other cement paste samples. The analysis was performed starting with the oldest samples (90 days of hydration). The lower boundary cut offs for C-S-H interlayer, gel, interhydrate and capillary pore water were set to 90, 250, 1500 and 10,000  $\mu\text{s}$ , respectively based on earlier ILT analysis. Fitting was progressively performed for younger samples. The lower boundaries were varied in line with discovered  $T_2$  of component. In the majority of the cases, especially for gel pore water, the  $T_2$  values were found without encountering the boundary. The upper boundaries were not restricted allowing the  $T_2$  values to be found.

The second boundary is the value of  $t_{long}$  for each fitting stage; the timeline of particular fittings. They were set based on the found  $T_2$  values for the older sample. The fittings of the longer  $T_2$  components start at time 3-5 times longer than the  $T_2$  of the next shorter component.

The analysis protocols for CPMG and  $T_1$  recovery experiments are summarised in table 4.4.

Table 4.4 Characteristic of experimental analysis.

<i>Experiment</i>	<i>Analysis method</i>
Sorption isotherm	ILT
Temperature dependence	Exponential stripping
Activation energy	ILT and multi-exponential fitting
Solvent exchange	ILT and exponential stripping

#### 4.4. THERMOGRAVIMETRIC ANALYSIS

Thermogravimetric analysis (TGA) involves monitoring of changes in sample mass as the temperature is gradually raised. For better interpretation of data, in parallel with the TG curve, the derivative thermogravimetric (DTG) curve is registered and presents the changes in the rate of material decomposition.

In a TGA experiment the sample is placed on the pan - made with alumina when studying cement pastes, and then on an ultra-sensitive balance to follow the changes in sample weight during heating. The balance with pan is loaded into the electric oven containing a thermocouple to accurately measure temperature during experiment.

The mass loss of cementitious materials is usually caused by dehydration – loss of water molecules, dehydroxylation – loss of hydroxyl groups, and decarbonation - thermal dissociation of calcites. The changes in weight of different cement phases appear at various temperatures and overlap (fig. 4.1). It makes it difficult to distinguish and assign changes to specific component.

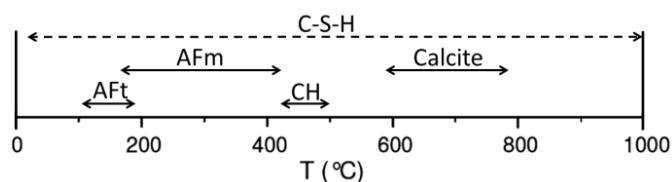


Figure 4.1 The range of temperature at which different phases loose mass (adopted from [108], [109]).

In this study TGA measurements were performed to define the content of Portlandite through loss of the water within it. At the temperature range when changes in CH mass happen, the decomposition of C-S-H also appears. However, as the rate of that decomposition is almost constant at those temperatures, it is overcome by applying the tangents method.

Experiments were made at University of Surrey<sup>13</sup> with TA Instruments Simultaneous Differential Technique SDT-Q600 Thermo Gravimetric Analyser with Differential Scanning Calorimeter (TGA-DSC). Samples were heated in temperature range between 20 and 1000°C at 10°C/min in the N<sub>2</sub> atmosphere (flow 100ml/min) to prevent carbonation. The temperature precision was 0.5°C and weight sensitivity was 0.1 µg.

#### 4.5. X-RAY DIFFRACTION

X-Ray diffraction is a non-destructive technique based on the fact that each crystal is characterised by a collection of atomic planes that are spaced  $d$  apart.

X-rays are diffracted according to Bragg's Law:

<sup>13</sup> in collaboration with Violeta Doukova

$$n\lambda = 2d \cdot \sin \theta_i \quad (4.8)$$

where  $n$  is the diffraction order (integer),  $\lambda$  is wavelength of the incident X-ray beam and  $\theta_i$  is angle of incidence.

X-ray diffracted beams are detected and registered as XRD pattern - intensity (counts) as a function of diffraction angle  $2\theta_i$ . To identify the phase composition of measured sample the diffraction pattern is compared with known ICDD (International Centre for Diffraction Data) standards or other databases. The quantitative XRD analysis is performed by Rietveld method based on the least square fitting of the simulated and measured pattern.

In this study XRD measurements have been performed on cement powder to define their phase composition and on cement pastes to define degree of hydration<sup>14</sup> ( $\alpha$ ) and content of ettringite ( $f_{Et}$ ).

The XRD experiments were performed at EPFL<sup>15</sup> with Panalatical X'Pert Pro MPD diffractometer using a CuK $\alpha$  source (wavelength 1.54Å) with a fixed divergence slit of 0.5°. Samples were scanned between  $2\theta_i = 7$  and 70° using a X'Celerator detector. The rotation step size was 0.0167° ( $2\theta_i$ ) and the time step was 77.5 s.

#### 4.6. SORPTION ANALYSER

The IGA<sub>sorp</sub> Moisture Sorption Analyser is a fully automated gravimetric analyser. It contains an ultra-sensitive microbalance which measures the changes in sample mass as humidity is changed. Those changes are measured with resolution of 0.1 µg. Constant monitoring of sample mass allows to determine when equilibrium has been reached [110].

The humidity in sample chamber is controlled and changed by mixing of dry and wet gas streams [110]. The wet stream is obtained by directing gas flow through water container. The flow rate is limited to 500 ml/min. To prevent carbonation of cement paste the nitrogen was used as a humidity controlling gas.

To perform the experiment, the sample is first placed in the conical holder with diameter of around 1 cm, hanged above humidity chamber and then the chamber is closed by moving up.

The IGA<sub>sorp</sub> Analyser was used in sorption experiment to equilibrate samples at desired humidity. The practice showed that the most time effective is to operate in the humidity range 80 to 5%. The humidity of 80% could be reached in the chamber after around 5 minutes whereas of 90% - after few hours.

---

<sup>14</sup> mass fraction of anhydrous cement consumed in the hydration reactions

<sup>15</sup> in collaboration with Arnaud Muller

#### 4.7. TEMPERATURE CONTROL

Two experimental NMR parts of this work involved temperature as an important factor. These were the NMR measurements to investigate the influence of curing temperature on cement microstructure and to establish the activation energy.

The former were always performed at the same temperature as samples curing. The reason for that was to not alter the conditions of samples curing. In the second case, the relaxation parameters were measured during progressive increasing of sample / experimental temperature in the range  $-20^{\circ}\text{C}$  to  $+60^{\circ}\text{C}$ .

The temperature on the bench top spectrometer is controlled by three means depending on the desired value. In all cases the flow of nitrogen gas is directed through meter long heater and spectrometer probe. That flow is cooled down or heated up to achieve the fix temperature. In the range  $-20$  to  $+5^{\circ}\text{C}$ , the set temperatures are reached by controlled heating of the nitrogen gas directed in pipe through dewar with liquid nitrogen. For temperatures between  $10$  and  $25^{\circ}\text{C}$  flow goes through pipe merged in polystyrene box filled with ice and water. Increasing temperature is possible by heating the gas flow by one ( $30-40^{\circ}\text{C}$ ) or two ( $45-60^{\circ}\text{C}$ ) heaters.

During NMR experiments temperature is monitored by a sensor placed around 2-3 cm below the actual position of sample in bench top spectrometer. Considering the sensitivity of experiments to temperature, it was important to verify what the actual sample temperature was. The difference between real temperature and sensor display was measured in a separate experiment by using copper-constantan thermocouple. The schematic diagram of system is shown in figure 4.2. Cement sample was prepared with one end of thermocouple wires merged inside at the position of coil. The other end was kept at  $0^{\circ}\text{C}$  and thermocouple was connected to voltage meter.

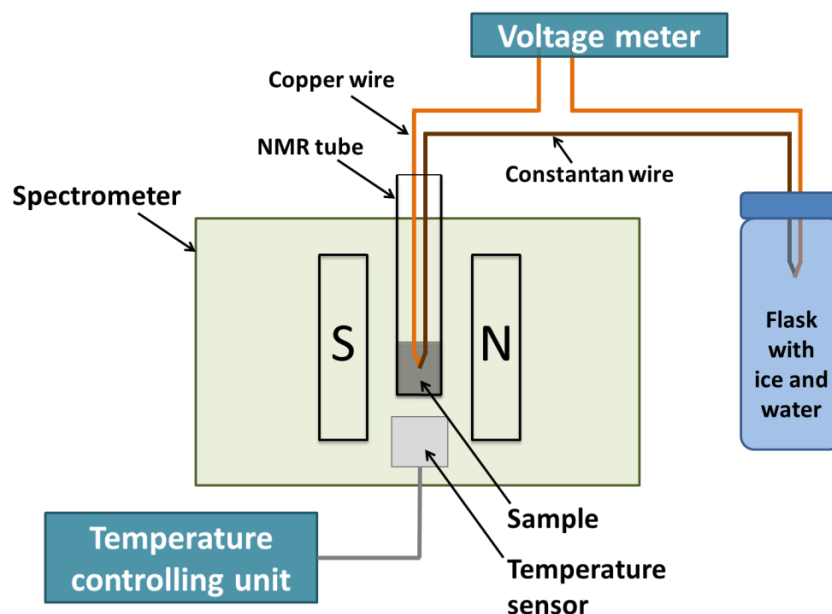


Figure 4.2 Schematic diagram of the system to calibrate the temperature: the copper – constantan thermocouple is merged into the cement sample and allows calculation of actual sample temperature, while the controlling unit displays the temperature recorded by sensor.

The voltage was recorded while the setting temperature was changed and equilibrated. The obtained voltage values ( $V$  [mV]) were converted to temperature ( $T$  [°C]) according to equation [111]:

$$T = A + B \cdot V - \frac{C}{V + D} - \frac{E}{V + F} \quad (4.9)$$

where  $A = 238.29^\circ\text{C}$ ,  $B = 13.364^\circ\text{C}\cdot\text{mV}^{-1}$ ,  $C = 4776.4^\circ\text{C}\cdot\text{mV}$ ,  $D = 21.867 \text{ mV}$ ,  $E = 154.83^\circ\text{C}\cdot\text{mV}$ ,  $F = 7.8242 \text{ mV}$

The calculated temperatures were plotted against the values of temperature displayed on controlling unit (fig. 4.3). The linear fittings to the data were performed. The formulas to calculate the set temperature ( $T_{set}$ ) required to achieve desired experimental temperature ( $T_{real}$ ) are:

$$\begin{aligned} T_{set} &= (T_{real} - 3.04)/0.94 & \text{for } -20 \leq T_{real} \leq +5^\circ\text{C} & \text{ (liquid N}_2\text{)} \\ T_{set} &= T_{real} - 0.94 & \text{for } 10 \leq T_{real} \leq 25^\circ\text{C} & \text{ (ice)} \\ T_{set} &= (T_{real} - 2.67)/0.93 & \text{for } 30 \leq T_{real} \leq 60^\circ\text{C} & \text{ (heater/s)} \end{aligned} \quad (4.10)$$

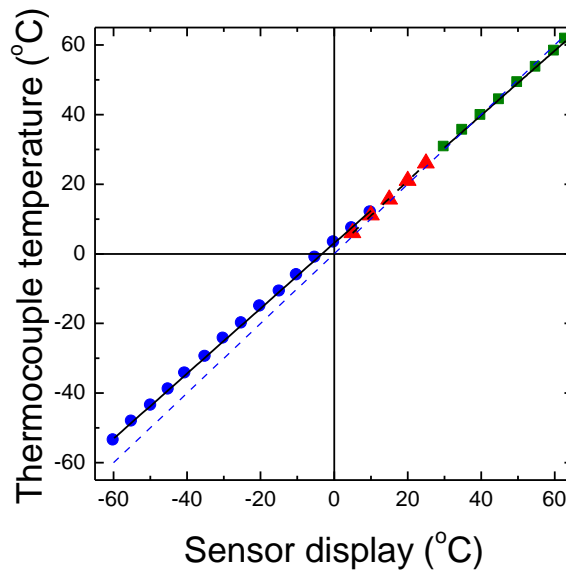


Figure 4.3 Temperature of thermocouple merged in cement sample and placed in spectrometer against the sensor display temperature of controlling system. Temperature of sample in spectrometer is controlled in three different ways: by using liquid nitrogen (blue circles), ice (red triangles) and heaters (green squares) combined with gas nitrogen flow. Dashed line is  $y = x$  plot.

## 5. Sorption hysteresis

### 5.1. CALIBRATION AND ASSIGNMENT OF SIGNALS

#### 5.1.1. Is all the water detected by NMR?

Figure 5.1 shows exemplar QE data recorded during a sorption experiment for a sample of white cement paste equilibrated at 23% RH on the first desorption branch of sorption isotherm. The data acquisition parameters are given in section 4.2.2. Data are shown for  $\tau$  values ranging from 12 to 45  $\mu\text{s}$ . Each decay curve comprises an echo centred on a time  $2\tau$  and an exponential decay. Also shown are the echo and exponential decay fits to the data. Their sum is fitted according to equation (4.3).

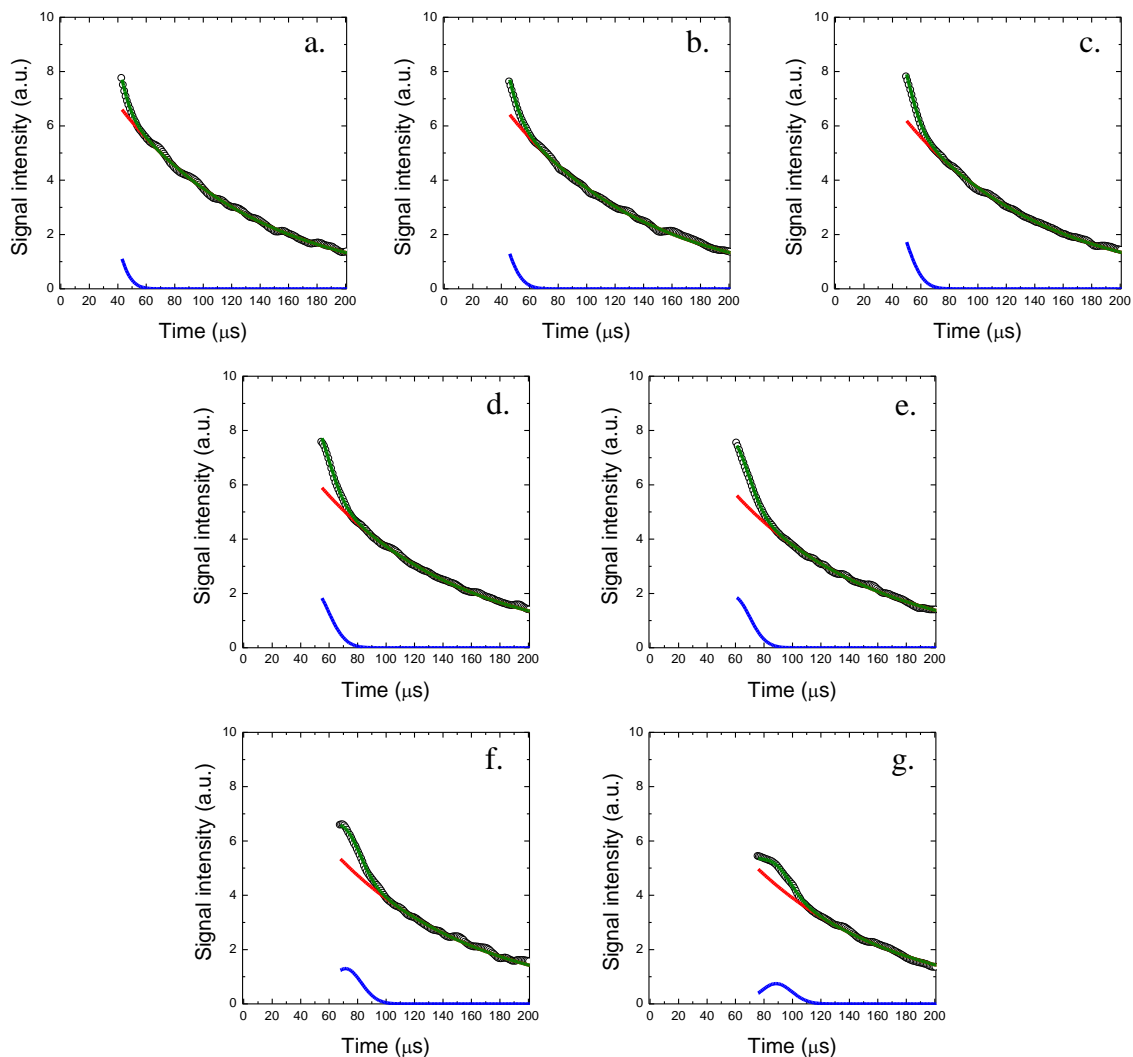


Figure 5.1 Quad echo signals recorded for white cement paste cure underwater ( $w/c_{mix} = 0.4$ ) for 28 days and equilibrated at 23% relative humidity (black circles). Pulse gap ( $\tau$ ) was: a: 12 $\mu\text{s}$ , b: 15 $\mu\text{s}$ , c: 19 $\mu\text{s}$ , d: 24 $\mu\text{s}$ , e: 30 $\mu\text{s}$ , f: 37 $\mu\text{s}$ , g: 45 $\mu\text{s}$ . The lines present fitting for solid (blue) and mobile (red) components; the green line is the total intensity fit. The zero time is taken as the end of first 90° pulse of the sequence.

The pulse gap ( $\tau$ ) dependence of the solid echo and mobile decay amplitudes resultant from this fitting are shown in figure 5.2. It can be seen that the mobile amplitude has very weak dependence on pulse gap while the solid echo amplitude is strongly pulse gap dependent. Increase of pulse gap causes the decrease of solid amplitude; the solid signal relaxes. Hence, to gain the true solid signal, not influenced by relaxation process, the amplitude was back-extrapolated to zero pulse gap ( $\tau = 0$ ). This is shown by solid line in figure 5.2: single exponential decay. The exponential fitting was performed as it has been found to be the best fit for cement materials according to McDonald *et al* [26]. For consistency, the mobile fraction was also back-extrapolated. The linear and exponential fittings gave almost the same mobile amplitude (within 0.5% difference).

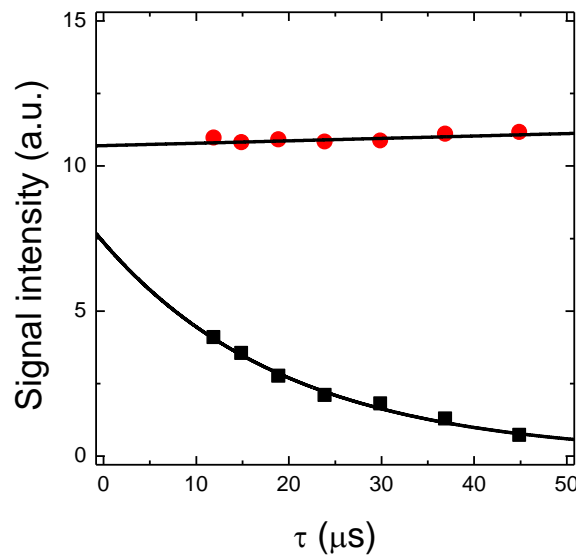


Figure 5.2 Solid echo (black squares) and mobile decay (red circle) signal amplitudes as a function of pulse gap ( $\tau$ ). The lines are the fits to the data: exponential for solid and linear for mobile signals.

It was critical for analysis to confirm that the NMR measurements ‘see’ all the water in the samples. In order to verify this, the total NMR signal - the sum of QE solid and mobile signals, was measured during progressive drying of a white cement paste ( $w/c_{mix} = 0.4$ ). The samples were dried by equilibration at progressively lower RH in the IGAsorp Analyser. The total NMR signal intensity as a function of sample mass displays linear behaviour (figure 5.3). This is as expected since loss of each water molecule contributes a proportional loss of signal intensity. The best fit to the total intensity ( $I_{Tot}$ ), excluding the point at 0.76 normalised sample mass, is expressed by equation  $I_{Tot} = 3.158 \cdot m - 2.158$  with coefficient of determination ( $R^2$ ) equal to 0.997. The intercept with the normalised sample mass axis allows calculation of the effective water to cement ratio. It is  $(w/c)_{eff} = 0.463$ . The sample was made at  $(w/c)_{mix} = 0.4$ . The increase of this ratio reflects the subsequent curing of samples under saturated CH solution. The measurements of  $(w/c)_{eff}$  based on the mass of paste samples after casting and after nominally 28 days of underwater curing were also performed and yield the same result. Taken together these results prove that there is no ‘hidden’ water reservoir within the sample that NMR cannot sense.

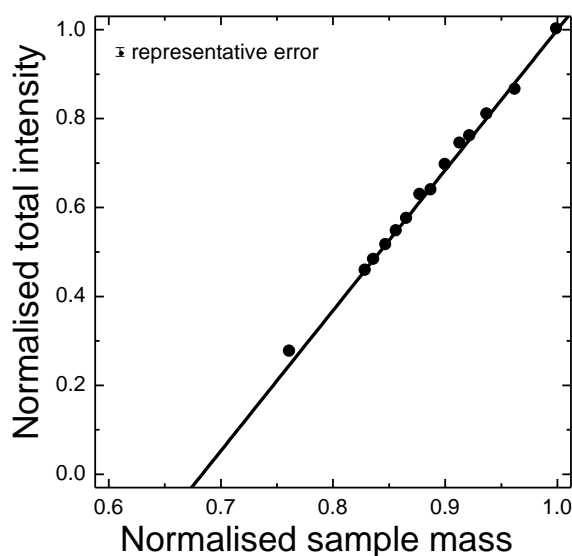


Figure 5.3 Changes in total NMR signal intensity as a function of normalised sample mass during drying of white cement paste.

### 5.1.2. Origin of the solid signal

The next step was to identify the origin of the QE solid signal. The QE measurements of powdered  $\text{Ca}(\text{OH})_2$  dried at  $120^\circ\text{C}$  for 48 hours were performed. The recorded signals are presented in figure 5.4. No mobile signal was observed. The echoes at the lower  $\tau$  values were followed by a negative signal transient – a typical feature of a Pake doublet in the time domain. As the Pake doublet is characteristic of dipolar coupled spins pairs, and there is no mobile contribution to the signal, it confirmed that protons of Portlandite (CH) are chemically bound and entirely observed in solid part of the QE signal.

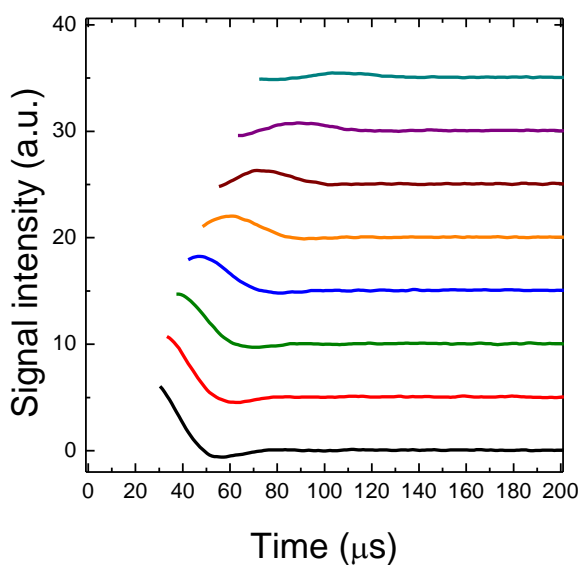


Figure 5.4 Stack plot of the Quad echo signals recorded for dried  $\text{Ca}(\text{OH})_2$ . Pulse gap,  $\tau$ , from bottom to top was: 12, 15, 19, 24, 30, 37, 45 and 54  $\mu\text{s}$ .

Thermogravimetric analysis (TGA), X-ray diffraction (XRD) and calculation using thermodynamic model GEMS were performed on an as prepared (100% RH) sample by Arnaud Muller during the author's visit to EPFL. These techniques gave the mass fraction of CH in the paste as 22.5%, 23.7% and 24% respectively. The average fraction  $23.4 \pm 0.6\%$  can be expressed as  $m_{CH} = 0.34 \pm 0.01$  g/g anhydrous cement. The mass fraction of ettringite measured by XRD was equal to  $5.7 \pm 1.0\%$  in the paste, equivalent to  $m_{Ett} = 0.083 \pm 0.015$  g/g anhydrous cement. The fraction of water combined into those two crystalline phases, CH and ettringite, is expressed as:

$$[(m_{CH} \cdot H_{CH}^{AMU} / CH^{AMU}) + (m_{Ett} \cdot H_{Ett}^{AMU} / Ett^{AMU})] / (w/c)_{eff} \quad (5.1)$$

where  $H_{CH}^{AMU}$  and  $H_{Ett}^{AMU}$  are the atomic mass units of water in CH and ettringite and  $CH^{AMU}$  and  $Ett^{AMU}$  are the atomic mass units of CH and ettringite.

The fraction of water obtained from equation (5.1) is equal to  $26 \pm 2\%$  and stays in reasonable agreement with NMR solid intensity of 24.3%. It provides confidence that the NMR QE solid signal arises from Portlandite and ettringite, and hence does not comprise any contribution from C-S-H (further evidence is presented in section 6.3.3).

### 5.1.3. Differentiation of the mobile water component

The mobile water fraction measured by the QE experiment was further decomposed into water reservoirs characterised by different  $T_2$  relaxation time by applying the CPMG pulse sequence. The echo decays were acquired and Laplace inverted as described in section 4.3.2.2.

An exemplary CPMG data treatment for white cement paste sample equilibrated at 90% RH is presented in figure 5.5. The Inverse Laplace Transform (ILT) of the CPMG signal (fig. 5.5 c) decomposes the mobile fraction into three components with  $T_2$  values of  $126 \pm 5$ ,  $412 \pm 20$  and  $1800 \pm 400$   $\mu$ s. The signal intensities normalised to the total CPMG intensity - mobile water, are 0.445, 0.546 and 0.009 respectively. The renormalisation of these fractions to the total intensity obtained from QE experiment yields 0.326, 0.399 and 0.007 respectively.

Figure 5.5 a and b shows the CPMG decay data and the fit based on the  $T_2$  values and intensities obtained from ILT analysis. The coefficient of determination ( $R^2$ ) for the fit presented was calculated according to:

$$R^2 = 1 - \frac{SS_R}{SS_{TOT}} = 1 - \frac{\sum_i (y_i - f_i)^2}{\sum_i (y_i - \bar{y})^2} \quad (5.2)$$

where  $SS_R$  and  $SS_{TOT}$  are the residual and total sum of squares,  $y_i$  and  $f_i$  are the observed and modelled values respectively and  $\bar{y}$  is the mean of observed data. The  $R^2$  for presented fit is equal to 0.999.

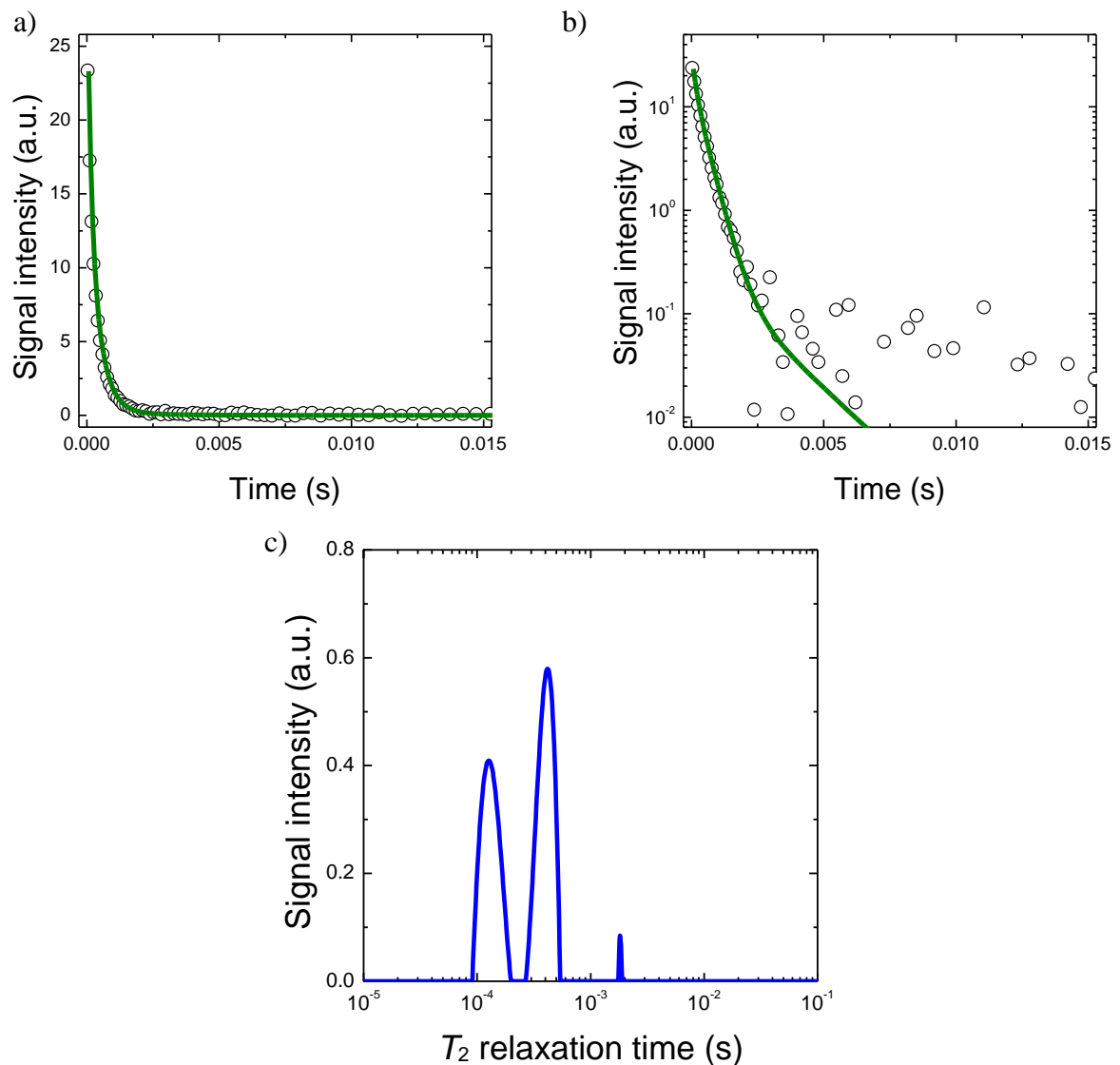


Figure 5.5 The CPMG signal recorded for white cement paste cure underwater ( $w/c_{mix} = 0.4$ ) and equilibrated at 90% RH. The echoes decay data (circles) are presented in form of linear-linear (a) and log-linear (b) plots. Green lines are the fits based on  $T_2$  and intensity values obtained from ILT. The inverse Laplace transform of the CPMG decay is presented in (c). In (b) negative baseline points are not shown.

The  $T_2$  relaxation time of mobile water increases with the increase of pore size. The signal with the shortest  $T_2$  is assigned to the smallest spaces whereas with the largest  $T_2$  to the biggest spaces. Since all solid signal is account for CH and ettringite as shown in previous section (5.1.2), water filling C-S-H interlayer spaces and specifically any  $\text{OH}^-$  groups in interlayers cannot contribute to the solid signal. Studies by Monteilhet *et al* [95] and Valori *et al* [112] suggested that for cementitious materials the  $T_2$  of order of few hundreds microseconds is characteristic for liquid in spaces of about few nanometers in C-S-H gel.

Taking these together, the  $T_2$  relaxation time component with smaller  $T_2$  ( $\sim 120 \mu\text{s}$ ) is assigned to water as well as to surface hydrogens and residual hydroxyl groups in interlayer pore spaces between calcium-silicate layers which exchange hydrogens. The components with

larger  $T_2$  are assigned to water in C-S-H gel pores ( $\sim 400 \mu\text{s}$ ) and to water in interhydrate spaces ( $\sim 1600 \mu\text{s}$ ). Components with  $T_2$  longer than those appearing in this sample originate from water in capillary pores and cracks. In this work the combined interhydrate and capillary pore water are defined as the ‘free’ water.

## 5.2. TOTAL INTENSITY HYSTERESIS LOOP

The normalised sample mass and total signal intensity have been plotted against relative humidity for cement samples spanning one and an half cycles of the desorption and adsorption isotherm – figure 5.6. The primary desorption shows the changes with humidity in the range from 100 to 0% RH. The data point at 100% RH represents the ‘as prepared’ cement paste and at 0% RH paste oven dried at  $180^\circ\text{C}$ . Other samples were equilibrated in the IGA-sorp Analyser. The adsorption and secondary desorption were measured for the cycles between 5 and 80% RH.

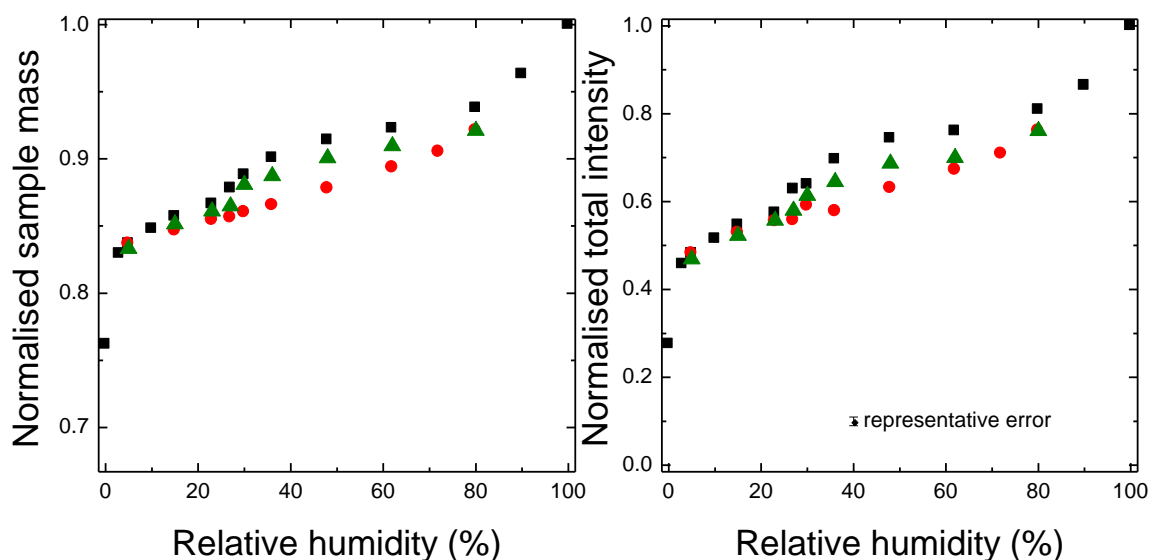


Figure 5.6 The normalised sample mass (left) and total NMR intensity (right) against relative humidity in progressively dried (black squares), wetted (red circles) and re-dried (green triangles) white cement paste.

The mass and NMR isotherm display an almost identical and characteristic hysteresis loop. This is not surprising as the sample mass and signal intensity are directly proportional.

The primary desorption results are consistent with larger pores emptying at high humidity ( $> 90\%$ ), smaller capillary and gel pores drying over a broad range down to 40% RH and finally loss of interlayer water at lower humidity ( $< 20\%$ ) [40].

The re-adsorption shows the signal and mass recovering to a lower value at any given humidity than was present during desorption. Initially up to around 20-25% RH water closely tracks the primary desorption. Above that value the adsorbed water increasingly lags behind the primary desorption. The maximum lag is equivalent to about 12% of the initial total water

content and occurs at about 40% RH. At the top of the loop at 80% RH the gap reduces to about 5% water content.

The existence of this loop in the NMR data confirms what is known from normal gravimetric data: the distribution of water in the different pore environments is different at any given RH on desorption and adsorption paths. The hysteresis between desorption and adsorption of cement based material has been reported in literature [113], [114]. The bigger hysteresis was also observed in middle range of humidity where the capillary condensation and evaporation are assumed to be dominating sorption mechanism. Below 33% humidity the hysteresis was reduced significantly and was less evident when adsorption started at higher RH values [114]. The possible reasons for hysteresis were explained by Feldman [113] in terms of irreversibility in removal and re-entering of water from interlayer spaces that collapse during drying or by Jennings [40] in terms of multi-size ink-bottle pores effect.

The secondary desorption presents the same trend as the original dehydration. However, as it starts at 80 not 100% RH, the water content is lower. In the humidity range below 30%, the water content tracks across to primary curve. The data reported in [114] showed that the secondary desorption from 100% RH initially overlaps the primary desorption but is shifted upwards, in comparison with primary desorption, at humidities below 44%. Nevertheless, if the starting humidity is lower the secondary desorption curve lays below primary desorption and the humidity at which they cross is lower. That agrees with the data reported here.

### 5.3. PORE-TYPE RESOLVED DESORPTION ISOTHERM

The NMR method has the advantage that it allows the isotherm to be resolved by pore type. Figure 5.7 shows the first pore-type resolved desorption isotherm to be measured in any cementitious material and possibly any nano-porous material. The total signal is decomposed into particular water populations: chemically combined water, C-S-H interlayer pore water, gel pore water and free (interhydrate and capillary) water.<sup>16</sup>

The plots show that the interhydrate and capillary porosity ('free' water) dries above 90% RH. That agrees with a calculation according to the Kelvin equation (eq. (2.6)) that all pores above 10 nm are empty at 90% RH. The gel pores become empty in the range between 100 and 25% RH equivalent to 1 and 0.6 relative water mass. The gel intensity plot plateaus for lower humidity, down to almost 0% RH, with a residual water content of about 5%. The origin of this gel intensity tail is not clear. It may indicate the presence of isolated smaller gel pores without connectivity to facilitate their drying. The other possibility, more favourable, is the presence of ink-bottle pores which cannot dry until drying of the smallest pores joining them with 'outside' occur. Almost no gel signal is observed at 0% RH for the oven dried sample.

A striking feature is that in the range 100 to 25% RH, as the gel signal decreases, an increase in the C-S-H interlayer signal is observed. This is explained by the relaxation behaviour of surface water molecules. When gel pores are full, gel surface water molecules

---

<sup>16</sup> sample at 100% RH was measured by Arnaud Muller during the author's visit to EPFL

are in rapid exchange with bulk gel pore water and therefore have the same  $T_2$  relaxation time. However, as gel pores dry, there is a layer of less mobile water left on the pore surface. The surface layer molecules are no longer able to exchange with more mobile bulk water of gel pore. Hence, in NMR terms, they appear more like C-S-H interlayer water with shorter  $T_2$  relaxation time.

Below 25% RH the C-S-H interlayer water signal decreases from about 0.3 to 0 at 0% RH. In this region, a similar rise in the component with the lowest  $T_2$  relaxation time, chemically bound water is observed as the mobility of residual water in interlayer spacing is reduced.

At the lowest humidity, the intensity of chemically combined water decreases back to the starting value of 0.24.

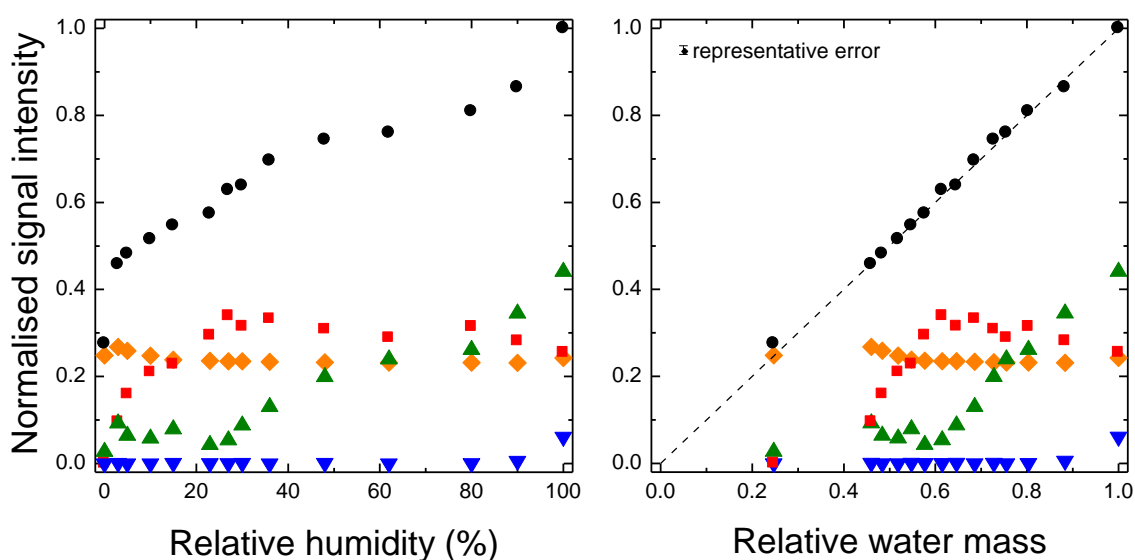


Figure 5.7 The normalised total signal intensity (black circle) as a function of relative humidity (left) and relative water mass (right). Total signal is further de-composed into chemically combined water (orange diamonds), C-S-H interlayer pore water (red squares), C-S-H gel pore water (green triangles) and ‘free’ water (blue inverted triangles).

The presented data allow a new schematic drawing of C-S-H morphology and water placement within C-S-H gel as ‘seen’ by NMR. This is shown in figure 5.8. The continuous network of C-S-H layers and gel pores is presented. At 100% RH all the surface water molecules in the interlayer and the gel pores are in rapid exchange with bulk pore water. They are seen as interlayer and gel water with two  $T_2$  components respectively. When the humidity is decreased down to 25% the gel pores empty. The interlayer spaces are full of water. There is also a residual water layer on gel pore surface. This all appears as interlayer water in the  $T_2$  spectrum. At even lower humidity, about 3%, the residual immobile water molecules left within structure appear solid like.

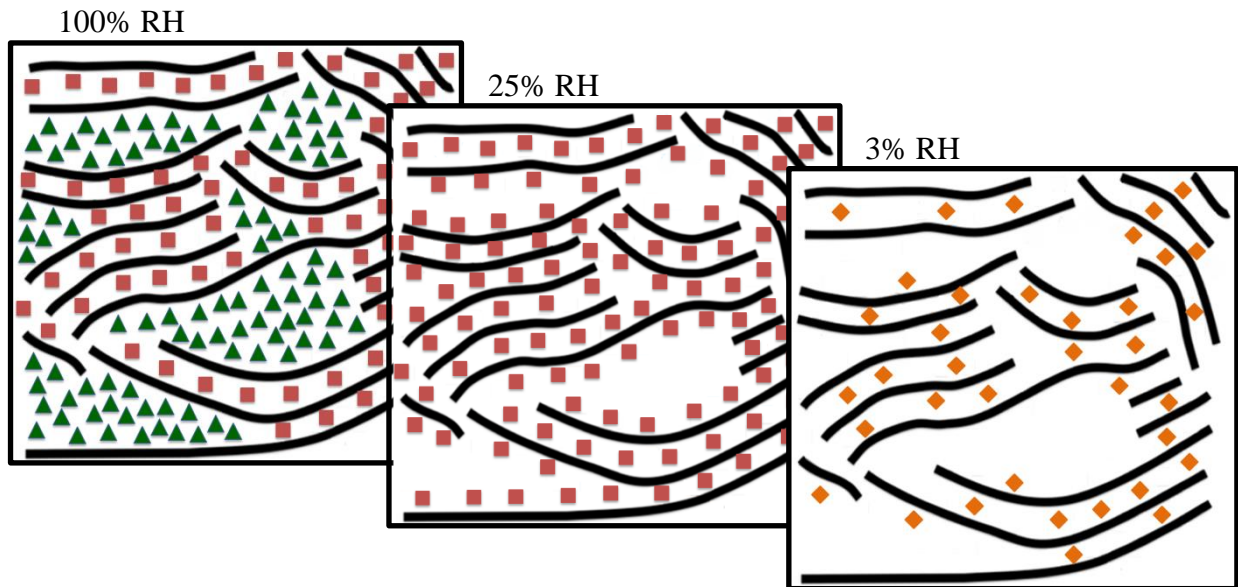


Figure 5.8 The schematic morphology of the C-S-H phase at 100, ~25 and ~3% RH. Black lines are Ca-O layers with  $\text{SiO}_4$  tetrahedra on both sides. The C-S-H gel water molecules are presented by green triangles. Red squares are the water molecules filling C-S-H interlayer spaces and surface molecules in C-S-H gel pores at lower humidity. At the lowest humidity water molecules in interlayer spaces appear as solid-like and are shown as orange diamonds.

#### 5.4. ISOTHERM LOOPS FOR PARTICULAR WATER RESERVOIRS

The separately resolved first desorption, re-adsorption and second desorption isotherm loops for chemically combined water, C-S-H interlayer space water, C-S-H gel pore water and ‘free’ water as a function of relative humidity are presented in figure 5.9 a-d.

The intensity of the chemically combined water follows the same pattern, within experimental error, for each sorption process (fig. 5.9a). Below about 25% RH there is a slight ( $\sim 0.04$ ) increase in the signal, otherwise it is flat.

The interhydrate and capillary pores do not refill in the range of the loop studied, 5 to 80% RH. Their intensity stays at 0 at all humidities below 90% (fig. 5.9d).

Although there is a scatter in the data, the primary desorption, adsorption and secondary desorption of the C-S-H interlayer water intensities are the same to within measurement error below  $\sim 20\%$  RH (fig. 5.9b). The interlayer intensity maxima appear at  $\sim 25\%$  RH for all three sorption processes. Above this humidity, a decrease in intensity is observed. On the adsorption path intensity is always less than for primary desorption with typically 9-5% below. The secondary desorption signals are in between those two, closer to primary desorption. The interpretation of the adsorption results is complicated by the fact that the interlayer signal has two parts. The first is C-S-H interlayer water. The second is refilled surface layers in the gel pores that appear in this category of signal until the gel pores are fully refilled. Potentially this leads to a complex curve shape dependent on the order in which pores/surfaces refill.

The rehydration shows that the gel pores start to fill at a humidity point slightly moved forward (by 5% RH) in comparison to the point at which they became empty in a course of

drying (fig. 5.9c). Nevertheless the gel intensity is much lower than for the primary desorption up to 80% RH where it becomes the same. The maximum difference in the gel intensity – 8%, is reached at about 50% RH which is displaced upwards in comparison with the maximum lag of total signal intensity. Secondary desorption causes the gel pore water intensity to decrease faster down to 40% RH and then behave in the same way as during first desorption.

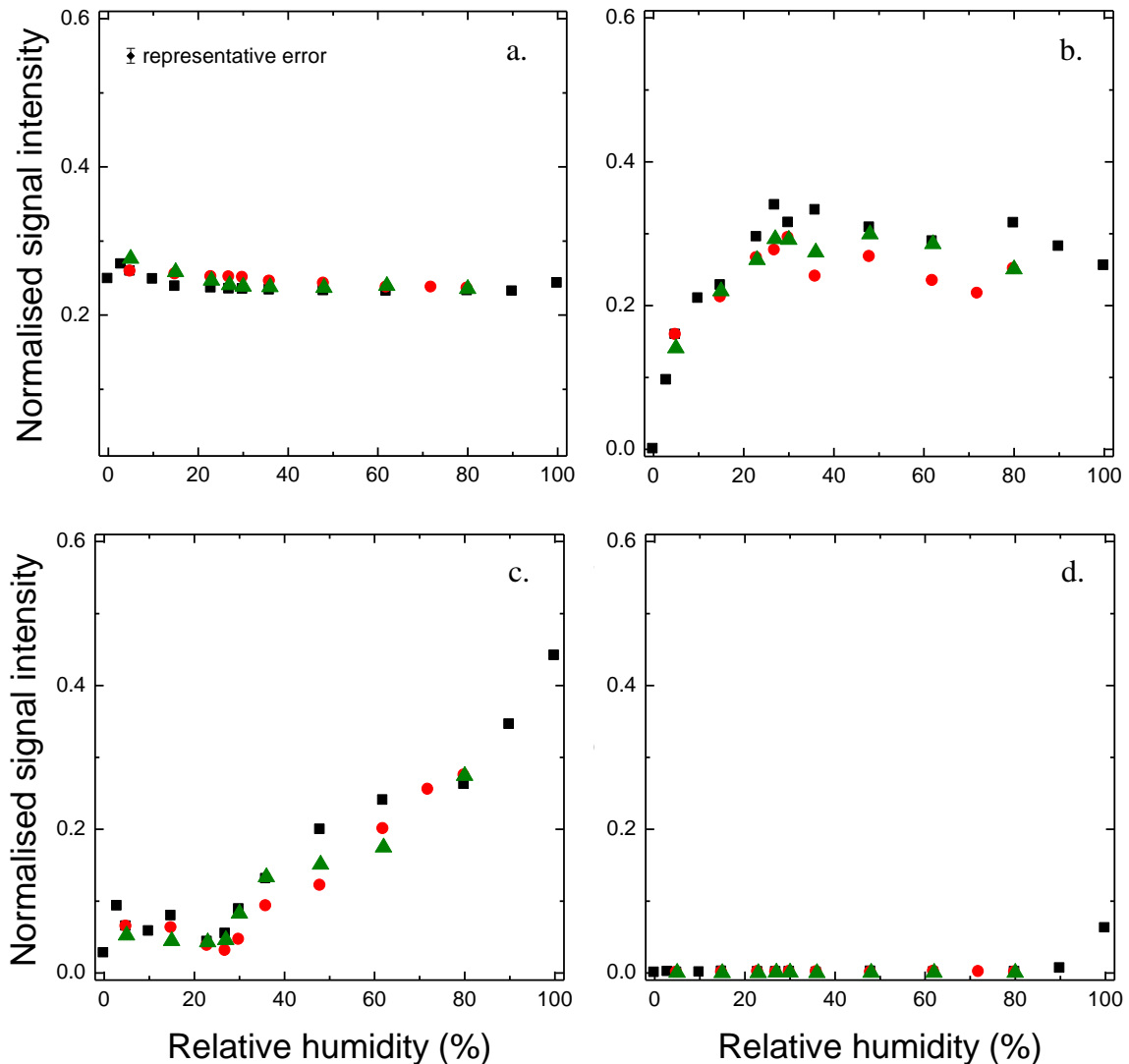


Figure 5.9 Signal intensity isotherm loops for chemically bound water (a), water in C-S-H interlayer (b) and gel (c) pores and ‘free’ water (d) during desorption (black squares), adsorption (red circles) and re-desorption (green triangles) as a function of relative humidity.

A better understanding of the effect of drying and wetting processes on the interlayer and gel pore water filling is provided by plotting the signal intensity as a function of relative water mass - figure 5.10 a-d.

Figure 5.10b shows that in the range of water mass fraction between 0.45 and about 0.55 the rate of filling interlayer spaces during adsorption is faster in comparison with the rate for both primary and secondary desorption branches. It is also observed that the maximum

interlayer water signal is reached earlier at about 0.55 water mass, in comparison with 0.6 for both desorption branches.

Above  $\sim 0.55$  relative water mass, the gel pore water signals begin to increase. At any given water mass the gel signal is considerably higher during adsorption than primary desorption. The secondary desorption is similar to primary desorption (fig. 5.10c). Correspondingly, the interlayer like signal is lower for both wetting and re-drying cycles in comparison with primary desorption (fig. 5.10b). It reaches the lowest values for the former which intensities do not rise above that occurring at  $\sim 0.9$  water mass fraction for primary desorption across the range 0.6 to 0.8 water mass. For later the values are averaged, more close to desorption.

These observations suggest that there is a much lower amount of interlayer-like monolayer water covering the surface of gel pores during adsorption compared to desorption. Hence the mechanism of filling the gel pores may be different during the adsorption process compared to emptying during desorption as discuss further in section 5.6.

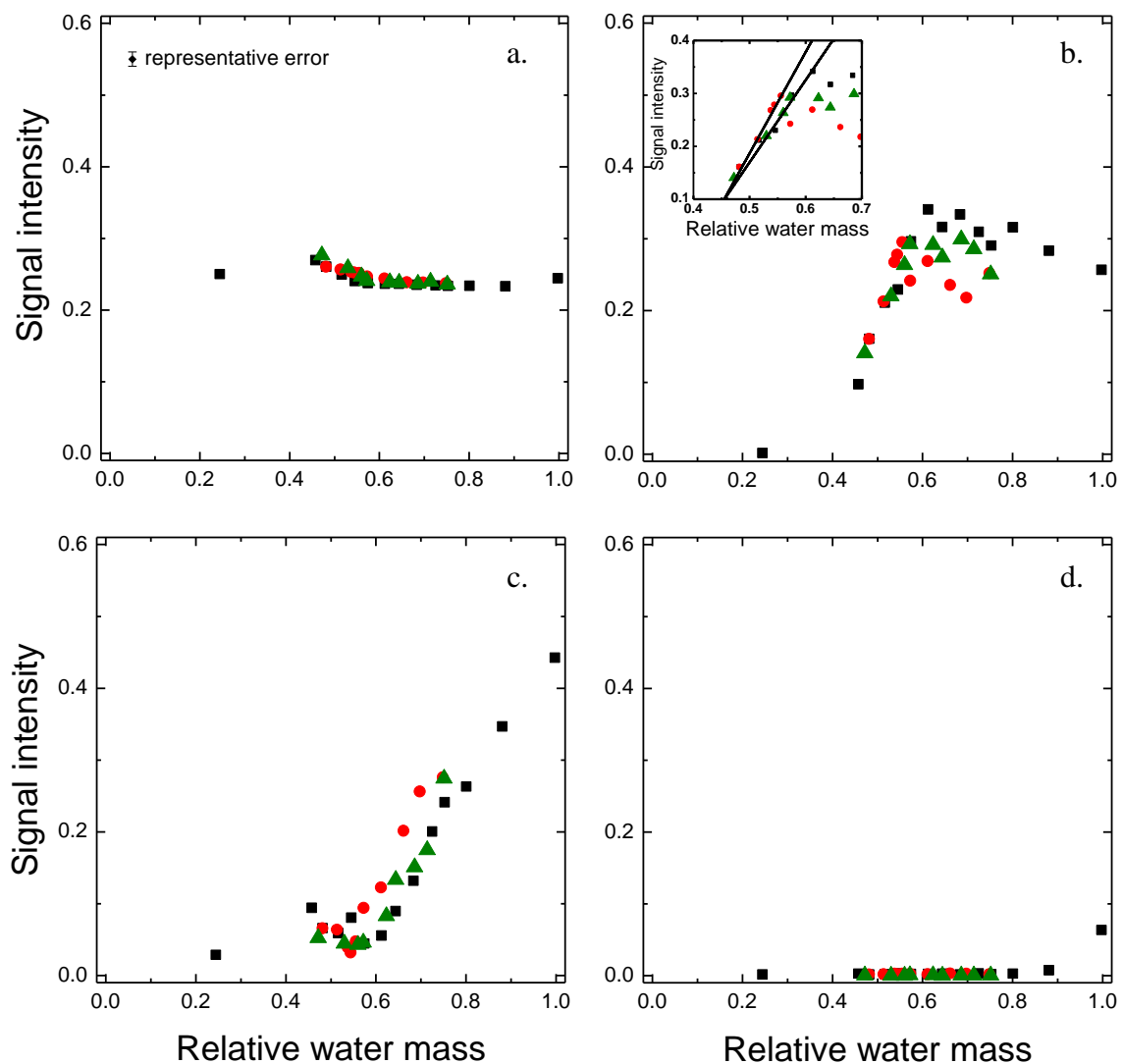


Figure 5.10 Signal intensity isotherm loops for chemically bound water (a), water in C-S-H interlayer (b) and gel (c) pores and 'free' water (d) during desorption (black squares), adsorption (red circles) and re-desorption (green triangles) as a function of relative water mass.

### 5.5. $T_2$ DISTRIBUTION

The  $T_2$  relaxation time distribution of C-S-H interlayer and gel water provides further information. The graphs in figure 5.11 a-c shows the  $T_2$  distribution where the markers present the time at which the maxima of ILT peaks appear and the bars are the widths of those peaks.

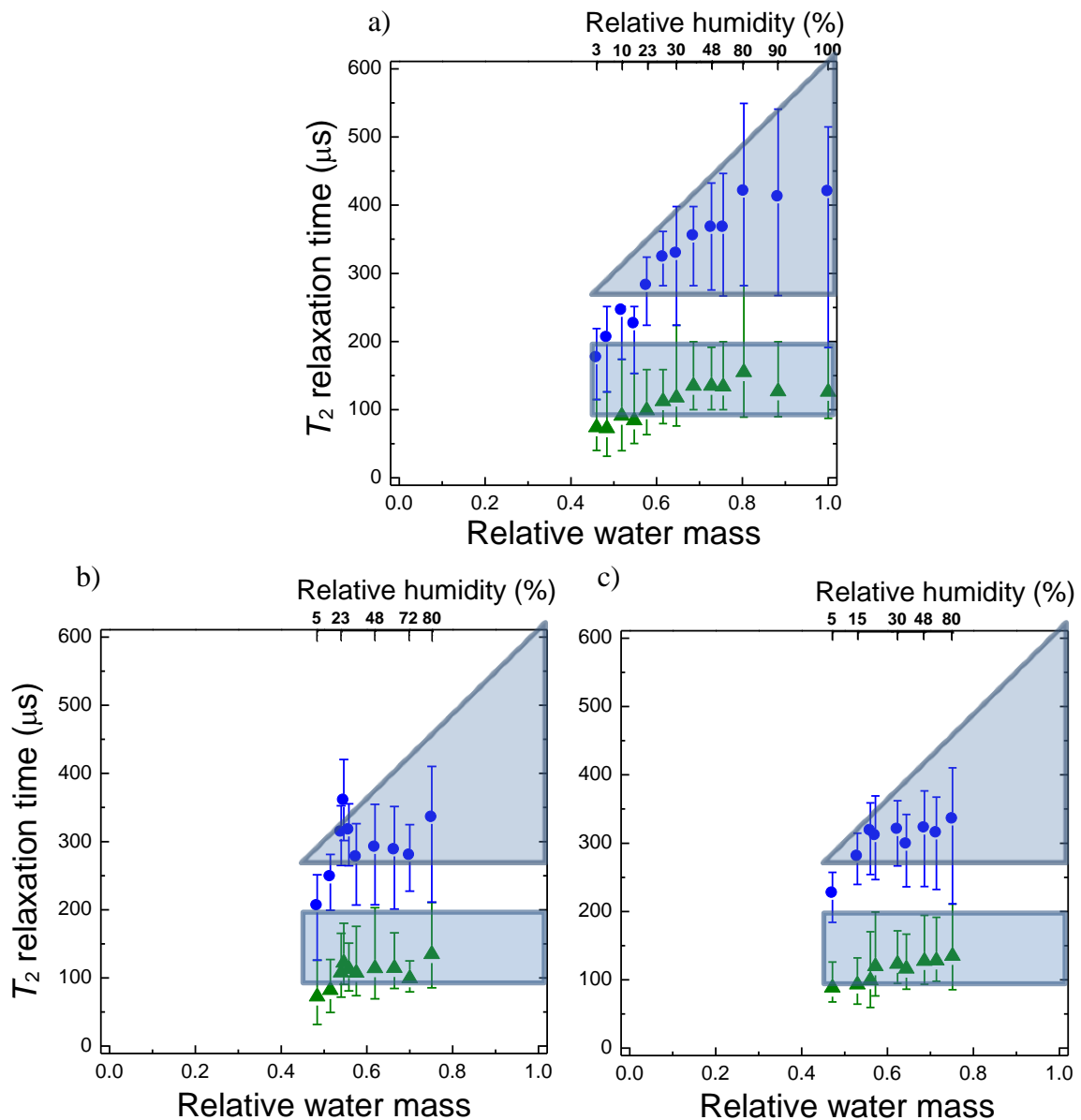


Figure 5.11 The  $T_2$  relaxation time distribution as a function of relative water mass – lower axis, and RH – upper axis, during desorption (a), adsorption (b) and re-desorption (c) for C-S-H interlayer pore water (green triangles) and gel pore water (blue circles). The light blue boxes span the width of  $T_2$  peaks of primary desorption and are provided as a guide to the eye.

During primary desorption the distribution of  $T_2$  relaxation time for gel pore water shows a constant lower boundary of  $T_2$  down to a relative water mass of about 0.6 at which point the gel signal intensity nears zero. This suggests a lower limit of filled pore sizes that does not change on desorption. The higher boundary of  $T_2$  progressively decreases with reduction of

the water mass and relative humidity. This in turns suggests that the largest gel pores empty first. There is a wider distribution of filled pore sizes at high humidity compared to low humidity. The distribution of interlayer pore water stays constant down to a water mass of about 0.65 – 0.70 (humidity around 35%). Then its value starts to decrease. It reaches 75  $\mu\text{s}$  at 3% RH. There may be several reasons for this. One possibility is that the surface mono-layer of water in empty pores has a slightly lower  $T_2$  than that of the interlayer water (which is a few monolayers wide). The ILT is not able to separately resolve them both and hence the average decreases as the gel pore empties and surface layer increases. Another possibility is that pearling artificially increases the interlayer water  $T_2$  at high humidity when there is a large gel pore signal.

Upon adsorption, the gel pore water  $T_2$  distribution does not recover to the previous level. The lower boundary value is approximately constant at around 200  $\mu\text{s}$ ,  $\sim 75 \mu\text{s}$  less than during desorption. Apart from one data point measured at 27% RH with intensity less than 0.03, the  $T_2$  times are also less than during desorption. Above a water mass fraction of 0.56 the times of peaks maxima are almost constant, close to the desorption lower boundary. Finally at water mass of 0.75 there is a substantial growth in  $T_2$  value to almost the same value ( $\sim 350 \mu\text{s}$ ) as on desorption path. The constant  $T_2$  value below 0.75 mass (equivalent 80% RH) may suggest that the surface to volume ratio of the pore water is also constant. The interlayer water  $T_2$  achieves fairly constant value at 0.55 water mass, same mass at which the interlayer signal reaches the highest value.

The secondary desorption presents the data similar to the first desorption. The higher limit of the gel water  $T_2$  decreases gradually. The lower limit is approximately constant at the  $\sim 50 \mu\text{s}$  lower  $T_2$  with the huge majority of peak widths covering the same  $T_2$  range.

## 5.6. ADSORPTION MECHANISM

The isotherm loops for interlayer and gel pore water allow an interpretation of the way the gel pores fills during adsorption. As shown in figure 5.10 b the maximum in interlayer water intensity is followed by sudden and significant drop of intensity ( $\sim 0.05$  at 36% RH). Afterwards the intensity seems to be constant in the range of experimental error (fig. 5.12) contrary to desorption processes where a gradient is observed. As the decrease in interlayer intensity is not observed, the intensity value is approximately the same as at 100% RH in ‘as prepared’ paste. The second desorption starts with an immediate rise of intensity. These observation suggest that the mechanism of adsorption differs from desorption and that interlayer signal belongs entirely to interlayer water and specifically not to surface water layer during adsorption above  $\sim 30\%$  RH.

Additionally, the gel pore water intensity is shifted upwards during adsorption in comparison to both desorption branches (fig. 5.10 c). The shift in signal fraction is  $\sim 0.05$  that corresponds to the value of decrease in interlayer water signal.

The decrease in interlayer signal accompanied by an increase of gel pore water intensity together strongly suggest that water layer created at the surface of gel pores is totally covered by the next layer of gel water at  $\sim 30\%$  RH in the course of adsorption. The refilling of gel

pores may occur layer by layer in which case after the second layer of water is drawn into gel pores the concept of surface layer is not anymore valid. Mechanisms of pores emptying during desorption and filling during adsorption is schematically presented in figure 5.13.

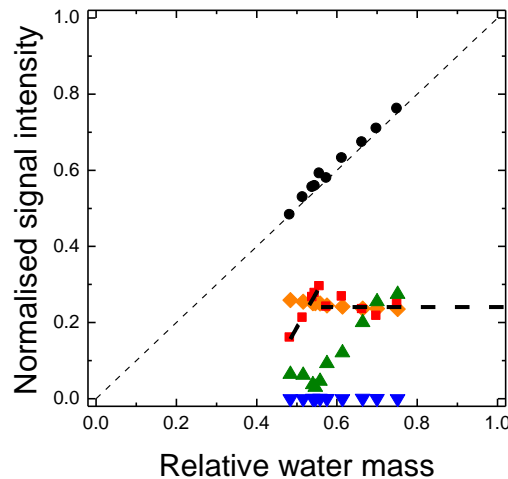


Figure 5.12 The fitting lines (thick dashed lines) of the interlayer signal for adsorption. Orange diamonds represent chemically combined water signal, red squares – the C–S–H interlayer pore water, green triangles – the C–S–H gel pore water and blue inverted triangles – the ‘free’ water signals. The black circles show the total water signal.

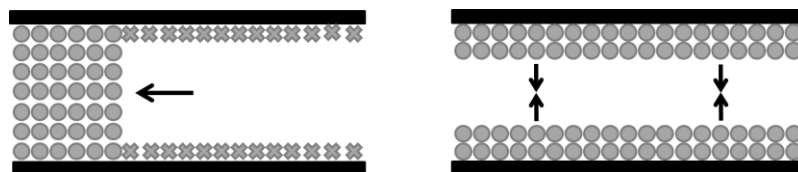


Figure 5.13 The schematic mechanism of desorption (a) and adsorption (b) processes. Circles represent mobile water molecules, crosses are immobile, surface water molecules.

## 5.7. PORE SIZE AND SPECIFIC SURFACE AREA CALCULATIONS

### 5.7.1. Specific surface area based on adsorption isotherm

The specific surface area of cement paste is evaluated from the adsorption isotherm based on both sample mass and total signal intensity. The data is fitted according to BET theory in the humidity range  $< 45\%$  - equation (2.4) in section 2.3.3 for amount of adsorbed water  $u$  (fig. 5.14).

The surface area ( $A$ ) is calculated according to equation (2.5) in section 2.3.3,  $A = N_A \cdot A_m \cdot u_m / M^{AMU}$  where  $N_A$  is Avogadro number,  $M^{AMU}$  – water molar mass,  $A_m$  - cross section area of water molecule ( $10.6 \cdot 10^{-20} \text{ m}^2$  [59]).

The BET fitting parameters based on changes in total intensity are  $u_m = 0.041$  and  $K = 7.19$ . The fitting of sample mass yields  $u_m = 0.037$  and  $K = 5.54$ . The calculated specific surface areas are  $144 \pm 24$  and  $130 \pm 5 \text{ m}^2/\text{g}$  of dried paste (3% RH) according to changes in intensity and mass respectively.

The calculated SSAs based on the changes in total signal intensity and mass are in good agreement with each other. The BET surface areas agree with the range reported by Baroghel-Bouny [114] – 85-143 m<sup>2</sup>/g of dried paste (3% RH).

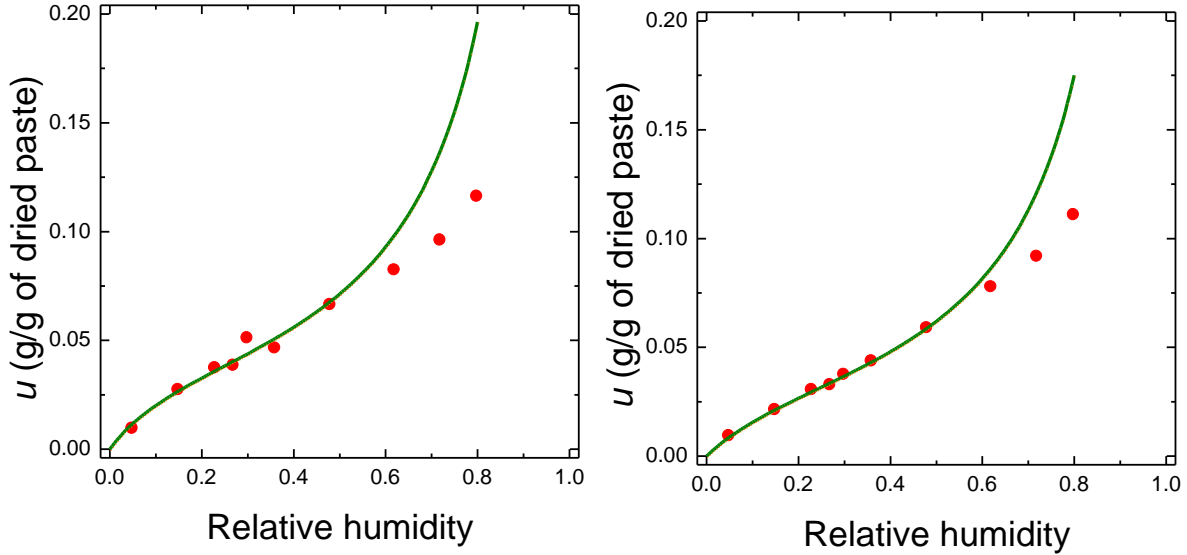


Figure 5.14 The adsorption isotherm in form of total NMR intensity sample mass (left) and sample mass (right). The green line presents the fitting according to BET equation.

## 5.7.2. Surface relaxation model

### 5.7.2.1. Pore size calculation

C-S-H interlayer and gel pore sizes were first calculated according to the fast exchange model of relaxation described in chapter 3.3.2 [27]. The model tells that, as water molecules undergo rapid exchange, the experimentally observed relaxation rate ( $1/T_2$ ) is the volume weighted average of slowly relaxing bulk pore water and fast relaxing molecules on the pore surface. Considering that the  $T_{2,bulk}$  relaxation time is very long, the contribution of bulk relaxation rate is negligible. This leads to the expression for observed relaxation rate:

$$\frac{1}{T_2} = \frac{\varepsilon S}{V} \cdot \frac{1}{T_{2,surf}} \quad (5.6)$$

where  $T_2$  and  $T_{2,surf}$  are the observed and surface relaxation times,  $S$  and  $V$  are the pore surface area and volume,  $\varepsilon$  is the thickness of water surface layer.

To calculate the surface-to-volume ratio, and hence pore size, the surface relaxivity ( $\lambda = \varepsilon/T_{2,surf}$ ) is required. In this study, a water monolayer thickness ( $\varepsilon = 0.28$  nm) and the relaxation time of the sample equilibrated at 3% RH ( $T_{2,surf} = 75$   $\mu$ s) has been used for calibration. They yield surface relaxivity equal to  $3.7 \cdot 10^{-3}$  nm/ $\mu$ s.

The pore size ( $d$ ) is related directly to the surface-to-volume ratio. That relation depends on the shape of the pores. The calculation based on planar pores ( $S/V = 2/d$ ) gives an equation for the width:

$$d = 2 \cdot \lambda \cdot T_2 \quad (5.4)$$

The C-S-H interlayer spacing based on the relaxation times (126  $\mu$ s) is  $0.94 \pm 0.04$  nm, gel pore size (420  $\mu$ s) is  $3.1 \pm 0.2$  nm and interhydrate size (1.4 ms) is  $10.5 \pm 1.8$  nm.

### 5.7.2.2. Specific surface area calculation

Given the pore size the equation of specific surface area ( $A$ ) can be evaluated. The volume of water in particular reservoirs is obtained by multiplication of signal intensities ( $I_{CSH/gel}$ ) and effective water to cement ratio ( $w/c_{eff}$ ). The SSA is calculated by dividing that volume by the width of pore expressed in cm. Further it is normalised to the volume of cement paste ( $V_p$ ). The equation of SSA expressed in  $m^2$  per  $cm^3$  of paste can be written as

$$A_{CSH/gel} = \frac{I_{CSH/gel} \cdot \left(\frac{w}{c}\right)_{eff} \cdot 10^{-4}}{2 \cdot \lambda \cdot T_{2,CSH/gel} \cdot V_p} \quad (5.5)$$

The SSA for C-S-H interlayer pores is  $175 \pm 12$   $m^2/cm^3$  of paste and for gel pores is  $91 \pm 4$   $m^2/cm^3$  of paste. Equivalent values in different units are presented in table 5.1. The ratio of interlayer to gel SSAs is 1.9. The value of total specific area stays in good agreement with value obtained by Powers and Brownyard [32] – 170-195  $m^2/g$  of anhydrous cement for 28 days old paste. It is however slightly lower than the values reported by Halperin *et al* [10] - 225  $m^2/g$  of anhydrous cement, and slightly higher than that BET surface areas presented by Baroghel-Bouny [114] and calculated in section 5.7.1. based on adsorption branch.

Table 5.1 Specific surface area of C-S-H interlayer pores, gel pores and both together.

	Specific surface area in $m^2$ per				
	$cm^3$ of paste	g of paste	g of anhydrous cement	g of dried paste (180°C)	g of dried paste (3% RH)
Interlayer Pores	175±12	86	125	113	103
Gel Pores	91±4	44	65	58	54
Total	266	130	190	171	157

### 5.7.3. Amplitude model for calculation of pore size

The second model applied in order to obtain the C-S-H interlayer and gel pore sizes is the amplitude model described in section 3.4.3.2. This study extends and improves this approach.

#### 5.7.3.1. Modification to the Amplitude model

The amplitude model by McDonald *et al* [26] presented in section 3.4.3.2 was relatively simplistic. The mobile signal was not differentiated between different pore types. In this thesis the application of CPMG pulse experiments facilitates such decomposition. Therefore, modifications to the calculation in the model are necessary.

The initial intensities in ‘as prepared’ paste (at 100% RH) for chemically combined water ( $I_{sol}$ ), C-S-H interlayer pores ( $I_{CSH}$ ), gel pores ( $I_{gel}$ ) and ‘free’ water ( $I_{cap}$ ) are expressed as:

$$I_{sol} = V_{sol} / V_{wp} = 0.243 \quad (5.6)$$

$$I_{CSH} = A_{CSH} \cdot (q + 2) \cdot d_{wat} / V_{wp} = 0.255 \quad (5.7)$$

$$I_{gel} = A_{gel} \cdot (p + 2) \cdot d_{wat} / V_{wp} = 0.441 \quad (5.8)$$

$$I_{cap} = V_{cap} / V_{wp} = 0.061 \quad (5.9)$$

where  $A_{CSH}$  and  $A_{gel}$  are the specific surface area of C-S-H interlayer and gel pores per unit volume of paste,  $V_{sol}$  and  $V_{cap}$  are volume of chemically bound and ‘free’ water per unit volume of paste,  $V_{wp}$  - volume of water in unit volume of paste ( $0.645 \text{ cm}^3/\text{cm}^3$  of paste),  $d_{wat}$  - the size of water molecule (0.28 nm). The definitions of  $p$  and  $q$  are presented in figure 5.15.

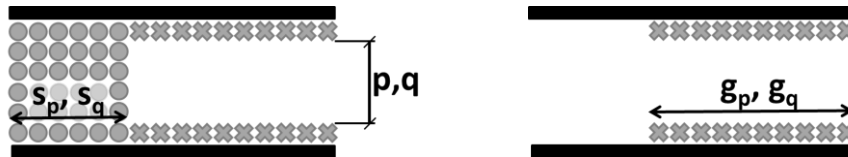


Figure 5.15 The parameters  $p$  and  $q$  are the gel and interlayer pore sizes respectively, without counting the surface water layer, expressed in number of water molecules;  $s_p$  and  $s_q$  are the fraction of specific surface area of gel and interlayer pores still filled with water during drying,  $g_p$  and  $g_q$  are the fraction of surface area covered by water layer.

The order at which water is removed is critical for analysis. Six stages of drying are identified and presented graphically in figure 5.16. (i) ‘Free’ water dries. (ii) Gel pores empty leaving a gel surface layer. (iii) The gel surface clears. (iv) The relatively mobile interlayer water is removed leaving a residual layer. (v) The residual interlayer water leaves. (vi) Chemically combined water from crystalline phases is removed.

The obtained NMR results do not show the fifth and sixth stages. Four stages in the data can at best be observed and further described including relevant equations:

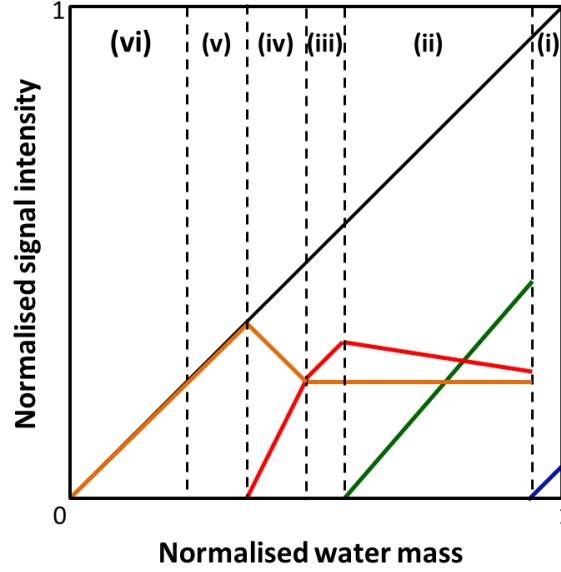


Figure 5.16. The scheme of five stages of cement paste drying according to NMR, description in text. Orange lines represent chemically combined water signal, red – the C–S–H interlayer pore water, green – the C–S–H gel pore water and blue– the ‘free’ water signals. The black line shows the total water signal.

(i) Evaporation of ‘free’ water occurs during primary desorption at the humidity above 90% RH. The normalised ‘free’ water mass,  $m_{cap}$ , is equivalent to its signal fraction at 100% RH ( $I_{cap}$ ). However, it is not possible to extract any further information about pore size and the way they dry. This stage is not observed for secondary desorption as it is investigated in the RH range from 80 to 5%.

(ii) The bulk gel pore water fills the fraction  $s_{p(ii)}$  of the gel surface area during drying (fig. 5.15). C-S-H interlayer water signal,  $I_{CSH(ii)}$ , consists of two parts: water fully filling interlayer spaces,  $s_{q(ii)} = 1$ , and two monolayers of water left on the gel pore surface fraction  $1-s_{p(ii)}$ . The water mass,  $m_{(ii)}$ , is lowered by ‘free’ water and progressively by drying of bulk gel pores water. This stage happens in the relative water mass range 0.94 to 0.6 (fig. 5.17). Hence:

$$I_{CSH(ii)} = [A_{CSH} \cdot (q + 2) \cdot s_{q(ii)} + A_{gel} \cdot 2 \cdot (1 - s_{p(ii)})] \cdot d_{wat}/V_{wp} \quad (5.10)$$

$$I_{gel(ii)} = A_{gel} \cdot (p + 2) \cdot s_{p(ii)} \cdot d_{wat}/V_{wp} \quad (5.11)$$

$$m_{(ii)} = 1 - m_{cap} - A_{gel} \cdot p \cdot (1 - s_{p(ii)}) \cdot d_{wat}/V_{wp} \quad (5.12)$$

$$I_{CSH(ii)} = a_{CSH(ii)} \cdot m_{(ii)} + b_{CSH(ii)} \quad (5.13)$$

$$I_{gel(ii)} = a_{gel(ii)} \cdot m_{(ii)} + b_{gel(ii)} \quad (5.14)$$

(iii) The gel surface water is removed gradually from  $1-g_{p(iii)}$  surface fraction. The interlayer spaces remain saturated with water,  $s_{q(iii)} = 1$ , and the chemically combined water signal is constant. Hence the gradient of the interlayer signal should be 1. Considering the small mass range of this stage spanning at most two data points recorded within it, any further attempt to evaluate relations of pore parameters and intercepts of fitting lines is not rational and meaningful in this region. However, the existence of this region is critical to numerical solution of the model.

(iv) The relatively mobile interlayer water is removed in relative water mass range below 0.57 (fig. 5.17). A residual layer of water remains at surface fraction  $1-s_{q(iv)}$  of interlayer pores. This layer contributes to solid signal intensity,  $I_{sol(iv)}$ .

$$I_{CSH(iv)} = A_{CSH} \cdot (q + 2) \cdot s_{q(iv)} \cdot d_{wat}/V_{wp} \quad (5.15)$$

$$I_{sol(iv)} = V_{sol}/V_{wp} + A_{CSH} \cdot 2 \cdot (1 - s_{q(iv)}) \cdot d_{wat}/V_{wp} \quad (5.16)$$

$$m_{(iv)} = 1 - m_{cap} - [A_{gel} \cdot (p + 2) + A_{CSH} \cdot q \cdot (1 - s_{q(iv)})] \cdot d_{wat}/V_{wp} + m_{gr} \quad (5.17)$$

$$I_{CSH(iv)} = a_{CSH(iv)} \cdot m_{(iv)} + b_{CSH(iv)} \quad (5.18)$$

$$I_{sol(iv)} = a_{sol(iv)} \cdot m_{(iv)} + b_{sol(iv)} \quad (5.19)$$

The model assumed that the gel intensity decreases to zero. In practice it does not. This leads to a systematic error in the resultant gel pore surface area. However, the earlier assumptions already made and the quality of the data do not warrant further analysis to incorporate this level of complexity. Nevertheless, the residual water mass  $m_{gr}$  have to be included into the total mass expressions for  $m_{(iv)}$  (eq. (5.17)). It is taken as the average of the gel pore water intensity below relative water fraction 0.6,  $m_{gr}$  is  $\sim 0.06$ .

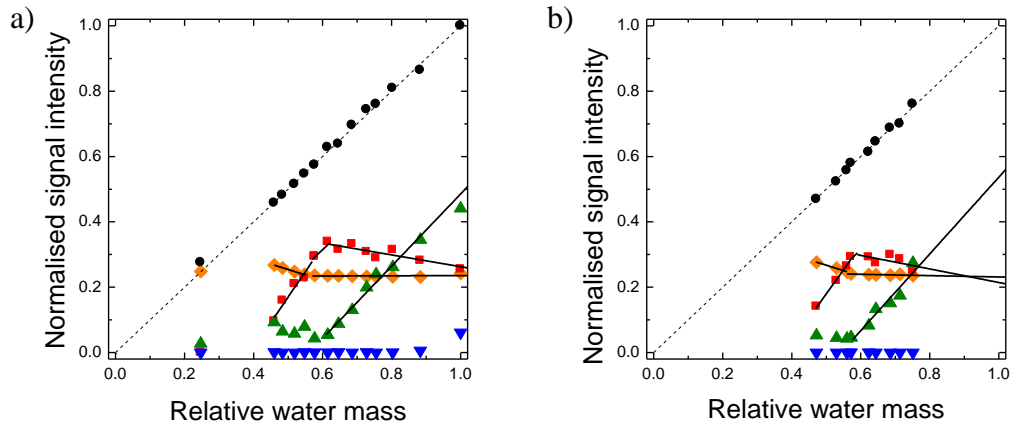


Figure 5.17 The fitting lines (solid lines) used to calculate the pore sizes from primary (a) and secondary desorption (b). Orange diamonds represent chemically combined water signal, red squares – the C–S–H interlayer pore water, green triangles – the C–S–H gel pore water and blue inverted triangles – the ‘free’ water signals. The black circles show the total water signal.

Solving equations (5.10) - (5.19) the expressions for fitting line slopes ( $a_{CSH(ii)}$ ,  $a_{gel(ii)}$ ,  $a_{CSH(iv)}$ ,  $a_{sol(iv)}$ ) and intercepts ( $b_{CSH(ii)}$ ,  $b_{gel(ii)}$ ,  $b_{CSH(iv)}$ ,  $b_{sol(iv)}$ ) are obtained:

$$a_{CSH(ii)} = -\frac{2}{p}; \quad a_{gel(ii)} = 1 + \frac{2}{p}; \quad (5.20)$$

$$a_{CSH(iv)} = 1 + \frac{2}{q}; \quad a_{gel(iv)} = \frac{V_{sol}}{V_{wp}} - \frac{2}{q} \quad (5.21)$$

$$b_{CSH(ii)} = \frac{2}{p} (1 - m_{cap}) + A_{CSH} \cdot \frac{d_{wat}}{V_{wp}} \cdot (q + 2); \quad (5.22)$$

$$b_{gel(ii)} = -1 + m_{cap} + A_{gel} \cdot \frac{d_{wat}}{V_{wp}} \cdot (p + 2) - \frac{2}{p} \cdot (1 - m_{cap}) \quad (5.23)$$

$$b_{CSH(iv)} = -1 + m_{cap} \cdot \left(1 + \frac{2}{q}\right) + A_{gel} \cdot \frac{d_{wat}}{V_{wp}} \cdot \left[p + 2 + \frac{2}{q}(p + 2)\right] - \frac{2}{q} - m_{gr} \cdot \left(1 + \frac{2}{q}\right) + A_{CSH} \cdot \frac{d_{wat}}{V_{wp}} \cdot (q + 2); \quad (5.24)$$

$$b_{sol(iv)} = \frac{V_{sol}}{V_{wp}} \cdot \frac{2}{q} + m_{gr} \left(\frac{2}{q} - 1\right) + A_{gel} \cdot \frac{d_{wat}}{V_{wp}} \cdot \left(\frac{4}{q} - 2\right) + A_{CSH} \cdot \frac{d_{wat}}{V_{wp}} \cdot \left(\frac{4}{q} - q \cdot s_{q(iv)}\right) \quad (5.25)$$

The pore characteristic parameters can be calculated from equations (5.6) - (5.9), (5.20) - (5.25) with additional conditions that:

$$I_{sol} + I_{CSH} + I_{gel} + I_{cap} = 1 \quad (5.26)$$

$$a_{CSH(ii)} + a_{gel(ii)} = 1 \quad (5.27)$$

$$a_{CSH(iv)} + a_{sol(iv)} = 1 \quad (5.28)$$

$$b_{CSH(ii)} + b_{gel(ii)} = 0 \quad (5.29)$$

### 5.7.3.2. Pore size calculation

In order to calculate the pore sizes the linear fits to interlayer, gel and chemically combined water intensities are performed and shown in figure 5.17. For primary desorption the fittings are made after ‘free’ water dries (without data point at water mass fraction 1) as it cannot be evaluated how this drying affects the behaviour of interlayer and gel pore signals.

Table 5.2 shows the gradients of the fitting lines for (ii) and (iv) stage of drying.

Table 5.2 Gradients and intercepts of fitting lines for (ii) and (iv) stage of drying.

	$a_{CSH(ii)}$	$a_{gel(ii)}$	$a_{CSH(iv)}$	$a_{sol(iv)}$	$b_{CSH(ii)}$	$b_{gel(ii)}$	$b_{CSH(iv)}$	$b_{sol(iv)}$
Desorption I	-0.180	1.103	1.557	0.335	0.443	-0.618	-0.609	0.422
Desorption II	-0.208	1.176	1.476	0.349	0.422	-0.639	-0.559	0.442

The gel pore size was calculated from equations (5.20) and (5.27) and interlayer pore size was based on eq. (5.21) and (5.28). The resultant pore sizes are presented in table 5.3. Errors in sizes were estimated based on the errors in the measured gradients of fitting lines for (ii) and (iv) stage of drying.

The gel pore size calculated from primary desorption is 4.5 nm. That is bigger than the value calculated from surface relaxation model – 3.1 nm, but close to the value obtained by

Table 5.3 Calculated size of C-S-H interlayer and gel pores.

Sorption cycle	Interlayer pore size [nm]	Gel pore size [nm]
Desorption I	$1.5 \pm 0.3$	$4.5 \pm 1.6$
Desorption II	$1.6 \pm 0.2$	$3.5 \pm 1.5$

McDonald *et al* [18] - 4.1 nm, when the amplitude model was developed based on oven drying of paste using simpler assumptions. The C-S-H interlayer pore size in ‘as prepared’ cement paste – before desorption, equals 1.5 nm. This value is the same as obtained by McDonald *et al* [18]. However, it is larger than expected and calculated from relaxation model. It is most likely because the assumptions of drying model break down in such a small space.

The results suggested that the mechanism of adsorption is not the same as for desorption (section 5.6). Therefore, the model cannot be used for the adsorption branch.

In figure 5.17 b it can be seen that secondary desorption proceeds in equivalent stages as primary desorption. It is assumed that the contribution of capillary water towards mass calculation is the same as for primary desorption. It is decided following the observation by Baroghel-Bouny [114] that initial water content is restored at 100% RH upon adsorption.

The gel pore size obtained from secondary desorption branch is affected by adsorption cycle. This is explained by adsorption mechanism - filling pores layer by layer. The adsorption was performed up to 80% RH hence the gel pores are not yet totally fill. The calculated values of gel pore size after adsorption and before secondary desorption is 3.5 nm.

Despite the size of interlayer pores based on primary desorption is lower than expected it is still possible to compare the values obtained from both desorption. After one sorption cycle the size comes back to the starting value.

### 5.7.3.3. Specific surface area calculation

The specific surface area of C-S-H interlayer pores ( $A_{CSH}$ ) was calculated by simultaneous least-square fittings of equations (5.7), (5.22), (5.24), (5.26) and (5.29). The gel pores SSA ( $A_{gel}$ ) was based on eq. (5.8), (5.23), (5.24), (5.26) and (5.29). The resultant specific surface areas are presented in table 5.4. Errors in specific surface areas were estimated based on the errors in the measured intercepts of fittings lines for (ii) and (iv) stage of drying and on the errors in C-S-H interlayer and gel pores estimated in previous section.

The calculated total surface area of C-S-H interlayer and gel pores from both desorption are very close. They are in the range of BET values measured by Baroghel-Bouny [114] but lower than that based on adsorption branch in this thesis (section 5.7.1). They are also below values reported by Powers and Brownyard [32], Halperin *et al* [10] and these based on surface relaxation model (section 5.7.2.2).

Table 5.4 Calculated specific surface area of C-S-H interlayer and gel pores.

Cycle	Desorption I			Desorption II		
	Specific surface area in m <sup>2</sup> per					
Pore types	cm <sup>3</sup> of paste	g of anh. cement	g of dried paste (3% RH)	cm <sup>3</sup> of paste	g of anh. cement	g of dried paste (3% RH)
Interlayer	128±30	92	76	112±40	80	66
Gel	65±10	47	38	89±20	64	53
Total	193	138	114	201	144	119

The values of C-S-H interlayer pores surface area are lower than obtained by the surface relaxation model by around 50-60 m<sup>2</sup>/cm<sup>3</sup> of paste (27-36%). It is almost certainly because the width of the interlayer pores is higher than expected. If the assumption is made that the interlayer space size is 1 nm, the SSA calculated from primary desorption according to equation (5.7) and (5.22) would be 164 and 199 m<sup>2</sup>/cm<sup>3</sup> of paste respectively, much closer to 175 m<sup>2</sup>/cm<sup>3</sup> of paste obtained by relaxation model.

The gel pore surface area calculated from primary desorption data is lower by ~25% compare to the value based on surface relaxation model. While the one from secondary desorption is basically the same. There are two main sources of complexity in calculation of gel pore surface area. First is the residual water left in the smaller gel pores at water mass fraction below ~0.6. The second is unknown exact contribution of capillary water towards secondary desorption.

## 6. Influence of curing temperature on cement microstructure

### 6.1. C-S-H DENSITY AND COMPOSITION CALCULATION MODEL

The C-S-H density and composition calculation model, presented in section 6.1.1.-6.1.3., contains the products of joint research between the author and Arnaud Muller, fellow Transcend doctoral student at EPFL, Switzerland.

#### 6.1.1. C-S-H density

Mass and volume balance equations for cement paste expressed per gram of anhydrous cement are written as:

$$1 + \frac{w_{mix}}{c} = (1 - \alpha) + \frac{w_{mix}}{c} \cdot [\beta_{sol} \cdot I_{sol} + \gamma_{CSH} \cdot I_{CSH} + \delta_w \cdot (I_{gel} + I_{cap})] \quad (6.1)$$

$$\frac{1}{\rho_c} + \frac{w_{mix}}{c \cdot \rho_w} = \frac{(1 - \alpha)}{\rho_c} + \frac{w_{mix}}{c} \cdot \left[ \frac{\beta_{sol} \cdot I_{sol}}{\rho_{sol}} + \frac{\gamma_{CSH} \cdot I_{CSH}}{\rho_{CSH}} + \frac{\delta_w \cdot (I_{gel} + I_{cap} + I_{void})}{\rho_w} \right] \quad (6.2)$$

where  $\alpha$  is the degree of hydration,  $I$  are NMR intensity fractions and  $\rho$  are densities. The parameters  $\beta_{sol}$ ,  $\gamma_{CSH}$  and  $\delta_w$  are the reciprocals water mass fractions of solid, C-S-H and water. The subscripts  $c$ ,  $w$ ,  $sol$ ,  $CSH$ ,  $gel$ ,  $cap$  and  $void$  correspond to cement, water, chemically combined water, C-S-H, gel pore water, ‘free’ water (capillary and interhydrate pore water) and chemical shrinkage voidage/filled porosity respectively.

The left side of equation (6.1) represents the sum of anhydrous cement (1) and water ( $w_{mix}/c$ ) masses at the time of mixing. The right side is the sum of the masses of unreacted cement ( $1 - \alpha$ ) and hydration products expressed in terms of signal intensities. In equation (6.2) the masses are divided by the respective densities to give the volume balance.

An important phenomenon to consider during hydration of cement paste is the chemical shrinkage. It is the volume reduction created because the volume of the hydration products is lower than the original volume of reactants: cement and water. Chemical shrinkage creates additional porosity – voids, inside cement paste in sealed cured systems. For *small* underwater cure paste samples voids are filled with water drawn into the sample [115]. Thus when following the hydration process of underwater cure paste the mass ( $m_{paste}$ ) increases while the overall volume stays constant. Therefore, to balance the cement paste mass and volume equations, the chemical shrinkage is included only in the volume calculation.

The intensity fractions ( $I$ ) of particular water reservoirs are normalised to the total intensity which does not include chemical shrinkage, hence  $I_{sol} + I_{CSH} + I_{gel} + I_{cap} = 1$ . The volume created by chemical shrinkage can be defined in terms of additional water signal intensity or mass  $I_{void} = I_{total} - 1 = (w_{paste} - w_{mix})/w_{mix}$ . The solid intensity originates from Portlandite ( $CH$ ) and ettringite ( $Ett$ ), so that  $I_{sol} = I_{CH} + I_{Ett}$ ;  $\beta_{sol} \cdot I_{sol} = \beta_{CH} \cdot I_{CH} + \beta_{Ett} \cdot I_{Ett}$ ;  $\beta_{sol} \cdot I_{sol} / \rho_{sol} = \beta_{CH} \cdot I_{CH} / \rho_{CH} + \beta_{Ett} \cdot I_{Ett} / \rho_{CH}$ . The constants  $\rho_{c,w,CH,Ett}$  are equalled to 3.15, 1.00, 2.24 and 1.77 g/cm<sup>3</sup> respectively [28]. From the atomic masses,  $\beta_{CH} = 74/18$ ,  $\beta_{Ett} = 1255/576$  and  $\delta_w = 1$ .

This leaves four unknowns:  $\alpha$ ,  $\gamma_{CSH}$ ,  $\rho_{CSH}$  and  $I_{CH}$  (or  $I_{Ett}$ , as knowing one, the other can be calculated through the relation for  $I_{sol}$ ). The incorporation of additional, non-NMR, measurements is required. In this study, the degree of hydration ( $\alpha$ ) and the content of CH or ettringite ( $m_{CH}$  or  $m_{Ett}$ ) is measured by XRD and, in case of CH, by TGA. The water intensity fraction of CH and ettringite are expressed by parallel sets of equations:  $I_{CH} = m_{CH} / (w_{mix} \cdot \beta_{CH})$  with  $I_{Ett} = I_{sol} - I_{CH}$ ; and  $I_{Ett} = m_{Ett} / (w_{mix} \cdot \beta_{Ett})$  with  $I_{CH} = I_{sol} - I_{Ett}$ . As a result, the density and reciprocal water mass fraction of C-S-H can be calculated.

### 6.1.2. C-S-H composition

The C-S-H composition is written as  $Ca_z (Si_y, Al_{(1-y)}) O_{(z+y/2+3/2)} (H_2O)_x$ . The reciprocal water content  $\gamma_{CSH}$  is expressed in terms of the water ( $x$ ), calcium ( $z$ ) and silicon ( $y$ ) contents as

$$\gamma_{CSH} = \frac{56z + 9y + 51 + 18x}{18x} \quad (6.3)$$

where the numerical constants are derived from atomic masses of Ca, Si, Al, O and Hyd<sup>17</sup>;  $y$  is defined as  $n_{Si}/(n_{Si} + n_{Al})$ ; and  $n$  is the molar content of respective element per mole of C-S-H.

An equality can be written for the Ca/(Si+Al) ratio for combined C-S-H and CH between reacted fractions of anhydrous cement and the hydration products<sup>18</sup>:

$$\begin{aligned} & 3 \left( \frac{f_{C3S}}{C_3 S^{AMU}} \right) + 2 \left( \frac{\alpha' - f_{C3S}}{C_2 S^{AMU}} \right) + 3 \left( \frac{f_{C3A} - f_{C3A}^{Ett}}{C_3 A^{AMU}} \right) \\ & \frac{f_{C3S}}{C_3 S^{AMU}} + \frac{\alpha' - f_{C3S}}{C_2 S^{AMU}} + 2 \left( \frac{f_{C3A} - f_{C3A}^{Ett}}{C_3 A^{AMU}} \right) = \\ & = \frac{\frac{I_{CH} n_{Hyd}}{2} + \frac{I_{CSH} n_{Hyd} z}{2x} + 3 \left( \frac{f_{C3A} - f_{C3A}^{Ett}}{C_3 A^{AMU}} \right)}{\frac{I_{CSH} n_{Hyd} y}{2x} + 2 \left( \frac{f_{C3A} - f_{C3A}^{Ett}}{C_3 A^{AMU}} \right)} \end{aligned} \quad (6.4a)$$

<sup>17</sup> Hyd is used as an abbreviation of hydrogen, as H in cement notation means water, H<sub>2</sub>O

<sup>18</sup>  $\alpha'$  – mass of reacted C<sub>3</sub>S and C<sub>2</sub>S divided by mass of anhydrous cement

The nominator on the left side of equation (6.4a) comprises the number of calcium moles derived from reacted  $C_3S$ ,  $C_2S$  and  $C_3A$ . The denominator is similarly constructed for the silicon and aluminium moles. On the right side the molar contents of Ca, Si and Al in CH and C-S-H are expressed in terms of NMR signal intensities, the C-S-H composition parameters ( $x$ ,  $z$ ,  $y$ ) and molar content of hydrogen in the mixed paste ( $n_{Hyd} = 2 \cdot w_{mix} / H^{AMU}$ ). Equation (6.4a) is written for the condition that degree of hydration is higher than the fraction of  $C_3S$  in anhydrous cement ( $\alpha' > f_{C_3S}$ ) and assuming that  $C_3S$  reacts before the more slowly reacting  $C_2S$ . Additionally, it is assumed that the fraction of  $C_3A$  which was not consumed to produce ettringite ( $f_{C_3A} - f_{C_3A}^{Ett}$ ) is incorporated in C-S-H.

Equivalent expressions based on similar assumptions can be written for lower degree of hydration ( $\alpha' < f_{C_3S}$ )

$$\begin{aligned} \frac{3 \left( \frac{\alpha'}{C_3S^{AMU}} \right) + 3 \left( \frac{f_{C_3A} - f_{C_3A}^{Ett}}{C_3A^{AMU}} \right)}{\frac{\alpha'}{C_3S^{AMU}} + 2 \left( \frac{f_{C_3A} - f_{C_3A}^{Ett}}{C_3A^{AMU}} \right)} &= \\ &= \frac{\frac{I_{CH} n_{Hyd}}{2} + \frac{I_{CSH} n_{Hyd} z}{2x} + 3 \left( \frac{f_{C_3A} - f_{C_3A}^{Ett}}{C_3A^{AMU}} \right)}{\frac{I_{CSH} n_{Hyd} y}{2x} + 2 \left( \frac{f_{C_3A} - f_{C_3A}^{Ett}}{C_3A^{AMU}} \right)} \end{aligned} \quad (6.4b)$$

A final equation is obtained from the equality  $y = \frac{n_{Si}}{n_{Si} + n_{Al}} = 1 - \frac{n_{Al}}{n_{Si} + n_{Al}}$ . If the sum of Al and Si molar content is written in terms of C-S-H intensity, then it follows that

$$y = 1 - \frac{4x \cdot (f_{C_3A} - f_{C_3A}^{Ett})}{I_{CSH} n_{Hyd} C_3A^{AMU}} \quad (6.5)$$

Simultaneous solution of equations (6.1), (6.2), (6.3), (6.4) and (6.5) enables the C-S-H density and composition to be calculated.

### 6.1.3. C-S-H ‘solid’ and ‘bulk’ density

The C-S-H density derived as in section 6.1.1. includes the calcium and silicon backbones of the structure and the water within interlayer spaces as shown in figure 6.1 left. It especially excludes water, as well as any OH groups, on the surfaces of C-S-H agglomerates as the water (hydrogens or perhaps magnetisation) is in rapid exchange with the bulk gel pore water and has longer  $T_2$ . This density is called C-S-H ‘solid’ density in this work.

The alternative C-S-H composition:  $\text{Ca}_z (\text{Si}_y, \text{Al}_{(1-y)}) \text{O}_{(z+y/2+3/2)} (\text{H}_2\text{O})_x$ , including the gel pore water, has water content  $x'$  and the C-S-H 'bulk' density  $\rho'_{CSH}$  (fig. 6.1 right)

$$x' = \frac{x \cdot (I_{CSH} + I_{gel})}{I_{CSH}} \quad (6.6)$$

and

$$\rho'_{CSH} = \frac{\gamma_{CSH} \cdot I_{CSH} + \delta_w \cdot I_{gel}}{\frac{\gamma_{CSH} \cdot I_{CSH}}{\rho_{CSH}} + \frac{\delta_w \cdot I_{gel}}{\rho_w}} \quad (6.7)$$

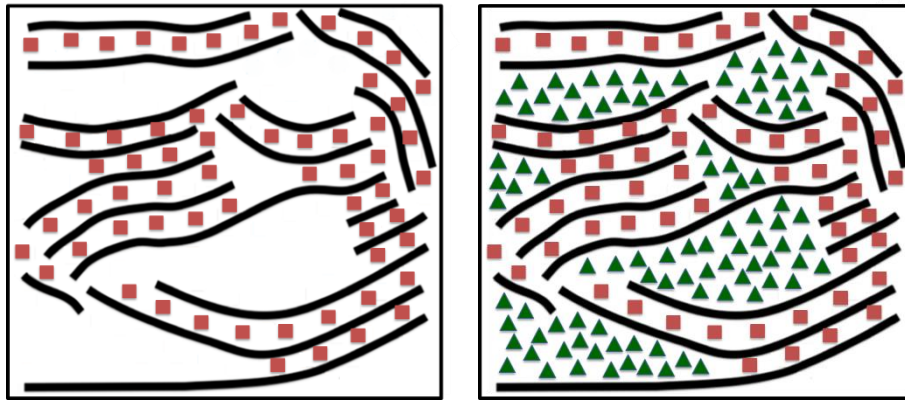


Figure 6.1 A scheme of water location inside C-S-H at 100% humidity for C-S-H 'solid' (left) and 'bulk' (right) density calculation. It shows that for C-S-H 'solid' density only water molecules in interlayer spaces (red squares) are included in calculation, while for C-S-H 'bulk' density water in interlayer and gel pores (green triangles) is considered.

## 6.2. MICROSTRUCTURE, C-S-H DENSITY AND COMPOSITION AT 20°C

### 6.2.1. Evolution of different water populations

The exemplary QE data recorded by Kea<sup>2</sup> spectrometer for white cement paste cured underwater at 20°C for 28 days are shown in figure 6.2. Here, the dead time is shorter (10  $\mu\text{s}$ ) than in previous experiments thus the solid echo is clearly visible. Data are presented for  $\tau$  ranging from 12 to 54  $\mu\text{s}$ . The echo, exponential decay and combined fits to the data are shown. The back-extrapolation of the solid echo and mobile intensity to  $\tau = 0$  were performed by Gaussian and linear fit to the data, respectively (figure 6.3).

The mobile fraction measured by QE was further decomposed by exponential stripping of CPMG decay data as described in section 4.3.2.3. This method of analysis was chosen due to inadequate signal to noise ratio of the data for ILT analysis.

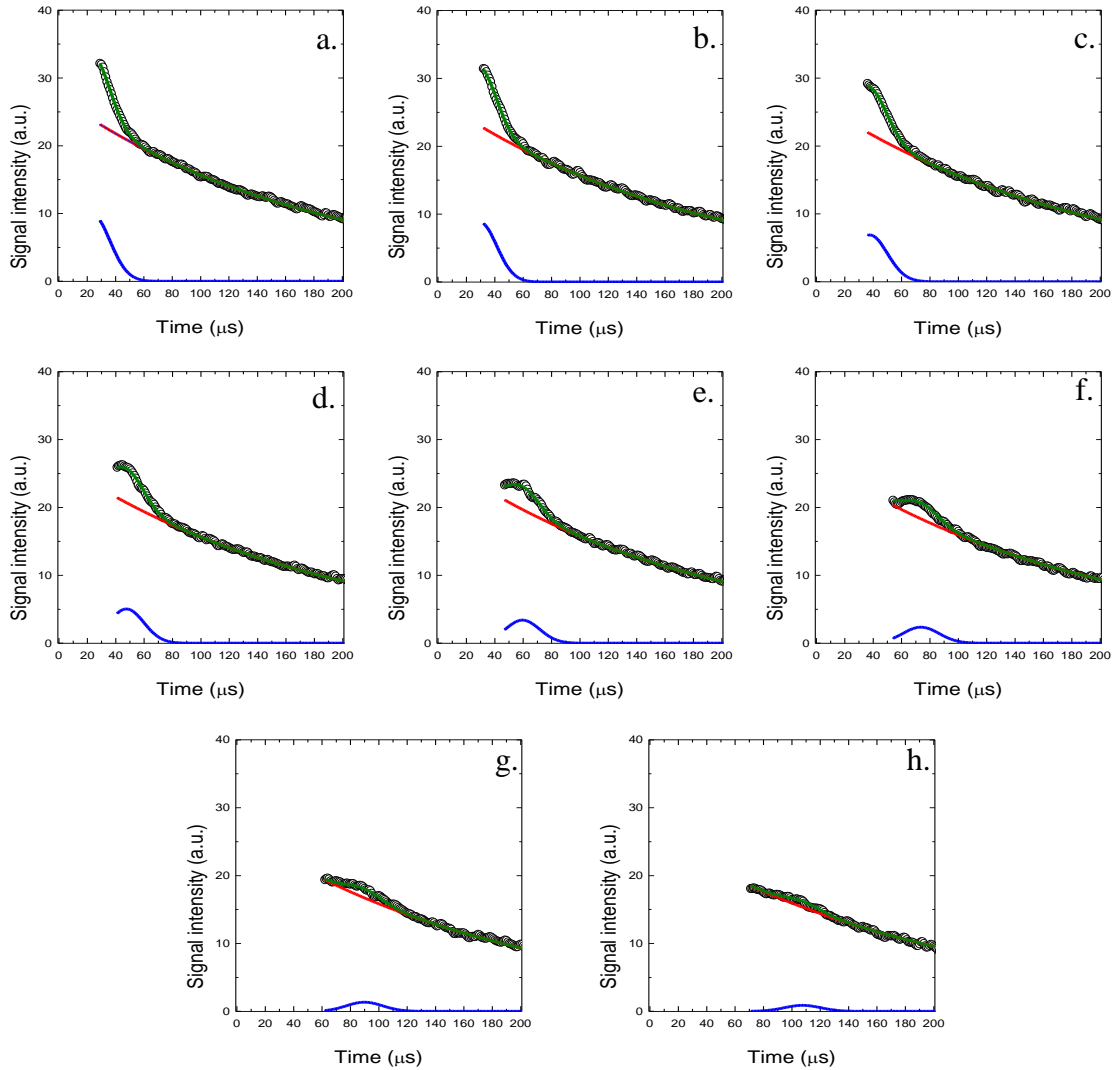


Figure 6.2 Quad echo signals recorded for 28 days old white cement paste (black circles) at eight values of  $\tau$ : a: 12 $\mu\text{s}$ , b: 15 $\mu\text{s}$ , c: 19 $\mu\text{s}$ , d: 24 $\mu\text{s}$ , e: 30 $\mu\text{s}$ , f: 37 $\mu\text{s}$ , g: 45 $\mu\text{s}$ , h: 54 $\mu\text{s}$ . The lines present fitting for solid (blue) and mobile (red) components; the green line is the total intensity fit. The zero time is taken as the end of first 90° pulse of the sequence.

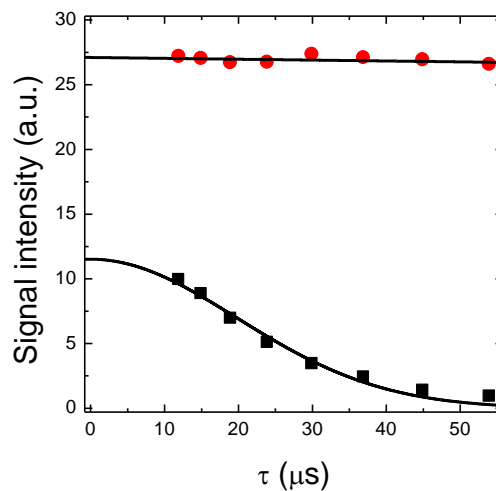


Figure 6.3 Solid echo (black squares) and mobile decay (red circle) signal amplitudes as a function of pulse gap ( $\tau$ ). The lines are the fits to the data: Gaussian for solid and linear for mobile signals.

Figure 6.4 shows the CPMG decay stripping for 28 days old white cement paste, the same as in examples of QE analysis. First, the interhydrate and capillary pore water were fitted to the decay beyond about 1.5 ms. The fitting line calculated based on obtained  $T_2$  relaxation times ( $T_{2,inthyd} = 1.6$  ms,  $T_{2,cap} = 28$  ms) and intensities ( $I_{inthyd} = 4\%$ ,  $I_{cap} = 1\%$ )<sup>19</sup> was subtracted from original decay. The residual data, starting from  $t_{long} = 300$   $\mu$ s, was fitted and gained parameters of gel pore water ( $T_{2,gel} = 291$   $\mu$ s,  $I_{gel} = 47\%$ ). Further subtraction leaves the data to yield the C-S-H interlayer parameters ( $T_{2,CSH} = 91$   $\mu$ s,  $I_{CSH} = 23\%$ ).

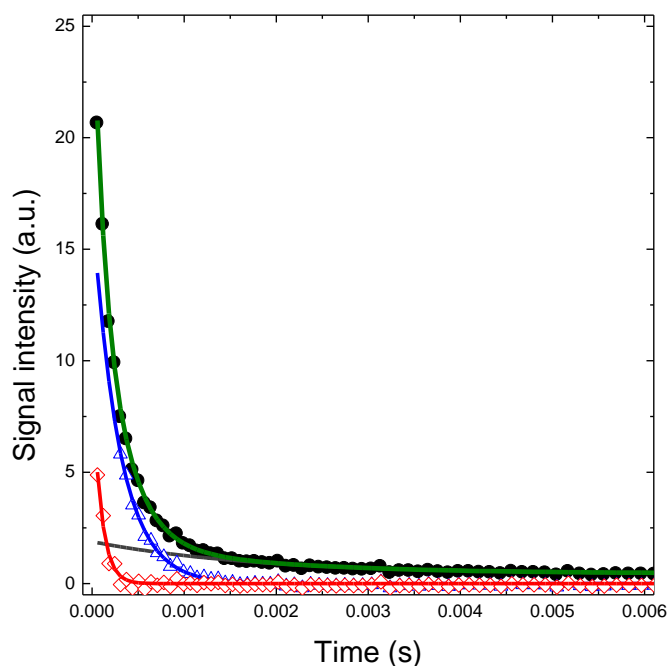


Figure 6.4 Graph presents the exponential stripping procedure for CPMG decay (black circles) of 28 days old white cement paste cure underwater ( $w/c_{mix} = 0.4$ ). The grey line is the ‘free’ water fit and blue triangles are the data after subtraction of that fit from CPMG decay. Blue line presents the fit of gel water intensity which further was subtracted, leaving red diamonds. Red line shows the fit for interlayer water signal. The green line is the total fit make as sum of the capillary, gel and interlayer fits.

NMR data were acquired during cement hydration starting from 2 h up to 90 days. Figure 6.5 presents the evolution of water populations for white cement paste mixed at  $w/c_{mix}$  ratio 0.4 and cured underwater at 20°C. The signal intensities are normalised to the intensity/water mass at the mixing time to show the actual changes and the uptake of water due to chemical shrinkage.

The ‘free’ water intensity is the sum of interhydrate and capillary pore water intensities with the low contribution of latter, about 2-1%, over whole hydration time. The ‘free’ water intensity decreases rapidly during first 3 days of hydration when the ‘free’ water is consumed by 57, 17 and 9% each day. After the third day the rate of consumption is significantly lower, below 3% per day, and gradually decreases with time. The signal of water in crystalline phases increases continuously throughout the entire examined hydration time. The C-S-H interlayer water appears after 6 h of hydration and rises gradually during the first 12 days.

<sup>19</sup> note: in the C-S-H density and composition calculation model the sum of  $I_{inthyd}$  and  $I_{cap}$ , is given as  $I_{cap}$

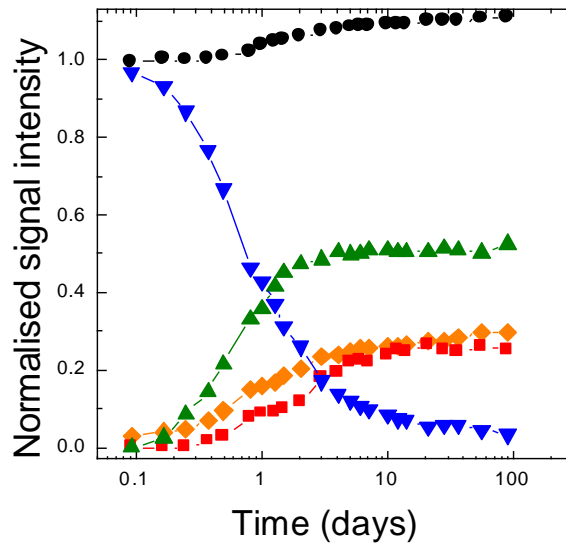


Figure 6.5 The evolution of different water population for white cement paste mixed at  $w/c_{mix}$  ratio 0.4 and cured underwater at 20°C. Orange diamonds represent chemically combined water signal, red squares – the C–S–H interlayer pore water, green triangles – the C–S–H gel pore water and blue inverted triangles – the ‘free’ water signals. The black circles show the total water signal normalized to the initial mass of water at the mixing point. Lines are guide for eyes.

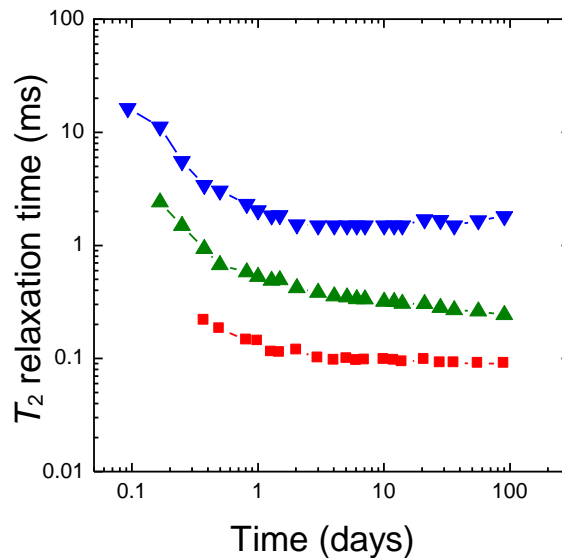


Figure 6.6 The evolution of  $T_2$  relaxation time for water populations of white cement paste mixed at  $w/c_{mix}$  ratio 0.4 and cured underwater at 20°C. Red squares represent the  $T_2$  relaxation time for C–S–H interlayer pore water, green triangles for C–S–H gel pore water and blue inverted triangles for ‘free’ water.

After that time there is only slight increase. The gel pore water signal increases at a very high rate up to 2 days and stays approximately constant after 4 days. The ratio of gel pore to interlayer water decreases from almost 9 at 9 hours of hydration through 4 at 2 days and down to 2 for later hydration ages.

Figure 6.6 shows the corresponding  $T_2$  relaxation times of the C-S-H interlayer, gel and ‘free’ – interhydrate, pore water. The  $T_2$  of the dominating ‘free’ water component falls rapidly during the first day of hydration. After two days its  $T_2$  already reaches the asymptotic

value of about 1.5-1.6 ms that corresponds to pore size<sup>20</sup> of  $11.2-11.9 \pm 1.8$  nm. The gel  $T_2$  drops considerably from around 2.5 ms ( $18.7 \pm 0.7$  nm) to 0.5 ms ( $3.7 \pm 0.2$  nm) over first 24 hours and then slowly but progressively down to about 0.3 ms ( $\sim 2.2 \pm 0.2$  nm). The values of  $T_2$  for interlayer water are almost constant from the moment when the component appears:  $\sim 220$   $\mu$ s at 9h,  $\sim 100$   $\mu$ s at 3 days and  $\sim 90$   $\mu$ s at 90 days that corresponds to pore sizes of:  $\sim 1.6 \pm 0.2$  nm at 9h,  $\sim 0.75 \pm 0.04$  nm at 3 days and  $\sim 0.67 \pm 0.04$  nm at 90 days.

### 6.2.2. Density and C-S-H composition

The C-S-H density and composition were calculated for the white cement paste ( $w/c_{mix} = 0.4$ ) used in the sorption experiment at 28 days of hydration and 100% RH: sample S28 (section 5.3) and for the samples used in the temperature dependence study both at 28 and 90 days of hydration: samples T28 and T90 (section 6.2.1).

The signal intensity fraction due to chemical shrinkage voids was calculated from the increase of water to cement ratio ( $w/c_{paste}$ ). The degree of hydration ( $\alpha$ ) was measured by XRD. The verification of crystalline phases fraction ( $m_{CH}$  and  $m_{Et}$ ) was performed by TGA and XRD measurements.

Table 6.1 shows the measured parameters. The NMR intensities are presented in table 6.2. The negative sign in the capillary intensity implies that water which is drawn into sample is used in the hydration process.

Table 6.1. Parameters for application of the C-S-H density and composition model for white cement paste at 20°C.

Sample	Age [days]	$(w/c)_{paste}$ [g/g <sub>anh</sub> ] ( $\pm 0.002$ )	$\alpha$ ( $\pm 0.02$ )	$m_{CH}$ [g/g <sub>anh</sub> ] ( $\pm 0.010$ )	$m_{Et}$ [g/g <sub>anh</sub> ] ( $\pm 0.010$ )
S28	28	0.463 <sup>21</sup>	0.77	0.342	0.083
T28	28	0.439 <sup>22</sup>	0.85	0.270	0.086
T90	90	0.443 <sup>22</sup>	0.90	0.311	0.086

Table 6.2. The intensities used to calculate C-S-H density and composition at 20°C. The error in intensities is around  $\pm 0.010$  based on standard deviation of the data for multiple samples.

Sample	Age [days]	$I_{sol}$	$I_{CH}$	$I_{Et}$	$I_{CSH}$	$I_{gel}$	$I_{Cap}$	$I_{void}$	$I_{tot}$
S28 <sup>23</sup>	28	0.281	0.185	0.096	0.295	0.510	-0.086	0.157	1.157
T28 <sup>24</sup>	28	0.276	0.164	0.112	0.252	0.512	-0.040	0.097	1.097
T90 <sup>24</sup>	90	0.297	0.189	0.108	0.252	0.525	-0.074	0.109	1.109

<sup>20</sup> pore sizes calculated using surface relaxivity equal to  $3.7 \cdot 10^{-3}$  nm/ $\mu$ s as obtained in section 5.7.2.1

<sup>21</sup> calculated from changes of total signal intensity during desorption experiment as presented in section 5.1.1.

<sup>22</sup> obtained from the sample mass changes

<sup>23</sup>  $I_{Et} = m_{Et} / (w_{mix} \cdot \beta_{Et})$  and  $I_{CH} = I_{sol} - I_{Et}$

<sup>24</sup>  $I_{CH} = m_{CH} / (w_{mix} \cdot \beta_{CH})$  and  $I_{Et} = I_{sol} - I_{CH}$

Solving equations (6.1) to (6.5) the resultant C-S-H ‘solid’ density and composition for underwater cured, never dried paste sample S28 are  $2.68 \pm 0.03 \text{ g/cm}^3$  and  $\text{Ca}_z = 1.54 (\text{Si}_y = 0.96, \text{Al}_{(1-y)} = 0.04) \text{O}_{(z+y/2+3/2)} = 3.51 (\text{H}_2\text{O})_x = 1.92$ . Water content excluding gel pore water is  $x = 1.92 \pm 0.05$ . Including the gel water, the C-S-H ‘bulk’ density and water content (eq. (6.6-6.7)) are  $\rho'_{CSH} = 1.89 \pm 0.02 \text{ g/cm}^3$  and  $x' = 5.25 \pm 0.04$ . (Errors represent the standard deviation of the data for multiple samples measured in course of temperature dependent investigation). The calculated parameters are reproduced as the top line of the table 6.3, and may be compared with the subsequent lines which are for samples T28 and T90.

Table 6.3. The C-S-H density and composition for white cement paste at 20°C.

Sample	$\rho_{CSH}$ [g/cm <sup>3</sup> ]	$\text{Ca}_z (\text{Si}_y, \text{Al}_{(1-y)}) \text{O}_{(z+y/2+3/2)} (\text{H}_2\text{O})_x$	$\rho'_{CSH}$ [g/cm <sup>3</sup> ]	$x'$
S28	2.68	$\text{Ca}_z = 1.54 (\text{Si}_y = 0.96, \text{Al}_{(1-y)} = 0.04) \text{O}_{(z+y/2+3/2)} = 3.51 (\text{H}_2\text{O})_x = 1.92$	1.89	5.25
T28	2.60	$\text{Ca}_z = 1.78 (\text{Si}_y = 0.98, \text{Al}_{(1-y)} = 0.02) \text{O}_{(z+y/2+3/2)} = 3.77 (\text{H}_2\text{O})_x = 1.51$	1.91	4.58
T90	2.65	$\text{Ca}_z = 1.65 (\text{Si}_y = 0.98, \text{Al}_{(1-y)} = 0.02) \text{O}_{(z+y/2+3/2)} = 3.64 (\text{H}_2\text{O})_x = 1.39$	1.93	4.29

If it is assumed that the lateral extent of gel pores and interlayer spaces is similar as suggested by figure 6.1 then the calculated stacks of C-S-H layers can only comprise two to three layers. Taking the layer repeat distance 1.4 nm of C-S-H mineral analogue, tobermorite-14, the C-S-H stack thickness is 2.8 - 4.2 nm. This thickness is close to the C-S-H globule size in Jennings Colloidal Model, CM-II [6]. Assuming C-S-H stacks of three layers, their volume excluding external water layers is  $V = 3 \cdot 1.4 \cdot 10^{-9} \text{ m}^3/\text{m}^2$  of layer. The additional volume of two external monolayers of water can be expressed as  $\Delta V = 2 \cdot 0.28 \cdot 10^{-9} \text{ m}^3/\text{m}^2$  of layer. Hence, if the outer surface water layer is included, the NMR density  $\rho_{CSH}$  is decreased to

$$\rho_{CSH}^{ext} = \frac{4.2 \cdot \rho_{CSH} + 0.56}{4.76} \quad (6.8)$$

The NMR calculated C-S-H ‘solid’ densities (with average  $\rho_{CSH} = 2.64 \pm 0.03 \text{ g/cm}^3$ ) are slightly higher than the values obtained by SANS measurements for a fully saturated CM-II globule density  $2.604 \text{ g/cm}^3$  [7], also excluding any water on the outer surface of particles. If the correction for outer surface water is applied the average  $\rho_{CSH}^{ext}$  is equalled to  $2.45 \pm 0.03 \text{ g/cm}^3$ . This value is very close to density of saturated globule with a monolayer of water on the surface at 11% RH reported by Jennings,  $2.47 \text{ g/cm}^3$  [6] and by Feldman,  $2.43\text{-}2.45 \text{ g/cm}^3$  [75].

The density of saturated C-S-H gel, including gel pore water, measured by NMR is about  $1.90 \pm 0.02 \text{ g/cm}^3$  with water content 4.58-5.25 at 28 days of hydration. It is close to the CM-II model quoted value  $1.83 \text{ g/cm}^3$  with water content 5 when the large gel pores (LGP) are

included [6] and measured by Young and Hansen [72] value of 1.85-1.90 g/cm<sup>3</sup> for saturated (90% RH) C-S-H of fully hydrated C<sub>3</sub>S paste with water content of ~4.0.

Water content of sample S28,  $x = 1.92 \pm 0.05$ , is a little over the content determined by SANS ( $x = 1.8$ ) [7]. The water content values for samples T28 and T90 are somehow lower. The reason for that is not fully understood. However, the sensitivity analysis presented in section 6.4.5 shows the complexity of the analysis and its high dependence on input parameters. It is possible that there is systematic error in one of the input parameters causing discrepancy of  $x$  and  $x'$  results. Otherwise, comparing the results of T28 and T90 with the relation of Ca/Si and H<sub>2</sub>O/Si reviewed by Chen [74] they are in very good agreement and this is the sample S28 that lies out of reported trend.

The values of the Ca/(Si+Al) ratio (calcium content -  $z$ ) are in fairly good agreement with the results of Rayment and Majumdar [70] who yielded the average Ca/(Si + Al + S + Fe) ratio of inner and outer C-S-H ranging from 1.70 at  $w/c = 0.3$  to 1.48 at  $w/c = 0.6$ .

### 6.2.3. C-S-H water content at different humidities

The first pore-type resolved desorption isotherm from section 5.3 and the NMR calculation model for C-S-H composition provide opportunity to draw the first water content isotherm for C-S-H differentiated by water environments – figure 6.7. The water contents have been recalculated based on the sum of interlayer, gel and solid-like surface water signals at 100% RH treated as the water content  $x'$ . Whereas, the C-S-H water mass originates from subtraction of capillary and chemically combined water contribution from total water mass.

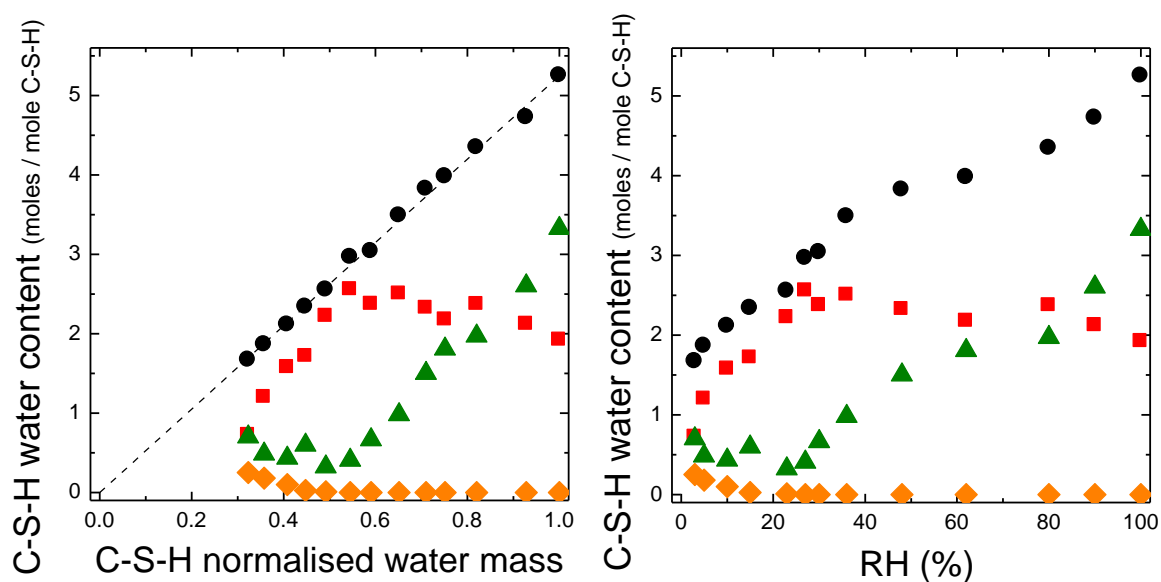


Figure 6.7 The C-S-H water content isotherm as a function of C-S-H water mass (left) and relative humidity (right). The black circles represent the C-S-H water content  $x'$ , including gel pores, which is divided into interlayer ‘solid’ water content  $x$  (red squares), gel water content (green triangles) and solid-like surface water (orange diamonds).

At 100% RH water content excluding and including gel pores water is  $x = 1.92$  and  $x' = 5.25$  respectively. When looking at the presented data, one has to remember that the

apparent increase in interlayer water content is actually the appearance of a surface layer of water in the emptying gel pores. A surface layer, in NMR terms, appears interlayer space – like. The other complication is the residual water staying in very small gel pores below 25% RH. The origin of this tail is not clear. It may indicate the presence of the isolated smaller gel pores without connectivity that cannot dry or of ink-bottle pores.

The obtained curve for water content, including gel pores, mirrors the curve presented by Jennings [6] which shows evolution of total water within C-S-H without division into particular components. At 11% RH, the water content is given as 2.1 by Jennings [6] for saturated C-S-H globule with a monolayer of water on the surface, as 2.0 by Feldman and Ramachandran [73] and 2.1 by Young and Hansen [72] in hydrated  $C_3S$ . The NMR results yield the water content, including gel pores,  $x' = 2.11$  at 10% RH, while the interlayer water content is 1.58. The former is in good agreement with literature value. However the water included in the calculation is the sum of interlayer, residual gel and solid-like surface water.

### 6.3. EVOLUTION OF WATER POPULATION FOR WHITE CEMENT PASTE AT DIFFERENT TEMPERATURE

The QE and CPMG NMR experiments were performed to identify quantitatively the influence of curing temperature on the population of water inside cement pastes over the time of hydration (2 h – 90 days). The applied curing temperatures were 10, 20, 30, 40, 50 and 60°C. The measurements were performed on white cement paste mixed at  $w/c_{mix} = 0.4$  and cured underwater.

#### 6.3.1. Uptake of water during hydration

The volume created by chemical shrinkage was defined based on the mass of water drawn into the sample to fill the voids. Figure 6.8 shows the increase of water mass as a function of hydration time for white cement pastes mixed at  $w/c_{mix}$  ratio 0.4 and cured underwater at different temperatures. Depending on the curing temperature, as the hydration proceeds, the different mass of water is drawn inside underwater cured sample.

The increase of curing temperature causes water uptake to start at earlier hydration times suggesting faster hydration at higher temperature. The acceleration of the hydration process at higher temperatures has been previously reported based on the measurements of chemical shrinkage [116], degree of hydration [109], [117], TGA [117] and strength development [117], [118]. The speed of that uptake is higher at the beginning and it slows down considerably later. With time, at lower curing temperature, the total water ingress rises to values comparable or higher than that found at higher curing temperatures at earlier times. The same behaviour for chemical shrinkage was observed by Geiker and Knudsen [116] through weighing of samples immersed in liquid paraffin. The higher mass can be seen for pastes cured at 40°C in comparison with 50 and 60°C already after half day of hydration (fig. 6.8). Nevertheless, at the later hydration time, beyond 60 days, the water mass at 40°C is slightly lower than for paste cured at 20°C. The continuous increase of water mass at 10°C is

observed through whole hydration time. However, in the experimental time it rises only above mass for paste at 50 and 60°C.

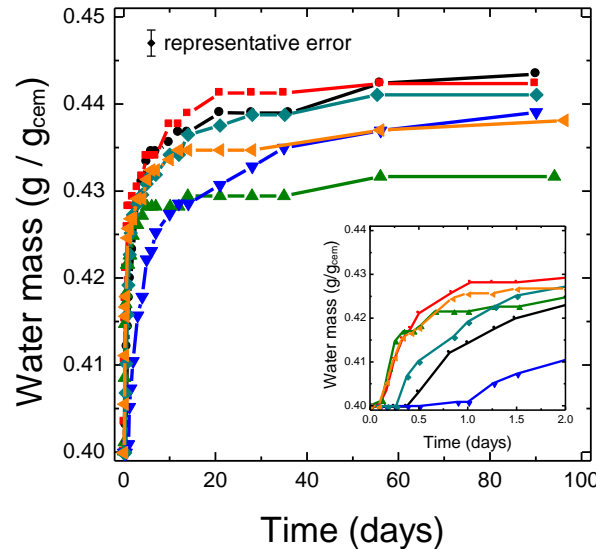


Figure 6.8 Uptake of water as a function of hydration time for white cement pastes mixed at  $w/c_{mix}$  ratio 0.4 and cured underwater at different temperature: blue inverted triangles: 10°C; black circles: 20°C; cyan diamonds: 30°C; red squares: 40°C; orange left-triangles: 50°C; and green triangles: 60°C.

### 6.3.2. 'Free' water evolution

One way to interpret the influence of temperature is by comparing the time at which a given amount of 'free' pore water<sup>25</sup> is consumed inside the sample. The age of sample at which the initial fraction of 'free' water is consumed by 50% and 80% decreases with increase in curing temperature in the range 10 to 60°C. However, the striking feature is that the consumption of 90% of 'free' water is achieved at much longer ages for samples cured at elevated temperatures (Figure 6.9).

Figure 6.10 presents the evolution of 'free' water intensity throughout experimental hydration time. At higher temperature and initial stages of hydration 'free' water is consumed faster. However, when samples are older there is more 'free' water left at elevated temperatures. Data suggests that coarser porosity is created and that it is subsequently much harder to fill this porosity with hydration products. The increased coarser porosity at higher temperatures has been previously reported in literature based mainly on SEM observation [109], [117], [119], [120] but also MIP results [119].

<sup>25</sup> 'free' water is the sum of interhydrate and capillary pore water intensities with the low contribution of latter, about 3-1%, over whole hydration time at all examined curing temperatures

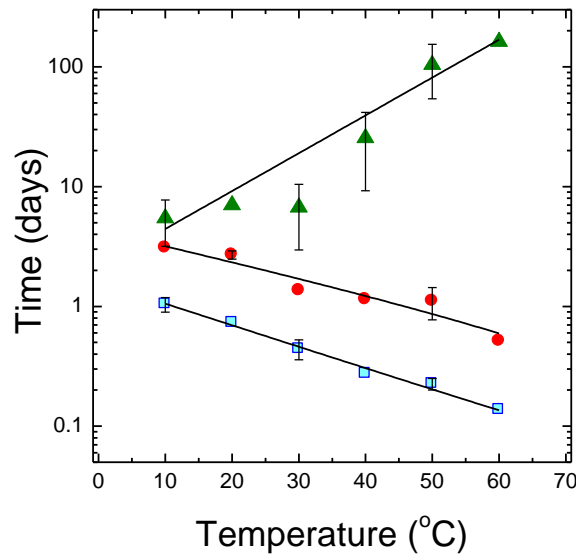


Figure 6.9 Consumption of ‘free’ water for white cement pastes mixed at  $w/c_{mix}$  ratio 0.4 and cured underwater at different temperature. The hydration time of sample at which the initial fraction of ‘free’ water is consumed by 50% is shown as blue squares, by 80% as red circles and by 90% as green triangles. The black lines are exponential fits to the data. (The consumption of ‘free’ water by 90% at 60°C is obtained by extrapolation as it was not achieved within experimental time).

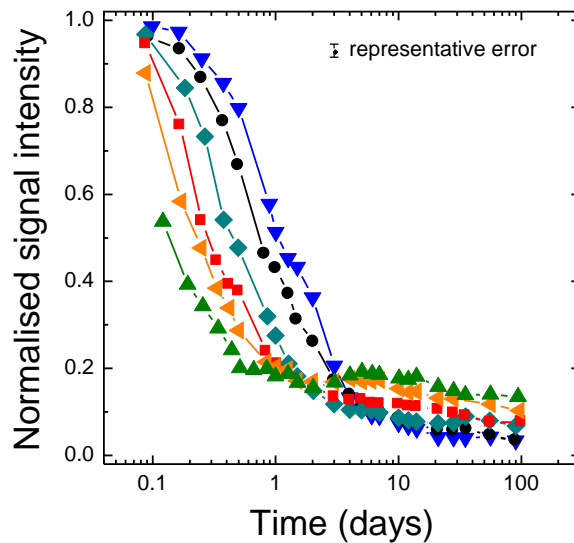


Figure 6.10 Evolution of ‘free’ water as a function of hydration time for white cement pastes mixed at  $w/c_{mix}$  ratio 0.4 and cured underwater at different temperature: blue inverted triangles: 10°C; black circles: 20°C; cyan diamonds: 30°C; red squares: 40°C; orange left-triangles: 50°C; and green triangles: 60°C. Lines are guides for eyes.

### 6.3.3. Chemically combined water evolution

The development of chemically combined water within CH and ettringite proceeds faster and earlier when the curing temperature is increased (figure 6.11). However, beyond about 5 days of hydration, when the intensity is  $\sim 24\text{-}25\%$ , the trend reverses. From that point on the quantity of water associated with those phases increases more slowly at elevated temperature

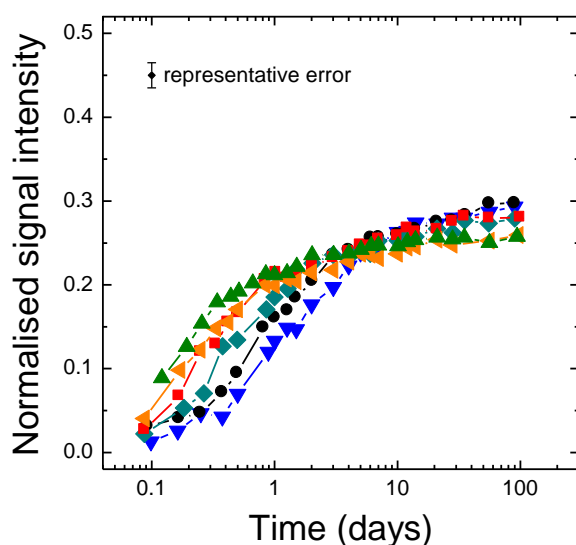


Figure 6.11 Evolution of chemically combined water as a function of hydration time for white cement pastes mixed at  $w/c_{mix}$  ratio 0.4 and cured underwater at different temperature blue inverted triangles: 10°C; black circles: 20°C; cyan diamonds: 30°C; red squares: 40°C; orange left-triangles: 50°C; and green triangles: 60°C. Lines are guides for eyes.

and as a result has lower values.

The verification of the amount and origin of the chemically combined water was performed by TGA and XRD measurements at 28 and 90 days of hydration. The results are presented in table 6.4. The obtained Portlandite and ettringite mass fractions are recalculated to evaluate the fractions of water within them based on their molecular composition, atomic masses and water to cement ratio at mixing point. The XRD patterns did not show the presence of calcium aluminate and monosulfoaluminate at any curing temperature. The sum of water fraction within CH and ettringite determined by TGA and XRD is within 3% of the NMR solid signal fraction.

The CH content as measured by TGA at University of Surrey gives systematically higher results than that measured at EPFL. The reasons for that are not fully understood. There are several factors to take into account. First, samples were posted to EPFL and hence curing temperatures were not maintained. Second, for all samples measured at EPFL hydration was stopped by isopropanol exchange in contrast to the measurement performed on not altered samples at University of Surrey. It has been reported in literature that the alcohols exchange, including isopropanol, may alter the portlandite and calcite determination by TGA method [121]. Finally, the measurements were performed in the temperature range up to 950 and 1000°C at EPFL and Surrey respectively. That this last explanation is not the source of discrepancy was confirmed by the analysis in the same temperature range. Nevertheless, the striking feature is the consistency between the TGA and XRD measurements facilitated at EPFL. However, the quantitative XRD analysis depends on parameters chosen for the Rietveld analysis and that may suggest a systematic calibration factor shifting results.

The results (table 6.4) show that the water content of CH and hence CH content at different curing temperature are fairly constant. The same observation are presented in [109], [120].

Table 6.4. CH and ettringite mass fractions measured by TGA and XRD, their water mass fractions calculated from mass fractions and measured solid NMR signals for white cement pastes mixed at  $w/c_{mix}$  ratio 0.4 and cured underwater at different temperature. The fraction of CH water at 90 days was calculated based on TGA measured at Surrey, while at 28 days on average XRD and TGA results obtained at EPFL.

Temp [°C]	Age [days]	Mass fraction [g/g <sub>anh</sub> ] ( $\pm 0.010$ )				Fraction of water			NMR solid signal ( $\pm 0.010$ )
		CH		Ett		CH	Ett	CH + Ett	
		TGA <i>measured at Surrey</i>	XRD <i>measured at EPFL</i>	TGA	XRD				
10	28		0.262	0.261		0.159	0.096	0.255	0.280
	90	0.298	0.261		0.084	0.181		0.277	0.293
20	28		0.276	0.264		0.164	0.099	0.263	0.276
	90	0.311			0.086	0.189		0.288	0.297
30	28		0.270	0.264		0.162	0.093	0.255	0.262
	90	0.311	0.278		0.081 <sup>♦</sup>	0.189		0.282	0.279
40	28		0.273 <sup>♦</sup>	0.272 <sup>♦</sup>		0.166	0.085	0.250	0.276
	90	0.309			0.074 <sup>♦</sup>	0.188		0.273	0.281
50	28		0.274	0.277		0.167	0.079	0.246	0.248
	90	0.307	0.279		0.069	0.187		0.266	0.259
60	28		0.277 <sup>♦</sup>	0.280 <sup>♦</sup>		0.169	0.063	0.233	0.254
	90	0.309			0.055	0.188		0.251	0.258

<sup>♦</sup> estimated by linear interpolation of data at different temperatures

With increase in temperature, there is a significant decrease in the ettringite content. The lower ettringite content at elevated temperatures was also found by Lothenbach *et al* [117] and Galluci *et al* [109]. The decrease could be associated with the thermodynamic instability of ettringite at different, higher temperatures. The thermal stability of the pure ettringite phase was investigated by Zhou and Glasser [122]. They show that at relative humidity over 80% and temperature below 75°C ettringite water content is fairly unchanged at about 31.6. The thermal stability of ettringite was also examined in the presence of water and gypsum. Hall *et al* [123] found that the ettringite decomposition occurs rapidly at 114°C and results in release of water and formation of monosulfoaluminate hydrate (AFm) and bassanite. The X-ray study by Christensen *et al* [124] followed the hydrothermal reactions of C<sub>3</sub>A-gypsum and Portland cement with water. The former showed no precipitation of ettringite in whole temperature range investigated (25-120°C). However, for C<sub>3</sub>A doped with Na<sup>+</sup> the ettringite forms in increasing amount up to 46°C. Following that the AFm grows in depletion of ettringite and finally above 68°C ettringite is not observed. During hydration of cement paste the ettringite is formed up to ~48°C when the conversion of ettringite to AFm starts. It remains in the structure up to ~70-75°C.

### 6.3.4. C-S-H interlayer and gel water evolution

The C-S-H interlayer and gel pore water appear earlier and develop at a higher rate when the curing temperature is increased (figure 6.12). However with time the intensities of gel and interlayer water for samples cured at lower temperature gradually exceed values for the higher temperatures. Eventually, after about 20 days of hydration for C-S-H interlayer water and 2 days for gel water, intensities are higher for samples cured at progressively lower temperature. The spread of the intensities at 90 days of hydration is ~5%. It is also observed that the change in the rate of gel pore formation happens earlier at higher temperature.

The ratio of C-S-H gel to interlayer signal decreases faster for paste cured at elevated temperature. For mature pastes, the ratio reaches value of about 2 at every temperature: 10°C: ~1.9, 60°C: ~2.2.

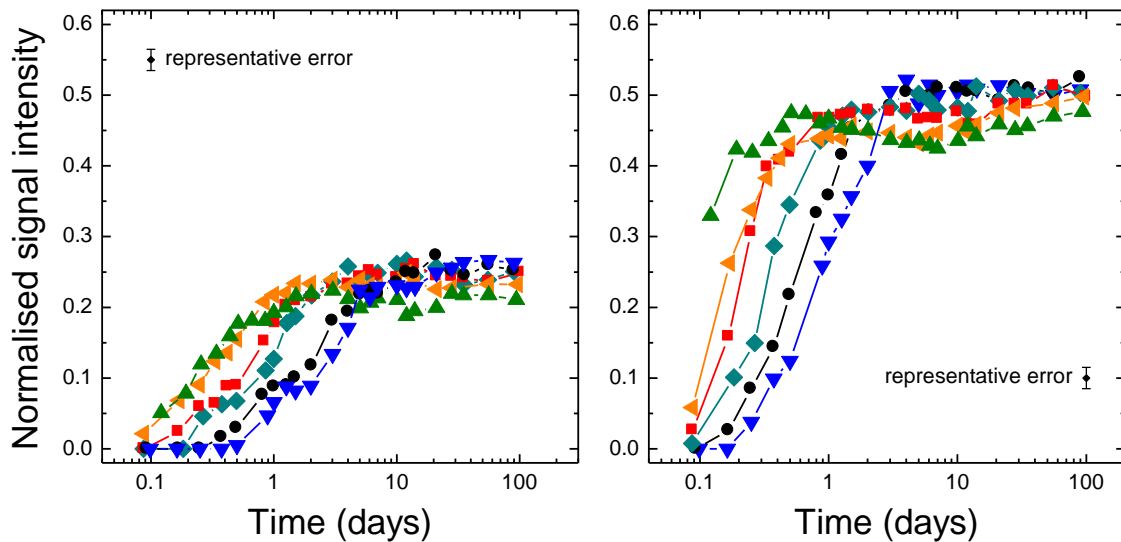


Figure 6.12 Evolution of C-S-H interlayer (left) and gel (right) pore water as a function of hydration time for white cement pastes mixed at  $w/c_{mix}$  ratio 0.4 and cured underwater at different temperature: blue inverted triangles: 10°C; black circles: 20°C; cyan diamonds: 30°C; red squares: 40°C; orange left-triangles: 50°C; and green triangles: 60°C.

### 6.3.5. $T_2$ relaxation times

Figure 6.13 illustrates how the associated  $T_2$  relaxation times of interlayer, gel and ‘free’ water vary with hydration time at different curing temperatures.

Initially, the  $T_2$  relaxation times of ‘free’ – interhydrate, water drop faster with the increase in curing temperature. Beyond about two days the reservoirs maintain the same  $T_2$  times implying constraining of capillary pore sizes. The exceptions are the  $T_2$  relaxation times at 10°C. Their higher values at longer hydration times are explained by a still significant ingress of water due to chemical shrinkage as indicated by increasing water uptake in figure 6.8. At elevated temperatures the  $T_2$  of gel pore water also has the smaller values and decreases more quickly as the hydration process is accelerated. However, after about a week, the trend reverses. The pastes cured at higher temperatures are characterised by the longer  $T_2$  indicating

that gel pore sizes may be bigger. The  $T_2$  of water within C-S-H interlayer spaces stays almost the same at all temperatures after 3 days of hydration.

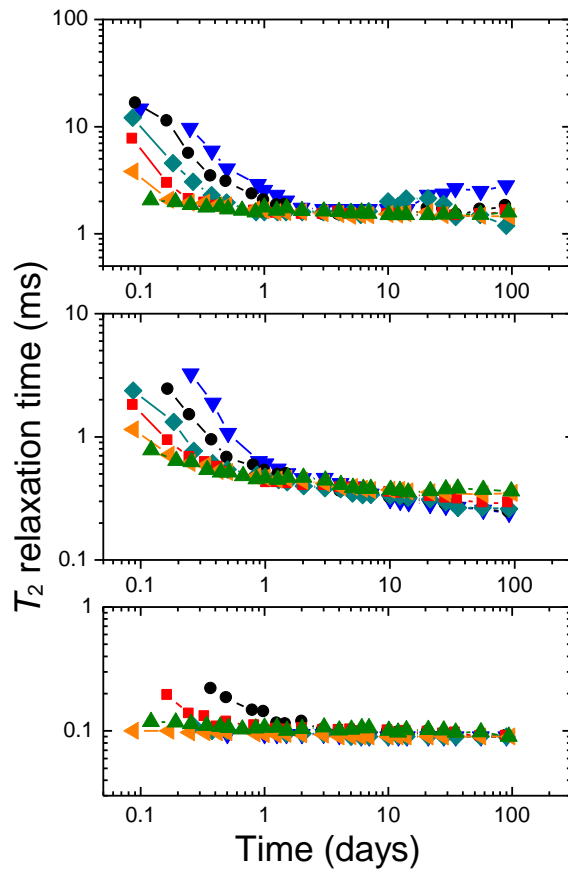


Figure 6.13 The evolution of  $T_2$  relaxation time for water populations of white cement pastes mixed at  $w/c_{mix}$  ratio 0.4 and cured underwater at different temperature. The upper graph shows the  $T_2$  of ‘free’ water, the middle graph -  $T_2$  of C-S-H gel pore water and the lower graph -  $T_2$  of C-S-H interlayer space water. Blue inverted triangles: 10°C; black circles: 20°C; cyan diamonds: 30°C; red squares: 40°C; orange left-triangles: 50°C; and green triangles: 60°C. Lines are guides for eyes.

#### 6.4. DENSITY AND COMPOSITION VS TEMPERATURE

The C-S-H density and composition for white cement paste cured at various temperatures were calculated based on model described in section 6.1.

##### 6.4.1. Input data

Additional XRD and TGA measurements were performed to obtain the degree of hydration  $\alpha$ , (table 6.5) and water content within CH (section 6.3.3 table 6.4) of samples at 28 and 90 days of hydration. The mass of samples was recorded to enable calculation of  $(w/c)_{paste}$  (table 6.5) which served to calculate the signal due to water filling chemical shrinkage voids.

Table 6.5. Water uptake and degree of hydration for white cement pastes mixed at  $w/c_{mix}$  ratio 0.4 and cured underwater at different temperature.

<b>Temp [°C]</b>	<b>Age [days]</b>	<b>(w/c)<sub>paste</sub> [g/g<sub>anh</sub>] (<math>\pm 0.002</math>)</b>	<b><math>\alpha</math> (<math>\pm 0.02</math>)<sup>§</sup></b>
10	28	0.433	0.81
	90	0.439	0.87
20	28	0.439	0.85
	90	0.443	0.90 <sup>♦</sup>
30	28	0.439	0.86
	90	0.442	0.93
40	28	0.441	0.88 <sup>♦</sup>
	90	0.442	0.94 <sup>♦</sup>
50	28	0.435	0.90
	90	0.438	0.94
60	28	0.429	0.92 <sup>♦</sup>
	90	0.432	0.95 <sup>♦</sup>

§ - measured at EPFL by Arnaud Muller

♦ - estimated by linear fitting of data at different temperatures

The intensities of water population used in calculation are presented in table 6.6.

Table 6.6 The intensities used to calculate C-S-H density and composition at 28 and 90 days of hydration. The error in intensities is around  $\pm 0.010$ .

<b>Temp [°C]</b>	<b>Age [days]</b>	<b><math>I_{sol}</math></b>	<b><math>I_{CH}</math></b>	<b><math>I_{Et}</math><sup>‡</sup></b>	<b><math>I_{CSH}</math></b>	<b><math>I_{gel}</math></b>	<b><math>I_{cap}</math></b>	<b><math>I_{void}</math></b>	<b><math>I_{tot}</math></b>
10	28	0.280	0.159	0.121	0.256	0.504	-0.040	0.082	1.082
	90	0.293	0.181	0.122	0.263	0.508	-0.064	0.098	1.098
20	28	0.276	0.164	0.112	0.252	0.512	-0.040	0.097	1.097
	90	0.297	0.189	0.108	0.252	0.525	-0.074	0.109	1.109
30	28	0.262	0.162	0.100	0.253	0.506	-0.021	0.097	1.097
	90	0.279	0.189	0.090	0.250	0.503	-0.033	0.104	1.104
40	28	0.276	0.166	0.110	0.243	0.487	-0.005	0.103	1.103
	90	0.281	0.188	0.093	0.249	0.498	-0.028	0.106	1.106
50	28	0.248	0.167	0.080	0.227	0.482	0.044	0.087	0.087
	90	0.259	0.187	0.072	0.232	0.498	0.011	0.095	1.095
60	28	0.254	0.169	0.085	0.219	0.451	0.075	0.074	1.074
	90	0.258	0.188	0.070	0.211	0.477	0.055	0.080	1.080

<sup>‡</sup>  $I_{Et} = I_{sol} - I_{CH}$

### 6.4.2. Density of C-S-H at various temperature

The data presented in section 6.4.1. allows calculation of the C-S-H density according to equations (6.1, 6.2, 6.7). Figure 6.14 shows the C-S-H ‘solid’ density, excluding gel water, and C-S-H ‘bulk’ density, including gel water, for white cement paste cured at different temperatures. Presented error represents the average standard deviation value. The sensitivity of the resultant C-S-H densities on input parameters is described in more details in section 6.4.5.

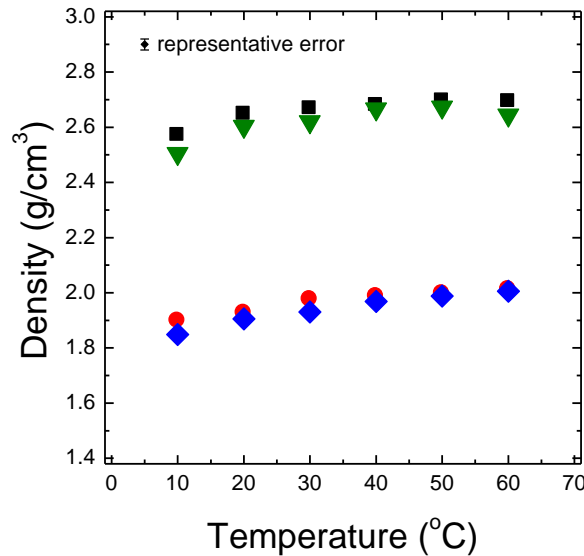


Figure 6.14 C–S–H density as a function of the curing temperature for 28 days (triangles and diamonds) and 90 days old (squares and circles) white cement pastes mixed at  $w/c_{mix}$  ratio 0.4 and cured underwater. The blue diamonds and red circles represent the C–S–H bulk density, inclusive of the gel water; green triangles and black squares represent the C–S–H ‘solid’ density, exclusive of the gel pore water.

The C-S-H ‘solid’ density increases with increase of temperature. One explanation could be that the interlayer space filled by water is smaller at higher temperature. That this is unlikely is shown as the  $T_2$  relaxation time of interlayer water does not vary with increase of curing temperature. However, its intensity is lower. Hence, the increase of density may arise from an arrangement of calcium silicate ( $l$ ) and water ( $l-1$ ) layers. The increase may be explained by the higher ratio of  $l/(l-1)$  at the elevated temperature (figure 6.15) as the calcium silicate layer is more dense than water.

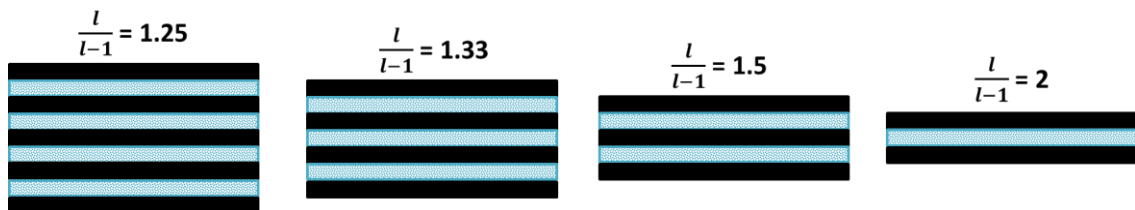


Figure 6.15 An arrangement of calcium silicate layers ( $l$ ) –black strips, and water ( $l-1$ ) layers – blue dotted strips, presenting the increase of the  $l/(l-1)$  ratio.

The C-S-H ‘bulk’ density also increases with temperature. The reason for that is twofold. On one hand, the higher ‘solid’ density contributes greatly to the rise of ‘bulk’ density. The density grows further as there is less gel pore water at higher temperatures. The rise of ‘bulk’ density between 10 and 60°C is equal to 0.16 and 0.11 g/cm<sup>3</sup> at 28 and 90 days of hydration respectively. The increase in bulk density with temperature was reported in recent study by Galluci *et al* [109] for sealed cement paste hydrated for 90 days. The calculation was based on SEM and XRD measurements. Nevertheless, the difference in obtained densities at 5 and 60°C (0.34 g/cm<sup>3</sup>) is higher than calculated in this thesis.

### 6.4.3. Composition of C-S-H at various temperature

The water content within C-S-H excluding,  $x$ , and including,  $x'$ , gel pore water is presented in figure 6.16. Presented error represents the standard deviation value. The sensitivity of the resultant C-S-H water content on input parameters is further described in in section 6.4.5.

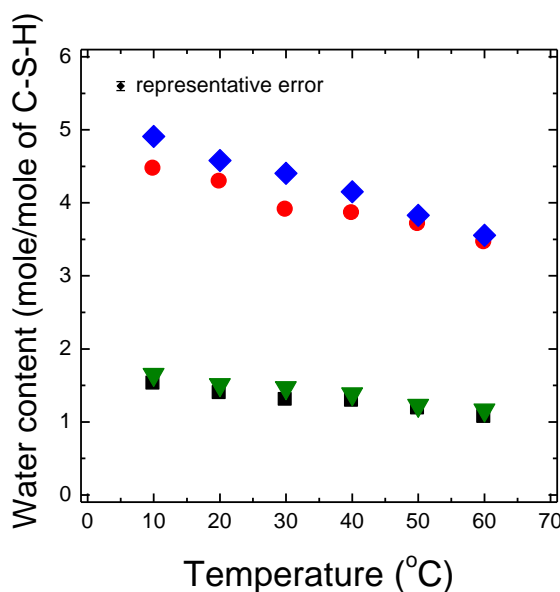


Figure 6.16 Water content in the C-S-H as a function of the curing temperature for 28 days (triangles and diamonds) and 90 days old (squares and circles) white cement pastes mixed at  $w/c_{mix}$  ratio 0.4 and cured underwater. The blue diamonds and red circles represent the water in the C-S-H, including the gel water ( $x'$ ); green triangles and black squares represent water in the C-S-H excluding the gel pore water ( $x$ ).

The  $x$  and  $x'$  follow the inverse trend of the density curves. The ‘solid’ water content declines with temperature indicating that the stack of C-S-H contains fewer layers and therefore fractionally less interlayers filled with water compared to these layers,  $(l-1)/l$ . The water content with gel water included also decreases with temperature. Again, it is the joint effect of reduction in number of locally aggregated C-S-H layers and gel water content. The decrease in the H<sub>2</sub>O content of C-S-H was reported by Gallucci *et al* [109]. Based on TGA and XRD measurements authors defined the H<sub>2</sub>O/SiO<sub>2</sub> ratio of sealed cement pastes hydrated for 90 days to decrease from 3.3 at 5°C to 2.3 at 60°C. The difference in the C-S-H water content between pastes cured at the lowest and highest temperature applied reported by Galluci *et al* and obtained in this study is the same and equalled to 1.0. Nevertheless the

comparison of absolute values is not possible as Galluci *et al* defined the water content as for filled interlayer spaces with the water layer remaining on the gel pore surface included.

The  $\text{Ca}/(\text{Si}+\text{Al})$  ratio,  $z$ , remains fairly constant with increasing temperature (figure 6.17 left). Its average value at 28 days of hydration is  $1.78 \pm 0.01$  and at 90 days it is lower with  $1.67 \pm 0.01$ . The Si content,  $y$ , remains fairly constant over whole temperature range as well as at 28 and 90 days of hydration (figure 6.17 right). The average  $y$  value is equal to  $0.97 \pm 0.01$ . The  $\text{Ca}/(\text{Si} + \text{Al})$  ratio of the sealed cement paste with  $w/c$  ratio 0.4 was reported by Gallucci *et al* [109]. Based on SEM-EDS analysis it remains the same in temperature range 5 to 60°C at around 1.8. Lothenbach *et al* [117] used the same method to estimate the ratio for sealed Portland-limestone cement paste. The ratio was found to not differ significantly (1.62 to 1.72) with increase of temperature (5 to 40°C); it remains fairly constant in the range of experimental errors.

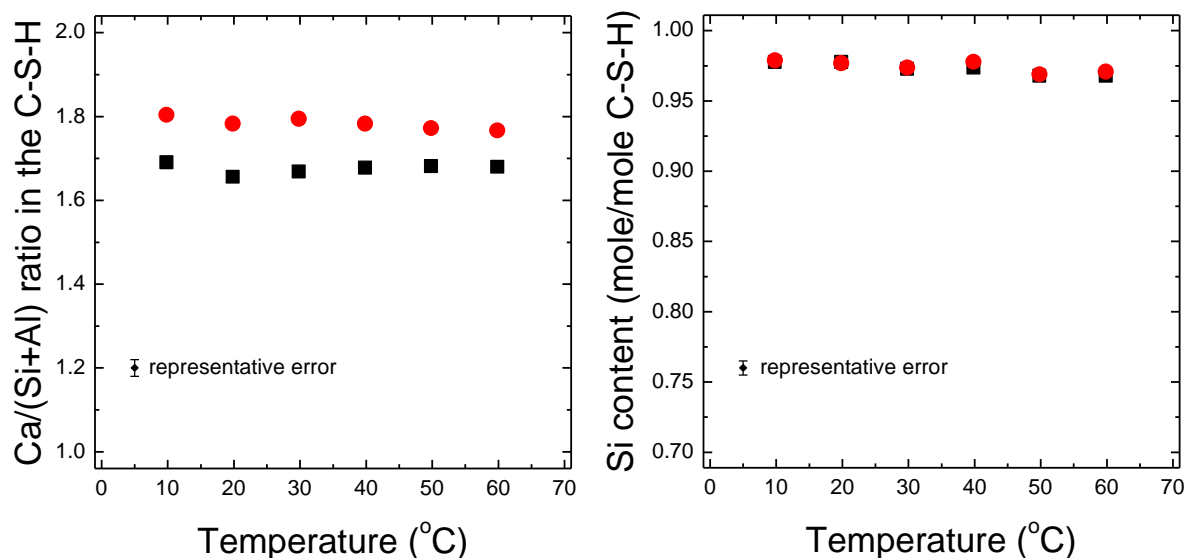


Figure 6.17  $\text{Ca}/(\text{Si}+\text{Al})$  ratio (left) and Si content (right) in the C–S–H as a function of the curing temperature for 28 days (red circle) and 90 days old (black squares) white cement pastes mixed at  $w/c_{mix}$  ratio 0.4 and cured underwater.

#### 6.4.4. Mass and volume composition of cement paste at various temperature

The phase composition diagrams for both mass and volume at various curing temperature are presented in figure 6.18 for 28 and 90 days of hydration. The diagrams show that pastes cured at higher temperature are more reacted. The constant amount of CH and decrease in ettringite content with temperature are observed. It is noticed that the mass and volume of C-S-H is greater at the elevated temperature, while the gel water content is slightly reduced. Pastes exposed to the higher temperature are characterised by larger content of sum ‘free’ and voids water – coarser porosity.

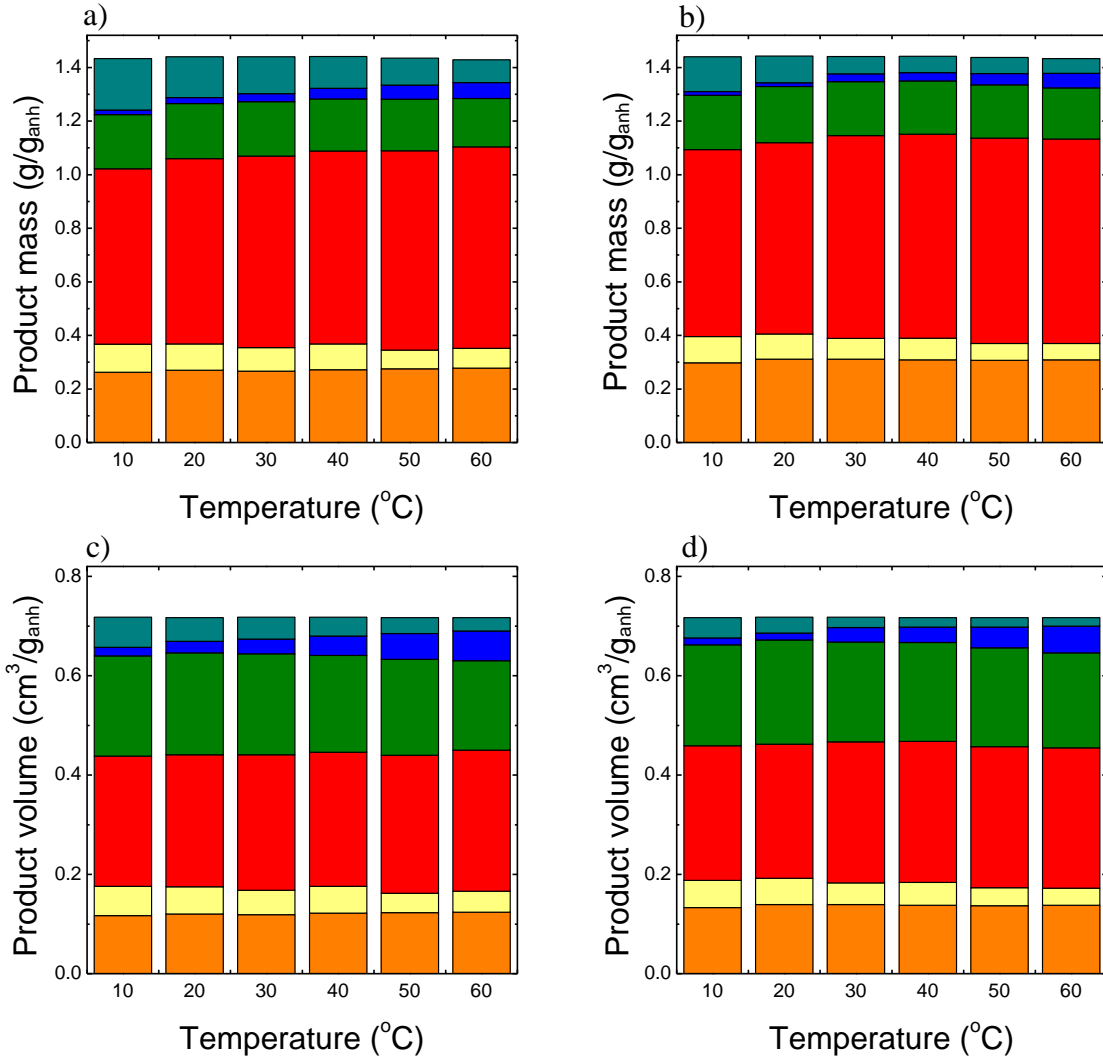


Figure 6.18 Mass and volume composition for 28 days (a and c) and 90 days old (b and d) white cement pastes mixed at  $w/c_{mix}$  ratio 0.4 and cured underwater. From bottom: the orange region corresponds to Portlandite, yellow to ettringite, red to the C-S-H, green to gel pore water, blue to joint 'free' and voids water and dark cyan to unreacted cement.

#### 6.4.5. Sensitivity analysis of C-S-H density and composition model

Investigation of the influence of input parameters on the resultant densities and composition of C-S-H is of high importance to this study.

The statistical analysis of the C-S-H densities and composition uncertainties is tedious and extremely complex. It arises from complex dependency between C-S-H characteristics and the uncertainty of many input parameters including  $\alpha$ ,  $w_{mix}/c$ ,  $(w/c)_{paste}$ ,  $I_{CH}$ ,  $I_{Et}$ ,  $I_{CSH}$ ,  $I_{gel}$ ,  $I_{cap}$ ,  $I_{void}$ ,  $\gamma_{CSH}$ ,  $f_{C3S}$ ,  $f_{C3A}$ ,  $f_{C3A}^{Ett}$ ,  $n_{Hyd}$ . As an example, the uncertainty analysis for the C-S-H 'solid' density is shown through equations (6.9)-(6.12). This includes the expressions for reciprocal of C-S-H 'solid' density, the general and detailed uncertainty of reciprocal and finally uncertainty of C-S-H 'solid' density, respectively.

$$\frac{1}{\rho_{CSH}} = \frac{1}{\rho_w \cdot \gamma_{CSH} \cdot I_{CSH}} + \frac{\alpha}{\frac{w_{mix}}{c} \cdot \rho_c \cdot \gamma_{CSH} \cdot I_{CSH}} - \frac{\beta_{CH} \cdot I_{CH}}{\rho_{CH} \cdot \gamma_{CSH} \cdot I_{CSH}} - \frac{\beta_{Ett} \cdot I_{Ett}}{\rho_{Ett} \cdot \gamma_{CSH} \cdot I_{CSH}} - \frac{\delta_w \cdot (I_{gel} + I_{cap} + I_{void})}{\rho_w \cdot \gamma_{CSH} \cdot I_{CSH}} \quad (6.9)$$

$$u\left(\frac{1}{\rho_{CSH}}\right) = \sqrt{\sum_v \left[ \frac{d(1/\rho_{CSH})}{dv} \cdot u(v) \right]^2} \quad (6.10)$$

where  $u$  is uncertainty and  $v$  is variable.

For density calculation  $v$  includes:  $\alpha$ ,  $w_{mix}/c$ ,  $I_{gel}$ ,  $I_{cap}$ ,  $I_{void}$ ,  $I_{CH}$ ,  $I_{Ett}$ ,  $I_{CSH}$  and  $\gamma_{CSH}$  leading to:

$$\begin{aligned} u\left(\frac{1}{\rho_{CSH}}\right) = & \left\{ \left[ \frac{1}{\frac{w_{mix}}{c} \cdot \rho_c \cdot \gamma_{CSH} \cdot I_{CSH}} \cdot u(\alpha) \right]^2 \right. \\ & + \left[ \frac{-\alpha}{\left(\frac{w_{mix}}{c}\right)^2 \cdot \rho_c \cdot \gamma_{CSH} \cdot I_{CSH}} \cdot u\left(\frac{w_{mix}}{c}\right) \right]^2 + \left[ \frac{-\delta_w}{\rho_w \cdot \gamma_{CSH} \cdot I_{CSH}} \cdot u(I_{gel}) \right]^2 \\ & + \left[ \frac{-\delta_w}{\rho_w \cdot \gamma_{CSH} \cdot I_{CSH}} \cdot u(I_{cap}) \right]^2 + \left[ \frac{-\delta_w}{\rho_w \cdot \gamma_{CSH} \cdot I_{CSH}} \cdot u(I_{void}) \right]^2 \\ & + \left[ \frac{-\beta_{CH}}{\rho_{CH} \cdot \gamma_{CSH} \cdot I_{CSH}} \cdot u(I_{CH}) \right]^2 + \left[ \frac{-\beta_{Ett}}{\rho_{Ett} \cdot \gamma_{CSH} \cdot I_{CSH}} \cdot u(I_{Ett}) \right]^2 \\ & + \left[ \left( \frac{-1}{\rho_w \cdot \gamma_{CSH} \cdot (I_{CSH})^2} + \frac{-\alpha}{\frac{w_{mix}}{c} \cdot \rho_c \cdot \gamma_{CSH} \cdot (I_{CSH})^2} + \frac{\beta_{CH} \cdot I_{CH}}{\rho_{CH} \cdot \gamma_{CSH} \cdot (I_{CSH})^2} \right. \right. \\ & \quad \left. \left. + \frac{\beta_{Ett} \cdot I_{Ett}}{\rho_{Ett} \cdot \gamma_{CSH} \cdot (I_{CSH})^2} + \frac{\delta_w \cdot (I_{gel} + I_{cap} + I_{void})}{\rho_w \cdot \gamma_{CSH} \cdot (I_{CSH})^2} \right) \cdot u(I_{CSH}) \right]^2 \\ & + \left[ \left( \frac{-1}{\rho_w \cdot (\gamma_{CSH})^2 \cdot I_{CSH}} + \frac{-\alpha}{\frac{w_{mix}}{c} \cdot \rho_c \cdot (\gamma_{CSH})^2 \cdot I_{CSH}} + \frac{\beta_{CH} \cdot I_{CH}}{\rho_{CH} \cdot (\gamma_{CSH})^2 \cdot I_{CSH}} \right. \right. \\ & \quad \left. \left. + \frac{\beta_{Ett} \cdot I_{Ett}}{\rho_{Ett} \cdot (\gamma_{CSH})^2 \cdot I_{CSH}} + \frac{\delta_w \cdot (I_{gel} + I_{cap} + I_{void})}{\rho_w \cdot (\gamma_{CSH})^2 \cdot I_{CSH}} \right) \cdot u(\gamma_{CSH}) \right]^2 \left. \right\}^{1/2} \quad (6.11) \end{aligned}$$

$$u(\rho_{CSH}) = \sqrt{\left[ -\rho_{CSH}^2 \cdot u\left(\frac{1}{\rho_{CSH}}\right) \right]^2} \quad (6.12)$$

However, analysis pre-supposed that the uncertainties in all the variables are independent. This is not the case because  $\sum I=1$ . Expressions for uncertainties in other derived parameters are even more complex.

Due to that complexity of statistical analysis the sensitivity of the calculated C-S-H characteristics is presented by the percentage changes caused by the changes of the input

parameters. Table 6.7 demonstrates the percentage changes of C-S-H ‘solid’ and ‘bulk’ densities ( $\rho_{CSH}$ ,  $\rho_{CSH'}$ ) as well as water ( $x$ ,  $x'$ ), calcium ( $z$ ) and silicon ( $y$ ) contents for C-S-H. The 5% increase of degree of hydration, water to cement ratio of paste, content of CH (with dropping content of ettringite), solid intensity (with simultaneous decrease of mobile intensity) and C-S-H interlayer water intensity (with decrease of gel water intensity) is implemented in a sensitivity analysis now presented.

Through analysis it was portrait that the C-S-H ‘solid’ and ‘bulk’ densities depend to the highest degree on the water to cement ratio of the paste which causes about 7% and 3% increase respectively. It arises as in the calculation model the measured fractional intensities are renormalised to the water content at the mixing time. Hence by misjudging the  $w/c_{paste}$  by +5% the intensity of ettringite, C-S-H interlayer and gel pore water populations would rise, capillary water intensity would decrease and CH intensity would not change as it is based on TGA and XRD measurements. The change of  $w/c_{paste}$  also causes the 56% increase of the voids intensity,  $I_{void}$ . Separately considered, a 5% imprecision in the voids intensity, and hence chemical shrinkage volume, affects  $\rho_{CSH}$  and  $\rho_{CSH'}$  by 0.7 and 0.4% respectively, and does not influence on any composition parameter. The calculated densities also depend on the accuracy of degree of hydration, 5% overvaluing causes 1 and 2% increase in  $\rho_{CSH}$  and  $\rho_{CSH'}$ .

The water contents rely on the precision of  $\alpha$  and  $w/c_{paste}$  measurements causing 6% decrease for former and 6% increase for later input. Additionally, the ‘solid’ water content would change by 5% if the interlayer water intensity,  $I_{sh}$ , had 5% inconsistency. The calcium content,  $z$ , is dependent essentially on the content of crystalline phases - CH and ettringite. The inaccuracy in the solid intensity has the least impact on the calculated C-S-H densities and composition.

Table 6.8 presents percentage changes in C-S-H densities and composition parameters caused by simultaneous changes of two input parameters. It is shown that the joint change of the degree of hydration  $\alpha$  and  $w/c_{paste}$  causes the highest change amongst all presented combination of parameters. When  $w/c_{paste}$  is increased by 5% and  $\alpha$  is decreased by 5% the C-S-H ‘solid’ and ‘bulk’ water contents increase by over 14%. The contents are also altered to high extend (by 11-12% and 6% respectively) by simultaneous increase of  $w/c_{paste}$  and  $I_{sh}$  as well as by decrease of  $\alpha$  and increase of  $I_{sh}$ . The ‘solid’ and ‘bulk’ C-S-H densities are affected by 5-9% and 1-5%, respectively, by all combination of the  $w/c_{paste}$  parameter. The overestimation of  $w/c_{paste}$  and underestimation of  $I_{sh}$  has the highest influence (~9%) amongst them on ‘solid’ C-S-H density. The calcium content,  $z$ , would rise by 3-4% if the  $\alpha$  and  $m_{CH}$  are misjudge in opposite manner. The silicon content,  $y$ , stays almost unchanged; changes are less than 1%, despite the dynamic nature of all input parameters.

Table 6.7 Sensitivity analysis of C-S-H density and composition calculation based on 28 days old paste cured at 20°C with initial parameters  $\rho_{CSH} = 2.60 \text{ g/cm}^3$ ,  $\rho_{CSH'} = 1.91 \text{ g/cm}^3$ ,  $x = 1.51$ ,  $x' = 4.58$ ,  $z = 1.78$  and  $y = 0.98$ . The parameters were changed by +5% ( $\uparrow$ ) or -5% ( $\downarrow$ ). Presented are the percentage changes in densities and elements contents. ('c' means that this is the parameter which compensates the 5% change of the given parameter so that  $I_{sol} + I_{CSH} + I_{gel} + I_{cap} = 1$  or  $I_{Et} = I_{sol} - I_{CH}$ ).

<i>Parameters Changed by 5%</i>	$\rho_{CSH}$	$\rho_{CSH'}$	$x$	$x'$	$y$	$z$
$\alpha \uparrow$	1.0 $\uparrow$	1.8 $\uparrow$	-6.3 $\downarrow$	-6.3 $\downarrow$	0.2 $\uparrow$	0.6 $\uparrow$
$w/c_{paste} \uparrow$	7.1 $\uparrow$	2.7 $\uparrow$	6.3 $\uparrow$	6.3 $\uparrow$	0.5 $\uparrow$	0.1 $\uparrow$
$m_{CH} \uparrow$ $m_{Et} \text{ c}$	-0.2 $\downarrow$	-0.3 $\downarrow$	-0.7 $\downarrow$	-0.7 $\downarrow$	-0.3 $\downarrow$	-2.8 $\downarrow$
$I_{sol} \uparrow$ $I_{mob} \downarrow$	-0.1 $\downarrow$	0.1 $\uparrow$	-0.5 $\downarrow$	-0.5 $\downarrow$	0.5 $\uparrow$	0.1 $\uparrow$
$I_{sh} \uparrow$ $I_{gel} \text{ c}$	-1.1 $\downarrow$	0.0	5.0 $\uparrow$	0.0	0.0	0.0

Table 6.8 Extension of the sensitivity analysis of C-S-H density and composition presented in table 6.7. Presented are the percentage changes in densities and elements contents caused by simultaneous changes of two input parameters.

<i>Changed Parameters</i>	$\rho_{CSH}$		$\rho_{CSH'}$		$x$		$x'$		$y$		$z$	
	$\alpha$		$\alpha$		$\alpha$		$\alpha$		$\alpha$		$\alpha$	
	$\uparrow$	$\downarrow$	$\uparrow$	$\downarrow$	$\uparrow$	$\downarrow$	$\uparrow$	$\downarrow$	$\uparrow$	$\downarrow$	$\uparrow$	$\downarrow$
$w/c_{paste} \uparrow$	7.8 $\uparrow$	6.3 $\uparrow$	4.5 $\uparrow$	0.8 $\uparrow$	-0.5 $\downarrow$	14.1 $\uparrow$	-0.5 $\downarrow$	14.1 $\uparrow$	0.6 $\uparrow$	0.4 $\uparrow$	0.8 $\uparrow$	-0.6 $\downarrow$
$w/c_{paste} \downarrow$	-5.0 $\downarrow$	-7.6 $\downarrow$	-0.8 $\downarrow$	-4.6 $\downarrow$	-12.0 $\downarrow$	0.7 $\uparrow$	-12.0 $\downarrow$	0.6 $\uparrow$	-0.3 $\downarrow$	-0.7 $\downarrow$	0.5 $\uparrow$	-0.8 $\downarrow$
$m_{CH} \uparrow$ $m_{Et} \text{ c}$	0.9 $\uparrow$	-1.3 $\downarrow$	1.6 $\uparrow$	-2.2 $\downarrow$	-7.0 $\downarrow$	6.4 $\uparrow$	-7.0 $\downarrow$	6.4 $\uparrow$	-0.1 $\downarrow$	-0.5 $\downarrow$	-2.0 $\downarrow$	-3.7 $\downarrow$
$m_{CH} \downarrow$ $m_{Et} \text{ c}$	1.2 $\uparrow$	-0.9 $\downarrow$	2.1 $\uparrow$	-1.6 $\downarrow$	-5.7 $\downarrow$	8.1 $\uparrow$	-5.7 $\downarrow$	8.1 $\uparrow$	0.4 $\uparrow$	0.1 $\uparrow$	3.3 $\uparrow$	2.4 $\uparrow$
$I_{sol} \uparrow$ $I_{mob} \downarrow$	1.0 $\uparrow$	-1.2 $\downarrow$	1.9 $\uparrow$	-1.9 $\downarrow$	-6.8 $\downarrow$	6.8 $\uparrow$	-6.8 $\downarrow$	6.8 $\uparrow$	0.6 $\uparrow$	0.4 $\uparrow$	0.8 $\uparrow$	-0.6 $\downarrow$
$I_{sol} \downarrow$ $I_{mob} \uparrow$	1.1 $\uparrow$	-1.0 $\downarrow$	1.7 $\uparrow$	-2.0 $\downarrow$	-5.8 $\downarrow$	7.7 $\uparrow$	-5.8 $\downarrow$	7.7 $\uparrow$	-0.3 $\downarrow$	-0.7 $\downarrow$	0.5 $\uparrow$	-0.8 $\downarrow$
$I_{sh} \uparrow$ $I_{gel} \text{ c}$	-0.1 $\downarrow$	-2.3 $\downarrow$	1.8 $\uparrow$	-1.9 $\downarrow$	-1.6 $\downarrow$	12.6 $\uparrow$	-6.3 $\downarrow$	7.3 $\uparrow$	0.2 $\uparrow$	-0.2 $\downarrow$	0.6 $\uparrow$	-0.7 $\downarrow$
$I_{sh} \downarrow$ $I_{gel} \text{ c}$	2.2 $\uparrow$	0.1 $\uparrow$	1.8 $\uparrow$	-1.9 $\downarrow$	-11.0 $\downarrow$	1.9 $\uparrow$	-6.3 $\downarrow$	7.3 $\uparrow$	0.2 $\uparrow$	-0.2 $\downarrow$	0.6 $\uparrow$	-0.7 $\downarrow$

	$\rho_{CSH}$		$\rho_{CSH}'$		$x$		$x'$		$y$		$z$	
<b>Changed Parameters</b>	$w/c_{paste}$		$w/c_{paste}$		$w/c_{paste}$		$w/c_{paste}$		$w/c_{paste}$		$w/c_{paste}$	
	↑	↓	↑	↓	↑	↓	↑	↓	↑	↓	↑	↓
$m_{CH} \uparrow m_{Et} \downarrow$	7.0 ↑	-6.4 ↓	2.4 ↑	-2.9 ↓	5.5 ↑	-6.8 ↓	5.5 ↑	-6.8 ↓	0.2 ↑	-0.8 ↓	-2.7 ↓	-2.9 ↓
$m_{CH} \downarrow m_{Et} \uparrow$	7.2 ↑	-6.0 ↓	3.0 ↑	-2.3 ↓	7.0 ↑	-5.5 ↓	7.1 ↑	-5.5 ↓	0.8 ↑	-0.2 ↓	3.0 ↑	2.7 ↑
$I_{sol} \uparrow I_{mob} \downarrow$	7.1 ↑	-6.3 ↓	2.8 ↑	-2.6 ↓	5.9 ↑	-6.7 ↓	5.9 ↑	-6.7 ↓	1.0 ↑	0.0	0.3 ↑	0.0
$I_{sol} \downarrow I_{mob} \uparrow$	7.1 ↑	-6.1 ↓	2.6 ↑	-2.7 ↓	6.7 ↑	-5.6 ↓	6.7 ↑	-5.6 ↓	0.0	-1.0 ↓	0.0	-0.3 ↓
$I_{sh} \uparrow I_{gel} \downarrow$	5.7 ↑	-7.1 ↓	2.7 ↑	-2.6 ↓	11.6 ↑	-1.5 ↓	6.3 ↑	-6.1 ↓	0.5 ↑	-0.5 ↓	0.1 ↑	-0.1 ↓
$I_{sh} \downarrow I_{gel} \uparrow$	8.6 ↑	-5.3 ↓	2.7 ↑	-2.6 ↓	1.0 ↑	-10.8 ↓	6.3 ↑	-6.1 ↓	0.5 ↑	-0.5 ↓	0.1 ↑	-0.1 ↓

	$\rho_{CSH}$		$\rho_{CSH}'$		$x$		$x'$		$y$		$z$	
<b>Changed Parameters</b>	$m_{CH} \uparrow$	$m_{CH} \downarrow$										
	$m_{Et} \downarrow$	$m_{Et} \uparrow$										
$I_{sol} \uparrow I_{mob} \downarrow$	-0.2 ↓	0.1 ↑	-0.2 ↓	0.4 ↑	-1.2 ↓	0.3 ↑	-1.2 ↓	0.3 ↑	0.2 ↑	0.8 ↑	-2.7 ↓	3.0 ↑
$I_{sol} \downarrow I_{mob} \uparrow$	-0.1 ↓	0.2 ↑	-0.4 ↓	0.2 ↑	-0.3 ↓	1.2 ↑	-0.3 ↓	1.2 ↑	-0.8 ↓	-0.2 ↓	-2.9 ↓	2.7 ↑
$I_{sh} \uparrow I_{gel} \downarrow$	-1.3 ↓	-1.0 ↓	-0.3 ↓	0.3 ↑	4.2 ↑	5.8 ↑	-0.7 ↓	0.7 ↑	-0.3 ↓	0.3 ↑	-2.8 ↓	2.9 ↑
$I_{sh} \downarrow I_{gel} \uparrow$	1.0 ↑	1.4 ↑	-0.3 ↓	0.3 ↑	-5.7 ↓	-4.3 ↓	-0.7 ↓	0.7 ↑	-0.3 ↓	0.3 ↑	-2.8 ↓	2.9 ↑

	$\rho_{CSH}$		$\rho_{CSH}'$		$x$		$x'$		$y$		$z$	
<b>Changed Parameters</b>	$I_{sol} \uparrow$	$I_{sol} \downarrow$										
	$I_{mob} \downarrow$	$I_{mob} \uparrow$										
$I_{sh} \uparrow I_{gel} \downarrow$	-1.2 ↓	-1.1 ↓	0.1 ↑	-0.1 ↓	4.5 ↑	5.4 ↑	-0.5 ↓	0.5 ↑	0.5 ↑	-0.5 ↓	0.1 ↑	-0.1 ↓
$I_{sh} \downarrow I_{gel} \uparrow$	1.1 ↑	1.3 ↑	0.1 ↑	-0.1 ↓	-5.5 ↓	-4.6 ↓	-0.5 ↓	0.5 ↑	0.5 ↑	-0.5 ↓	0.1 ↑	-0.1 ↓

## 6.5. EVOLUTION OF WATER POPULATION FOR WHITE CEMENT PASTE WITH 10% OF SILICA FUME

Preparation of cement paste with silica fume involved addition of superplasticizer. The amount of superplasticizer added was 0.1% by weight of the binder. This is equivalent to 0.25% of the mass of water for  $w/b = 0.4$ . This quantity of superplasticizer is sufficiently low so as not to be considered as a separate component in relaxation analysis.

### 6.5.1. Uptake of water during hydration

The water ingress during hydration for cement paste with addition of 10% silica fume (SF) mixed at  $w/b_{mix} = 0.4$  and cured at different temperature is presented in figure 6.19.

The uptake of water starts at earlier hydration time and proceeds more quickly for pastes cured at elevated temperature. However, samples cured at lower temperature catch up and in some cases overtake their higher temperature counterparts and finally uptake more water. In comparison with plain white cement paste, more water is drawn into samples.

Pastes cured at the highest temperature presents a distinguishing behaviour. Their water mass increases significantly during first 4h of hydration and consequently shows water content values higher by about 0.015  $g/g_{anh}$ . The observation is believed to be caused by the observed cracking of the SF samples cured at 60°C.

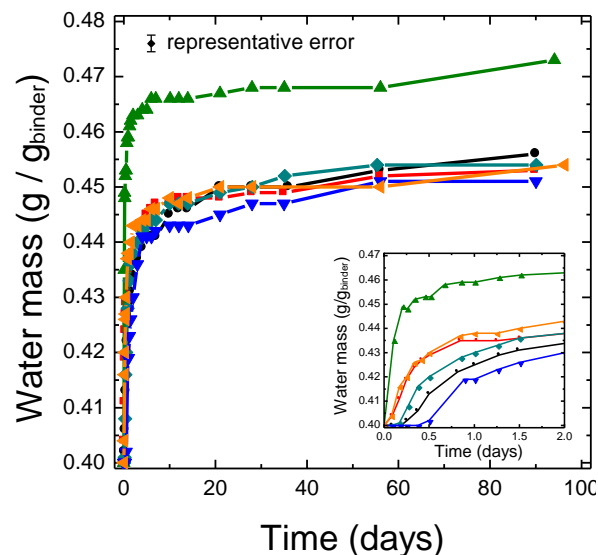


Figure 6.19 Uptake of water mass as a function of hydration time for white cement pastes with addition of 10% silica fume mixed at  $w/b_{mix}$  ratio 0.4 and cured underwater at different temperature: blue inverted triangles: 10°C; black circles: 20°C; cyan diamonds: 30°C; red squares: 40°C; orange left-triangles: 50°C; and green triangles: 60°C.

### 6.5.2. ‘Free’ water evolution

The ‘free’ water<sup>26</sup> signal evolution for pastes with addition of silica fume is presented in figure 6.20.

At early age, ‘free’ water is consumed faster at higher temperature compared to lower temperature. The hydration time at which ‘free’ water is consumed by 50% is about 3, 5, 8 and 13 hours at 60, 40, 30 and 20°C respectively. The characteristic feature is the minimum in the ‘free’ water intensity followed by weak local maximum and subsequent steady decline, more visible for samples cured at higher temperatures. The reason for this behaviour is not clear. One may think that as the samples are cured underwater there is ingress of water which accounts for these behaviours. However, the changes in the total signal intensity shown in an upper plot of figure 6.20 are not adequate to explain free water data. It is noticed that the hydration times at which minima in ‘free’ water signal appear, at different temperatures, coincide with times of maxima in chemically combined water signal presented in the following section. It suggests that the appearance of trough and increase of signal is the consequence of a pozzolanic reaction of CH and SF. It may imply that the product of reaction is the C-S-H with interhydrate spaces in between. The following decline in signal indicates that the ‘free’ water is again consumed in hydration process.

When samples are older, more ‘free’ water remains at higher curing temperature. However, the difference in ‘free’ water content at different temperature is reduced notably with time.

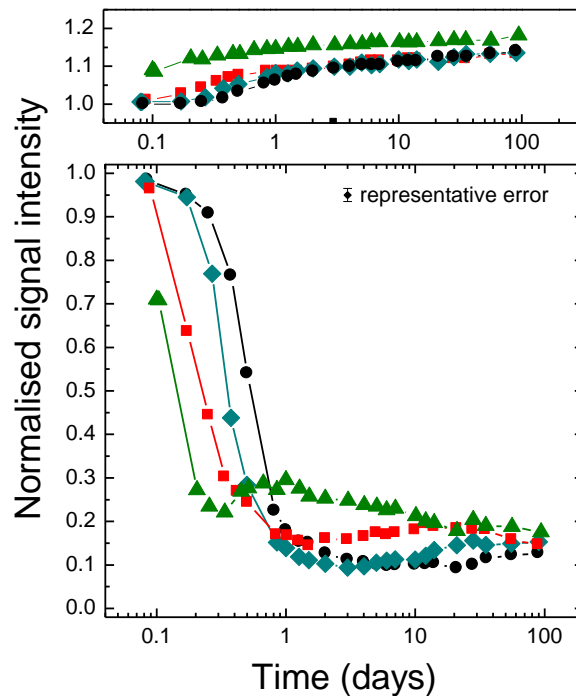


Figure 6.20 Evolution of ‘free’ water as a function of hydration time for white cement pastes with addition of 10% silica fume mixed at  $w/b_{mix}$  ratio 0.4 and cured underwater at different temperature: black circles: 20°C; cyan diamonds: 30°C; red squares: 40°C and green triangles: 60°C. The upper plot shows the evolution of total signal intensity. Lines are guides for eyes.

<sup>26</sup> ‘free’ water is the sum of interhydrate and capillary pore water intensities with the low contribution of latter, about 3-1%, over whole hydration time at all examined curing temperatures

### 6.5.3. Chemically combined water evolution

Figure 6.21 shows the evolution of chemically combined water intensity. At early stage of hydration the crystalline phases are created faster at elevated temperatures. Nonetheless, progressively with time and lower curing temperature solid water fractions are larger than at higher temperatures. It is observed that there is an apparent maximum in the signal fraction, which moves toward shorter hydration times with rise of curing temperature (10°C: ~60 days, 20°C: ~28 days, 30°C: ~5 days, 40°C: ~36 hours, 50°C: ~20 hours, 60°C: ~12 hours). Maxima

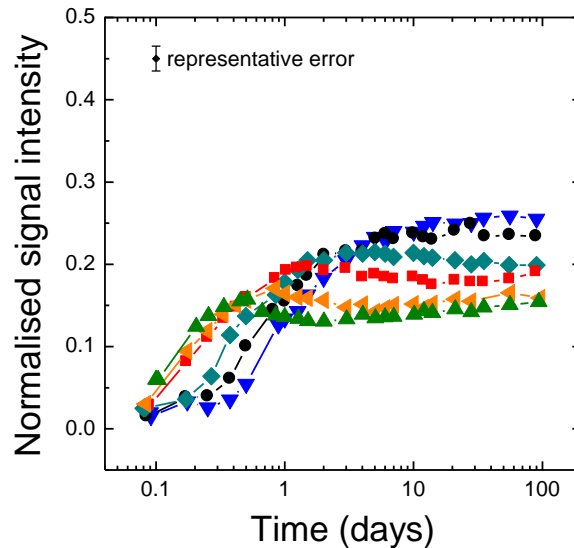


Figure 6.21 Evolution of chemically combined water as a function of hydration time for white cement pastes with addition of 10% silica fume mixed at  $w/b_{mix}$  ratio 0.4 and cured underwater at different temperature: blue inverted triangles: 10°C; black circles: 20°C; cyan diamonds: 30°C; red squares: 40°C; orange left-triangles: 50°C; and green triangles: 60°C. Lines are guides for eyes.

Table 6.9 The mass and water content of CH measured by TGA; the NMR solid signal; ettringite water content calculated as the difference of solid signal and CH water content; and ettringite content based on its water content; at 90 days of hydration for white cement pastes with addition of 10% silica fume mixed at  $w/b_{mix}$  ratio 0.4 and cured underwater at different temperature.

Temp [°C]	$m_{CH}$ [g/g <sub>bin</sub> ] (±0.010)	Water Content <sup>27</sup> at 90days			$m_{Ett}$ [g/g <sub>bin</sub> ]
		TGA CH ( $I_{CH}$ )	NMR solid ( $I_{sol}$ )	$Ett$ ( $I_{sol} - I_{CH}$ )	
10	0.235	0.143	0.255	0.113	0.098
20	0.217	0.132	0.229	0.097	0.084
30	0.201	0.122	0.199	0.076	0.066
40	0.193	0.117	0.180	0.063	0.055
50	0.190	0.116	0.159	0.044	0.038
60	0.184	0.112	0.154	0.042	0.037

<sup>27</sup> 1 - water content at the mixing time,  $w/b_{mix} = 0.4$

coincidence with the minima in free water signal intensity. These maxima and subsequent decline of intensity indicates the consumption of CH in a pozzolanic reaction with silica fume to create C-S-H. For mature paste significantly lower chemically combined water content is observed for paste cured at elevated temperature.

The TG analysis of pastes at 90 days of hydration permit calculation of the water fraction in CH. Based on the analysis results for plain white cement paste, the ettringite water fraction was determined as a difference between NMR solid signal and CH water fraction. The results presented in Table 6.9 shows that with increase of curing temperature the CH and ettringite water fractions and hence the CH and ettringite contents decrease.

#### 6.5.4. C-S-H interlayer and gel water evolution

The evolution of C-S-H interlayer and gel pore water signal for white cement paste prepared with addition of silica fume is presented in figure 6.22.

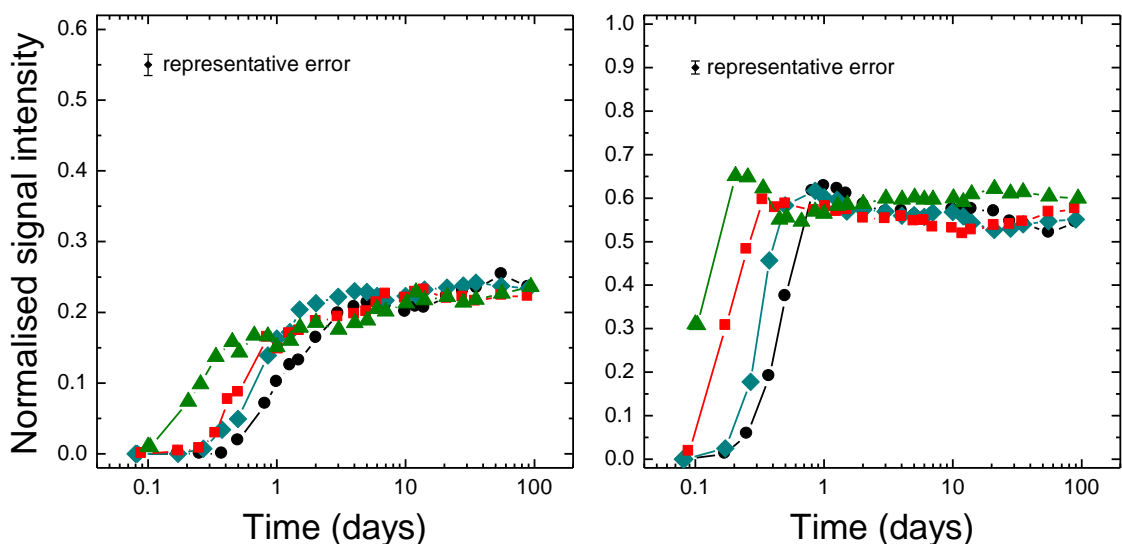


Figure 6.22 Evolution of C-S-H interlayer (left) and gel (right) pore water as a function of hydration time for white cement pastes with addition of 10% silica fume mixed at  $w/b_{mix}$  ratio 0.4 and cured underwater at different temperature: black circles: 20°C; cyan diamonds: 30°C; red squares: 40°C and green triangles: 60°C.

At higher curing temperatures, the acceleration of C-S-H interlayer and gel pore development takes place. For mature pastes, after 10 days of hydration, the interlayer water signal rises steadily and similarly across all temperatures. The gel water signal, at first, grows attaining a maximum value and thereafter declines. This indicates the consumption of gel water. For pastes cured at 60, 40 and 30°C the gel signal increases again beyond 1, 10 and 20 days respectively, at the times when the ‘free’ water signal begin to decrease again. This is a result of a complex process of hydration in presence of silica fume: the C-S-H is created as cement phases hydrate as well as due to CH and SF reaction.

### 6.5.5. $T_2$ relaxation times

Figure 6.23 illustrates how the associated  $T_2$  relaxation times of interlayer, gel and ‘free’ water vary with hydration time at different curing temperatures for white cement pastes with addition of 10% silica fume.

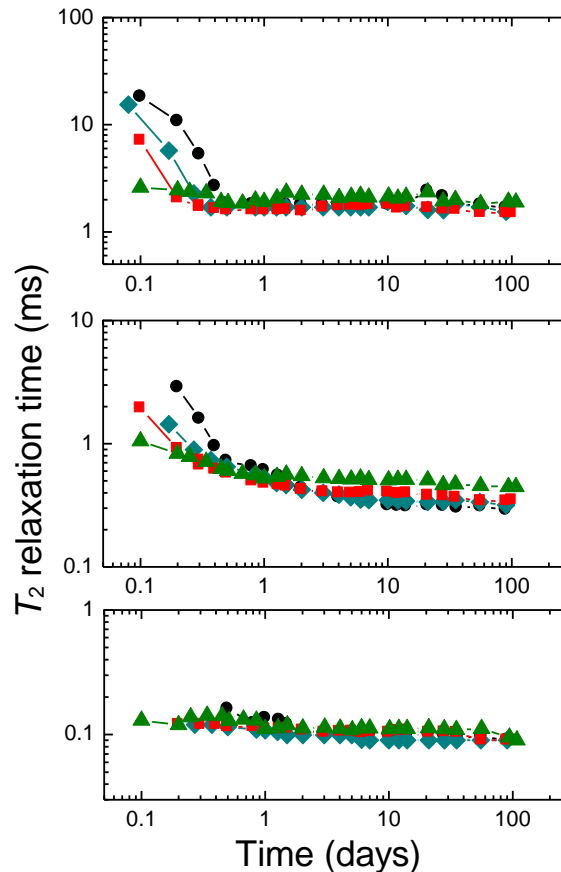


Figure 6.23. The evolution of  $T_2$  relaxation time for water populations of white cement pastes with addition of 10% silica fume mixed at  $w/b_{mix}$  ratio 0.4 and cured underwater at different temperature. The upper graph shows the  $T_2$  of ‘free’ water, the middle graph -  $T_2$  of C-S-H gel pore water and the lower graph -  $T_2$  of C-S-H interlayer space water. Black circles: 20°C; cyan diamonds: 30°C; red squares: 40°C; and green triangles: 60°C. Lines are guides for eyes.

At early hydration time, the  $T_2$  relaxation times of ‘free’ – interhydrate, water decrease faster as curing temperature increases. Beyond about 12 hours the reservoirs are characterised by the same  $T_2$  times suggesting same capillary pore sizes. Initially at higher temperatures, the  $T_2$  of gel pore water also has the smaller values as the hydration process is accelerated. At later ages of pastes, the trend reverses and pastes cured at higher temperatures are characterised by the longer  $T_2$  implying larger gel pore sizes. The  $T_2$  of water within C-S-H interlayer spaces stays almost the same at all temperatures with slight decrease with time.

## 6.6. COMPARISON: WHITE CEMENT PASTE VS WHITE CEMENT PASTE WITH SILICA FUME

### 6.6.1. Evolution of water populations at 20°C

Figure 6.24 compares the evolution of NMR water populations during hydration for plain white cement paste and white cement paste with silica fume (SF) cured underwater at 20°C. The same populations are observed with differences in intensities. The total signal intensity for paste with SF is higher than for plain paste suggesting higher chemical shrinkage.

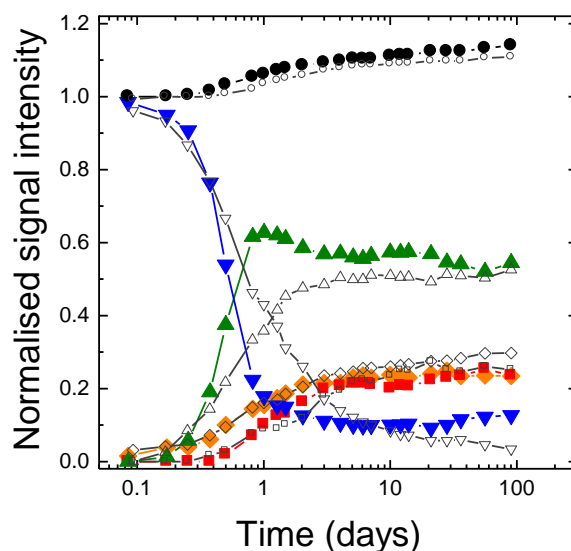


Figure 6.24 The evolution of different water population for white cement paste with 10% addition of silica fume mixed at  $w/b_{mix}$  ratio 0.4 and cured underwater at 20°C. Orange diamonds represent chemically combined water signal, red squares – the C–S–H interlayer pore water, green triangles – the C–S–H gel pore water and blue inverted triangles – the ‘free’ water signals. The black circles show the total water signal normalized to the initial mass of water at the mixing point. Open black symbols are corresponding signals for reference white cement paste cured at 20°C.

Initially, up to 9 hours, the ‘free’ water intensities are very close. Later, the consumption is much faster for paste containing silica fume. At 1 day of hydration there is only 18% of ‘free’ water left in comparison with 43% for plain paste. After 3 days the intensity remains at fairly constant level of 10%, while for plain cement it decreases gradually down to 3% at 90 days. The development of the ‘free’ water signal indicates the ‘finer’ porosity of the SF paste between 0.5 and 7 days in comparison with plain cement paste. Beyond 7 days the situation reverses – plain cement paste shows less capillary porosity.

Addition of silica fume causes more prompt development of gel pores. Throughout the whole experimental time the gel water intensity is higher than for white cement paste. Moreover, it presents different behaviour: the intensity attains a maximum after 20h and beyond that point it gradually decreases. In contrast for plain cement the gel intensity increases up to 4 days and stays relatively constant afterwards without a maximum.

The C–S–H interlayer water signal follows the same trend for both mixes and is only slightly lower in the presence of SF.

The intensities of crystalline phases increase at the same rate in both pastes during the first 2 days. Following that, as a result of silica fume impact, the increase in signal lessens. Hence, the difference in signals for both pastes increases with time with the gap of 7% at 90 days.

The associated  $T_2$  relaxation times for water within C-S-H interlayer spaces, gel and interhydrate pores are presented in figure 6.25. The ‘free’ – interhydrate, water  $T_2$  relaxation times are the same at the beginning of hydration for paste with and without silica fume. They are slightly smaller between 0.3 and 2 days and higher beyond 2 days in presence of SF. However, they reach fairly constant value already after 12 hours in comparison with two days for paste without SF. The  $T_2$  of the gel water is slightly higher after 20 days. The C-S-H interlayer water is characterised by almost the same relaxation times throughout whole hydration process.

The reasons for changes in water intensities and  $T_2$  relaxation times in the presence of SF are twofold. The cement hydration is accelerated as the fine silica fume provides additional nucleation sites for C-S-H. Further modifications of microstructure are caused by the pozzolanic reaction of silica fume and CH that results in creation of C-S-H.

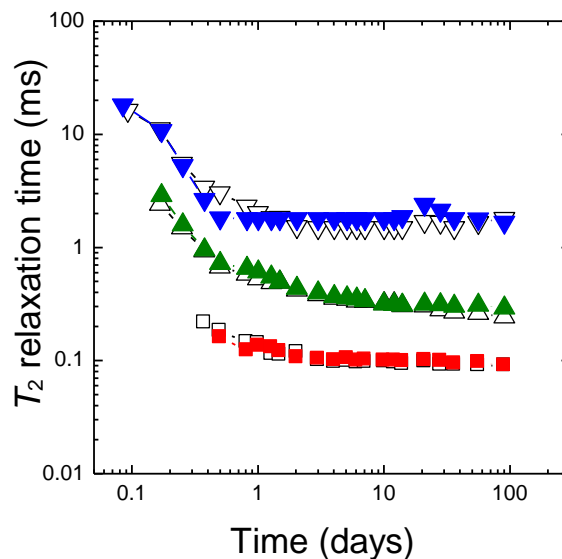


Figure 6.25 The evolution of  $T_2$  relaxation time for white cement paste with 10% addition of silica fume mixed at  $w/b_{mix}$  ratio 0.4 and cured underwater at 20°C. Red squares represent the  $T_2$  of C-S-H interlayer pore water, green triangles – the C-S-H gel pore water and blue inverted triangles – the ‘free’ water. Open black symbols are corresponding times for reference white cement paste cured at 20°C.

### 6.6.2. The comparison for the full range of temperature

The comparison of the NMR results for white cement paste with and without addition of silica fume at different temperatures is presented in figure 6.26.

The significant differences in the amount of chemically combined water are noticeable. At earlier ages, the signal in presence of SF follows the signal for plain white cement. However, after 2 days at 20°C, 36 h at 30°C, 36h at 40°C and 6h at 60°C the lower values are observed. The maximum difference in intensities is about 10%.

The consumption of ‘free’ water is faster for pastes with SF at the beginning of hydration. The inflection point appears at progressively longer times with decrease of temperature: ~10h for 60°C and 7 days for 20°C. Beyond that point there is more ‘free’ water within structure of SF pastes.

It is also shown that pastes contain more gel pore water at the same temperature and time when the silica fume is incorporated. The difference becomes gradually smaller with hydration time. The content of C-S-H interlayer water is influenced by addition of silica fume to the smallest extend. The intensities are just slightly lower by 1-3%.

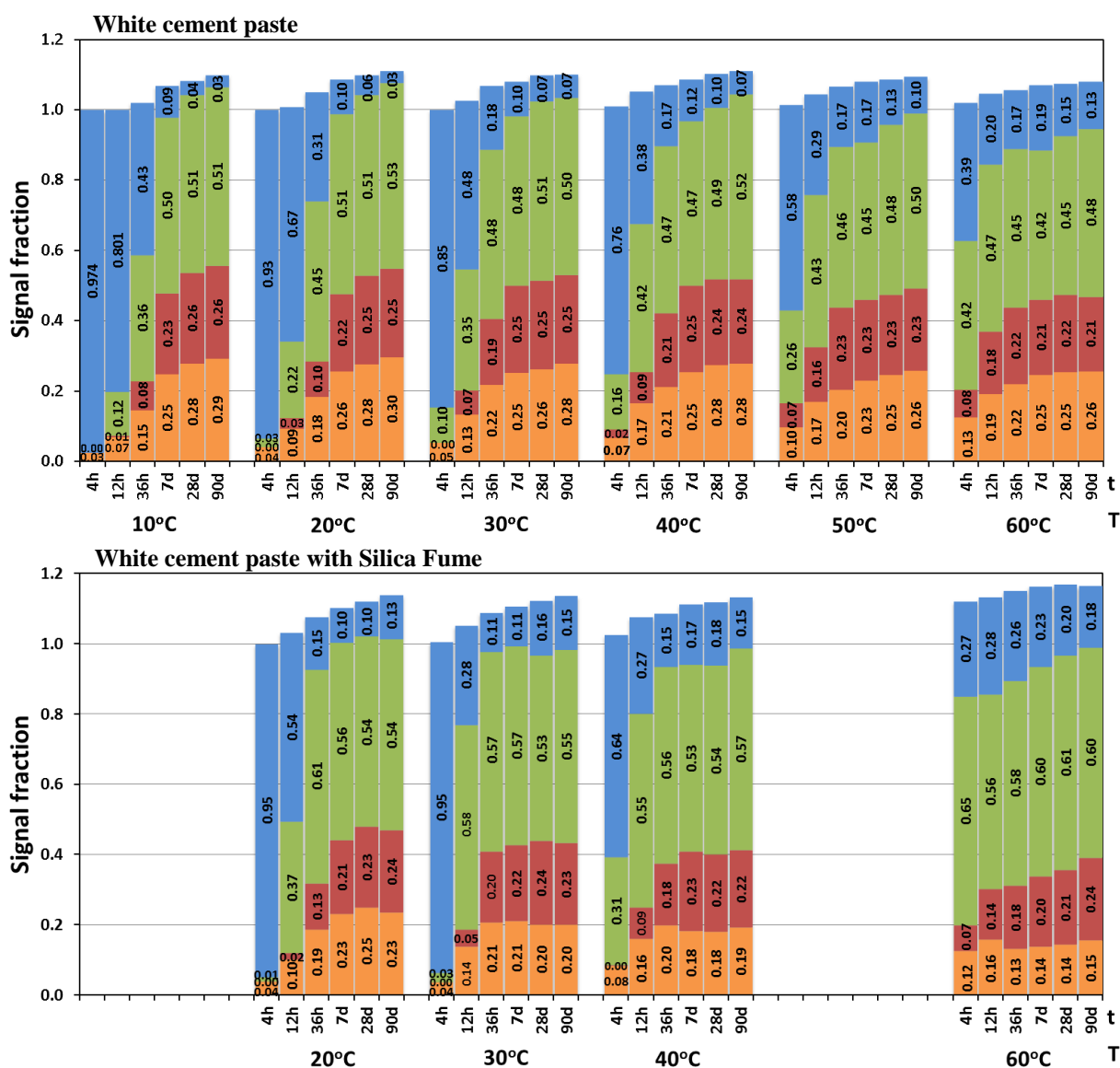


Figure 6.26 The evolution of different water population for white cement paste (top) and white cement paste with silica fume (bottom) over the time of hydration for samples cured underwater at various temperature. Total signal is de-composed into chemically combined water (orange), water in C-S-H interlayer spaces (red), C-S-H gel pores (green) and ‘free’ water (blue). The total signal fractions go above 1 indicating the underwater curing.

## 7. Other experimental insight

### 7.1. ACTIVATION ENERGY OF WATER DYNAMIC

#### 7.1.1. Verification of experiments integrity

##### 7.1.1.1. Water $T_1$ relaxation time as a function of temperature

Inversion recovery measurements of distilled water were performed at different temperature ( $T$ ) to validate the behaviour of the  $T_1$  relaxation time against literature data [125]. Figure 7.1 presents the change in  $T_1$  relaxation time expressed as  $\ln(T_1(T_{ref})/T_1(T))$  to account for different frequencies at which experiments were performed (28 vs 20 MHz). Good agreement is found between data sets.

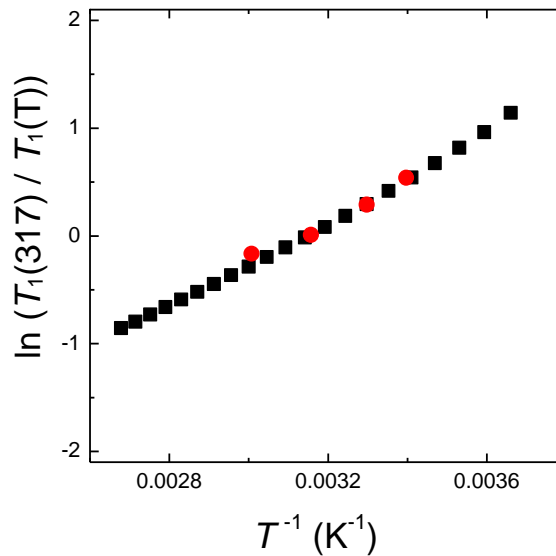


Figure 7.1 The changes in the  $T_1$  relaxation time of water as a function of temperature. Red circles are the author experimental data, black squares are the data reported by Krynicki [125].

##### 7.1.1.2. The total signal intensity as a function of temperature

The activation energy experiments presented in the following section were performed by  $T_1$  recovery. The total signal intensity - ‘net’ magnetization,  $M_o$ , along the  $z$  direction is the measure of the excess of parallel state magnetic moments population. Considering the Boltzmann’s distribution equation (section 3.1) and the fact that energy difference between  $\alpha$  and  $\beta$  spin states,  $\Delta E$ , is much lower than the thermal energy,  $kT$ , the expression for  $M_o$  as a function of temperature is well approximated by [78]:

$$M_o = N \cdot \frac{(\gamma \cdot \hbar)^2 \cdot B_o}{4 \cdot k_B \cdot T} = C \cdot \frac{1}{T} \quad (7.1)$$

where  $N$  is the total number of nuclei in sample,  $B_o$  is magnetic field,  $\gamma$  is the gyromagnetic ratio,  $k_B$  is Boltzmann constant,  $\hbar$  is the Planck constant divided by  $2\pi$  and  $C$  is constant.

Figure 7.2 a and b demonstrate that the measured total signal intensity for mature white cement paste, at 28 and 90 days of hydration, behaves linearly and increases proportionally with increase in  $1/T$  according to equation (7.1). The saturation recovery technique was used to measure those samples. Data sets took two days to record. A further set was recorded at days 7 and 8 using inversion recovery. However, it showed too much systematic variation during measurements due to ongoing hydration to be trusted. These measurements are not included.

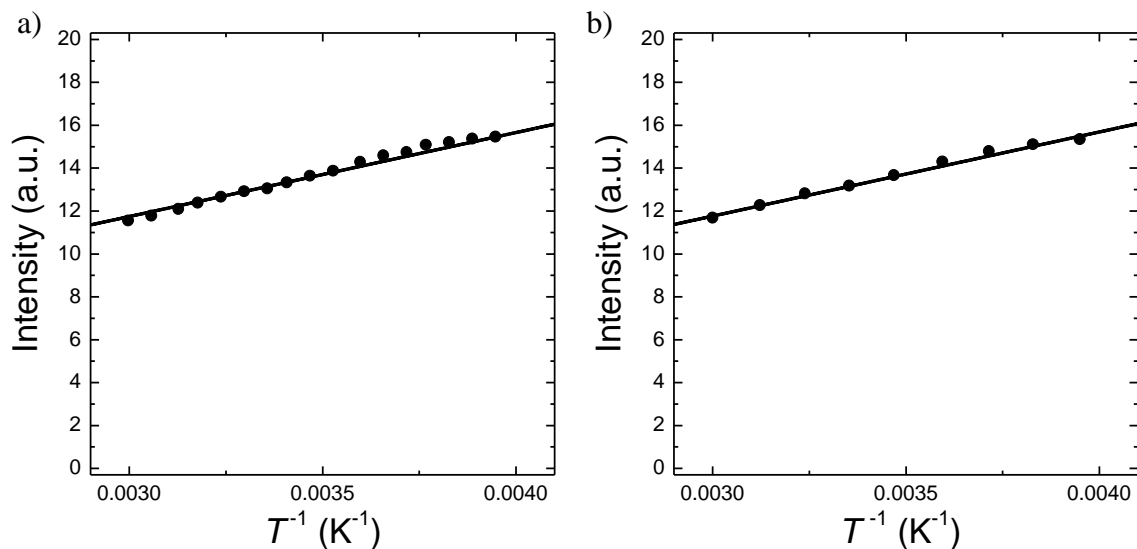


Figure 7.2 Total signal intensity for white cement paste cured underwater ( $w/c_{mix} = 0.4$ ) for 28 (a) and 90 (b) days of hydration as a function of temperature at which measurements were performed.

## 7.1.2. Activation energy

### 7.1.2.1. The analysis of $T_1$ relaxation measurements

The  $T_1$  recovery measurements were performed in the experimental temperature range from  $-20$  to  $+60^\circ\text{C}$ . The data were originally analysed by Inverse Laplace Transform (ILT). However they showed fluctuations in intensities of the C-S-H interlayer and gel pore water due to low signal to noise ratio. Hence, the fractional intensities for particular water populations were averaged and intensities recalculated. Further, multi-exponential analyses with constrained intensities were performed. The  $T_1$  relaxation times obtained in such way served to plot the  $\ln(1/T_1)$  dependence on temperature (figure 7.3) used in further calculations.

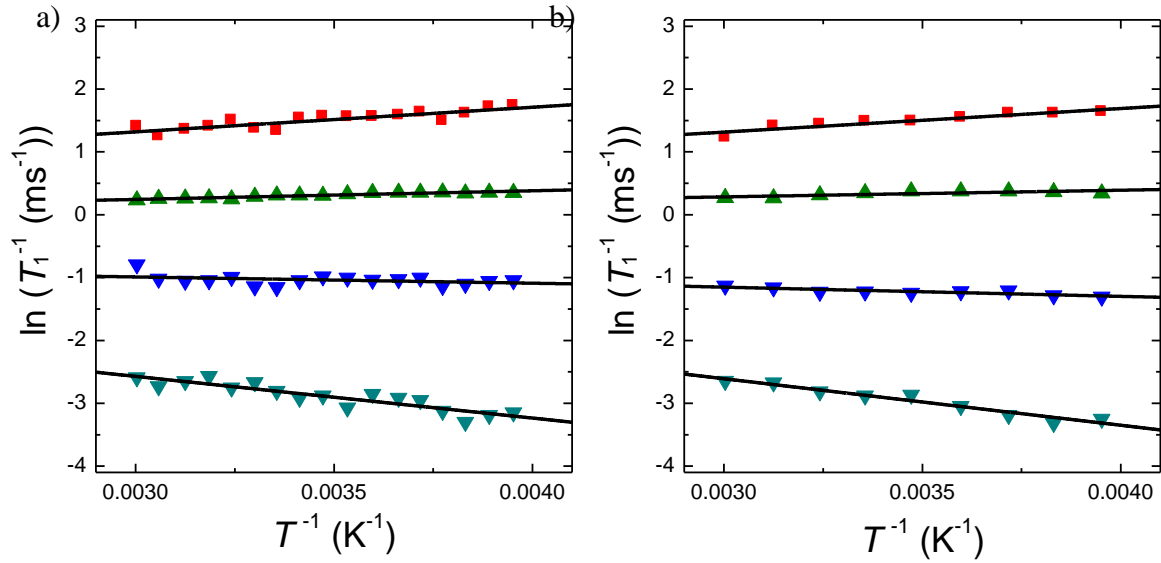


Figure 7.3 The changes in  $\ln(1/T_1)$  as a function of temperature for white cement paste at 28 (a) and 90 (b) days of hydration based on multi-exponential analysis with constrained intensities. Lines are the linear fit to the data.

### 7.1.2.2. Activation energy

The basic law of chemistry, developed by Svente Arrhenius, relates the constant rate of reaction ( $k$ ) with temperature ( $T$ ) at which the reaction/process occurs

$$k = A \cdot e^{-\frac{E_A}{k_B T}} \quad (7.2)$$

where  $A$  is prefactor and  $E_A$  is the activation energy.

This law can be adapted for NMR analysis. As water, or more precisely hydrogens, in different pore environments have specific relaxation rates ( $1/T_1$ ), by looking at the changes in these rates with temperature it is possible to calculate the activation energy for relaxation processes in associated pore types. The correlation time ( $\tau_c$ ) of molecular motion causing relaxation can be written as an Arrhenius type rate process

$$\tau_c = \tau_o \cdot e^{\frac{E_A}{k_B T}} \quad (7.3)$$

According to BPP theory [89], the  $T_1$  relaxation time for magnetic dipole-dipole interactions is expressed in terms of spectral density function  $J^\times(\omega)$ , given in section 3.3.1, and hence is related to correlation time as:

$$\frac{1}{T_1} = C \cdot J^\times(\omega) = C' \cdot \left( \frac{2 \cdot \tau_c}{1 + \omega^2 \cdot \tau_c^2} \right) \quad (7.4)$$

where  $C$  and  $C'$  is constant.

The  $T_1$  relaxation time as a function of  $\tau_c$  shows a minimum at  $\omega_o \cdot \tau_c \approx 1$  (section 3.3.1. figure 3.11). Therefore depending on the  $\omega_o \cdot \tau_c$  value relaxation rate can be expressed as:

$$\omega_o \tau_c \ll 1 \rightarrow \ln\left(\frac{1}{T_1}\right) = C'' + \frac{E_A}{k_B \cdot T}; \quad \omega_o \tau_c \gg 1 \rightarrow \ln\left(\frac{1}{T_1}\right) = C'' - \frac{E_A}{k_B \cdot T} \quad (7.5)$$

where  $C''$  is constant.

The evaluated relation of relaxation rate considers only  $^1\text{H}$  dipolar spin-pair interactions through the molecular rotations and translational motions. Considering the measurements of distilled water which is characterised by long  $T_1$  and  $T_2$  relaxation in the fast motion regime, the gradient sign is consistent with equation (7.5).

For cementitious materials the mechanism of relaxation and the obtained values of  $T_1$  are induced/dominated by  $^1\text{H}$  interaction with paramagnetic impurities,  $S$ , and modulated by translational diffusion of the mobile spins,  $I$ , with reference to  $S$  as described in section 3.3.3. For relaxation of spins in cement paste pores the correlation time,  $\tau_c$ , may be taken to be the surface hopping time,  $\tau_m$ , of Korb's model. The expression  $\omega_o \cdot \tau_c$  becomes  $\omega_S \cdot \tau_m$ , where  $\omega_S \approx 650 \cdot \omega_o$  is the electron resonance frequency.

### 7.1.2.3. The activation energy calculation for cement paste

The fitting lines of function  $\ln(1/T_1) = A \pm E_A/(k_B \cdot T)$  for mobile relaxation time components of white cement paste are shown in figure 7.3a at 28 days and figure 7.3b at 90 days of hydration. The gradients of these lines are presented in table 7.1.

Table 7.1. The gradients of the fitting lines of  $\ln(1/T_1)$  as a function of temperature for cement paste at 28 (fig 7.3 a) and 90 (fig. 7.3 b) days of hydration and activation energy of water transport in associated pores calculated based on these gradients.

Pore water	Gradient		Activation energy [eV]	
	28 days	90 days	28 days	90 days
C-S-H interlayer	392.0	375.2	0.034 ±0.003	0.032 ±0.002
C-S-H gel	137.2	106.0	0.012 ±0.001	0.009 ±0.002
Interhydrate	-99.6	-146.2	0.009 ±0.002	0.013 ±0.002
Capillary	-663.2	-740.1	0.057 ±0.005	0.064 ±0.007

The first observation is the change in gradient from positive values for C-S-H interlayer and gel pore water to negative for two capillary reservoirs. This suggests that the relaxation times of cement paste pore water are placed in close proximity of the  $T_1$  ( $\omega_o \cdot \tau_c$ ) minimum. At 20 MHz and taking  $\tau_m \approx 1$  ns [99]  $\omega_S \cdot \tau_m$  has a value of  $\approx 80$  that is much greater than 1. This clarifies the gradient sign for interhydrate and capillary water. Nevertheless the change of the sign for interlayer and gel pore water is surprising and not fully understood at this stage of work. Ongoing Molecular Dynamics and Monte Carlo simulation studies of relaxation in small pores by TRANSCEND student Serge Henri Cachia (Project 1) and EPSRC student Nicholas Howlett may help clarify the situation.

The activation energies of molecular motion within cement paste porosities, calculated based on gradients, are presented in table 7.1 and in figure 7.4 as a function of hydration time and  $T_1$  relaxation time at 298 K. Water in capillary pores, with higher  $T_1$  and pore size of order of micrometres, is characterised by the greatest activation energy. With increase of hydration time the values of capillary activation energies stay fairly constant within range of experimental accuracy. The calculated values ( $\sim 0.060$  eV) are about one third of that for bulk water. For water in spaces with smaller pore sizes the activation energy may go through a minimum. The lowest values are observed for water in interhydrate pores which size is about 10 nm and gel pores with size of  $\sim 3$  nm. Following that the activation energy is higher in C-S-H interlayer spaces. It is also noted that the C-S-H interlayer, gel and interhydrate water activation energies do not vary significantly within hydration time at which experiments were performed in this study.

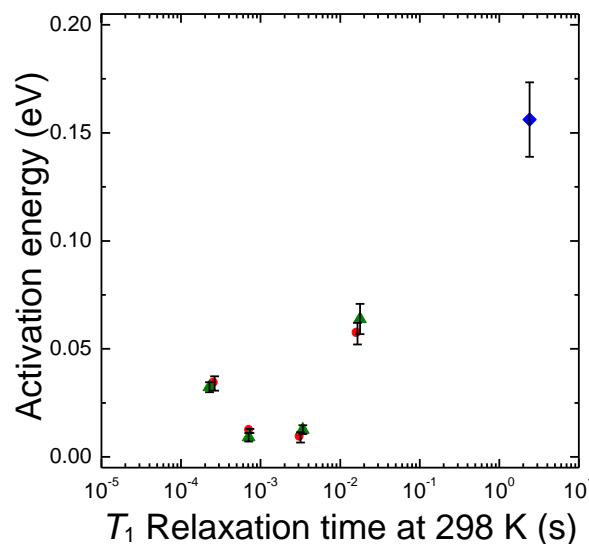


Figure 7.4 The activation energy dependence on  $T_1$  relaxation time for white cement paste 28 (red circles) and 90 (green triangles) days of hydration. The blue diamond represents the approximated water activation energy based on fitting line of  $\ln(1/T_1)$  of experimental data presented in figure 7.1.

The activation energy for relaxation in bulk fluid is determined by the activation energy for rotational and translational motion of spins in bulk. The activation energy for surface adsorbed species is that for surface diffusion. Since the observed relaxation rate is the

weighted average of surface and bulk relaxation, this suggests that the surface mobility has lower activation energy than the bulk, as more confined water has a lower energy. This is perhaps surprising and is a subject of ongoing MD simulations by Serge Henri Cachia. The increase for interlayer water may reflect that the relaxation model breaking down in such a small space, especially given water associated with interlayer calcium.

## 7.2. WATER - ISOPROPANOL EXCHANGE

This section contains the product of joint research between author and Dr Radoslaw Kowalczyk. The author's contribution was the experimental examination of the time dependency of exchange and the exponential stripping analysis of both deuterated and protonated sample data (latter for comparison with ILT). More details on the sample preparation, experiments and analysis are presented in [105] (Appendix 2).

### 7.2.1. Protonated cement paste

The  $T_2$  relaxation time distributions for cement pastes prepared with  $H_2O$  are presented in figure 7.5 and table 7.2. The distribution of as prepared paste (top graph) shows peaks associated with chemically combined water (24% with  $T_2 \sim 10 \mu s$ ), C-S-H interlayer (21%,  $90 \mu s$ ), gel (44%,  $300 \mu s$ ), interhydrate (8%,  $1 ms$ ) and capillary pore (3%,  $4$  and  $15 ms$ ) water.

The isopropanol exchange (middle graph of figure 7.5 and 2<sup>nd</sup> line in table 7.2) causes a slight decrease in the total signal intensity in comparison with as prepared paste. The reduction could be explained by lower proton density of isopropanol ( $0.105N_A \text{ cm}^{-3}$  where  $N_A$  is Avogadro number) than of water ( $0.111N_A \text{ cm}^{-3}$ ). The 3% decline in intensity would be achieved by exchanging 60% of mobile water with isopropanol. However, the  $T_2$  distribution reveals important changes in populations. The interhydrate and capillary liquid intensities increase markedly from a sum of 11% to 39%. At the same time, the intensity of liquid within gel pores decreases drastically by 28%. Only a small change is observed (by 3%) in interlayer intensity. The solid signal is unchanged.

One may think that there is increase in the amount of large pores and a parallel decrease of gel pore volume due to damage to pore network. That this is unlikely is proven by the result of back exchanging an isopropanol exchanged sample with water (bottom graph of figure 7.5). In the 3<sup>rd</sup> line of the table it is shown that gel, interhydrate and capillary water intensities are reversed almost to the level of as prepared paste. This suggests that larger pores, even for underwater cured samples, are inaccessible to water and are hence empty. It arises because the very small permeability of paste restrains curing water from getting into and saturating the capillary porosity. At reduced relative humidity the Kelvin Laplace equation ensures that large pores are not liquid filled. Even at 98% RH, pores with size above 53 nm are empty of liquid water. However, isopropanol can access these bigger pores as its contact angle is smaller compared to water [126].

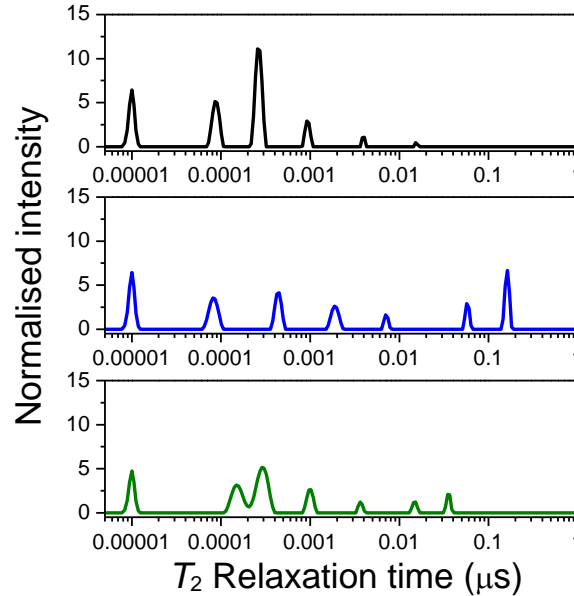


Figure 7.5 The  $T_2$  relaxation times distribution of as prepared paste with  $H_2O$  (top), exchanged with isopropanol (middle) and exchanged back with  $H_2O$  (bottom) – analysis performed by Dr R. Kowalczyk.

Table 7.2 Signal intensities of different water populations in as prepared and isopropanol exchanged pastes normalised to ignited paste mass and ‘as prepared’ paste with  $H_2O$ .

<i>Sample</i>	$I_{sol}$	$I_{CSH}$	$I_{gel}$	$I_{Int-hyd}$	$I_{cap}$	$I_{tot}$
as prepared $H_2O$	0.24	0.21	0.44	0.08	0.03	1.00
+ IPA	0.24	0.18	0.16	0.11	0.28	0.97
+ IPA + $H_2O$ back exchanged	0.21	0.18	0.37	0.10	0.11	0.97
as prepared $D_2O$	0.01	0.01	0.03	0.00	0.02	0.07
+ $H_2O$	0.21	0.18	0.40	0.09	0.10	0.98
+ IPA(D)	0.02	0.11		0.06	0.24	0.43
+IPA	0.18	0.11	0.14	0.13	0.15	0.71

The expected capillary liquid fraction can be calculated. Assuming that 0.38 gram of water are required to fully hydrate 1 gram of cement [28] and taking the water to cement ratio at the mixing time ( $w/c_{mix} = 0.46$ ), then there are  $0.08 \text{ cm}^3$  of water available to create interhydrate and capillary pores at full cement hydration ( $\alpha = 100\%$ ). Additionally, the chemical shrinkage creates the voids accessible to isopropanol in the amount of  $0.075 \cdot \alpha \text{ g/cm}^3$  of anhydrous cement<sup>28</sup>. Therefore, there is  $0.155 \text{ cm}^3$  of capillary porosity at full hydration, or 29% of the total liquid volume. However, considering that paste did not reach the full hydration, the realistic degree of hydration ( $\alpha = 85\%$ ) leads to capillary liquid volume  $0.201 \text{ cm}^3$  and fraction of 38%. This is in very good agreement with the sum of interhydrate and capillary liquid intensity in the isopropanol exchanged paste (39%).

<sup>28</sup> defined by Arnaud Muller and presented in [128]

The changes in gel pore intensity upon isopropanol exchange can be explained as the isopropanol draws water out of gel pores but cannot itself get into the smaller gel pores. That isopropanol only fills the bigger gel pores are evidenced by longer  $T_2$  of gel liquid and the fact that the isopropanol has a molecular size too big to access the smaller gel pores. Considering that the solvent do not enter smaller gel pores and that the intensity of the C-S-H interlayer is changed minimally, the water in the interlayer spaces is not replaced by isopropanol.

### 7.2.2. Deuterated cement paste

In order to distinguish which pores are filled by water and which by isopropanol the exchange experiments were repeated on the samples made with  $D_2O$ .

The as prepared  $D_2O$  paste shows negligible signal (4<sup>th</sup> line in table 7.2). The minimal signal present is caused by hydrogen-deuterium (Hyd-D) exchange during sample preparation and curing. When deuterated paste is exchanged with  $H_2O$  the signals from the original water populations are recorded (1<sup>st</sup> and 5<sup>th</sup> line in table 7.2). The recovery of chemically combined water signal suggests that the solid phases have high SSA, enabling Hyd-D chemical exchange, and hence they exist in nanocrystalline forms. The solid, C-S-H interlayer and gel water intensities are slightly lower than for as prepared  $H_2O$  paste. However, the total interhydrate and capillary intensity is almost double. This suggests that the paste prepared with  $D_2O$  hydrates more slowly than that with  $H_2O$ , as already reported [127]. It is further evidenced as the  $T_2$  relaxation times of gel, interhydrate and capillary water, and hence pore sizes, are bigger for deuterated paste (375  $\mu s$ , 2.6 and 15.5 ms against 300  $\mu s$ , 1.0 and 4 ms).

The partially deuterated isopropanol,  $(CH_3)_2CDOD$ , was used to register only the isopropanol – water molecular exchange and to prevent the Hyd-D chemical exchange (as the hydrogens likely to undergo such exchange are deuterated). The analysis (6<sup>th</sup> line in table 7.2) shows the minimal chemically combined signal – in contrast to  $H_2O$  replacement, proving that the Hyd-D chemical exchange did not occur. The modest signal was obtained from C-S-H gel (11%). It is assumed to originate from the isopropanol entering the larger gel pores. Results can be compared with solvent replaced  $H_2O$  paste by multiplying by 8/6 (number of Hyd in isopropanol by number of Hyd in deuterated isopropanol). The multiplication yields 15% of intensity for C-S-H gel water which is in good agreement with the gel intensity for  $H_2O$  paste exchanged with isopropanol (16%). This strongly suggests that isopropanol molecules do not replace water within C-S-H interlayer spaces and demonstrates the connectivity of C-S-H gel pore network with larger interhydrate and capillary pores. The total signal intensity acquired from interhydrate and capillary liquid is equalled to 30%. Multiplication gives 40% which is also closed to 39% for  $H_2O$  paste.

The deuterated paste was also exchanged with regular isopropanol (7<sup>th</sup> line in table 7.2). The analysis shows that signals recover hugely for all population demonstrating both isopropanol – water molecular and Hyd-D chemical exchange processes. The increase in chemically combined and interlayer intensities indicates the appearance of Hyd-D chemical exchanged as now all hydrogens sites are protonated. However, these intensities do not reach the intensity levels of  $H_2O$  paste suggesting that the chemical exchange is not yet completed.

The gel intensity is slightly smaller than for solvent replaced H<sub>2</sub>O paste (14% -16%). However the larger pores are not yet filled to the same level (28% - 39%).

### 7.2.3. Time dependency of exchange

The full equilibration of the solvent replacement is a very slow process for the large cement paste samples. Figure 7.6 presents how the combined signal intensities of liquids in capillary and interhydrate and in C-S-H interlayer and gel pores change over exchange time for white cement paste mixed at  $w/c_{mix} = 0.4$  and cured underwater. The measured sample had length and diameter of 8 mm. This size is considerably bigger in comparison with millimetre pieces of paste measured in previous sections when the exchange occurred after 3 days.

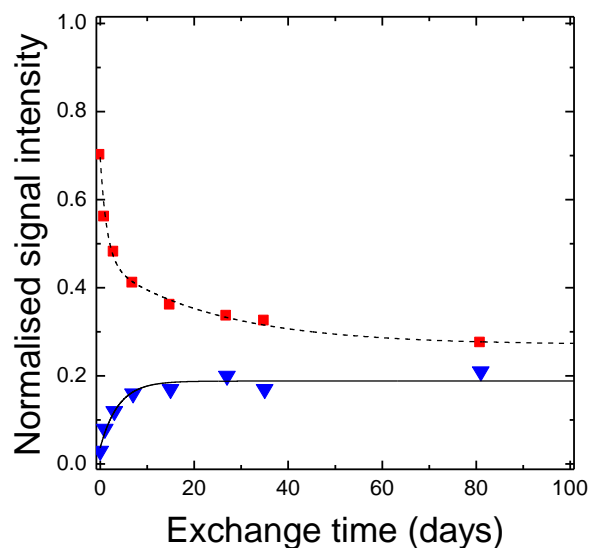


Figure 7.6 The increase of sum interhydrate and capillary pore water intensity (blue triangles) and decrease of sum C-S-H interlayer and gel pore water intensity (red squares) for isopropanol exchange of large paste sample. The lines are the exponential fits – solid with one and dashed with two components.

The sum interhydrate and capillary intensity increases significantly from ~3 to 20% showing again that even though the sample is cure underwater many of large pores are not filled with water. The calculated fraction of capillary water, as presented in section 7.3.1, for fully hydration paste in that case is 20%. The exchange was performed on 6 month old sample, the hydration is almost completed (definitely over 90% as shown for 90 days old paste in section 6.6.1). Hence, experimental and estimated fractions are in good agreement.

The decrease of combined fraction of C-S-H interlayer and gel liquid (from ~70% to 27%) again suggests that isopropanol draws water out of C-S-H gel but not replace it to the same extend. The exponential fits yield the time constant of the signals changes. The capillary pores are filled by isopropanol with a time constant of about 4 days for the 8 mm sample. Water is drawn out from gel pores within 1.5 days. The longest process (25 days) is surprisingly the equilibration of water within interlayer spaces and on the surface of gel pores which appears interlayer-like during drying. The full equilibration of solvent exchange in sample of larger, centimetre size takes about two months.

## 8. Summary / Conclusion

---

---

It has been shown in this thesis that NMR Relaxometry provides a great level of valuable information concerning cement microstructure as a function of hydration time, temperature, relative humidity and mix composition. Furthermore, better insight into pore-water interactions in cementitious materials was obtained.

It was shown that NMR experiments are quantitative. The linear dependence of total signal intensity with sample mass during drying proved that NMR senses all water within samples. The origin of the solid Quad Echo signal was verified by thermogravimetric analysis and X-ray diffraction. The signal arises entirely from Portlandite and ettringite, and does not comprise any contribution from C-S-H. Five distinct NMR hydrogen populations were observed and assigned as chemically combined water, C-S-H interlayer, gel and interhydrate pore water and finally water in larger capillary pores and cracks.

### 8.1. SORPTION ISOTHERM

The NMR Relaxometry has revealed the first pore-type resolved sorption isotherm of any cementitious material. Such an isotherm facilitates the assessment of porosity types that are dried or filled at different humidity conditions. The striking feature of the data is the re-assignment of the NMR signal of the surface water layer remaining in gel pores during drying to the C-S-H interlayer water signal. The results allow an interpretation of the way the pores empty during desorption and fill during adsorption branches. Six stages of desorption process were identified. It was observed that drying progresses through the removal of the bulk pore water with a water layer remaining at the pore surfaces. For adsorption the results suggests refilling of gel pores layer by layer. The results allow schematic presentation of the C-S-H morphology. It is similar to the picture of C-S-H proposed by Feldman and Sereda [38] and consistent with interpretation of their model.

Pore sizes in ‘as prepared’ cement paste were independently calculated based on the  $T_2$  relaxation times in accordance with fast exchange model of relaxation and based on the rate of signal amplitude loss during drying. The relaxation time model gives the C-S-H interlayer spacing of  $0.94 \pm 0.04$  nm and gel pore size of  $3.1 \pm 0.2$  nm. The value of gel pore size obtained by amplitude model from primary desorption branch is higher -  $4.5 \pm 1.6$  nm, but close to that obtained by McDonald *et al* [18]. The amplitude model gives the  $1.5 \pm 0.3$  nm for C-S-H interlayer pore size. That is larger than expected and than the value from the relaxation model calculation. It is attributed to the breakdown of the drying model assumptions in small interlayer space.

The specific surface area was calculated by three means: BET theory; fast exchange model of relaxation; and amplitude model. The amplitude model gives systematically lower values in comparison with the other two methods. This is explained by the high sensitivity of SSA analysis on pore size and attributed to the higher size of C-S-H interlayer pores than expected. The total specific surface area evaluated based on mass and intensity BET fits and on relaxation times yields close values of  $130 \pm 5$ ,  $144 \pm 24$  and  $157 \pm 9$  m<sup>2</sup>/g of dried paste (3%

RH) respectively. These values were shown to be relatively close to previous estimates by Baroghel-Bouny [114] and by Powers and Brownyard [32] but lower than that measurements by Halperin *et al* [10]. The analysis allows differentiation of SSA between C-S-H interlayer and gel pores. Given the pore widths from fast exchange model, the specific surface areas are  $91 \pm 4 \text{ m}^2/\text{cm}^3$  of paste for gel pores and  $175 \pm 12 \text{ m}^2/\text{cm}^3$  for C-S-H interlayer pores.

## 8.2. INFLUENCE OF CURING TEMPERATURE ON CEMENT MICROSTRUCTURE

The quantitative NMR data lead to a full description of cement paste and C-S-H characteristics. The density, Ca/(Si+Al) ratio and water content of C-S-H were measured in never dry white cement pastes using NMR Relaxometry supported by TGA and XRD analysis. The NMR evaluated C-S-H ‘solid’ and ‘bulk’ densities in cement paste cured at 20°C for 28 days are  $2.64 \pm 0.03 \text{ g/cm}^3$  and  $1.90 \pm 0.02 \text{ g/cm}^3$ . The values of C-S-H ‘solid’ density are at the upper end of earlier estimates by helium pycnometry [28], [75], [76] but are in good agreement with the well cited measurement using SANS by Jennings [7]. The ‘bulk’ density is close to the CM-II model value [6] and that measured by Young and Hansen [72].

Changes of curing temperature cause important alteration to the C-S-H characteristics and cement paste. With increase of curing temperature the increase of both C-S-H ‘solid’ and ‘bulk’ densities was revealed with accompanying decrease in C-S-H water content. It was interpreted as evidence for fewer locally stacked calcium silicate layers and further explained by a slightly lower amount of the gel pore water at the elevated temperature. The increase of C-S-H ‘bulk’ density and decline of water content with temperature was also observed by Galluci *et al* [109]. The calcium and silicon content remain constant despite the changes in curing temperatures. The cement paste composition is affected. An increase of curing temperature accelerates cement hydration and growth of hydrates. Pastes cured at higher temperature are ‘more’ hydrated. At mature age, they are characterised by larger capillary porosity, greater amount of C-S-H phase and lower content of ettringite and gel pores.

The combined results of the desorption and C-S-H composition studies allowed the creation of the C-S-H ‘solid’ and ‘bulk’ water content desorption isotherm that can be evaluated to define the C-S-H composition at various humidities. In particular water content at 10% RH is measured as 2.11 moles/mole of C-S-H. It is in agreement with values at 11% RH reported by Jennings [6], Feldman and Ramachandran [73] and Young and Hansen [72].

<sup>1</sup>H NMR Relaxometry enabled determination of the evolution of the nanoscale porosity for white cement pastes and comparison between pastes with and without addition of silica fume, cured at different temperatures. In general, with the hydration time, the consumption of interhydrate/capillary pore water and the development of three water populations (chemically combined water within crystalline phases; and water in interlayer spaces and gel pores of C-S-H) were registered. For white cement paste the amount of chemically combined water and C-S-H interlayer water increase continuously in course of hydration. Initially the content of gel pore water increases more rapidly and later becomes approximately constant (after ~4 days at 20°C). The observation of two nanoscale pore types intrinsic to the C-S-H is distinctive in comparison with Jennings’ CM-II model [6] that identifies four populations:

interlayer spaces; intra-globular pores; small pores between globules (SGP) and large pores between globule flocs (LGP). The gel pores as measured in this thesis are comparable in size with SGP while the interhydrate size is in the range of the LGP size. However, as the latter is consumed in the hydration process, it is not treated as part of C-S-H structure in this study.

The evolution of NMR signals for white cement paste with silica fume shows the formation of C-S-H due to pozzolanic reaction of silica fume with CH and acceleration of hydration due to silica fume filler effect. The major influence of silica fume is observed in the reduced amount of chemically combined water and much higher of gel pore water in comparison with plain white cement paste. The maximum gel pore water content for paste cured at 20°C appears earlier than for plain white cement, already at ~20h, and coincidental in time with the change in capillary water consumption and stability of interhydrate pore size. In mature pastes with silica fume considerably higher capillary porosity is seen. However the sizes of C-S-H interlayer, gel and interhydrate/capillary pores are very similar as for plain cement paste. The investigation of SF pastes with increase of curing temperature reveals more complex hydration behaviour as there are two factors contributing: the C-S-H is created due to silicates reaction with water and silica fume reaction with CH.

### 8.3. ACTIVATION ENERGY OF WATER DYNAMIC

The activation energy for water relaxation processes in C-S-H interlayer, gel, interhydrate and capillary pores was determinate based on  $T_1$  relaxation time measurements. The prior verification of acquired data for water against literature and the linear increase of total signal intensity with increase in  $1/T$  gave the confidence in obtained results.

It is observed that the activation energy decreases with confinement of space to the certain pore size /  $T_1$  level at which it may go through a minimum and after which the energy reaches higher values for water within even smaller spaces. The results suggest that the translational and rotational motion of spins has higher activation energy than the surface diffusion. The increase of activation energy for interlayer water may reflect that the relaxation model breaks down in such a small space. Otherwise the activation energy and mechanism of spin relaxation in cement paste pores may be explained as an effect of balance between surface diffusion and rotational-translation interactions.

### 8.4. WATER - ISOPROPANOL EXCHANGE

NMR relaxation analysis was performed to assess the mechanism of water-isopropanol replacement method used for arresting cement hydration. The results showed that water-isopropanol exchange essentially do not alter the water within the C-S-H interlayer spaces. However, isopropanol draws water out of C-S-H gel pores and refill the bigger, more accessible amongst them. It invades the interhydrate and capillary pores giving significantly higher intensity than in 'as prepared' paste. That suggests the presence of the large capillary pores in cement paste that are inaccessible to water and explains the lower capillary porosity recorded by NMR than expected from Powers and Brownyard model [32], [34].

The connectivity of C-S-H gel pore network with larger interhydrate and capillary pores was revealed through the exchange of deuterated paste with deuterated isopropanol. It also demonstrated that isopropanol molecules do not enter the C-S-H interlayer spaces and do not replace water within those spaces. Furthermore, the chemical exchange between deuterons and protons proves experimentally for the first time the interconnectivity of C-S-H interlayer and gel pores with interhydrate and capillary pores.

## 8.5. FUTURE WORK

It has been shown in this thesis that NMR relaxometry is an excellent source of valuable information about cement microstructures, especially C-S-H, and water within them. The NMR relaxometry opens the door to a routine way of cementitious materials characterisation needed by researchers and industry to rapidly describe novel cements. Nevertheless there are several factors to consider in context of making NMR the routine test. In particular NMR laboratories use different variants of pulse sequence; perform the experiments by using spectrometers with different operating characteristics; and analyse the data following different protocols. Additional level of variation arises from the examined samples themselves: their sizes; geometry; preparation; and curing conditions. All these make the comparison between different NMR laboratories and instruments difficult and the interpretation of results complex. The need to standardise the NMR characterisation of cementitious materials was identified. The project with aim to fulfil that gap and define, validate and disseminate the appropriate protocols for NMR measurements and analysis has already begun in collaboration between University of Surrey and National Physical Laboratory.

The research presented in this thesis could be complemented and extended in many aspects. The possible extensions are: examination of the influence of curing temperature on the C-S-H characteristics for cement paste with addition of silica fume; calculation of the pore sizes for cement paste with silica fume; deeper investigation of empty capillary pores etc.

The other proposition could be examination of the activation energy for water relaxation at younger pastes ages. Nevertheless the activation energy results are surprising and at first the deeper understanding of the experimentally yielded values of activation energy and their behaviour with the decrease of pore size is required. Ongoing Molecular Dynamics and Monte Carlo simulation studies of relaxation in small pores of calcium silicate hydrates by Serge Henri Cachia and Nicholas Howlett may help to clarify the results.

Other areas for further studies includes: a re-evaluation of  $T_2$ - $T_2$  experiments in the light of this work and of the simulations of Serge Henri Cachia and Nicholas Howlett; and further investigation of the lateral extend of C-S-H pores using double quantum and diffusion methods. In a wider aspect the next important stage is to create the link between the resultant information and knowledge gained from this thesis and the properties of cementitious materials and concrete structures.

## Appendixes

---

---

### Appendix 1:

A.C.A. Muller, K. L. Scrivener, A. M. Gajewicz, P. J. McDonald, "Use of bench-top NMR to measure the density, composition and desorption isotherm of C-S-H in cement paste", *Microporous and Mesoporous Materials*, vol. 178, pp. 99-103, 2013

### Appendix 2:

R. M. Kowalczyk, A. M. Gajewicz, P. J. McDonald, "The mechanism of water-isopropanol exchange in cement pastes evidenced by NMR relaxometry", *RSC Advances*, vol. 4, pp. 20709-20715, 2014

### Appendix 3:

A.C.A. Muller, K. L. Scrivener, A. M. Gajewicz, P. J. McDonald, "Densification of C-S-H measured by  $^1\text{H}$  NMR Relaxometry," *The Journal of Physical Chemistry C*, vol. 117, pp. 403–412, 2013



## Use of bench-top NMR to measure the density, composition and desorption isotherm of C–S–H in cement paste

A.C.A. Muller<sup>a</sup>, K.L. Scrivener<sup>a</sup>, A.M. Gajewicz<sup>b</sup>, P.J. McDonald<sup>b,\*</sup>

<sup>a</sup>Laboratory of Construction Materials, Ecole Polytechnique Fédérale de Lausanne, CH-1015 Lausanne, Switzerland

<sup>b</sup>Department of Physics, University of Surrey, Guildford, Surrey GU2 7XH, UK

### ARTICLE INFO

Article history:  
Available online 9 February 2013

Keywords:  
Calcium silicate hydrate  
Density  
Nuclear magnetic resonance  
Pore size distribution  
Desorption isotherm

### ABSTRACT

<sup>1</sup>H nuclear magnetic resonance (NMR), supported by a measurement of the degree of hydration using X-ray diffraction, has been used to fully characterise the nano-scale porosity and composition of calcium–silicate–hydrate (C–S–H), the active component of cement. The resultant “solid” density and composition are  $\rho = 2.68 \text{ g/cm}^3$ ;  $(\text{Ca})_{1.53} \cdot (\text{Si}_{0.96}\text{Al}_{0.04})\text{O}_{3.51} \cdot (\text{H}_2\text{O})_{1.92}$  for an underwater cured, never-dried cement paste with an initial mix water-to-cement ratio of 0.4 after 28 days of hydration. In addition, the first pore-type resolved desorption isotherm of cement that shows the location of water as a function of relative humidity has been measured. Critical to our results is verification of the assignment of the different NMR spin–spin relaxation time components. These have been corroborated with conventional analyses. The new methodology is key to enabling design of cement pastes with lower environmental impact.

© 2013 Elsevier Inc. All rights reserved.

### 1. Introduction

Cement production currently accounts for 5–8% of global CO<sub>2</sub> emissions [1]. One route to reducing this impact is to introduce new supplementary cementitious materials. However, for this to become routine, it is necessary to fully characterise calcium–silicate–hydrate (C–S–H), the active phase of cement, and then to have means to assess changes made to it by the new materials. The problem is that C–S–H is a highly heterogeneous, nano-porous and delicate material comprising disordered sheets of calcium and oxygen atoms and silicate tetrahedra separated by sheets of water. Regions of stacked sheets are reported to be separated by nano-sized gel pores and larger capillary pores. However, beyond this basic picture, there remains considerable uncertainty [2–6].

Literature reports various densities for C–S–H dependent on the measurement methodology and sample preparation. A review by Jennings [7] reported values from 1.83 to 2.85 g/cm<sup>3</sup>. At the lower end, both C–S–H and gel water are encompassed so the measurement says little about morphology. At the higher end, the gel water is not included. However, to make the measurement, the gel water must generally be removed. This disturbs the structure and hence the result. Attempts to measure the “solid” C–S–H density in the presence of water have hitherto required small angle neutron scattering (SANS) [2]. However, SANS is complex and not widely available.

NMR of cement directly probes water in different environments [8–11] but to date there has been disagreement on the assignment of signals so limiting the interpretation of results. We provide clarification by cross-referencing NMR results to thermogravimetric (TGA), X-ray diffraction (XRD) and thermodynamic modelling analyses of the same samples. We show how widely available bench-top nuclear magnetic resonance (NMR) relaxometry in combination with XRD may be used to measure the density (both “solid” and inclusive of gel water), composition and morphology of C–S–H of never-dried cement pastes, thereby meeting the need for a routine characterisation technique. The C–S–H density and composition follow from solution of mass, volume and oxide content balance equations written in terms of the NMR signal intensities; the degree of hydration; the chemical shrinkage volume; and the anhydrous cement composition. XRD is used to measure the degree of hydration. It is also used here to measure the ettringite fraction so as to allow an improved estimate of the C–S–H density and composition. The chemical shrinkage is determined from the difference in water-to-cement (*w/c*) ratio of an under-water cured paste, compared to that of the mix. The paste *w/c* ratio is calculated from the NMR signal intensity of partially dried material *after* measurement of the “never-dried” parameters.

The NMR analysis is extended to a full study of hydrated samples subsequently equilibrated to constant relative humidity. These measurements enable the first pore size resolved desorption isotherm to be measured. Pore sizes, and in particular gel pore sizes, are independently inferred both from the spin–spin relaxation times in accordance with the well known fast diffusion model of relaxation and from the rate of signal amplitude loss with drying.

\* Corresponding author. Tel.: +44 (0) 1483 686798.  
E-mail address: [p.mcdonald@surrey.ac.uk](mailto:p.mcdonald@surrey.ac.uk) (P.J. McDonald).

Taken together, the experiments suggest a picture of C–S–H morphology that, while incorporating aspects of widely promulgated models (due to Feldman and Sereda (FS) [12] and to Jennings (CM-II) [7]) nonetheless differs from both.

## 2. Experimental

### 2.1. Methods

Hydrogen NMR was performed at 20 MHz. The chemically combined, or “solid”, water fraction was measured by quadrature echo (QE) with pulse gaps,  $\tau$  between 12 and 45  $\mu\text{s}$  [13]. QE signals were decomposed into Gaussian (solid) and exponential (more mobile) water parts. The solid component was back extrapolated to  $\tau = 0$  to yield the solid fraction free from relaxation artefact. The solid fraction was confirmed by TGA operating between 30 and 950 °C at 10 °C/min. under  $\text{N}_2$  gas flow and by XRD in a  $\theta$ – $\theta$  configuration between  $2\theta = 7$  and  $70^\circ$  using a  $\text{CuK}\alpha$  source. NMR Carr–Purcell–Meiboom–Gill (CPMG) decays were recorded to separate the mobile water into different components [14]. Decays comprised 128 echoes logarithmically spaced from 50  $\mu\text{s}$  to 70 ms and were Laplace inverted using the algorithm developed by Venkataraman et al. [15].

### 2.2. Materials

Low  $\text{C}_3\text{A}^1$  white cement (67%  $\text{C}_3\text{S}$ ; 20%  $\text{C}_2\text{S}$ ; 3.5%  $\text{C}_3\text{A}$  with other phases all as minor components as measured by XRD with Reitveld analysis) was mixed with water in a  $w/c$  mass ratio 0.4 for 3 min at 500 rpm, rested for 2 min and further mixed for 2 min at 2000 rpm. Aliquots,  $\approx 0.35 \text{ cm}^3$ , were inserted into moulds and covered with a small quantity of saturated CH solution (less than 10% sample volume) for underwater curing, all at 20 °C. For the desorption isotherm measurements, underwater cured samples were broken into millimetre sized pieces after 28 days and equilibrated at constant relative humidity (RH) to constant mass in a moisture sorption analyser using  $\text{N}_2$  gas. At every significant stage, samples were weighed with a microbalance.

## 3. Results

Critical to our analysis is verification that the NMR measurement senses all the water in the sample. Fig. 1 (inset) shows the total NMR intensity at 20 MHz as a function of sample mass during controlled drying of an underwater cured cement paste. The plot is linear. The intercept with the mass axis implies an effective  $w/c = 0.463$ . The increase reflects that the sample is cured underwater and proves that there is no “hidden” water as discussed below in the analysis section.

Next we demonstrate that the QE solid fraction of the signal (24.3%) arises predominantly from CH and ettringite, and in particular does not contain any component of C–S–H. TGA, XRD and calculation using the thermodynamic model GEMS [16] give the mass fraction of CH in the paste as  $22.5 \pm 1\%$ ,  $23.7\%$  and  $24\%$ , respectively. The average,  $23.4 \pm 0.6\%$ , is equivalent to,  $m_{\text{CH}} = 0.34 \pm 0.01 \text{ g/g}$  anhydrous cement. XRD gives the mass fraction of ettringite in the paste as  $5.7 \pm 1.0\%$ , equivalent to  $m_{\text{ett}} = 0.083 \pm 0.015 \text{ g/g}$  of anhydrous cement. Hence, the fraction of water combined into the solid phases is  $[(0.34 \times 18^{\text{AMU}}/74^{\text{AMU}}) \pm (0.083 \times$

<sup>1</sup> Cement chemistry notation is used throughout this paper to refer to the compositional oxides. In addition, we refer to atomic elements in conventional manner. Hence: C = CaO; S =  $\text{SiO}_2$ ; H =  $\text{H}_2\text{O}$ ; A =  $\text{Al}_2\text{O}_3$  and so CH =  $\text{Ca}(\text{OH})_2$ . To avoid confusion within the text, where it is ambiguous, atomic hydrogen is notated *Hyd*. The abbreviation AMU denotes atomic mass units;  $n$  is molar content and  $f$  is mass fraction of anhydrous powder.

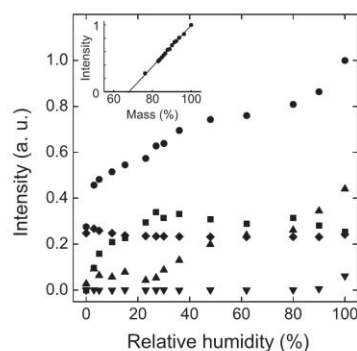


**Fig. 1.** Inset: The total normalised NMR signal against relative sample mass in progressively dried white cement paste. Main: The total signal plotted against relative humidity (circles) and de-composed into chemically combined water (diamonds), and water in C–S–H interlayer spaces (squares), gel pores (triangles) and capillary pores (inverted triangles): the pore-specific desorption-isotherm. Notice that, as gel pores empty, so residual water on the C–S–H surface appears interlayer space-like. Hence this signal increases.

$576^{\text{AMU}}/1255^{\text{AMU}})/0.463 = 26 \pm 2\%$  in reasonable agreement with the NMR value, 24.3%.

The CPMG experiment subdivides the mobile water fraction into components with  $T_2$  of  $126 \pm 5 \mu\text{s}$  (25.5%),  $420 \pm 20 \mu\text{s}$  (44.1%),  $1.4 \pm 0.4 \text{ ms}$  and  $12 \pm 2 \text{ ms}$  (6.1% taken together). We assign the component with  $T_2 \approx 126 \mu\text{s}$  to water (and surface hydrogen contacting water) in interlayer spaces of the C–S–H since the immobile water associated with solid is already fully accounted for by CH and ettringite; with  $T_2 \approx 420 \mu\text{s}$  to water in C–S–H gel pores; and with  $T_2 \approx 1.4 \text{ ms}$  and  $T_2 \approx 12 \text{ ms}$  to water in interhydrate spaces, capillary pores and cracks, hereafter abbreviated simply to capillary water. This assignment is similar to that proposed by Holly et al. [11].

The main part of Fig. 1 shows the amplitude of these 4 components as a function of relative humidity. As such, it is the pore-size resolved desorption isotherm. The total signal loss closely resembles the first-drying weight-loss isotherm as reviewed by Jennings [7]. The capillary pore water dries above 90% RH. The gel pore water decreases from 50% of the total to practically zero between 100% and 25% RH. In the same range, the interlayer water apparently increases. This is because water associated with surface sites in a full gel pore rapidly exchanges with the pore fluid and therefore has the same  $T_2$ . However, as the pore empties, so surface water is left as a less mobile monolayer that, in NMR terms, more resembles interlayer water with shorter  $T_2$ . Below 25% RH, water is rapidly lost from the C–S–H interlayer spaces with a noticeable acceleration around 10% RH. At low RH there is an increase in the solid signal. Similar to the gel, as interlayer water is lost, so hydrogen in, for example, residual silanol groups appears solid-like.

## 4. Analysis

To measure the C–S–H density, we need to know the change in volume of the paste during hydration. Chemical shrinkage, due to the lower specific volume of the hydration products compared to the solid reactants and water, creates porosity that is expected to be of the order of 7–10% the total volume [17]. In small underwater cured samples as here, water is drawn into the chemical shrinkage volume and so the extra porosity is calculated from the increase in the  $w/c$  ratio of the hydrated paste compared to the mix. The macroscopic volume change, a small swelling in underwater cured material, is negligible in comparison and is ignored. The  $w/c$  ratio

of the paste,  $w/c = 0.463$ , is calculated from the intercept with the mass axis of the NMR signal during controlled drying (inset to Fig. 1).

Simultaneous equations for mass and volume conservation expressed per gram anhydrous cement are:

$$1 + \frac{w_{mix}}{c} = (1 - \alpha) + \frac{w_{mix}}{c} [\beta I_{solid} + \gamma I_{CSH} + \delta (I_{gel} + I_{cap})] \text{ and} \quad (1)$$

$$\frac{1}{\rho_{uc}} + \frac{w_{mix}}{c\rho_w} = \frac{(1 - \alpha)}{\rho_{uc}} + \frac{w_{mix}}{c} \left[ \frac{\beta I_{solid}}{\rho_{solid}} + \frac{\gamma I_{CSH}}{\rho_{CSH}} + \frac{\delta (I_{gel} + I_{cap} + I_{void})}{\rho_w} \right] \quad (2)$$

Here,  $\rho$  is density and  $I$  are signal fractions normalised to the total signal before chemical shrinkage (i.e. the creation of filled voids) so that  $I_{void} = (w_{paste} - w_{mix})/w_{mix}$  and  $I_{solid} + I_{CSH} + I_{gel} + I_{cap} = 1$ . The subscript  $uc$  refers to unreacted cement; others are clear from the text. The parameters  $\alpha$ ,  $\beta$ ,  $\gamma$  and  $\delta$  are the degree of hydration and the reciprocal water mass fractions of the solid, C–S–H and pore fluid, respectively.

The solid signal is assumed to comprise two parts, CH and ettringite, so that  $I_{solid} = I_{CH} + I_{Ett}$ ;  $\beta I_{solid} = \beta_{CH} I_{CH} + \beta_{Ett} I_{Ett}$  and  $\beta I_{solid}/\rho_{solid} = \beta_{CH} I_{CH}/\rho_{CH} + \beta_{Ett} I_{Ett}/\rho_{Ett}$ . The constants  $\rho_{uc,CH,Ett,w} = 3.15, 2.24, 1.77$  and  $1 \text{ g/cm}^3$  respectively,  $\beta_{CH} = 74/18$ ,  $\beta_{Ett} = 1255/576$  and  $\delta = 1$ . We take the mass of ettringite per gram anhydrous from XRD, calculate the associated water content,  $I_{Ett} = m_{Ett}/(0.4\beta_{Ett})$  and subtract this from  $I_{solid}$  to get  $I_{CH}$ . An alternate method of dividing  $I_{solid}$  between  $I_{CH}$  and  $I_{Ett}$  is to use the mass ratio of ettringite and CH determined by XRD. It leads to slightly different results because of the discrepancy between the total solid fractions determined by XRD and NMR. We do not favour this alternate route. The reason is that, whilst the ettringite content is hard to determine accurately, it is essentially constant after the early stages of hydration. Hence, using the former method of signal split, the average ettringite content of multiple samples measured at one, relatively early, time point may be used to increase accuracy in temporal studies of sealed cured samples reported elsewhere [18].

This leaves  $\alpha$ ,  $pCSH$  and  $\gamma$  unknown. A measurement of  $\alpha$ , the degree of hydration, was made using XRD so enabling the C–S–H density and water fraction to be found. Assuming  $Ca_z(Si_y, Al_{(1-y)})O_{(z+y/2+3/2)}(H_2O)_x$ , the water fraction  $x$  is related to  $\gamma$  as

$$x = (56z + 9y + 51)/(18(\gamma - 1)) \quad (3)$$

where  $y = n_{Si}/(n_{Si} + n_{Al})$  and  $n_{Si,Al}$  are the molar content of Si and Al in the C–S–H. The numerical constants derive from the atomic masses of C, S and H. The alternate C–S–H composition including gel water,  $Ca_z(Si_y, Al_{(1-y)})O_{(z+y/2+3/2)}(H_2O)_x$ , has  $x' = x(I_{CSH} + I_{gel})/I_{CSH}$ .

A further conservation equation is written for the overall Ca/(Si + Al) ratio before and after reaction:

$$\frac{3 \left( \frac{f_{C3S}}{C_3S^{AMU}} \right) + 2 \left( \frac{\alpha - f_{C3S}}{C_2S^{AMU}} \right) + 3 \left( \frac{f_{C3A} - f_{C3A}^{Ett}}{C_3A^{AMU}} \right)}{\frac{f_{C3S}}{C_3S^{AMU}} + \frac{\alpha - f_{C3S}}{C_2S^{AMU}} + 2 \left( \frac{f_{C3A} - f_{C3A}^{Ett}}{C_3A^{AMU}} \right)} = \frac{\frac{I_{CH} n_{Hyd}}{2} + \frac{I_{CSH} n_{Hyd}^2}{2x} + 3 \left( \frac{f_{C3A} - f_{C3A}^{Ett}}{C_3A^{AMU}} \right)}{\frac{I_{CSH} n_{Hyd}^2}{2x} + 2 \left( \frac{f_{C3A} - f_{C3A}^{Ett}}{C_3A^{AMU}} \right)} \quad (4)$$

Here, the first term of the numerator gives the number of moles of reacted Ca in the CH and C–S–H per gram of anhydrous cement that are derived from  $C_3S$ . The other terms give the moles of reacted Ca from  $C_2S$  and  $C_3A$  respectively. The denominator is similarly constructed for reacted Si and Al. On the right hand side, the corresponding molar contents of Ca, Si and Al are written in terms of the NMR signal fractions, the C–S–H composition parameters and  $n_{Hyd} = 2w_{mix}/H^{AMU} = 0.044$ , the molar content of hydrogen

in the paste mix. The derivation of Eq. (4) assumes that, for the degree of hydration considered ( $\alpha = 0.77$ ), all the  $C_3S$  of the anhydrous cement ( $f_{C3S} = 67\%$ ) is consumed in the reaction before the more slowly reacting  $C_2S$  ( $f_{C2S} = 20\%$ ). Additionally, it is assumed that the  $C_3A$  not required for ettringite formation is incorporated within the C–S–H. It was shown above that the mass of ettringite is  $0.083 \text{ g/g}$  anhydrous cement. To produce this amount consumes  $f_{C3A}^{Ett} = 1.79\%$  of the anhydrous cement in the form of  $C_3A$  and  $0.0383 \text{ g}$  of water. Hence the remaining  $C_3A$  is  $f_{C3A} - f_{C3A}^{Ett} = 1.72\%$ .

Finally, the equality  $y = \frac{n_{Si}}{n_{Si} + n_{Al}} = 1 - \frac{n_{Al}}{n_{Si} + n_{Al}}$ , leads, after substitution of the two terms in the denominator on the right hand side of Eq. (4) to

$$y = 1 - \frac{4x(f_{C3A} - f_{C3A}^{Ett})}{I_{CSH} n_{Hyd} C_3A^{AMU}} \quad (5)$$

The intensities,  $I$ , of the solid, C–S–H interlayer, gel, capillary and void water NMR signals at 100% RH defined as above are 0.281, 0.295, 0.510,  $-0.086$  and  $0.157$ , respectively, the negative sign implying that some water drawn into the sample has been used for hydration products. The solid signal splits into that from CH and ettringite as 0.185 and 0.096 respectively. The degree of hydration is  $\alpha = 0.77$  from XRD. Solving Eqs. (1)–(5), the resultant C–S–H density is  $2.68 \text{ g/cm}^3$ , with composition  $Ca_{2.153}(Si_{0.96}, Al_{(1-y)=0.04})O_{(z+y/2+3/2)} = 3.51(H_2O)_x = 1.92$ . The calculated density and composition are for the calcium–oxygen layers and silicate of C–S–H with the interlayer space fully saturated. They are for “never-dried” material. This is because, even though a sample was dried to determine the actual, as opposed to mix, water-to-cement ratio, and hence chemical shrinkage, all the NMR signal intensities needed to calculate the density and composition were recorded before the drying procedure.

C–S–H is often considered to form in agglomerates of sheets. The NMR derived “solid” C–S–H density excludes water (and any OH groups) on the surfaces of the agglomerates since surface water is in rapid exchange with the gel pore fluid (longer  $T_2$ ). This may explain both a  $w/c$  and an  $\alpha$  dependence of the density that is reported elsewhere [18], since the agglomerate size and hence apparent density may depend on both parameters. If gel water is included in the composition, the “bulk” density and water content are  $\rho_{CSH}^x = 1.89 \text{ g/cm}^3$  and  $x' = 5.25$ , respectively.

We note that taking the alternate means of dividing the solid signal between ettringite and CH changes the derived parameters typically by  $<1\%$ . The biggest impact is upon  $z$  which changes by about 3%.

Pore sizes may be measured by NMR using either the fast exchange model of relaxation [19] or the change in signal amplitudes with drying [20]. We have used both methods. In the case of the fast exchange model we combine a water monolayer thickness of  $0.28 \text{ nm}$  and the interlayer water  $T_2$  at low RH,  $75 \mu\text{s}$  ( $20 \text{ MHz}$ ), for the fast-exchange surface-relaxivity and thereby calculate  $3.1 \text{ nm}$  for the gel pores and  $0.94 \text{ nm}$  for the interlayer spacing. Sample drying yields  $3.4 \text{ nm}$  and  $1.6 \text{ nm}$  respectively. This last result is larger than expected, almost certainly because the underlying assumptions of the drying model break down in such a small space. Given the pore widths, the specific surface area (SSA) can be evaluated. From fast exchange, it is  $91 \text{ m}^2/\text{cm}^3$  of paste for gel pores and  $175 \text{ m}^2/\text{cm}^3$  for interlayer spaces in accord with earlier undifferentiated estimates [8,9].

## 5. Discussion

A feature of the data is that we see much less (about  $\frac{1}{3}$  to  $\frac{1}{2}$ ) capillary porosity than expected from the Powers and Brownward model [21,22]. In further work [18], we show that the primary capillary pore reservoir quickly diminishes in total volume throughout

hydration and that the characteristic pore size asymptotically decreases to circa 10 nm. We propose that this reservoir corresponds to inter-hydrate water and that it is not intrinsic to the C–S–H.

The lack of capillary porosity is significant as it strongly affects mechanical and transport properties of cement. It impacts the way in which the C–S–H gel fills space and hence the design of hydration models that seek to describe cement morphology numerically. Also, it implies that the finer gel pores must play a correspondingly greater role in controlling the rate of ingress of dissolved, aggressive ions such as chlorides and sulphates.

Fig. 2 is a pictorial representation of C–S–H morphology and water placement consistent with our results. It depicts a continuous network of C–S–H layers and gel pores. The picture is similar to the widely reproduced figure of the FS model [12]. The principle difference is that FS viewed it as a picture of C–S–H only with interlayer spaces and pores due to local disorder in C–S–H stacking; together accounting for most of the C–S–H water as defined by Powers and Brownyard [21] at full saturation.

The alternate model, CM-II [7], describes C–S–H as colloidal globules, the globules being made up of particles each comprising a few C–S–H sheets. Particle sizes are 2–5 nm from SANS. As well as the interlayer spaces, CM-II proposes intra-globular pores within particles due to stacking faults (circa 1 nm), “small” pores between particles (circa 1–3 nm) and “large” pores between globule flocs (circa 3–12 nm). As evidenced by growth during the early stages of hydration, NMR shows evidence of only 2 nanoscale pore types intrinsic to the C–S–H, interlayer spaces and gel pores. In particular, there is no evidence for intra-globular pores. This is discussed more fully elsewhere [18].

Assuming that the lateral extent of C–S–H sheets and gel pores are similar, then, by comparing their respective SSA the sheet stacks can only be about two to three sheets thick. Based on the mineral analogue tobermorite-14 [3], the thickness is 2.8–4.2 nm. Interestingly, this is in accord with the particle size of CM-II.

With density and water fraction, one has to be careful to compare like-with-like. Most results are either for fully saturated gel (C–S–H plus gel water) in which case  $x' \approx 5$   $\rho \approx 1.8$  g/cm<sup>3</sup> is typical, or for dried material in which case  $x = 1.3$ –1.5  $\rho = 2.2$ –2.6 g/cm<sup>3</sup> [7]. SANS gives  $\rho = 2.604$  g/cm<sup>3</sup> and  $x = 1.8$

for a fully saturated globule of CM-II [2], excluding water adsorbed on the outer particle surfaces. The NMR density also excludes water on the outer surface of locally aggregated C–S–H sheets since this water is in fast exchange with the gel pore water.

If, based on the pore size and SSA reported above, we assume that C–S–H typically comprises 3 sheets of repeat thickness 1.4 nm (based on tobermorite-14) including 2 external monolayers of water, compared to 3 sheets without the external monolayer, then the additional volume is  $\Delta V = 2 \times 0.28 \times 10^{-9}$  m<sup>3</sup>/m<sup>2</sup> of sheet on an original volume of  $V = (3 \times 1.4 - 2 \times 0.28) \times 10^{-9}$  m<sup>3</sup>/m<sup>2</sup>. If this volume is filled with water, then the density of the C–S–H is reduced from 2.68 to 2.46 g/cm<sup>3</sup>. This is now very close to the value of,  $\rho = 2.47$  g/cm<sup>3</sup> reported by Jennings for a saturated globule with a monolayer of water at 11% RH. The water content result  $x' = 5.25$ , applicable when all the gel water is included in the calculation, is close to 5 as arises in CM-II with saturated LGP. Thus, throughout, the NMR structural parameters are in reasonable agreement with those of CM-II derived primarily from SANS, even though the NMR and SANS results are not interpreted in terms of the same morphological model. Finally we note that our value of Ca/(Si + Al) (1.53 at  $w/c = 0.463$ ) is consistent with the results of Rayment and Majumdar [23], who found average inner and outer product values of Ca/(Si + Al + S + Fe) ranging from 1.70 at  $w/c = 0.3$  to an average of 1.48 at  $w/c = 0.6$ , and also the results of Q. Li as reported in [24] who found values of 1.56 and 1.73 after 7 days hydration for inner and outer product respectively in cement similar to that used in this study.

## 6. Conclusion

To conclude, we have measured the density, Ca/(Si + Al) ratio and water fraction of C–S–H pertaining to never-dried white cement using widely available NMR equipment supported by XRD. Controlled sample drying and NMR were used to determine a pore size resolved desorption isotherm and the chemical shrinkage. The quick and easily performed experiments create means to characterise rapidly many novel, potentially improved, cements.

## Acknowledgements

We thank Y.-Q. Song (Schlumberger-Doll Research) for 2D-FLI software. Funding was provided by the European Union (FP7/2007–2013 grant 264448), the UK EPSRC (grant EP/H033343/1) and Nanocem.

## References

- [1] World Business Council for Sustainable Development, Cement Sustainability Initiative, <http://www.wbcsdcement.org> (accessed 1st December 2011).
- [2] A.J. Allen, J.J. Thomas, H.M. Jennings, *Nat. Mater.* 6 (2007) 311–316.
- [3] I.G. Richardson, *Cem. Conc. Res.* 38 (2008) 137–158.
- [4] R.J.-M. Pellenq, A. Kushimac, R. Shahsavari, K.J. Van Vliet, M.J. Buehler, S. Yip, F.-J. Ulm, *PNAS* 106 (2009) 16102–16107.
- [5] J.J. Thomas, J.J. Biernacki, J.W. Bullard, S. Bishnoi, J.S. Dolado, G.W. Scherer, *A. Luttg. Cem. Conc. Res.* 41 (2011) 1257–1278.
- [6] L.B. Skinner, S.R. Chae, C.J. Benmore, H.R. Wenk, P.J.M. Monteiro, *Phys. Rev. Lett.* 104 (2010) 195502-1–195502-4.
- [7] H.M. Jennings, *Cem. Conc. Res.* 38 (2008) 275–289.
- [8] W.P. Halperin, J.-Y. Jehng, Y.-Q. Song, *Magn. Reson. Imaging* 12 (1994) 169–173.
- [9] F. Barberon, J.-P. Korb, D. Petit, V. Morin, E. Bermejo, *Phys. Rev. Lett.* 90 (1034) (2003) 116103-1–116103-4.
- [10] P.J. McDonald, J.-P. Korb, J. Mitchell, L. Monteilhet, *Phys. Rev. E* 72 (2005) 011409-1–011409-9.
- [11] R. Holly, E.J. Reardon, C.M. Hansson, H. Peemoeller, *J. Am. Ceram. Soc.* 90 (2007) 570–577.
- [12] R.F. Feldman, P.J. Sereda, *Eng. J.* 53 (1970) 53–59.
- [13] J.G. Powles, J.H. Strange, *Proc. Phys. Soc. London* 82 (1963) 6–15.
- [14] S. Meiboom, D. Gill, *Rev. Sci. Instr.* 29 (1958) 688–691.
- [15] L. Venkataraman, Y.-Q. Song, M.D. Hurlimann, *IEEE Trans. Signal Process* 50 (2002) 1017–1026.

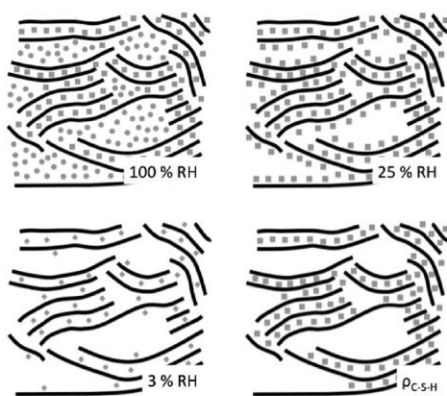


**Fig. 2.** A schematic of C–S–H morphology at 100,  $\approx 25$ , and  $\approx 3\%$  RH. Solid lines are sheets of Ca ions and SiO<sub>2</sub> tetrahedra. Circles are water molecules in gel pores with intermediate  $T_2 \approx 420$   $\mu$ s. Squares are molecules in interlayer spaces and, at lower RH, residual gel pore surface molecules with  $T_2 \approx 126$   $\mu$ s. Diamonds are immobile molecules that appear solid like at the lowest RH values, with  $T_2 \approx 10$   $\mu$ s. Bottom right shows only those water molecules that, at 100% RH, are included in the density measurement. Note that where locally there are, e.g. 3 sheets, then there are 2 interlayers and where there are 2 sheets there is 1 interlayer. The apparent density therefore varies with the number of sheets. Additional Ca ions associated with the water between the sheets are not shown.

- [16] D. Kulik, GEMS-PSI 2.1, PSI-Villigen, Switzerland, 2005. <http://les.web.psi.ch/Software/GEMS-PSI/>.
- [17] D.P. Bentz, *Cem. Conc. Res.* 38 (2008) 196–204.
- [18] A.C.A. Muller, K.L. Scrivener, A.M. Gajewicz, P.J. McDonald, *J. Phys. Chem. C* 117 (2013) 403–412.
- [19] F. D'Orazio, S. Bhattacharja, W.P. Halperin, K. Eguchi, T. Mizusaki, *Phys. Rev. B* 42 (1990) 9810–9818.
- [20] P.J. McDonald, V. Rodin, A. Valori, *Cem. Conc. Res.* 40 (2010) 1656–1663.
- [21] T.C. Powers, T.L. Brownyard, Portland Cement Association (Bulletin 22), Chicago (1948), reprinted from *Proc. J. Am. Concr. Inst.* 43 (1947) p. 101, 249, 469, 549, 669, 845, 993.
- [22] H.F.W. Taylor, *Cement Chemistry*, Thomas Telford, London, 1997. p. 238.
- [23] D.L. Rayment, A.J. Majumdar, *Cem. Conc. Res.* 12 (1982) 753–764.
- [24] V. Kocaba, Development and evaluation of methods to follow microstructural development of cementitious systems including slags, Ph.D. thesis, Ecole Polytechnique Fédérale de Lausanne, 2009.



## The mechanism of water–isopropanol exchange in cement pastes evidenced by NMR relaxometry

Cite this: *RSC Adv.*, 2014, 4, 20709

Radoslaw M. Kowalczyk, Agata M. Gajewicz and Peter J. McDonald\*

Received 30th January 2014  
Accepted 28th April 2014

DOI: 10.1039/c4ra00889h

www.rsc.org/advances

<sup>1</sup>H nuclear magnetic resonance (NMR) relaxometry shows that arresting the hydration of cement paste by isopropanol exchange does not involve simple replacement of the pore water with isopropanol. Isopropanol fills capillary voids. It removes and replaces the water in the calcium-silicate-hydrate (C-S-H) interhydrate pores. In the C-S-H gel pores, the isopropanol draws water out, but does not replace it to the same extent. The exchange has only a minor impact on C-S-H interlayer water. The connectivity of the interlayer-gel network and interhydrate pores and capillary voids is evidenced by proton–deuteron chemical exchange in the C-S-H pore structure which is observed experimentally for the first time. Isopropanol also reveals the presence of large capillary voids that are not detected in samples saturated with water.

### 1. Introduction

Arresting the growth of calcium-silicate-hydrate (C-S-H) and other hydration products both effectively and efficiently is a precursor to many studies seeking to understand the properties and morphology of cement pastes.<sup>1,2</sup> Removing the free water available for hydration processes is an important route for achieving this. Numerous studies have therefore addressed the structural and chemical changes which occur during different drying (*e.g.* oven, vacuum, freeze) and solvent exchange procedures.<sup>3,4</sup> They have been reviewed by Zhang and Scherer.<sup>2</sup> The method of exchanging water with organic solvents such as methanol, isopropanol and acetone has been found to be very effective and relatively quick in stopping hydration.<sup>5</sup> However, the influence of the solvent on the physical and chemical properties of the paste can be substantial and may cause irreversible damage to the microstructure.<sup>6–8</sup> The predominant conclusion is that isopropanol causes the least damage as evidenced by measurable macroscopic shrinkage and therefore isopropanol exchange is often the method of choice for arresting the hydration of cement.<sup>5,6,9,10</sup>

The drying of either water or solvent can modify the structure of even well matured pastes due to the loss of water from the different nano-scale pore reservoirs of the hydrate products.<sup>3,4</sup> Therefore, a key limitation of almost all the prior studies of solvent exchange is that the cement samples have been characterised not only after the water, but also the solvent, was removed.<sup>4,8,11</sup> The structure is not characterised in the presence of either the water or the solvent in “never-dried” conditions. Studying “as-prepared” samples is necessary to understand the

influence of the exchange *per se* on the nano-scale morphology. However, there are only very limited reports of such experiments.<sup>7,9</sup> In the case of morphology, these experiments have been made at the macroscopic level by measurement of expansion/contraction and solvent diffusion (weight loss).

Nuclear Magnetic Resonance (NMR) relaxometry is one of the most powerful techniques to study porous materials.<sup>12,13</sup> By monitoring differences in the spin–spin,  $T_2$ , and spin–lattice,  $T_1$ , relaxation times of liquids within pores it is possible to obtain direct information about the pore size distribution and pore connectivity in porous media in general and cements and mortars in particular.<sup>14–17</sup> A key advantage of NMR relaxometry over alternative methods for the study of cements is that the pore water is itself the direct probe of the confining nano-structure. There is no requirement to dry or otherwise prepare the sample. In the case of cement pastes, <sup>1</sup>H NMR of water reveals the hierarchy of water combined in nano-crystallites (Ca(OH)<sub>2</sub> and ettringite in the approximate mass ratio 4 to 1 (ref. 18)), calcium-silicate-hydrate (C-S-H) interlayer space and gel pore water, interhydrate pore water and capillary pore reservoirs shown schematically in Fig. 1.

NMR has been used to study kinetics and microstructural consequences of the drying and rewetting of the cement pastes and mortars.<sup>19–21</sup> Isopropanol drying, that is isopropanol exchange followed by its removal by slow oven drying, has been used in conjunction with NMR to conclude that oven drying has significantly more destructive influence on mortar microstructure than isopropanol drying.<sup>22</sup> The direct effect of the isopropanol on the microstructure, without solvent removal has not been investigated.

This contribution reports a study of the mechanism of isopropanol drying in cement pastes and of the changes to microstructure that it induces. The focus is an analysis of the

Department of Physics, University of Surrey, Guildford, GU2 7XH, UK. E-mail: p.mcdonald@surrey.ac.uk

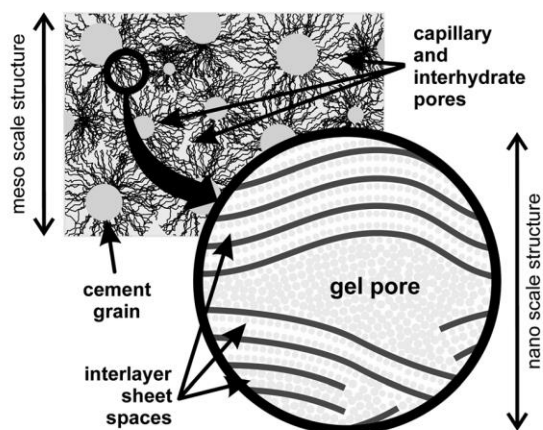


Fig. 1 The schematic structure of the calcium-silicate-hydrate (C-S-H) on the meso- and nano-scale (white cement paste).

filled porosity directly through the exchange solvent using  $^1\text{H}$  relaxometry. Without drying the sample, the reversibility of the process is investigated. Measurements have been made on samples prepared with both  $\text{H}_2\text{O}$  and  $\text{D}_2\text{O}$  and exchanged with both isopropanol and partially deuterated isopropanol.

This study finds that isopropanol acts as a drying agent by removing and selectively replacing water molecules in the interhydrate and capillary network. It also draws out the gel pore water but does not fully replace it in these spaces. It has more minor impact on the C-S-H interlayer water. There is however contact between the highly confined water in the interlayers and the network of larger pores as evidenced by the observation of the proton–deuteron chemical exchange between the liquids.

## 2. Materials and methods

Cement pastes were prepared by mixing white Portland cement powder with distilled water in the water to cement (w/c) mass ratio 0.46 (except where stated otherwise) using an electric blender. The ratio was adjusted to 0.51 when the cement powder was mixed with deuterated water (Sigma-Aldrich) to account for the larger atomic mass of  $\text{D}_2\text{O}$  compared to  $\text{H}_2\text{O}$ . The mixing was carried out in cylindrical polyethylene beakers in three steps: (i) mixing for 3 minutes with the rotor speed 500 rpm, (ii) 2 minutes of resting and (iii) mixing for 2 minutes at 2000 rpm. Directly after mixing, the paste was transferred to polyethylene moulds 8 mm in diameter and 20 mm long. Special care was taken to avoid entrapping any air bubbles. The moulds were transferred to containers filled with lime water, air sealed and left to allow the cement paste to harden. After 24 h the cement paste cylinders were removed from the moulds and transferred to small glass bottles filled with lime water (*ca.* 1 part of lime water to 15 parts of sample) in order to continue curing underwater. In the case of deuterated samples,  $\text{D}_2\text{O}$  was used in all curing steps (>99.9% purity). Samples were cured for 50 days at 21 °C. Underwater curing caused the effective w/c

ratio to increase to >0.5 as evidenced by recording the mass of selected samples dried above the 1000 °C.

Post-curing, some samples were crushed into millimetre sized granules and solvent exchange was carried out in glass bottles for 72 h. Reagent grade isopropanol (Sigma-Aldrich) was used as the primary exchange solvent. Exchange was performed over 3 wash cycles of 24 hours each using fresh solvent for each cycle. The solvent to sample volume ratio was at least 20 : 1. Bottles were constantly rolled to assure homogeneity of the exchange fluid. To test reversibility, a second exchange was carried out using deionised water (Sigma-Aldrich) following the same procedure. Further, to ensure that three washes was sufficient for full exchange, some measurements were carried out after as many as five washes. The results were substantially the same.

As well as regular isopropanol,  $(\text{CH}_3)_2\text{CHOH}$ , partially deuterated isopropanol with the composition  $(\text{CH}_3)_2\text{CDOD}$  was also used. The level of deuteration was greater than 98%. The specific isotopic substitution was chosen to negate the impact on  $^1\text{H}$  NMR measurements of H–D exchange between the solvent and pastes prepared with  $\text{D}_2\text{O}$ . Isopropanol hydroxyl hydrogens are expected to exchange easily with deuterons in  $\text{D}_2\text{O}$ . A  $^1\text{H}$  NMR spectrum of regular isopropanol (0.2%) in  $\text{D}_2\text{O}$  was acquired at 500 MHz in order to assess whether isopropanol methyl and, in particular, C2 hydrogens also exchange. The spectrum is shown in Fig. 2. The methyl doublet at 1.05 ppm has a total intensity 6 times that of the 7 line multiplet of the C2 hydrogen at 3.9 ppm. This implies that if hydrogen at these two sites exchange with deuterated water, then they exchange directly in proportion to their  $^1\text{H}$  number density. The  $\text{H}_2\text{O}/\text{HDO}$  line at 4.7 ppm is 1.67 times as intense as that of the C2 hydrogen. One unit of this intensity arises from the exchanged  $\text{OH}-\text{D}_2\text{O}$ . The remaining 0.67 is attributed to hydrogen impurity in the  $\text{D}_2\text{O}$ . An intensity of 0.67 is less than would be expected based on the minimum stated purity of the  $\text{D}_2\text{O}$  (99.9%). This is strong evidence that no measurable fraction of methyl or C2

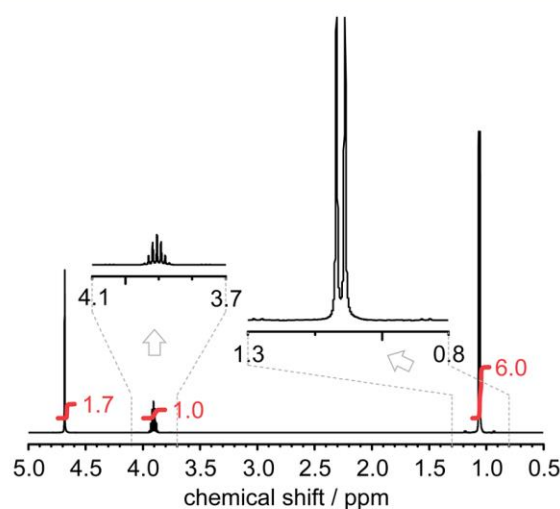


Fig. 2 The  $^1\text{H}$  high resolution spectrum of 0.2%  $(\text{CH}_3)_2\text{CHOH}$  in  $\text{D}_2\text{O}$ .

hydrogen exchanges. Therefore by using  $(\text{CH}_3)_2\text{CDOD}$ , we eliminate concern about D associated with water-of-mixing contaminating the isopropanol  $^1\text{H}$  NMR signal. Of course,  $(\text{CH}_3)_2\text{CHOD}$  would have been equally useful, but was not available.

Relaxation NMR measurements were performed using a  $^1\text{H}$  NMR Kea benchtop spectrometer operating at 20 MHz (Magritek, New Zealand). The Carr–Purcell–Meiboom–Gill (CPMG) pulse sequence<sup>23</sup> was applied to record a train of logarithmically spaced echoes in the range of 26  $\mu\text{s}$  to 1.5 s (typically 512 echoes, 32 points per echo with a sampling rate 1 MHz). The lower time limit was governed by duration of the pulse ( $P_{90} = 5 \mu\text{s}$ ) and dead time of the spectrometer (10  $\mu\text{s}$ ). Up to 1024 averages were acquired with a recycling time of 2.5 s.

The crystalline solid fraction of the distribution was measured using the solid (or quadrature) echo experiment.<sup>24</sup> Two  $90^\circ$  radio frequency pulses were applied to refocus static dipolar interactions. The signal was recorded as a function of the spacing,  $\tau$ , between the pulses in the range 10 and 35  $\mu\text{s}$ . The solid echo and mobile water amplitudes as a function of  $\tau$  were back extrapolated to zero time thus providing a good estimate of the fraction of water combined in  $\text{Ca}(\text{OH})_2$  and ettringite as previously described.<sup>25</sup>

In justification of these parameters, we note that the maximum pore water  $T_1$  values encountered are of the order of 0.1 s, with the overwhelming majority of the pore water volume having  $T_1$  less than 0.01 s. The  $T_1$  of the crystalline solids is of the order of 1 s at high frequency, but less at frequencies comparable to that used here, 20 MHz.<sup>26,27</sup> We measured  $290 \pm 30$  ms. The isopropanol  $T_1$  in large pores is  $\approx 300$  to 400 ms; comparable to, and therefore hard to distinguish from, the solids. That the method is quantitative was previously demonstrated by cross checking against thermal gravimetric analysis and X-ray diffraction.<sup>18</sup>

Measurements were made on two sets of samples. The results were the same within experimental error. For the repeats, that are the samples reported here, the ignited mass of samples was additionally measured by controlled drying to temperatures in excess of 1000  $^\circ\text{C}$  so as to allow more quantitative comparison of results. Unfortunately, insufficient  $(\text{CH}_3)_2\text{CDOD}$  was available for one of the seven experimental repeats, so, for this case alone, normalisation was performed by cross reference to a measurement of normal paste.

The exponential decay of the CPMG echo train intensity provides an estimate of the  $T_2$  relaxation time. This in turn relates to pore size through the fast diffusion model of relaxation.<sup>28,29</sup> Hence, inverse Laplace transform (ILT) of the decay yields the pore size distribution. The inverse Laplace transforms were carried out on echo train decays using the algorithm proposed by Venkataramanan *et al.*<sup>30</sup> In the case of deuterated samples, the signal to noise ratio of the data was sometimes insufficient to properly resolve all the distribution features. In these cases, multiple exponential fitting using the relaxation times known from protonated material was used instead.

There are three aspects to consider with respect to accuracy and reproducibility. The first relates to the ILT. The output of the ILT routine depends to a limited extent on the input

parameters, specifically the regularisation parameter introduced by Venkataramanan *et al.*<sup>30</sup> If it is too small, then the output spectrum is highly broadened and individual peaks merge together. If it is too big then the spectrum breaks up into a very large number of individual peaks. Venkataramanan *et al.* provide a quantitative procedure for optimising this parameter that has been extensively tested on synthetic data. So long as the peaks have not merged the integral intensity (*i.e.* area) of peaks is essentially independent of the regularisation although the height and width measured separately do change. It is therefore the area that is used as “intensity” in this and our earlier<sup>18</sup> work. A related effect is “pearling” whereby two closely neighbouring peaks in a spectrum tend to move towards each other leading to systematic error in the measured  $T_2$ .<sup>31</sup> For this reason, far greater emphasis is placed on the peak intensities than on the  $T_2$  values in the analysis.

In cases where multi-exponential fitting is used, fitting with both intensity and decay constants allowed to float is highly dependent on the initial guess values. This is not a problem when the decay constants are constrained, as here: the algorithm generates reproducible intensities. However, the intensities do depend of the  $T_2$  constraints chosen. As stated, values obtained with ILT from fully protonated material analysis are used.

The second issue arises from measurement uncertainty in the echo data. We have previously made multiple repeats of the NMR measurement on the same sample. We have also analysed data to which synthetic noise has been added. In particular, in order to use the ILT we seek an NMR signal-to-noise ratio in excess of 400. Considering both analysis issues together, the standard deviation of multiple analyses is  $\pm 1\%$  absolute in the peak intensities.

The third source of uncertainty is variability arising from different samples. Since the samples are necessarily small, they are affected by inhomogeneity of mixing, by slight differences in temperature during curing, and especially by surface drying during the short times that they are exposed to air. To mitigate against the first two of these, all but one of the samples reported are from the same batch of cement and were cured together. To mitigate against the last, the samples were exposed for as little time as possible.

The combined uncertainty from all sources is estimated from repeated measurements of the 6 pairs of duplicated samples, and, for protonated samples, direct comparison of ILT and multi-exponential fitting analyses. It is  $\pm 3\%$  absolute in peak intensity in the worst cases.

## 3. Results and discussion

### 3.1 Protonated cement paste

Fig. 3a and the first line of Table 1 show the  $T_2$  distribution in as prepared paste made with  $\text{H}_2\text{O}$ . The distribution shows the expected peaks corresponding to crystalline solid ( $\text{Ca}(\text{OH})_2$  and ettringite) from the quadrature echo experiment at 10  $\mu\text{s}$  with a relative intensity of 24%; to C-S-H interlayer water at 90  $\mu\text{s}$ , 21%; to gel pore water at 300  $\mu\text{s}$ , 44%; to interhydrate pore water at 1.5 ms, 8%; and to capillary pore water at higher  $T_2$  values

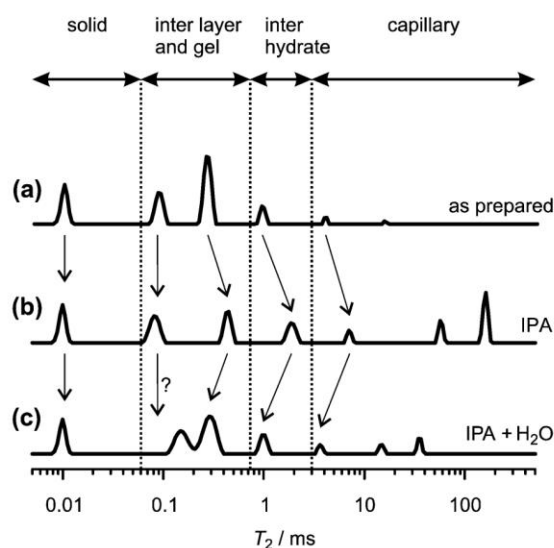


Fig. 3 The distribution graph of the  $T_2$  relaxation times for cement paste. The as-prepared sample cured under  $H_2O$ , (a); exchanged with isopropanol (b); and exchanged back with  $H_2O$  (c).

totaling 3%. These intensities and  $T_2$  values are consistent with previously reported results for a sample cured sealed with  $w/c = 0.48$  (ref. 18) and a sample cured underwater with  $w/c = 0.40$ .<sup>32</sup>

The distribution for an isopropanol exchanged sample, Fig. 3b and the second line of Table 1 is compared to the as prepared paste. The intensities are shown relative to it, per gram of anhydrous cement. The first observation is that the overall signal intensity is scarcely changed at 97%. At first site, this is unsurprising. The  $^1H$  density of water and isopropanol are  $0.111N_A$  and  $0.105N_A \text{ cm}^{-3}$  respectively. Hence, for an equal volume exchange of all the evaporable liquid (approximately 76% of the total water), one expects a 4.1% decrease in signal. However, a more careful examination of the data reveals that the fraction of capillary and interhydrate pore liquid has increased dramatically, from 11% of the total to 39% whereas the C-S-H interlayer and gel pore fraction has decreased from 65% of the total to 34% with most of this change being in the gel

pore fraction. The signal from the crystalline solid is unchanged.

The easiest explanation is that isopropanol exchange damages the pore network resulting in an increase in the number of large pores and a decrease in the number of small pores. That this is unlikely to be a correct explanation is revealed by an experiment to investigate the reversibility of the isopropanol exchange.

The third line of Table 1 and Fig. 3c report results obtained when an as prepared sample is first exchanged with isopropanol and then exchanged back with water. Comparing line 3 of the table with lines 1 and 2, it is seen that the changes in line 2 are substantially reversed. The critical gel, interhydrate and capillary liquid signal intensities are all intermediate between the earlier values. We cannot explain why the  $T_2$  associated with the interlayer component is slightly increased save that the ILT algorithm is known to be susceptible to "pearling".

A better explanation leads to two conclusions. The first is that isopropanol invades large capillary pores that are inaccessible to water. There is considerable previous NMR<sup>18</sup> and other<sup>33</sup> evidence that larger capillary pores are empty in as prepared material, even when the sample is cured underwater. The curing water cannot cross the very low permeability paste sufficiently quickly to maintain full saturation of the capillary porosity created by chemical shrinkage as hydration proceeds. The resultant reduced internal relative humidity of the paste ensures self desiccation of larger pores. For instance, the Kelvin–Laplace radius for water at 98% RH is 53 nm. That isopropanol can enter these larger pores is suggested by the very much smaller contact angle of isopropanol (at least with  $SiO_2$ ) compared to water.<sup>34</sup> It might be considered that the large pores contain a mixture of isopropanol and water. However, it should be remembered that the exchange isopropanol is at least 20 times the sample volume, while the mobile water is only about 44% of the sample volume. Hence the dilution is less than 2.2%. Moreover the system is washed 3 times leading to further dilution: *circa* 10 ppm.

The combined interhydrate and capillary pore signal intensity of the exchanged sample is consistent with this explanation. If it is assumed that 0.38 g of water are required to hydrate 1 g of cement<sup>35</sup> then, given the  $w/c$  ratio at mixing (0.46),  $0.08 \text{ cm}^3$  of

Table 1  $^1H$  signal intensities recorded for water in different environments of as prepared and solvent exchanged pastes. The intensities are normalised to ignited sample mass and such that 100% is the total signal for the normal paste

Sample	Non-evaporable water		Evaporable water			Total signal intensity%
	Nano-crystalline solids	C-S-H interlayer	C-S-H gel pore	Interhydrate spaces	Capillary pores	
As prepared paste	24	21	44	8	3	100
+ IPA	24	18	16	11	28	97
+ IPA + $H_2O$	21	18	37	10	11	97
Paste prepared with $D_2O$	1	1	3	0	2	7
+ $H_2O$	21	18	40	9	10	98
+ IPA(D)	2		11	6	24	43
+ IPA	18	11	14	13	15	71

water are available for interhydrate and capillary pores at full hydration. Further, the sample undergoes chemical shrinkage of about  $0.075 \text{ cm}^3 \text{ g}^{-1}$  of anhydrous cement.<sup>18</sup> This creates voidage that is accessible to isopropanol. Hence, in an exchanged sample, the capillary liquid occupies  $0.155 \text{ cm}^3$ , or 29% of the total liquid volume, at full hydration. At a more realistic value of degree of hydration (85% (ref. 18)) the expected capillary liquid fraction is 38%. A similar dilution argument applies for reverse exchange. However, in this case, what is now nearly pure water cannot enter large pores due to the Kelvin–Laplace law. They are once again left empty.

The second conclusion is that isopropanol dries gel pores by drawing water out of the C-S-H network, without fully invading and replacing it. The evidence is the hugely reduced gel pore signal in line 2 compared to line 1 in Table 1. This is presumably because the gel pore entrances are small, isopropanol has a larger molecular size than water and isopropanol is very hygroscopic. The interlayer signal is reduced to a much lesser extent in the isopropanol exchange sample compared to the as prepared material. This suggests that isopropanol does not replace water in the interlayer spaces. It seems unreasonable to assume that the isopropanol has exchanged these (smaller) sites if it cannot exchange the larger gel pores, an assumption verified in the experiments using deuterated cement paste discussed below.

A further observation of these first experiments is that the  $T_2$  associated with the gel-pore liquid is somewhat greater in the exchanged sample than in the as prepared sample. There are two possible reasons for this. First, the surface relaxation time of isopropanol molecules in cement, that controls the pore liquid  $T_2$ , may be greater than that of water molecules. One reason is that the average distance of closest approach of an isopropanol  $^1\text{H}$  may be greater than that of a water  $^1\text{H}$ . A second reason may be that there is a distribution of gel pore sizes. They are all empty of water, but the isopropanol only re-invades the larger of them. Since the observed  $T_2$  varies with pore size, the bias to larger pores increases the mean gel pore liquid  $T_2$ . The former explanation is preferred since a similar fractional increase is seen for the other mobile reservoirs.

### 3.2 Deuterated cement paste

The experiments so far reported cannot distinguish between water and isopropanol molecules. The fourth line of Table 1 shows that negligible signal is recorded from a paste made with, and cured under,  $\text{D}_2\text{O}$ . The signal that does appear is almost certainly due to H–D exchange occurring during the mixing and curing process.

If a deuterated sample is subsequently exchanged with  $\text{H}_2\text{O}$ , then all the original peaks occur as shown by line 5 of the table. The signals recorded for the crystalline solid, C-S-H interlayer and gel porosity are almost exactly as in line 1. In the case of the solid, this is somewhat surprising. It suggests that the solid is nanocrystalline with a very high specific surface area in close contact with the porosity. Otherwise, such H–D exchange would seem unlikely to occur. In the case of the interhydrate and capillary pores, the signal is somewhat larger than originally

seen. There is no obvious reason for this. It has been reported elsewhere that cement mixed with  $\text{D}_2\text{O}$  hydrates more slowly than that cured with  $\text{H}_2\text{O}$ .<sup>36</sup> It is possible that this results in more numerous, smaller, pores that water can invade more easily. However, there is minimal evidence for this in the measured  $T_2$  values, that, if anything are larger. It may be that a more slowly developing capillary porosity is less susceptible to self desiccation in under-deuterated-water cured paste and that subsequently the  $\text{D}_2\text{O}$  can readily exchange by H–D exchange, if not full molecular transport.

The sixth line of the table reports the results of a  $\text{D}_2\text{O}$  mixed and cured paste exchanged with partially deuterated isopropanol. Recall, that the isopropanol is deuterated at all sites likely to undergo H–D exchange with  $\text{D}_2\text{O}$  but is otherwise protonated so that a  $^1\text{H}$  NMR signal can be measured from it. The first observation is that minimal signal is measured from the crystalline solid (2%). As expected, and unlike  $\text{H}_2\text{O}$ , there is no significant H–D exchange taking place from the deuterated isopropanol. The second observation is the modest signal from the C-S-H gel (11%). It is almost impossible to divide this 11% between C-S-H interlayer and gel pore signal. We surmise that it comes from isopropanol molecules able to invade the largest gel pores. This conclusion agrees with the interpretation of the data in line 2. If 11% is multiplied by 8/6 to account for the partial deuteration, then this becomes 15%, close to the corresponding entry in line 2, 16%. A third observation is that a large signal is seen from the capillary network, totaling 30%. Multiplying this by 8/6 yields a 40% signal associated with large pores compared to 39% in the regular paste exchanged with regular isopropanol.

Finally, we report in line seven, the results of exchanging the deuterated paste with regular isopropanol. There is now the opportunity for both isopropanol–water molecular exchange and H–D chemical exchange. We see evidence of both. There are strong signals from all environments including the solid and C-S-H interlayer (indicating chemical exchange) and all the pore reservoirs. However, overall, the signal intensities are consistently about 3/4 as intense as those observed in protonated paste exchanged with protonated isopropanol suggesting that perhaps the H–D exchange is not complete.

### 3.3 Time dependency of exchange

As a final note of caution, we present evidence that full equilibration of the exchange process is very slow in larger paste samples. The work presented so far was carried out on millimetre sized pieces of paste and exchange occurred in 1–3 days. Fig. 4 shows the change in signal fraction attributed to liquid in the interlayer and gel pores combined and the capillary pores during isopropanol exchange for a centimetre sized cylinder mixed at w/c ratio 0.4. The capillary component increases from about 3 to 20% of the water fraction showing that the capillary pores are not filled initially even though the sample is cured underwater.<sup>33</sup> The revealed capillary porosity is comparable to expectation. The combined interlayer and gel fraction decreases from about 70 to 27% showing as before water drawn out, but not replaced, in comparable fraction. The surprise is the time constants involved. Based on the dotted line exponential fits to

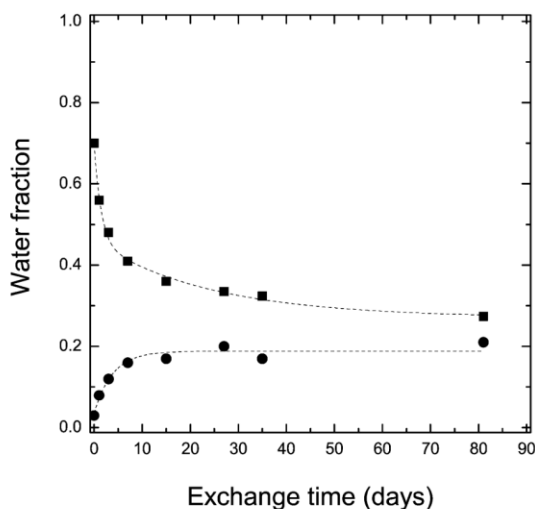


Fig. 4 The decrease of the combined gel and interlayer pore signal (squares) and increase of the capillary pore signal (circles) during isopropanol exchange of a large sample. The dotted lines are exponential fits to the data, the upper one having two components.

the data, these are 1.5 days to draw water out from the gel, 4 days to fill the capillaries, and 25 days to equilibrate water in the interlayer spaces and on the gel surface that appears interlayer-like in partially dried material.<sup>32</sup> It is evident that full equilibration takes of the order of 1 to 2 months.

## 4. Conclusions

The study shows that, during arrestation of hydration in cement pastes by isopropanol exchange, isopropanol invades empty capillary pores. Isopropanol draws water out of C-S-H gel pores and to a much lesser extent interlayer spaces. However, isopropanol does not enter the C-S-H to the same extent. It only invades the more accessible (larger?) gel pores.

The work also shows that water confined in the interlayer-gel network chemically exchanges deuterons and protons with liquid residing in the larger interhydrate and capillary pore network. This demonstrate experimentally for the first time the interconnectivity of interlayers and gel pores with large interhydrate pores and capillary voids.

Water-isopropanol exchange reveals the presence of large capillary pores which water is unable to fill but which are fully accessible to isopropanol. This confirms earlier explanations as to why NMR porosimetry with water is unable to detect large pores – they are empty.

## Acknowledgements

We thank Goss Scientific Instruments Ltd. for providing the partially deuterated isopropanol; Aalborg Portland for providing white cement; and Patrik Galvosas for making available ILT software. This work was funded by the European Commission (grant no. FP7/2007-2013-264448) and the UK

Engineering and Physical Sciences Research Council (grant no. EP/H033343/1).

## Notes and references

- J. W. Bullard, H. M. Jennings, R. A. Livingston, A. Nonat, G. W. Scherer, J. S. Schweitzer, K. L. Scrivener and J. J. Thomas, *Cem. Concr. Res.*, 2011, **41**, 1208–1223.
- J. Zhang and G. W. Scherer, *Cem. Concr. Res.*, 2011, **41**, 1024–1036.
- A. Korpa and R. Trettin, *Cem. Concr. Res.*, 2006, **36**, 634–649.
- N. C. Collier, J. H. Sharp, N. B. Milestone, J. Hill and I. H. Godfrey, *Cem. Concr. Res.*, 2008, **38**, 737–744.
- L. Konecny and S. J. Naqvi, *Cem. Concr. Res.*, 1993, **23**, 1223–1228.
- J. J. Beaudoin, P. Gu, J. Marchand, B. Tamtsia, R. E. Myers and Z. Liu, *Adv. Cem. Based Mater.*, 1998, **8**, 56–65.
- D. C. Hughes, *Cem. Concr. Res.*, 1988, **18**, 321–324.
- R. F. Feldman and J. J. Beaudoin, *Cem. Concr. Res.*, 1991, **21**, 297–308.
- J. J. Beaudoin, B. Tamtsia, J. Marchand and H. R. Myers, *Cem. Concr. Res.*, 2000, **30**, 359–370.
- R. F. Feldman, *Cem. Concr. Res.*, 1987, **17**, 602–612.
- E. Knapen, O. Cizer, K. Van Balen and D. Van Gemert, *Construct. Build. Mater.*, 2009, **23**, 3431–3438.
- R. Kimmich, *NMR: Tomography, Diffusometry, Relaxometry*, Springer, 1st edn, 2001.
- Y.-Q. Song, *New J. Phys.*, 2012, **14**, 055017.
- R. Blinc, M. Burgar, G. Lahajnar, M. Rozmarin, V. Rutar, I. Kocuvan and J. Ursic, *J. Am. Ceram. Soc.*, 1978, **61**, 35–37.
- K. S. Mendelson, W. P. Halperin, J.-Y. Jehng and Y.-Q. Song, *Magn. Reson. Imaging*, 1994, **12**, 207–208.
- P. J. McDonald, J. P. Korb, J. Mitchell and L. Monteilhet, *Phys. Rev. E: Stat., Nonlinear, Soft Matter Phys.*, 2005, **72**, 011409.
- R. Holly, E. J. Reardon, C. M. Hansson and H. Peemoeller, *J. Am. Ceram. Soc.*, 2007, **90**, 570–577.
- A. C. A. Muller, K. L. Scrivener, A. M. Gajewicz and P. J. McDonald, *J. Phys. Chem. C*, 2013, **117**, 403–412.
- R. Valckenborg, L. Pel, K. Hazrati, K. Kopinga and J. Marchand, *Mater. Struct.*, 2001, **34**, 599–604.
- S. D. Beyea, B. J. Balcom, T. W. Bremner, R. L. Armstrong and P. E. Grattan Bellew, *J. Am. Ceram. Soc.*, 2003, **86**, 800–805.
- P. F. Faure, S. Caré, J. Magat and T. Chaussadent, *Construct. Build. Mater.*, 2012, **29**, 496–503.
- L. Pel, K. Hazrati, K. Kopinga and J. Marchand, *Magn. Reson. Imaging*, 1998, **16**, 525–528.
- S. Meiboom and D. Gill, *Rev. Sci. Instrum.*, 1958, **29**, 688–691.
- J. G. Powles and J. H. Strange, *Proc. Phys. Soc., London*, 1963, **82**, 6–15.
- P. J. McDonald, V. Rodin and A. Valori, *Cem. Concr. Res.*, 2010, **40**, 1656–1663.
- L. J. Schreiner, J. C. Mactavish, L. Miljkovic, M. M. Pintar, R. Blinc, G. Lahajnar, D. D. Lasic and L. W. Reeves, *J. Am. Ceram. Soc.*, 1985, **68**, 10–16.
- J. P. Korb, *Curr. Opin. Colloid Interface Sci.*, 2009, **14**, 192–202.

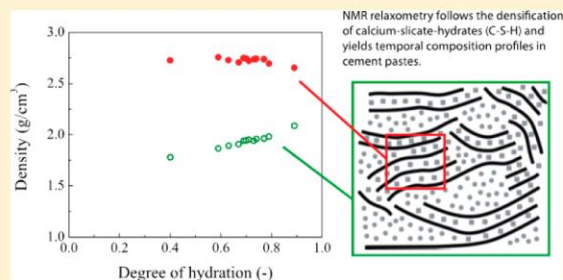
## Paper

## RSC Advances

- 28 K. R. Brownstein and C. E. Tarr, *J. Magn. Reson.*, 1977, **26**, 17–24.
- 29 F. D’Orazio, J. C. Tarczoz, W. P. Halperin, K. Eguchi and T. Mizusaki, *J. Appl. Phys.*, 1989, **65**, 742.
- 30 L. Venkataramanan, Y.-Q. Song and M. D. Hurlimann, *IEEE Trans. Signal Process.*, 2002, **50**, 1017–1026.
- 31 P. T. Callagan, *Translational Dynamics and Magnetic Resonance*, Oxford University Press, 2011.
- 32 A. Muller, K. L. Scrivener, A. M. Gajewicz and P. J. McDonald, *Microporous Mesoporous Mater.*, 2013, **178**, 99–103.
- 33 H. Chen, M. Wyrzykowski, K. Scrivener and P. Lura, *Modelling of internal relative humidity in cement pastes at early-ages* in 2nd International Conference on Microstructural-related Durability of Cementitious Materials, eds. G. Ye, K. van Breugel, W. Sun and C. Miao, RILEM Publications SARL, 2012, 342–349.
- 34 H. J. Busscher, G. A. M. Kip, A. van Silfhout and J. Arends, *J. Colloid Interface Sci.*, 1986, **114**, 307–313.
- 35 H. F. W. Taylor, *Cement Chemistry*, Academic Press, 1990.
- 36 J. J. Thomas, H. M. Jennings and A. J. Allen, *Cem. Concr. Res.*, 1998, **28**, 897–905.

Densification of C–S–H Measured by  $^1\text{H}$  NMR RelaxometryArnaud C. A. Muller,<sup>†</sup> Karen L. Scrivener,<sup>†</sup> Agata M. Gajewicz,<sup>‡</sup> and Peter J. McDonald<sup>\*‡</sup><sup>†</sup>Laboratory of Construction Materials, Ecole Polytechnique Fédérale de Lausanne, CH-1015 Lausanne, Switzerland<sup>‡</sup>Department of Physics, University of Surrey, Guildford, Surrey, GU2 7XH, U.K.

**ABSTRACT:** The nanoscale morphology of, and pore water interactions in, calcium silicate hydrate (C–S–H), the active component of cement, remain uncertain.  $^1\text{H}$  nuclear magnetic resonance (NMR) can fully characterize the nanoporosity of C–S–H in as-prepared material without the need for damaging sample drying. We use NMR to follow the density of C–S–H in sealed cured pastes as a function of degree of hydration ( $\alpha$ ) and water to cement ratio. We show clear evidence for C–S–H densification. The C–S–H “solid” density, exclusive of gel pore water, slightly decreases from  $\rho_x = 2.73 \text{ g/cm}^3$  at  $\alpha \approx 0.4$  to  $2.65 \text{ g/cm}^3$  at  $\alpha \approx 0.9$  due to an increase in the number of layers in the nanocrystalline aggregates. In the same range, the C–S–H “bulk” density, including gel water, increases from around  $1.8$  to  $2.1 \text{ g/cm}^3$ . The increase corresponds to a transition from growth of low-density product containing gel pores to higher density product devoid of gel pores. We update Powers’ classical model from 1947. In contrast to the single “hydrate” of Powers, NMR differentiates between C–S–H and calcium hydroxide and separates out the interlayer water within the C–S–H. It shows a clear nonlinearity in the growth of the different fractions with  $\alpha$ .



NMR relaxometry follows the densification of calcium silicate hydrates (C–S–H) and yields temporal composition profiles in cement pastes.

## ■ INTRODUCTION

Calcium silicate hydrate (C–S–H) is a highly disordered nanoscale material composed of layers of calcium and oxygen, with  $\text{SiO}_2$  tetrahedra attached and interspersed by water and further Ca ions. It is formed in a dissolution–precipitation reaction involving mixtures of tricalcium silicate (Alite) and dicalcium silicate (Belite) with water. Due to the importance of C–S–H as the binder phase of Portland cement, it has been widely studied over many decades. Current interest in C–S–H is fuelled by the substantial contribution of cement production to global  $\text{CO}_2$  production (currently 5–8%<sup>1</sup>) and the requirement to reduce this by the incorporation of supplementary cementitious materials without impacting long-term mechanical performance or durability of concrete.

Notwithstanding extensive effort, the morphology, density, and composition of C–S–H continue to be the subject of active debate in the literature.<sup>2–5</sup> The primary reasons are 2-fold. First, the structures formed are highly dependent on the chemical mixtures and reaction conditions and they may evolve over long periods of time. Second, until very recently, there has not been an experimental method available that is able to adequately characterize as-prepared C–S–H without removing the water: a procedure that damages the very nanoscale structures that are of interest.

In 1947, Powers and Brownard published seminal work<sup>6</sup> that is still widely used and cited. They reported the composition of hydrated cements based on careful study of the water adsorption and desorption isotherms. In the case of white Portland cement, the principal hydration components are solid calcium hydroxide and nanocrystalline C–S–H gel. These products are interspersed with unreacted cement grains,

capillary pores filled with water, and void space. Grudemo<sup>7</sup> was one of the first to propose that the C–S–H gel comprised “solid” regions of layers including some “chemically combined” water with small water-filled pores between these regions now widely known as gel pores. Subsequent work identified two broad types of C–S–H in cement pastes, a more and a less dense phase.<sup>8</sup> These are sometimes attributed to C–S–H that forms in spaces within and between the confines of the original anhydrous cement particles referred to as inner and outer product, respectively.<sup>9</sup> Richardson<sup>10</sup> identified different morphologies of C–S–H by TEM: a fine-scale homogeneous morphology for the inner product and two distinct morphologies for outer product, a fibrillar-like structure and a foil-like structure that appear to correlate with the C/S ratio. [A note on notation: in cement chemistry, C =  $\text{CaO}$ , S =  $\text{SiO}_2$ , H =  $\text{H}_2\text{O}$ , A =  $\text{Al}_2\text{O}_3$ , and CH =  $\text{Ca}(\text{OH})_2$ . The atomic elements without oxides are expressed in a conventional manner. In this work, where it is ambiguous, atomic hydrogen is notated “Hyd”. The abbreviation “AMU” denotes atomic mass units,  $n$  is molar content, and  $f$  is mass fraction of anhydrous powder.] The foil-like structure preferentially forms below a C/S ratio of about 1.5.

Growth mechanisms are likely to play a crucial role in determining the evolved structure. Several authors have proposed mechanisms of C–S–H nucleation and growth from existing surfaces with a quasi-continuous network of C–S–H layers extending from one nanocrystalline region to

Received: October 17, 2012

Revised: December 7, 2012

Published: December 7, 2012

another interspersed by gel pores.<sup>11</sup> Other authors propose nucleation of colloidal particles of C–S–H within the pore solution leading to a morphology arising from coalesced or flocculated particles.<sup>4</sup> In either case, different authors distinguish various types of water-filled spaces including nanometer-thick layers of water between the calcium silicate sheets and slightly larger gel pores between the nanocrystalline regions. In the colloidal model of Jennings,<sup>4</sup> the nanocrystalline regions are referred to as globules and comprise calcium silicate layers with water between. Additionally, there are intraglobular pores within nanocrystallites formed by heterogeneities in the sheet packing, small globular pores between the nanocrystalline particles and large globular pores between particle flocs all within the size range <1–12 nm.

Measurements of the density of C–S–H depend upon method and sample preparation. Results of different studies and calculations have been reviewed by Jennings<sup>4</sup> in the context of the colloidal model and vary between 1.8 and 2.8 g/cm<sup>3</sup>. Much of this variability arises from the fraction of the gel pore water and other nanoscale confined or bound water that is, or is not, inferred to be included in the measurement. It also depends on whether or not the sample has been dried, a process that potentially damages the delicate nanostructure. A recent and widely cited result<sup>12</sup> is the density obtained by small-angle neutron scattering (SANS) for C–S–H in Portland cement hydrated for 28 days at 20 °C. This measurement is made in saturated material but is specifically for the solid nanocrystalline C–S–H excluding the gel pore water:  $\rho = 2.604 \text{ g/cm}^3$ .

In a recent paper,<sup>13</sup> we showed how a simple benchtop <sup>1</sup>H NMR experiment can be used to measure the density of the C–S–H layers and interlayer water exclusive of the gel water and how the water fractions in each of the primary components of the paste may be quantified. The measurement was performed on a 28-day-old paste cured underwater. We also reported the first pore-type resolved desorption isotherm for cement paste. It is the purpose of this paper to exploit this new capability to follow the density of C–S–H throughout the hydration of cement pastes cured under sealed conditions at different water to cement ratios and to show how this leads naturally to clear evidence for densification during growth. The results shed light on the possible ways in which the C–S–H can grow. In a subsequent paper we will extend the adsorption isotherm study to show one and a half complete cycles of the desorption–adsorption isotherm and thus shed light on the manner in which pores first empty and then refill with water.

## ■ THEORY

**C–S–H Density and Composition.** The interpretation of <sup>1</sup>H NMR relaxation data in cements as presented in ref 13 and further discussed in the Results section is based on the observation that the NMR signal can be resolved into five discrete populations of water. The first is a fast relaxing component with a <sup>1</sup>H nuclear spin–spin relaxation time  $T_2$  of the order of 10  $\mu\text{s}$ . It is assigned to <sup>1</sup>H chemically combined in the solid crystalline phases calcium hydroxide and ettringite. Two further components have relaxation times of the order 80–120 and 300–500  $\mu\text{s}$ . These are attributed to water in C–S–H interlayers and to gel pore water, respectively. The fourth and fifth components are assigned to water in nanoscale interhydrate spaces and to water in larger capillary pores and microcracks. A key test that proper account has been taken of all the water in the sample was provided in our earlier paper

where we showed that the total NMR signal loss with drying is linear and consistent with the known water to cement ratio.<sup>13</sup>

This assignment is generally in accord with earlier observations of similar materials made with comparable equipment by Holly et al.<sup>14</sup> However, we note that some other prior studies have lacked the temporal resolution to see the fastest relaxing components, in particular the CH and ettringite while others have failed to separately resolve the C–S–H layer and gel pore water. Moreover, some earlier studies have lacked quantification of signal amplitudes and hence water mass in different environments due to the difficulty of measuring the intensity fraction of chemically combined <sup>1</sup>H. We have overcome this last difficulty by use of a quadrature echo pulse sequence method.<sup>15,16</sup>

With this assignment, mass, and volume balance equations can be written for the paste per gram of anhydrous powder:

$$1 + \frac{w}{c} = (1 - \alpha) + \frac{w}{c} [\beta I_{\text{solid}} + \gamma I_{\text{CSH}} + \delta (I_{\text{gel}} + I_{\text{cap}})] \quad (1)$$

$$\frac{1}{\rho_{\text{uc}}} + \frac{w}{c\rho_w} = \frac{(1 - \alpha)}{\rho_{\text{uc}}} + \frac{w}{c} \left[ \frac{\beta I_{\text{solid}}}{\rho_{\text{solid}}} + \frac{\gamma I_{\text{CSH}}}{\rho_{\text{CSH}}} + \frac{\delta (I_{\text{gel}} + I_{\text{cap}} + I_{\text{void}})}{\rho_w} \right] \quad (2)$$

The subscripts uc, w, solid, CSH, gel, cap, and void refer to unreacted cement, water, chemically combined water, C–S–H, gel pore water, capillary pore water, and chemical shrinkage, respectively. In eq 1, the left-hand side is the sum of the original anhydrous powder and the mix water mass. The right-hand side is the sum of the masses of the different products, written in terms of their respective water contents and signals,  $I$ , as detailed below. Equation 2 reworks eq 1 for volume by dividing by the product densities,  $\rho$ , and adding a term for the chemical shrinkage volume (voidage). The measured water signal intensities,  $I$ , are expressed as a fraction of total signal intensity arising from the original water of mixing which for a sealed paste, is  $I_{\text{solid}} + I_{\text{CSH}} + I_{\text{gel}} + I_{\text{cap}} = 1$ . The signal fraction,  $I_{\text{void}}$ , takes the total above unity. It corresponds to water occupying the chemical shrinkage volume. In underwater-cured samples,  $I_{\text{void}}$  is measured by NMR as explained elsewhere.<sup>13</sup> For sealed cured samples, as here,  $I_{\text{void}}$  is calculated from a separate (not NMR) measurement of the chemical shrinkage volume.

The parameter  $\alpha$  is the degree of hydration, defined as the mass fraction of anhydrous powder consumed in the reactions. The parameters  $\beta$ ,  $\gamma$ , and  $\delta$  are the inverse mass fractions of water in the solid, C–S–H, and pore fluid, respectively. The solid signal is assumed to comprise two parts, CH and ettringite:  $I_{\text{solid}} = I_{\text{CH}} + I_{\text{ett}}$ . The molecular mass of CH, i.e.,  $\text{Ca}(\text{OH})_2$ , is 74 while that of water is 18. Hence,  $\beta_{\text{CH}} = 74/18$ . The fraction of the total water consumed in the CH is  $I_{\text{CH}}$  so that the mass of CH per gram anhydrous cement is  $w\beta_{\text{CH}}I_{\text{CH}}/c$ . Similarly,  $\beta_{\text{ett}} = 1255/576$  and the mass of ettringite is  $w\beta_{\text{ett}}I_{\text{ett}}/c$ . It follows that the total mass and volume of the solid products (CH and ettringite) per gram of anhydrous powder are given by  $(w/c)\beta I_{\text{solid}} = (w/c)(\beta_{\text{CH}}I_{\text{CH}} + \beta_{\text{ett}}I_{\text{ett}})$  and  $(w/c)(\beta I_{\text{solid}}/\rho_{\text{solid}}) = (w/c)(\beta_{\text{CH}}I_{\text{CH}}/\rho_{\text{CH}} + \beta_{\text{ett}}I_{\text{ett}}/\rho_{\text{ett}})$ , respectively. We treat the pore fluid as water, so that  $\delta = 1$ . We take  $\rho_{\text{uc,CH,ett,w}} = 3.15, 2.24, 1.77, \text{ and } 1 \text{ g/cm}^3$ , respectively. Once  $I_{\text{ett}}$  is known,  $I_{\text{CH}}$  may be calculated from  $I_{\text{solid}}$  and known constants, as may  $\beta$  and  $\rho_{\text{solid}}$ .

The unknowns are therefore  $\alpha$ ,  $I_{\text{ett}}$ ,  $\rho_{\text{CSH}}$ , and  $\gamma$ . A measurement of  $\alpha$ , the degree of hydration can be made independently, using, for instance, XRD.  $I_{\text{ett}}$  can be calculated from the mass fraction of ettringite also measured independently, using, for instance, XRD. Hence we have two equations that enable the C–S–H density,  $\rho_{\text{CSH}}$ , and inverse mass fraction of water,  $\gamma$ , to be found.

The C–S–H composition is expressed as  $\text{Ca}_z \cdot (\text{Si}_y\text{Al}_{(1-y)}) \cdot \text{O}_{(z+1/2y+3/2)} \cdot (\text{H}_2\text{O})_x$ . The parameters  $x$ ,  $y$ , and  $z$  may be determined from three further equations. First,  $\gamma$  is related to the number of water molecules  $x$  as

$$x = \frac{56z + 9y + 51}{18(\gamma - 1)} \quad (3)$$

where  $y = n_{\text{Si}}^{\text{CSH}} / (n_{\text{Si}}^{\text{CSH}} + n_{\text{Al}}^{\text{CSH}})$  and  $n_{\text{Si,Al}}^{\text{CSH}}$  are the molar content of Si and Al in the C–S–H. The numerical constants derive from the atomic masses of Ca, Si, Al, O, and H.

Second, a conservation equation can be written for the overall Ca/(Si + Al) ratio. If  $\alpha'$  is defined as the mass of reacted ( $\text{C}_3\text{S} + \text{C}_2\text{S}$ ) divided by the mass of the anhydrous powder, and ignoring minor reactive components other than  $\text{C}_3\text{A}$ , then

$$\frac{3 \left( \frac{0.9\alpha'}{\text{C}_3\text{S}^{\text{AMU}}} \right) + 2 \left( \frac{0.1\alpha'}{\text{C}_2\text{S}^{\text{AMU}}} \right) + 1.5n_{\text{Al}}^{\text{CSH}}}{\left( \frac{0.9\alpha'}{\text{C}_3\text{S}^{\text{AMU}}} \right) + \left( \frac{0.1\alpha'}{\text{C}_2\text{S}^{\text{AMU}}} \right) + n_{\text{Al}}^{\text{CSH}}} = \frac{I_{\text{CH}}^{\text{Hyd}}}{2} + \frac{I_{\text{CSH}}^{\text{Hyd}z}}{2x} + 1.5n_{\text{Al}}^{\text{CSH}} = \frac{I_{\text{CSH}}^{\text{Hyd}y}}{2x} + n_{\text{Al}}^{\text{CSH}} \quad (4)$$

The first term of the numerator of the left-hand side of this expression expresses the fact that there are 3 mol of Ca per mole of  $\text{C}_3\text{S}$ ;  $1/\text{C}_3\text{S}^{\text{AMU}}$  moles per gram of  $\text{C}_3\text{S}$ ; and that, subject to the assumptions detailed below,  $0.9\alpha'$  grams of  $\text{C}_3\text{S}$  is consumed in reactions per gram of anhydrous cement. Similar arguments for Ca from  $\text{C}_2\text{S}$  and for Si from  $\text{C}_3\text{S}$  and  $\text{C}_2\text{S}$  lead to the second term of the numerator and the first two of the denominator, respectively. Ca and Al derived from  $\text{C}_3\text{A}$  lead to the final term in the numerator and denominator, respectively. On the right-hand side,  $n_{\text{Hyd}} = (2/18)(w/c)$  is the molar content of hydrogen in the paste per gram anhydrous powder. The moles of Ca and Si in the CH and C–S–H are written in terms of the signal fractions and  $n_{\text{Hyd}}$ . The Ca and Al contributions to the C–S–H from the  $\text{C}_3\text{A}$  are the same as on the left-hand side. Equation 4 is an elaborated version of eq 4 in our earlier paper.<sup>13</sup> The further assumptions leading to eq 4 as now stated are as follows. First, it is known that in the hydration reaction,  $\text{C}_3\text{S}$  is consumed much more quickly than  $\text{C}_2\text{S}$ .<sup>17</sup> Hence, we assume a consumption ratio of 9:1 in favor of  $\text{C}_3\text{S}$  until it is used up. This implies that eq 4 is valid in the range  $0 < \alpha' \leq f_{\text{C}_3\text{S}}/0.9$  where  $f_{\text{C}_3\text{S}}$  is the fraction of  $\text{C}_3\text{S}$  in the anhydrous powder (assuming  $f_{\text{C}_3\text{S}}/9 < f_{\text{C}_2\text{S}}$ , the  $\text{C}_2\text{S}$  fraction). Equation 4 may be recast for  $f_{\text{C}_3\text{S}}/0.9 < \alpha' \leq 1$  by replacing  $\alpha'$  in the first two terms in both the denominator and numerator of eq 4 by  $f_{\text{C}_3\text{S}}/0.9$  and adding an additional term to the numerator of  $2(\alpha' - f_{\text{C}_3\text{S}}/0.9)/\text{C}_2\text{S}^{\text{AMU}}$  and of half this value to the denominator. Second, X-ray analysis of samples at different ages, to be described in the next section, shows that ettringite all forms early, at most within the first 3 days. Since our analysis mainly focuses on data acquired after 3 days, we make the simplifying assumption that the ettringite forms at the start of the process. Third, we assume that the aluminum from the  $\text{C}_3\text{A}$

remaining after ettringite formation is included in the C–S–H from the start. The factors determining the extent of aluminum uptake into the C–S–H are not well understood.<sup>18</sup> This hypothesis implies there is a negligible amount of alumina in the pore solution, which is in accord with thermodynamics and experimental results.<sup>19</sup> It follows that  $n_{\text{Al}}^{\text{CSH}} = 2(f_{\text{C}_3\text{A}} - f_{\text{C}_3\text{A}}^{\text{ett}})/\text{C}_3\text{A}^{\text{AMU}}$ , where  $f_{\text{C}_3\text{A}}$  and  $f_{\text{C}_3\text{A}}^{\text{ett}}$  are the mass fractions of  $\text{C}_3\text{A}$  in the anhydrous powder and the  $\text{C}_3\text{A}$  mass fraction used to form ettringite, respectively.

Finally, given the above assumptions concerning the formation of ettringite, the Si to (Si + Al) ratio,  $y$ , can be expressed as

$$y = \frac{n_{\text{Si}}^{\text{CSH}}}{n_{\text{Si}}^{\text{CSH}} + n_{\text{Al}}^{\text{CSH}}} = 1 - \frac{4x(f_{\text{C}_3\text{A}} - f_{\text{C}_3\text{A}}^{\text{ett}})}{I_{\text{CSH}}n_{\text{Hyd}}\text{C}_3\text{A}^{\text{AMU}}} \quad (5)$$

The alternate C–S–H composition including gel water,  $\text{Ca}_z \cdot (\text{Si}_y\text{Al}_{(1-y)}) \cdot \text{O}_{(z+1/2y+3/2)} \cdot (\text{H}_2\text{O})_{x'}$ , has

$$x' = x(I_{\text{CSH}} + I_{\text{gel}})/I_{\text{CSH}} \quad (6)$$

In summary, therefore, we find the inverse water content,  $\gamma$ , from eq 1, the NMR intensities and an XRD measurement of the degree of hydration and ettringite content. We go on to find the C–S–H density from eq 2 knowing additionally the chemical shrinkage. Finally, using eqs 3, 4, and 5 and the anhydrous powder composition, we find the three C–S–H composition parameters,  $x$ ,  $y$ , and  $z$ . Of these,  $x$  gives the water content and  $z$  the Ca/(Si + Al) ratio of the C–S–H.

As a final observation, we note that there will always be a (small) experimental discrepancy between the solid content measured by NMR and by, e.g., XRD. This means that there are two means by which the NMR CH content may be determined. One is to subtract the XRD ettringite mass, converted to water fraction from the NMR solid signal. The other is to apportion the NMR solid signal between CH and ettringite in the same ratio as measured by XRD, converted to water fraction. We use the former for two reasons. First, beyond the early stages of hydration that are not considered in this study, the ettringite content is constant (see below) whereas the CH content is increasing. Thus, in principle, a measurement is only required at one time point. Second, the ettringite content is relatively difficult to measure, so an average content from multiple samples may be used. We have tested the alternate method. For our results it leads to changes in the measured parameters at the 1% level. The biggest discrepancy is for  $z$ , where the difference is about 3%.

**Cement Pore Size Distribution.** It is well accepted in the NMR literature that the size of pores may be inferred from NMR relaxation times using the fast diffusion model of relaxation. According to this model,<sup>20</sup> first applied to cement by Halperin et al.,<sup>21</sup> the surface to volume ratio of a filled pore is given by

$$\frac{1}{T_{1,2}} \sim \frac{\varepsilon S}{V} \frac{1}{T_{1,2}^{\text{surf}}} \quad (7)$$

where  $T_{1,2}$  are the measured spin–lattice and spin–spin relaxation times,  $T_{1,2}^{\text{surf}}$  are the corresponding values for surface-adsorbed molecules,  $S$  and  $V$  are the pore surface area and volume, respectively, and  $\varepsilon$  is the thickness of the adsorbed layer. The key unknown here is the surface relaxivity,  $\varepsilon/T_{1,2}^{\text{surf}}$ . In cements, the primary  $^1\text{H}$  relaxation mechanism is interaction with surface  $\text{Fe}^{3+}$  paramagnetic impurities. Korb and co-

workers<sup>22,23</sup> have shown how the relaxivity may be calculated given the surface density of paramagnetic  $\text{Fe}^{3+}$  impurities within the pore and other parameters such as the distance of closest approach of a water molecule to an impurity and the thickness of an adsorbed water layer. In our previous paper,<sup>13</sup> we made an empirical measurement of the surface relaxivity based on the asymptotic value of the relaxation time as the pore water is removed down to monolayer surface coverage ( $75 \mu\text{s}$  at an NMR frequency of 20 MHz) combined with the diameter of a water molecule, 0.28 nm. This gave  $3.73 \times 10^{-3} \text{ nm}/\mu\text{s}$ , an indicative value we use here since the NMR frequency is different. In subsequent calculations we assume planar pores of area  $A$  so that, ignoring edge effects,  $S = 2A$ ,  $V = Ad$ , and hence  $S/V = 2/d$ , where  $d$  is the pore width or "size".

## EXPERIMENTAL METHODS

White cement paste was obtained from Aalborg Portland. The composition of the anhydrous powder is 66.9%  $\text{C}_3\text{S}$ , 20.0%  $\text{C}_2\text{S}$ , 3.5%  $\text{C}_3\text{A}$ , and 4.4% calcium sulfates, with all other phases less than 1%. Typically, 80 g of anhydrous powder was mixed in the desired water to cement ratio,  $w/c$ , for 2 min at 1600 rpm. Aliquots about  $0.35 \text{ cm}^3$  were deposited directly into NMR tubes and tightly sealed with parafilm. A glass rod was included to reduce the free air volume. Samples were stored in a temperature-controlled room at  $20^\circ\text{C}$  during hydration. Samples were periodically measured as prepared, in a temperature-controlled NMR probe. Considerable care was taken to ensure the reproducibility of the results across multiple repeat samples and repeat measurements.

$^1\text{H}$  NMR measurements were made on a Bruker Minispec NMR spectrometer operating at 7.5 MHz. The  $90^\circ$  pulse length was  $2.9 \mu\text{s}$ . Both quadrature (solid) echo<sup>15</sup> and Carr–Purcell–Meiboom–Gill CPMG<sup>24</sup> (spin) echo measurements were made. The quadrature echo signals were recorded as a function of pulse gap in the range  $\tau = 15\text{--}45 \mu\text{s}$ . They were deconvoluted into a Gaussian and an exponential decay part. The exponential fraction was attributed to mobile water. The Gaussian had a very short time constant, of the order of  $10 \mu\text{s}$ , and was assigned to water in crystalline solid phases. Its amplitude was back extrapolated to zero pulse gap using Gaussian fitting to elucidate the solid fraction. The mobile part of the signal was separately resolved into different  $T_2$  components using the CPMG sequence. Typically, 128 echoes were recorded, logarithmically spaced from  $50 \mu\text{s}$  to 68 ms. The repetition time was progressively decreased from 1000 to 500 ms, and the number of averages increased from 512 to 1024 echo trains as the relaxation times and signal-to-noise ratio decreased from initially high values to lower values in mature pastes. The signal-to-noise ratio was typically 1500:1. A minimum of three repeat samples were measured in every case. To find the  $T_2$  components from the echo decays, the inverse Laplace transform algorithm developed by Venkatar-aman<sup>25</sup> was applied to the CPMG echo intensity decay. The regularization parameter was optimized as described in ref 25 and a value of  $1.5 \times 10^{-4}$  used. While the widths of the  $T_2$  components depend upon the regularisation parameter, the integrated "peak" intensities as reported and used in this work are robust to its variation.

In sealed cured samples, the  $w/c$  ratio is known from mixing. The key unknown is the chemical shrinkage. This was measured by the conventional method of following the height of a column of water in a capillary above a sample during hydration.

Further experiments to ascertain and confirm the cement composition were carried out using X-ray diffraction with Rietveld analysis (XRD) and thermogravimetric analysis (TGA) for samples cured for 10 and 28 days. At 10 days the hydration was stopped by isopropanol exchange in one set of samples and freeze-drying in another, duplicate, set. At 28 days, only isopropanol exchange was used. XRD measurements were made with a Panalytical X'Pert Pro MPD diffractometer in a  $\theta$ – $\theta$  configuration using a  $\text{Cu K}\alpha$  source (wavelength  $1.54 \text{ \AA}$ ) with a fixed divergence slit of  $0.5^\circ$ . Samples were scanned on a rotating stage between  $7$  and  $70^\circ$  ( $2\theta$ ) using a X'Celerator detector with a step size of  $0.0167^\circ$  ( $2\theta$ ) and a time step of 77.5s. TGA measurements were made with a Mettler Toledo (Switzerland) TGA/SDTA 851 analyzer operating between 30 and  $950^\circ\text{C}$  at  $10^\circ\text{C}/\text{min}$  under  $\text{N}_2$  gas flow to prevent carbonation.

## RESULTS

Figure 1 shows the  $T_2$  distribution map for sealed cured cement pastes after 10 days of hydration with initial  $w/c$  ratios of 0.32,

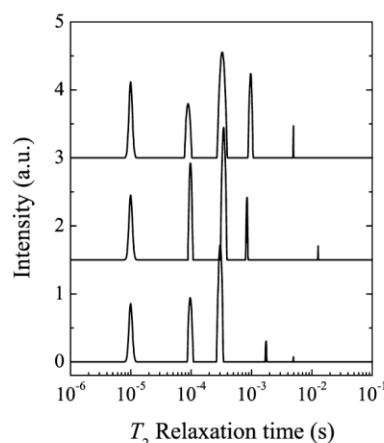


**Figure 1.**  $T_2$  distribution map of different pastes at 10 days hydration. The water-to-cement ratios, from bottom to top, are  $w/c = 0.32, 0.40$ , and  $0.48$ .

0.40, and 0.48. Taking the  $w/c = 0.40$  data as an example, the map shows five principal components: 22.6% at  $10 \mu\text{s}$ ; 25.7% at  $100 \mu\text{s}$ ; 46.7% at  $340 \mu\text{s}$ ; 4.9% at  $845 \mu\text{s}$ ; and  $<0.5\%$  at 12 ms. The first three of these components are assigned to CH plus ettringite, to interlayer water within the C–S–H, and to C–S–H gel pore water, respectively. The last two components are attributed to water in interhydrate spaces and to large capillary pores. They can be combined and defined as the "free" water within the paste.

In support of this assignment, we show that the water in CH and ettringite fully accounts for the shortest  $T_2$  component and hence that no interlayer water or residual hydroxyl group signal of C–S–H is within it so that the next shortest  $T_2$  component must be attributable to the interlayer water in C–S–H.

The ettringite mass fraction in each of the pastes was measured by XRD after 3, 6, and 10 days. It did not change appreciably during this time as might be expected since calcium sulfates have all reacted by 1 day<sup>26</sup> and the small  $\text{C}_3\text{A}$  content does not allow a significant precipitation of AFm at later ages. As the precision of XRD for such low amounts of ettringite is not good, the average of all measurements, 0.066 g of ettringite

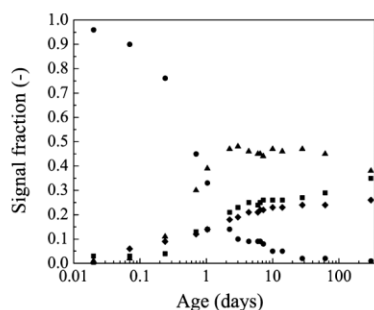
**Table 1.** CH and Ettringite Mass Fractions Measured by XRD and TGA and Calculated and Measured NMR Signals

<i>w/c</i>	age	mass fraction (g/g anhydrous)					fraction of water consumed			NMR signals solids	
		CH		ett.	av	CH	ett.	CH + ett.			
		isopropanol exchange	freeze-drying								
XRD	TGA	XRD	TGA	XRD av							
0.32	10	0.207	0.200	0.212	0.209	0.207	0.066	0.157	0.095	0.252	0.248
	28	0.217	0.218			0.218	0.066	0.165	0.095	0.260	0.258
0.40	10	0.260	0.231	0.255	0.238	0.246	0.066	0.150	0.076	0.225	0.226
	28	0.266	0.286			0.276	0.066	0.168	0.076	0.243	0.241
0.48	10	0.305	0.311	0.296	0.294	0.302	0.066	0.153	0.063	0.216	0.207
	28	0.313	0.323			0.318	0.066	0.161	0.063	0.224	0.230

per gram anhydrous cement, was taken as the value for all samples as shown in Table 1. The CH fraction measured using XRD and TGA at 10 and 28 days is also shown in Table 1. From the solid-phase mass fractions, and known molecular compositions,<sup>27</sup> it is possible to evaluate the fraction of water consumed. This is directly comparable to the normalized NMR signal attributed to the solid. Table 1 shows that the combined water in the CH and ettringite as determined by XRD/TGA is within 1% of that determined by NMR in all the samples. This degree of agreement is better than we might have expected given the inherent uncertainties in each of the methodologies. Notwithstanding, the trend is clear and we judge that there are no immobile hydrogens within the C–S–H. The degree to which the interlayer is protonated by OH groups remains a matter of contention and indeed such OH groups as exist in the interlayer may be associated with relatively (rotationally?) mobile Ca ions.<sup>3,28</sup> In further support of the assignment, we also note our earlier result<sup>13</sup> that, upon sample drying, the NMR signal decreases linearly and yields a *w/c* ratio entirely consistent with the paste composition. This result verifies that we are “seeing” all the water by NMR.

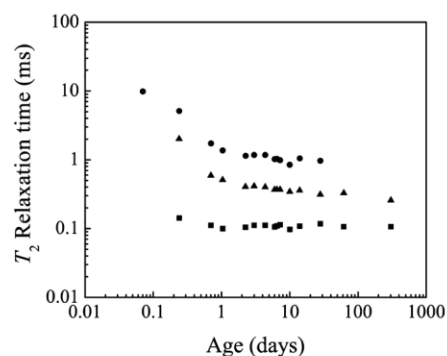
NMR data has been acquired for samples as a function of hydration time. As an example, Figure 2 shows the amplitude of the NMR response assigned to crystalline solids (CH and ettringite), C–S–H interlayer water, gel pore water, and free water for the *w/c* = 0.4 paste.

The free water signal decreases rapidly during the first 2 days to just over 10% of the initial value, after which it decreases much more slowly. It is of negligible amplitude at ca. 28 days. During the first two days, the signals attributed to crystalline solids, to C–S–H layers, and to gel pores all increase. The volume ratio of interlayer water and gel water is approximately

**Figure 2.** Evolution of NMR signal amplitude of different water populations with hydration time (*w/c* = 0.40). Diamonds are solids such as CH, squares are interlayer water, triangles are gel pore water, and solid circles are free water, becoming interhydrate water.

constant, 1:2. After 2 days, the gel pore water signal stops increasing and stabilizes at a constant value before eventually decreasing beyond 62 days. On the other hand, the water in the crystalline solids (CH and ettringite) and C–S–H interlayer water continue to grow throughout the entire experimental period (300 days). Hence, after 2 days, the volume ratio of interlayer water to gel water monotonically increases.

The corresponding  $T_2$  relaxation times of the interlayer, gel, and free water fractions are shown in Figure 3. Initially, while

**Figure 3.** Evolution of  $T_2$  relaxation time of the different water populations throughout the hydration (*w/c* = 0.40). Squares are interlayer water, triangles are gel pore water, and solid circles are free water, becoming interhydrate water.

the signal is dominated by the single  $T_2$  component corresponding to free water in the mix, the  $T_2$  is long. However, it falls rapidly, along with the  $T_2$  signal for the gel pores, approaching asymptotic values of about 1000 and 300  $\mu$ s, respectively, as early as 0.5 days. As might be expected, the values for the C–S–H interlayer are fairly constant from the beginning of the measurement time at 100  $\mu$ s.

Figure 4 shows the chemical shrinkage volume as measured by the conventional capillary height method for different *w/c* ratios and sample age. A linear best fit to the data yields a chemical shrinkage of  $0.075 \pm 0.003 \text{ cm}^3 \text{ g}^{-1}$  of reacted anhydrous powder. We use this as our measure of the signal voidage in eqs 1–5. In our previous work,<sup>13</sup> NMR measurements were made on underwater-cured material. In that case, the voidage was determined directly from the increase in the *w/c* ratio of the paste measured by NMR and was very comparable to the voidage measured here by chemical shrinkage. An attempt to use NMR for sealed cured samples, by measuring the increase in signal intensity for rewetted samples, consistently underestimated the voidage by ca. 50%.

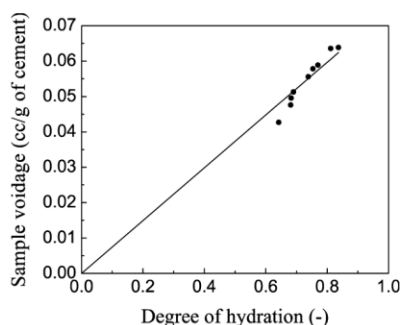


**Figure 4.** Voidage volume measured by following the height of a column of water in a capillary above a sample during hydration. The solid line is a linear least-squares fit to the data.

## ANALYSIS AND DISCUSSION

**Porosity and  $T_2$  Analysis.** The relaxation times reported above may be interpreted in terms of pore sizes according to the fast diffusion model of relaxation.<sup>20,21,23,29</sup> Since the relaxation times rapidly approach constant values, it is concluded that the pores rapidly approach constant size. Application of eq 7 with surface relaxivity  $0.00373 \text{ nm}/\mu\text{s}$  gives averages of  $0.85 \text{ nm}$  (C–S–H interlayer spacing),  $2.5 \text{ nm}$  (gel pores), and  $8.0 \text{ nm}$  (interhydrate pores). These values are fractionally smaller than previously reported ( $0.94$ ,  $3.1$ , and  $10 \text{ nm}$ ), probably because the surface relaxivity is frequency dependent (earlier measurements were made at  $20 \text{ MHz}$ ). We note that the interlayer spacing is a little larger than might be expected based on the mineral analogue of C–S–H, tobermorite 14.<sup>30</sup> However, in such small spaces, the concept of mobile pore water above an adsorbed layer that underpins the model starts to break down.

A key feature of the NMR data is that the total gel porosity and gel pore size reach a plateau after about 1–2 days whereas the volume of hydrates continues to grow. We speculate that this marks a transition from the growth of “less dense” to “more dense” product. At the same time, the size of the pores containing free water stabilizes at around  $8\text{--}10 \text{ nm}$  and we assign this reservoir to interhydrate pores. This category of pores does not seem to be an intrinsic part of the C–S–H hydrate, because the total porosity in this category decreases with the degree of hydration, rather than increasing, reaching zero at about 2 months hydration. Since the gel porosity does not decrease from ca. 2 to 60 days hydration, we infer that the C–S–H is growing in the interhydrate spaces, using the interhydrate pore water during this time. Since the interhydrate pores do not decrease much in size below about  $8\text{--}10 \text{ nm}$ , it is as if the interhydrate spaces are either present or filled with C–S–H. We do not see evidence for a halfway house. Only when all of this space is consumed, beyond 2 months, is there any evidence that the C–S–H grows within the gel pore space with a small decrease in the gel pore size.

The signal intensities can be recalibrated as volume of water per unit volume of paste. Given the pore sizes, the specific surface area of the C–S–H interlayer spaces and of the gel pores may be calculated. They are  $171$  and  $111 \text{ m}^2 \text{ cm}^{-3}$ , respectively, for the  $w/c = 0.4$  paste at 28 days. Given the specific surface area and sizes of the interlayer and gel pores, we conclude that the number of locally stacked layers comprising a region of C–S–H can only be 2 or 3 at 28 days hydration.

**Density of C–S–H over Time ( $w/c = 0.40$ ).** The data presented in the foregoing sections allows us to calculate the C–S–H density and composition according to eqs 1–5. The results can be presented either exclusive (called “C–S–H solid density”) or inclusive (called “C–S–H bulk density”) of the gel water. We present both, as together they reveal interesting observations about the underlying C–S–H morphology. Figure 5 (solid circles) shows the solid C–S–H density in the  $w/c =$

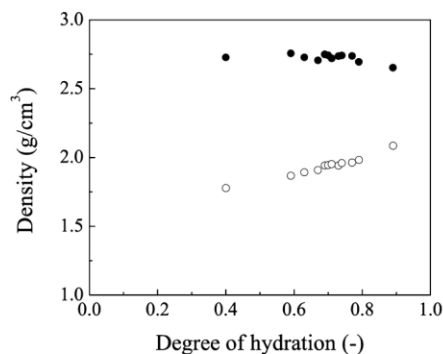


**Figure 5.** C–S–H density as a function of the degree of hydration ( $w/c = 0.40$ ). Solid symbols are the C–S–H solid density, exclusive of the gel water; empty symbols are for C–S–H bulk density, inclusive of the gel water.

$0.4$  paste as a function of degree of hydration. To help interpret the data, Figure 6 shows a schematic of the C–S–H as envisaged.

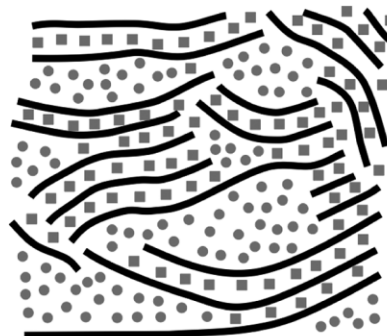


**Figure 6.** A schematic of the calcium silicate layers (solid lines), interlayer water (squares), and gel pore water (circles). The solid density includes only the calcium silicate layers and the interlayer water. As it excludes water on the outer surfaces of locally aggregated layers, it is clearly a function of the average number of aggregated layers,  $s$ . The bulk density includes both types of water.

The solid C–S–H density, exclusive of the gel pores,  $\rho_x$ , is largely independent of degree of hydration, decreasing only very slightly from  $\rho_x = 2.73 \pm 0.01 \text{ g/cm}^3$  at 1 day ( $\alpha = 0.4$ ) to  $\rho_x = 2.69 \pm 0.01 \text{ g/cm}^3$  at 2 months ( $\alpha = 0.8$ ) and on to  $\rho_x = 2.65 \pm 0.01 \text{ g/cm}^3$  at 10 months ( $\alpha = 0.9$ ). Perversely, the decrease arises due to “densification” of the C–S–H. The NMR C–S–H “solid” density includes the Ca–O layers with  $\text{SiO}_2$  tetrahedra and the interlayer water of the C–S–H but specifically excludes the water and any hydroxyls on the outermost C–S–H surfaces. These outer hydrogens are in rapid exchange with gel water and consequently have a longer relaxation time (ca.  $300 \mu\text{s}$ ). As C–S–H densifies, the local

number of aggregated layers increases. Hence, the ratio of calcium silicate layers ( $s$ ) to interlayers of water ( $s - 1$ ) asymptotically decreases to 1 (Figure 6). As the calcium silicate layer is more dense than water, the average density falls.

The “bulk” C–S–H density, including the gel water,  $\rho_x$ , (open circles), behaves in the opposite manner. It increases, and markedly so, during hydration. After 1 day ( $\alpha = 0.4$ ), the total volume of gel water first reaches a plateau but the hydrates continue to grow by consuming the interhydrate water. The bulk C–S–H density necessarily increases. Later, when the interhydrate water is fully consumed in 2 months ( $\alpha = 0.8$ ), hydrates grow at the expense of gel water. The density rise continues and the values for the mature pastes agree very well with the densities calculated by other methods. The reader is referred to ref 4 for a review of the relevant literature. We speculate that the C–S–H growing in the very early stages, in parallel with gel pores, corresponds to the low density C–S–H and that which grows thereafter, devoid of corresponding new gel porosity, corresponds to the high-density C–S–H that other authors have detected by, for instance, nanoindentation measurements.<sup>31</sup>

#### Corrections to the Density for C–S–H Surface Water.

As explained, the solid C–S–H density excludes the adsorbed layer of water on the outer surface of agglomerates of C–S–H layers. If we take tobermorite 14 Å as a C–S–H analogue, then the layer repeat distance is 1.4 nm. If there are three layers as the NMR results suggest, then the NMR thickness is  $3 \times 1.4 - 2 \times 0.28 = 3.64$  nm. If a monolayer coverage of water molecules is added on the outer surface of the C–S–H agglomerate, the NMR density  $\rho_x$  is decreased to  $\rho_x^m = (3.64\rho_x + 0.56)/4.2$ . For example, for  $\rho_x = 2.70$  g/cm<sup>3</sup>, the density reduces to 2.47 g/cm<sup>3</sup>.

**Density as a Function of  $w/c$ .** Figure 7 shows the calculated densities as a function of  $w/c$  at 28 days hydration

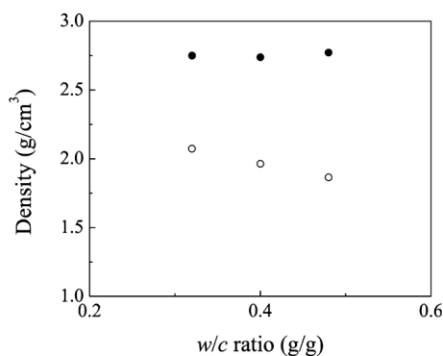


**Figure 7.** C–S–H density as a function of  $w/c$  at 28 days of hydration. Solid rounds are for solid C–S–H and open rounds are for bulk C–S–H, including the gel water.

time. Since the solid C–S–H density probes only the locally stacked C–S–H layers, in the  $w/c$  ratio range studied  $\rho_x$  is constant as expected. The slight increase in  $\rho_x$  for  $w/c = 0.48$  may be explained by a lower ratio of layers to interlayer spaces,  $s/(s - 1)$ . Likewise, at 28 days of hydration the bulk density,  $\rho_x$ , decreases with increasing water content as expected. There is simply more water available for gel pores.

**Chemical Composition.** We first focus on the Ca/(Si + Al) ratio,  $z$ , of the C–S–H. The results are shown as a function of degree of hydration for the  $w/c = 0.4$  paste in Figure 8a. Overall,  $z$  decreases with increasing degree of hydration. At 300

days, the Ca/(Si + Al) ratio of the C–S–H is  $1.70 \pm 0.02$ , which is in good agreement with previous studies.<sup>32</sup> We note that there is a clear difference in the calculated Ca/(Si + Al) ratio between the C–S–H that forms during the first few days ( $\alpha < 0.63$ ,  $z \approx 1.84$ ) and the C–S–H that forms later ( $\alpha > 0.63$ ,  $z \approx 1.70$ ). A transition in the rate of increase of gel porosity at around 2–3 days was previously identified with a transition from growth of low- to high-density C–S–H. It is conceivable that the Ca/(Si + Al) ratio may be different in the two types of product, as suggested by, for instance, Taylor et al.<sup>32</sup>

The water content of C–S–H without and with the gel water included,  $x$  and  $x'$ , are shown in Figure 8b for the  $w/c = 0.4$  paste as a function of degree of hydration. The value  $x$  for the water content excluding gel water follows the inverse trend of  $\rho_x$ . The slight increase in  $x$  beyond 2 days ( $\alpha \approx 0.6$ ) is attributed to densification. As the average number of locally aggregated C–S–H sheets,  $s$ , increases, there are fractionally more interlayers containing water compared to solid sheets,  $(s - 1)/s$  (Figure 6), and hence more water molecules,  $x$ , per Si or Al atom. The average value of  $x$  between 7 and 300 days is  $1.80 \pm 0.03$ . On the other hand, the value of  $x'$ , which includes the gel water, decreases as the paste densifies. These results are entirely consistent with the changes in the densities.

Figure 9a presents the dependence of Ca/(Si + Al) ratio on the  $w/c$  ratio after 28 days of hydration. The higher the water-to-cement ratio, the fewer calcium ions are incorporated into the C–S–H nanostructure. Figure 9b shows the associated  $x$  and  $x'$  as a function of  $w/c$ . Again, the trends of water bound in the C–S–H microstructure,  $x$  and  $x'$ , follow the inverse behavior of  $\rho_x$  and  $\rho_x'$ .

Finally, we note that the parameter  $y = n_{\text{Si}}^{\text{CSH}}/(n_{\text{Si}}^{\text{CSH}} + n_{\text{Al}}^{\text{CSH}})$  ranges from 0.94 at 2 days hydration to 0.96 in the mature paste, reflecting the fact that the Al is incorporated early in the process.

**Implications for Powers and Brownard Composition Model.**<sup>6</sup> Figure 10a–c brings all our data together and shows revised composition diagrams of cement with  $w/c = 0.32$ , 0.40, and 0.48 as a function of degree of hydration, in a manner akin to the well-known results of Powers and Brownard. The phase compositions are presented in terms of both mass and volume fractions. Two factors are immediately apparent. The first is that Powers and Brownard did not distinguish between C–S–H and CH. Nor did they separate out interlayer water within the C–S–H layers. The NMR experiments clearly differentiate all these components. The second is that there is a clear nonlinearity in the growth of the different fractions with degree of hydration. In particular, NMR data shows that the development of gel porosity from  $\alpha = 0$  to  $\alpha = 1$  is nonlinear, contrary to the Powers and Brownard proposal. We see that the gel porosity of C–S–H develops mainly at early age when the volume of capillary water still remains significant. The gel water volume then plateaus and does not increase after,  $\alpha = 0.33$  for  $w/c = 0.32$ ,  $\alpha = 0.56$  for  $w/c = 0.40$ , and  $\alpha = 0.79$  for  $w/c = 0.48$ . This limitation of the gel pore volume can be interpreted by the transition between the formation of low- and high-density C–S–H, as already discussed in the previous sections. That the transition is dependent on the initial  $w/c$  ratio is related to the mean distance between anhydrous cement particles. A “space-filling” model has previously been applied with success by Bishnoi and Scrivener<sup>33</sup> to model hydration kinetics. Notwithstanding the mismatch in the gel/capillary water volumes at early age between NMR and the Powers and

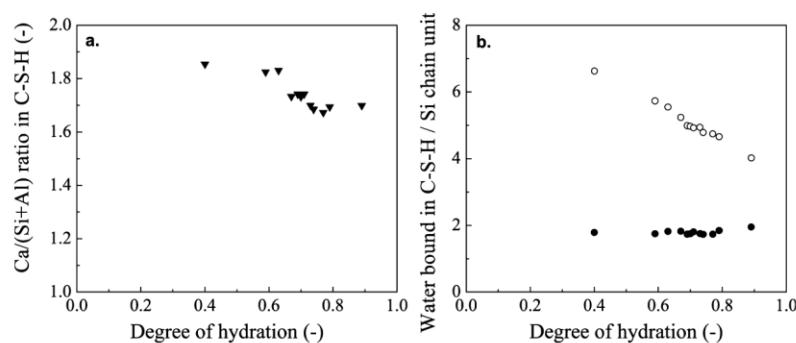


**Figure 8.** (a) Ratio  $\text{Ca}/(\text{Si} + \text{Al})$  and (b) the water in the C–S–H, excluding ( $x$ , solid circles) and including ( $x'$ , open circles) gel water as a function of degree of hydration for a  $w/c = 0.40$  paste.

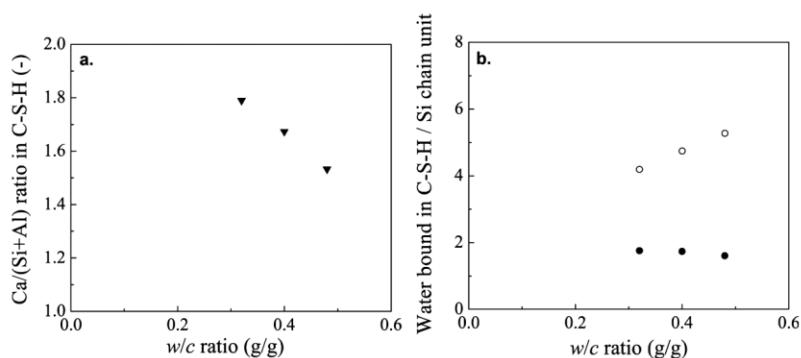


**Figure 9.** (a) Ratio  $\text{Ca}/(\text{Si} + \text{Al})$  and (b) the water in the C–S–H, excluding ( $x$ , solid circles) and including ( $x'$ , open circles) gel water as a function of  $w/c$  ratio.

Brownyard model, we note that the latter produces good result at later ages/larger degrees of hydration and therefore that it remains a powerful tool to predict long-term paste composition.

**Implications for Jennings Colloidal Model, CM-II.<sup>4</sup>** As well as the interlayer water, Jennings suggests three nanoscale pore sizes associated with C–S–H: intraglobular pores associated with stacking heterogeneities of the calcium silicate layers (ca. 1 nm), small globule pores between particles (ca. 1–3 nm), and large globule pores between particle flocs (3–12 nm). We find just two: the interlayer spaces between the calcium silicate sheets and the gel pores of comparable size to the small globule pores. The large globule pores reported by Jennings are comparable in size to what we call the interhydrate spaces (10 nm). However, we do not believe that the interhydrate pores that NMR sees are integral to the C–S–H since they always decrease in volume as C–S–H grows. What is interesting, however, is that NMR suggests that C–S–H aggregates of layers are approximately 3 layers thick. Based on the analogue tobermorite 14, this leads to a stack thickness of 4.2 nm, close to the CM-II globule size.

Care must be taken when comparing the density and water fraction of C–S–H according to different models. NMR “solid” density probes locally stacked C–S–H layers excluding any water molecule adsorbed on the outer surface of the agglomerates. SANS measurements,<sup>12</sup> upon which much of CM-II is built, also exclude water on particle surfaces and give the result  $\rho = 2.604 \text{ g/cm}^3$ . NMR gives a slightly larger average value of  $\rho_x = 2.71 \text{ g/cm}^3$  between 7 and 300 days hydration. If the surface water correction is applied,  $\rho_x$  drops to  $2.47 \text{ g/cm}^3$ , identical to the value reported by Jennings,  $\rho = 2.47 \text{ g/cm}^3$ , for

a saturated globule with a monolayer of water at 11% RH. The water content of “solid” C–S–H determined by SANS is in good agreement with the average NMR result between 7 and 300 days,  $x = 1.8$ . It is difficult to make meaningful comparisons of the water content inclusive of gel water as it constantly decreases while C–S–H densifies.

**Implications for Feldman and Sereda Model.<sup>11</sup>** The primary difference between the picture of C–S–H morphology emergent from NMR and that proposed by Feldman and Sereda is that the latter propose C–S–H with mainly interlayer water and physically adsorbed water but no larger intrinsic reservoirs. The Feldman and Sereda model additionally proposes small nanometer pores that arise from irregularities in the C–S–H layer stacking. The picture of C–S–H coming from NMR relaxometry displays two distinct categories of pores: interlayer spaces of about 1 nm and gel pore spaces in the order of 3 nm. The remaining nanometer pores are interhydrate in character.

## CONCLUSION

<sup>1</sup>H relaxation NMR measurements have enabled a remarkably complete and self-consistent picture of C–S–H morphology to be established as a function of hydration degree and water to cement ratio of cement paste. The experiments show that initially (during the first few days) C–S–H grows as a loose-packed assembly of nanocrystalline regions in which the calcium silicate layers are well stacked with interlayer water, interspersed with fine “gel” pores, of characteristic and relatively constant size, 3–5 nm. During this period, the amount and size of large capillary pores decrease rapidly. Once the size reaches

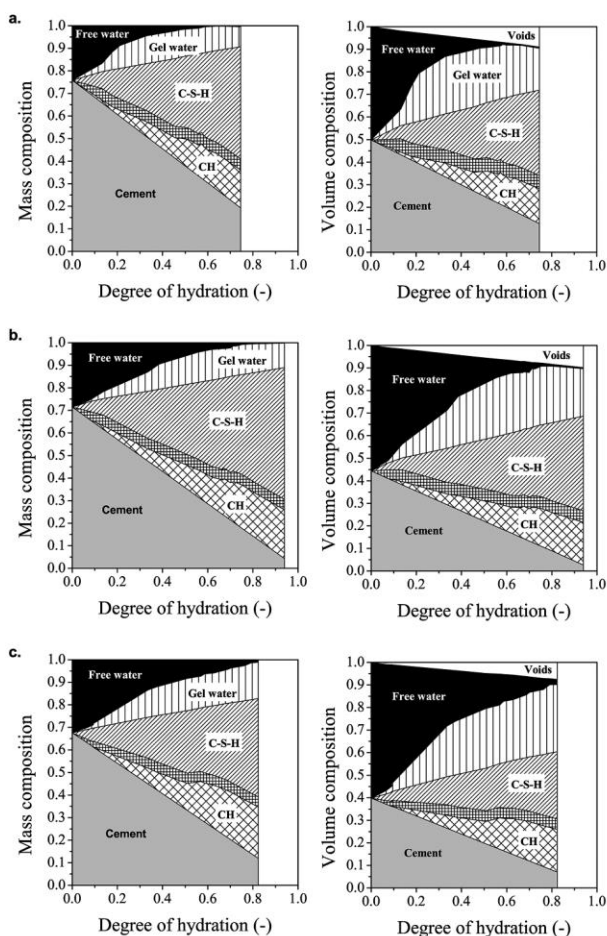


**Figure 10.** Mass and volume composition of cement paste for (a)  $w/c = 0.32$ , (b)  $w/c = 0.40$ , and (c)  $w/c = 0.48$ . In each figure, from top, the shaded regions correspond to free water, gel pore water, C–S–H, ettringite, CH, and unreacted cement. These results are calculated from the NMR signal intensities of samples measured as prepared throughout hydration (eqs 1–5) and are presented as a function of degree of hydration.

around 10 nm, the number of “gel” pores in the C–S–H no longer increases, even though CH and C–S–H with interlayer water continue to form. The transition to the formation of this dense C–S–H (without gel pores) leads to an overall increase in the “bulk” density of the C–S–H with time from around 1.8  $\text{g}/\text{cm}^3$  at 1 day to around 2.1  $\text{g}/\text{cm}^3$  at 1 year. Throughout the hydration process the density of the solid nanocrystalline C–S–H remains fairly constant, decreasing slightly from around 2.73  $\text{g}/\text{cm}^3$  at 1 day to 2.65  $\text{g}/\text{cm}^3$  at 1 year, due to an increase in the number of layers in the nanocrystalline regions.

From this new data, we have updated Powers–Brownayard’s classic model of 1947 and identified nonlinear growth of the gel porosity. This has largely all come from a single technique:  $^1\text{H}$  NMR relaxometry, supported by an XRD measurement of the degree of hydration and ettringite mass fraction. The quick and easy experiments have been performed on fully hydrated material without destructive drying using widely available equipment. We suggest that this opens the door to the rapid characterization of novel, potentially improved, cements.

## ■ AUTHOR INFORMATION

### Notes

The authors declare no competing financial interest.

### ■ ACKNOWLEDGMENTS

We thank Y.-Q. Song of Schlumberger-Doll Research for 2D Fast Laplace Inversion software. White cement was provided by Aalborg Portland, Denmark. The research leading to these results has received funding from the European Union Seventh Framework Programme (FP7/2007–2013) under grant agreement 264448. P.J.M. thanks Nanocem ([www.nanocem.org](http://www.nanocem.org)) and the UK Engineering and Physical Sciences Research Council (grant no. EP/H033343/1) for financial support.

### ■ REFERENCES

- (1) World Business Council for Sustainable Development, Cement Sustainability Initiative, <http://www.wbcsdcement.org> (accessed 1st December 2011).
- (2) Chiang, W.-S.; Fratini, E.; Baglioni, P.; Liu, D.; Chen, S.-H. *J. Phys. Chem. C* **2012**, *116*, 5055–5061.
- (3) Richardson, I. G. *Cem. Concr. Res.* **2008**, *38*, 137–158.
- (4) Jennings, H. M. *Cem. Concr. Res.* **2008**, *38*, 275–289.
- (5) Thomas, J. J.; Biernacki, J. J.; Bullard, J. W.; Bishnoi, S.; Dolado, J. S.; Scherer, G. W.; Luttge, A. *Cem. Concr. Res.* **2011**, *41*, 1257–1278.
- (6) Powers T. C.; Brownayard T. L. “Studies of the physical properties of hardened Portland cement paste”; Portland Cement Association (Bulletin 22): Chicago, 1948; reprinted from *Proc. J. Am. Concr. Inst.* **1947**, *43*, 101, 249, 469, 549, 669, 845, 993.
- (7) Grudemo, A. An Electronographic Study of the Morphology and Crystallization Properties of Calcium Silicate Hydrates; *Proc. Swedish Cem. Concr. Res. Inst. R. Inst. Technol.*, Stockholm (Handlinger—Svenska Forskningsinstitutet för Cement Och Betong vid Kungliga Tekniska Högskolan i Stockholm) **1955**, *26*, 1–103.
- (8) Tennis, P.; Jennings, H. M. *Cem. Concr. Res.* **2000**, *30*, 855–863.
- (9) Scrivener, K. L. The Microstructure of Concrete. In *Materials Science of Concrete I*; Skalny, J. P., Ed.; American Ceramic Society: Columbus, OH, 1989; pp 127–161.
- (10) Richardson, I. G. *Cem. Concr. Res.* **1999**, *29*, 1131–1147.
- (11) Feldman, R. F.; Sereda, P. J. *Eng. J.* **1970**, *53*, 53–59.
- (12) Allen, A. J.; Thomas, J. J.; Jennings, H. M. *Nat. Mater.* **2007**, *6*, 311–316.
- (13) Muller, A. C. A.; Scrivener, K. L.; Gajewicz, A. M.; McDonald, P. J. Submitted to *Microporous Mesoporous Mater.*
- (14) Holly, R.; Reardon, E. J.; Hansson, C. M.; Peemoeller, H. J. *Am. Ceram. Soc.* **2007**, *90*, 570–577.
- (15) Powles, J. G.; Strange, J. H. *Proc. Phys. Soc. London* **1963**, *82*, 6–15.
- (16) McDonald, P. J.; Rodin, V.; Valori, A. *Cem. Concr. Res.* **2010**, *40*, 1656–1663.
- (17) Taylor, H. F. W. *Cement Chemistry*, 2nd ed.; Academic Press: London, 1997.
- (18) Brydson, R. M. D.; Richardson, I. G.; Groves, G. W. *Mikrochim. Acta* **1994**, *114–5*, 221–229.
- (19) Lothenbach, R.; Winnefeld, F. *Cem. Concr. Res.* **2006**, *36*, 209–226.
- (20) D’Orazio, F.; Bhattacharja, S.; Halperin, W. P.; Eguchi, K.; Mizusaki, T. *Phys. Rev. B* **1990**, *42*, 9810–9818.
- (21) Halperin, W. P.; Jehng, J.-Y.; Song, Y.-Q. *Magn. Reson. Imag.* **1994**, *12*, 169–173.
- (22) Korb, J.-P.; Whaley-Hodges, M.; Bryant, R. G. *Phys. Rev. E* **1997**, *56*, 1934–1945.
- (23) Monteilhet, L.; Korb, J.-P.; Mitchell, J.; McDonald, P. J. *Phys. Rev. E* **2006**, *74*, 061404-1–9.
- (24) Meiboom, S.; Gill, D. *Rev. Sci. Instr.* **1958**, *29*, 688–691.
- (25) Venkataraman, L.; Song, Y.-Q.; Hürlimann, M. D. *IEEE Trans. Signal Process* **2002**, *50*, 1017–1026.
- (26) Scrivener, K. L.; Nonat, A. *Cem. Concr. Res.* **2011**, *41*, 651–665.

- (27) Moore, A. E.; Taylor, H. F. W. *Nature* **1968**, *218*, 1048–1049.
- (28) Nonat, A. *Cem. Concr. Res.* **2004**, *34*, 1521–1528.
- (29) McDonald, P. J.; Korb, J. P.; Mitchell, J.; Monteilhet, L. *Phys. Rev. E.* **2005**, *72*, 011409-1–9.
- (30) Bonaccorsi, E.; Merlino, S.; Kampf, A. R. *J. Am. Ceram. Soc.* **2005**, *88*, 505–512.
- (31) Constantinides, G.; Ulm, F.-J. *J. Mech. Phys. Solids* **2007**, *55*, 64–69.
- (32) Taylor, R.; Richardson, I. G.; Brydson, R. M. D. *Cem. Concr. Res.* **2010**, *40*, 971–983.
- (33) Bishnoi, S.; Scrivener, K. L. *Cem. Concr. Res.* **2009**, *39*, 266–274.

## Bibliography

---

---

- [1] “World Business Council for Sustainable Development, Cement Sustainability Initiative, <http://www.wbcdcement.org>,” 2014.
- [2] K. L. Scrivener, “Introduction : basic concepts.” 1st Marie-Curie RTN training course, Denmark, 2006.
- [3] J.-P. Mercier, G. Zambelli, and W. Kurz, *Introduction à la science des matériaux*. Lausanne: Presses Polytechniques et Universitaires Romandes, 1999.
- [4] H. G. van Oss, “U. S. Geological Survey, Mineral Commodity Summaries,” 2014.
- [5] I. G. Richardson, “The calcium silicate hydrates,” *Cem. Concr. Res.*, vol. 38, pp. 137–158, 2008.
- [6] H. M. Jennings, “Refinements to colloid model of C-S-H in cement: CM-II,” *Cem. Concr. Res.*, vol. 38, no. 3, pp. 275–289, 2008.
- [7] A. J. Allen, J. J. Thomas, and H. M. Jennings, “Composition and density of nanoscale calcium-silicate-hydrate in cement,” *Nat. Mater.*, vol. 6, pp. 311–316, 2007.
- [8] A. Muller, K. L. Scrivener, and P. J. McDonald, “Porosity characterisation across different binders by a multi-technic approach.” Poster on 2nd Official Transcend Meeting, Morges, 2012.
- [9] “MC ITN TRANSCEND <http://www.nanocem.org/index.php?id=282>,” 2014.
- [10] W. P. Halperin, J. Y. Jehng, and Y.-Q. Song, “Application of spin-spin relaxation to measurement of surface area and pore size distributions in a hydrating cement paste,” *Magn. Reson. Imaging*, vol. 14, pp. 169–173, 1994.
- [11] P. D. M. Hughes, “A study of water transport in zeolite 4A powder beds and sodium silicate films using broadline Magnetic Resonance Imaging; PhD thesis,” University of Surrey, 1996.
- [12] M. Fleury, S. Gautier, F. Norrant, and E. Kohler, “Characterisation of Nanoporous Systems with Low Field NMR: Application to Kaolinite and Smectite Clays,” in *International Symposium of the Society of Core Analysts*, 2011, pp. 1–12.
- [13] F. Jaeger, A. Shchegolikhina, H. Van As, and G. E. Schaumann, “Proton NMR Relaxometry as a Useful Tool to Evaluate Swelling Processes in Peat Soils,” *Open Magn. Reson. J.*, pp. 27–45, 2010.
- [14] D. V. Ellis and J. M. Singer, *Well Logging for Earth Scientists*. Dordrecht: Springer, 2008.
- [15] V. Baukh, H. P. Huinink, O. C. G. Adan, S. J. F. Erich, and L. G. J. van der Ven, “Water-Polymer Interaction during Water Uptake,” *Macromolecules*, vol. 44, pp. 4863–4871, 2011.
- [16] H. C. Bertram, S. B. Engelsens, H. Busk, A. H. Karlsson, and H. J. Andersen, “Water properties during cooking of pork studied by low-field NMR relaxation: effects of curing and the RN<sup>-</sup> gene,” *Meat Sci.*, vol. 66, pp. 437–46, 2004.
- [17] M. Jones, “Mobile nuclear magnetic resonance characterisation of water distribution and movement in living trees and felled timber; PhD thesis,” University of Surrey, 2012.

- [18] R. Blinc, M. Burgar, G. Lahajnar, M. Rozmarin, V. Rutar, I. Kocuvan, and J. Ursic, "NMR Relaxation Study of Adsorbed Water in Cement and C<sub>3</sub>S Pastes," *J. Am. Ceram. Soc.*, vol. 61, pp. 35–37, 1978.
- [19] L. J. Schreiner, J. C. Mactavish, L. Miljkovic, M. M. Pintar, R. Blinc, G. Lahajnar, D. Lasic, and L. W. Reeve, "NMR line shape-spin-lattice relaxation correlation study of Portland cement hydration," *J. Am. Ceram. Soc.*, vol. 68, pp. 10–16, 1985.
- [20] D. D. Lasic, J. M. Corbett, J. Jian, J. C. MacTavish, M. M. Pintar, R. Blinc, and G. Lahajnar, "NMR Spin Grouping in Hydrating Cement at 200 MHz," *Cem. Concr. Res.*, vol. 18, pp. 649–653, 1988.
- [21] L. Miljkovic, D. Lasic, J. C. Mactavish, M. M. Pintar, R. Blinc, and G. Lahajnar, "NMR study of hydrating cement: A spin-spin study of the early hydration stage," *Cem. Concr. Res.*, vol. 18, pp. 951–956, 1988.
- [22] A. J. Bohris, U. Goerk, P. J. McDonald, M. Mulheron, B. Newling, and B. L. E. Page, "A Broad Line NMR and MRI Study of Water and Water Transport in Portland Cement Pastes," *Magn. Reson. Imaging*, vol. 16, pp. 455–461, 1998.
- [23] A. Plassais, M.-P. Pomiès, N. Lequeux, P. Boch, J.-P. Korb, and D. Petit, "Micropore size analysis in hydrated cement paste by NMR," *C. R. Acad. Sci. Paris, Chim. / Chem.* 4, vol. 4, pp. 805–808, 2001.
- [24] J. Greener, H. Peemoeller, C. Choi, R. Holly, E. J. Reardon, C. M. Hansson, and M. M. Pintar, "Monitoring of Hydration of White Cement Paste with Proton NMR Spin–Spin Relaxation," *J. Am. Ceram. Soc.*, vol. 83, pp. 623–627, 2000.
- [25] R. Holly, E. J. Reardon, C. M. Hansson, and H. Peemoeller, "Proton Spin-Spin Relaxation Study of the Effect of Temperature on White Cement Hydration," *J. Am. Ceram. Soc.*, vol. 90, pp. 570–577, 2007.
- [26] P. J. McDonald, V. Rodin, and A. Valori, "Characterisation of intra- and inter-C–S–H gel pore water in white cement based on an analysis of NMR signal amplitudes as a function of water content," *Cem. Concr. Res.*, vol. 40, pp. 1656–1663, 2010.
- [27] F. D. Orazio, S. Bhattacharja, and W. P. Halperin, "Molecular diffusion and nuclear-magnetic-resonance relaxation of water in unsaturated porous silica glass," *Phys. Rev. B*, vol. 42, pp. 9810–9818, 1990.
- [28] H. F. W. Taylor, *Cement chemistry*. London: Academic Press Limited, 1990.
- [29] K. L. Scrivener, "Hydration and Microstructure." 1st Marie-Curie ITN training course, Maastricht, 2011.
- [30] J. W. Bullard, H. M. Jennings, R. A. Livingston, A. Nonat, G. W. Scherer, J. S. Schweitzer, K. L. Scrivener, and J. J. Thomas, "Mechanisms of cement hydration," *Cem. Concr. Res.*, vol. 41, pp. 1208–1223, 2011.
- [31] K. L. Scrivener, "Backscattered electron imaging of cementitious microstructures: understanding and quantification," *Cem. Concr. Compos.*, vol. 26, pp. 935–945, 2004.
- [32] T. C. Powers and T. L. Brownyard, "Studies of the Physical Properties of Hardened Portland Cement Paste Part 3. Theoretical Interpretation of adsorption Data," *J. Am. Concr. Inst.*, vol. 18, pp. 469–504, 1946.

- [33] T. C. Powers and T. L. Brownyard, "Studies of the Physical Properties of Hardened Portland Cement Paste Part 9. General Summary of Findings on the Properties of Hardened portland Cement Paste," *J. Am. Concr. Inst.*, vol. 18, pp. 971–992, 1947.
- [34] T. C. Hansen, "Physical structure of hardened cement paste. A classical approach," *Mater. Constr.*, vol. 19, pp. 423–436, 1986.
- [35] P. K. Mehta and P. J. M. Monteiro, *Concrete Structure, Properties and Materials*. New Jersey: Prentice-Hall, 1993.
- [36] T. C. Powers, "Structure and Physical Properties of Hardened Portland Cement Paste," *J. Am. Ceram. Soc.*, vol. 41, pp. 1–6, 1958.
- [37] O. M. Jensen, "Powers' model." Lecture COE Hokkaido University, 2005.
- [38] R. F. Feldman and P. J. Sereda, "A model for hydrated portland cement paste as deduced from sorption- length change and mechanical properties," *Mater. Constr.*, vol. 1, pp. 509–520, 1968.
- [39] R. F. Feldman and P. J. Sereda, "A New Model for Hydrated Portland Cement and its Practical Implications," *Eng. J.*, vol. 53, pp. 53–59, 1970.
- [40] H. M. Jennings, "A model for the microstructure of calcium silicate hydrate in cement paste," *Cem. Concr. Res.*, vol. 30, pp. 101–116, 2000.
- [41] P. D. Tennis and H. M. Jennings, "A model for two types of calcium silicate hydrate in the microstructure of Portland cement pastes," *Cem. Concr. Res.*, vol. 30, pp. 855–863, 2000.
- [42] J. J. Thomas, H. M. Jennings, and A. J. Allen, "The surface area of hardened cement paste as measured by various techniques," *Concr. Sci. Eng.*, vol. 1, pp. 45–64, 1999.
- [43] X. Cong and R. J. Kirkpatrick, "<sup>29</sup>Si MAS NMR Study of the Structure of Calcium Silicate Hydrate," *Adv. Cem. Based Mater.*, vol. 3, pp. 144–156, 1996.
- [44] S. Grangeon, F. Claret, C. Lerouge, F. Warmont, T. Sato, S. Anraku, C. Numako, Y. Linard, and B. Lanson, "On the nature of structural disorder in calcium silicate hydrates with a calcium/silicon ratio similar to tobermorite," *Cem. Concr. Res.*, vol. 52, pp. 31–37, Oct. 2013.
- [45] J. J. Chen, J. J. Thomas, H. F. W. Taylor, and H. M. Jennings, "Solubility and structure of calcium silicate hydrate," *Cem. Concr. Res.*, vol. 34, pp. 1499–1519, 2004.
- [46] T. Maeshima, H. Noma, M. Sakiyama, and T. Mitsuda, "Natural 1.1 and 1.4 nm tobermorites from Fuka, Okayama, Japan: Chemical analysis, cell dimensions, <sup>29</sup>Si NMR and thermal behavior," *Cem. Concr. Res.*, vol. 33, pp. 1515–1523, 2003.
- [47] I. G. Richardson, "The nature of C-S-H in hardened cements," *Cem. Concr. Res.*, vol. 29, pp. 1131–1147, 1999.
- [48] M. Geiker, "Porosity development and moisture fixation, mechanisms." 1st Marie-Curie ITN training course, Maastricht, 2011.
- [49] *CEB - Design Guide - Durable concrete structures. Chapter 2*. London: Thomas Telford Services Ltd, 1992.
- [50] *Manual of Symbols and Terminology for Physicochemical Quantities and Units - Appendix II Definitions, Terminology and Symbols in Colloid and Surface Chemistry - Part I*. prepared for publication by D. H. Everett, London: International Union of Pure and Applied Chemistry - Devision of Physical Chemistry, 1971.

- [51] M. Geiker, "Porosity and water fixation; characterization." 1st Marie-Curie ITN training course, Maastricht, 2011.
- [52] M. Petri, "Metody badan porowatosci," in *Materialy Budowlane Podstawy technologii i metody badan*, J. Malolepszy, Ed. Krakow: AGH Uczelniane Wydawnictwo Naukowo Dydaktyczne, 2008, pp. 270–277.
- [53] S. Diamond, "Mercury porosimetry an inappropriate method for the measurement of pore size distributions in cement-based materials," *Cem. Concr. Res.*, vol. 30, pp. 1517–1525, 2000.
- [54] E. W. Washburn, "The Dynamics of Capillary Flow," *Phys. Rev.*, vol. 17, pp. 273–283, 1921.
- [55] R. A. Cook and K. C. Hover, "Mercury porosimetry of hardened cement pastes," *Cem. Concr. Res.*, vol. 29, pp. 933–943, 1999.
- [56] C. Gallé, "Effect of drying on cement-based materials pore structure as identified by mercury intrusion porosimetry A comparative study between oven-, vacuum-, and freeze-drying," *Cem. Concr. Res.*, vol. 31, pp. 1467–1477, 2001.
- [57] R. A. Cook and K. C. Hover, "Mercury porosimetry of cement-based materials and associated correction factors," *Constr. Build. Mater.*, vol. 7, pp. 231–240, 1993.
- [58] K. L. Scrivener and E. Gallucci, "Microstructural Characterisation Methods for Cementitious Materials." 1st Marie-Curie ITN training course, Maastricht, 2011.
- [59] L. Wadsö, "Sorption I." 3rd Marie-Curie ITN training course, Lund, 2011.
- [60] S. Brunauer, P. H. Emmett, and E. Teller, "Adsorption of Gases in Multimolecular Layers," *J. Am. Chem. Soc.*, vol. 60, pp. 309–319, 1938.
- [61] L. Wadsö, "Capillarity," no. July. 3rd Marie-Curie ITN training course, Lund, 2011.
- [62] G. G. Litvan, "Variability of the Nitrogen Surface Area of Hydrated Cement Paste," *Cem. Concr. Res.*, vol. 6, pp. 139–143, 1976.
- [63] A. M. Kjeldsen and M. Geiker, "On the interpretation of low temperature calorimetry data," *Mater. Struct.*, vol. 41, pp. 213–224, 2007.
- [64] Z. Sun and G. W. Scherer, "Pore size and shape in mortar by thermoporometry," *Cem. Concr. Res.*, vol. 40, pp. 740–751, 2010.
- [65] D. P. Bentz, "NISTIR 7267 Low Temperature Calorimetry Studies of Hydrating Portland Cement Pastes," *Natl. Inst. Stand. Technol.*, pp. 1–125, 2005.
- [66] A. J. Allen and J. J. Thomas, "Analysis of C–S–H gel and cement paste by small-angle neutron scattering," *Cem. Concr. Res.*, vol. 37, pp. 319–324, 2007.
- [67] H. F. W. Taylor, "Hydrated Calcium Silicates. Part I. Compound Formation at Ordinary Temperatures," *J. Chem. Soc.*, pp. 3682–3690, 1950.
- [68] W. Kurdowski, "Faza C-S-H – stan zagadnienia. Część 1; C-S-H – state of art. Part 1," *Cem. Wapno Bet.*, vol. 4, pp. 216–222, 2008.
- [69] A. Nonat, "The structure and stoichiometry of C-S-H," *Cem. Concr. Res.*, vol. 34, pp. 1521–1528, Sep. 2004.
- [70] D. L. Rayment and A. J. Majumdar, "The composition of the C-S-H phases in portland cement pastes," *Cem. Concr. Res.*, vol. 12, pp. 753–764, 1982.

- [71] I. G. Richardson, "Tobermorite/jennite- and tobermorite/calcium hydroxide-based models for the structure of C-S-H: applicability to hardened pastes of tricalcium silicate,  $\beta$ -dicalcium silicate, Portland cement, and blends of Portland cement with blast-furnace slag, metakaol," *Cem. Concr. Res.*, vol. 34, pp. 1733–1777, 2004.
- [72] J. F. Young and W. Hansen, "Volume Relationships for C-S-H Formation Based on Hydration Stoichiometries," *Mater. Res. Soc. Proc.*, vol. 85, pp. 313–321, 1986.
- [73] R. F. Feldman and V. S. Ramachandran, "A Study of the State of Water and Stoichiometry of Bottle Hydrated  $\text{Ca}_3\text{SiO}_5$ ," vol. 4, pp. 155–166, 1974.
- [74] J. J. Chen, "The Nanostructure of Calcium Silicate Hydrate; PhD thesis," Chapter 2.3, Northwestern University, 2003.
- [75] R. F. Feldman, "Helium Flow and Density Measurement of the Hydrated Tricalcium Silicate - Water System," *Cem. Concr. Res.*, vol. 2, pp. 123–136, 1972.
- [76] R. F. Feldman, "Density and porosity studies of hydrated portland cement," *Cem. Technol.*, vol. 3, pp. 5–14, 1972.
- [77] B. Blümich, *Essential NMR for Scientists and Engineers*. Springer, 2005.
- [78] R. H. Harris, *Nuclear Magnetic Resonance Spectroscopy*. London: Longman, 1986.
- [79] P. T. Callaghan, *Principles of Nuclear Magnetic Resonance Microscopy*. Oxford Science Publications, 2011.
- [80] B. Cowan, *Nuclear Magnetic Resonance and Relaxation*. Cambridge University Press, 1997.
- [81] T. C. Farrer and E. D. Becker, *Pulse and Fourier Transform NMR Introduction to Theory and Methods*. New York - London: Academic Press, 1971.
- [82] A. Valori, P. J. McDonald, and K. L. Scrivener, "The morphology of C-S-H: Lessons from  $^1\text{H}$  nuclear magnetic resonance relaxometry," *Cem. Concr. Res.*, vol. 49, pp. 65–81, 2013.
- [83] E. L. Hahn, "Spin echoes," *Phys. Rev.*, vol. 80, p. 580–, 1950.
- [84] H. Y. Carr and E. M. Purcell, "Effects of Diffusion on Free Precession in Nuclear Magnetic Resonance Experiments," *Phys. Rev.*, vol. 94, pp. 630–638, 1954.
- [85] S. Meiboom and D. Gill, "Modified Spin-Echo Method for Measuring Nuclear Relaxation Times," *Rev. Sci. Instrum.*, vol. 29, pp. 688–691, 1958.
- [86] J. G. Powles and J. H. Strange, "Zero Time Resolution Nuclear Magnetic Resonance Transient in Solids," *Proceedings of the Physical Society*, vol. 82, pp. 6–15, 1963.
- [87] N. Boden and M. Mortimer, "An NMR 'Solid' Echo Experiment for the Direct Measurement of the Dipolar Interaction Between Spin-1/2 Pairs in Solid," vol. 21, pp. 538–540, 1973.
- [88] A. Abragam, *Principles of Nuclear Magnetism*. New York: Oxford University Press, 1961.
- [89] N. Bloembergen, E. M. Purcell, and R. V. Pound, "Relaxation Effects in Nuclear Magnetic Resonance Absorption," *Phys. Rev.*, vol. 73, pp. 679–712, 1948.
- [90] D. A. Faux, P. J. McDonald, N. C. Howlett, J. S. Bhatt, and S. V. Churakov, "Nuclear magnetic resonance relaxometry of water in two- and quasi-two-dimensions," *Phys. Rev. E - Stat. Nonlinear, Soft Matter Phys.*, vol. 87, pp. 062309–1–18, 2013.

- [91] J.-P. Korb, M. Whaley-Hodges, and R. G. Bryant, "Translational diffusion of liquids at surfaces of microporous materials: Theoretical analysis of field-cycling magnetic relaxation measurements," vol. 56, pp. 1934–1945, 1997.
- [92] P. J. McDonald, J.-P. Korb, J. Mitchell, and L. Monteilhet, "Surface relaxation and chemical exchange in hydrating cement pastes: a two-dimensional NMR relaxation study," *Phys. Rev. E. Stat. Nonlin. Soft Matter Phys.*, vol. 72, pp. 011409–1–9, 2005.
- [93] J.-P. Korb, M. Whaley-Hodges, and R. Bryant, "Translational Diffusion of Liquids at Surface of Microporous materials: New Theoretical Analysis of Field Cycling Magnetic Relaxation Measurements," *Magn. Reson. Imaging*, vol. 16, pp. 575–578, 1998.
- [94] P. J. McDonald, J. Mitchell, M. Mulheron, P. S. Aptaker, J.-P. Korb, and L. Monteilhet, "Two-dimensional correlation relaxometry studies of cement pastes performed using a new one-sided NMR magnet," *Cem. Concr. Res.*, vol. 37, pp. 303–309, 2007.
- [95] L. Monteilhet, J.-P. Korb, J. Mitchell, and P. J. McDonald, "Observation of exchange of micropore water in cement pastes by two-dimensional  $T_2$ - $T_2$  nuclear magnetic resonance relaxometry," *Phys. Rev. E*, vol. 74, pp. 061404–1–9, 2006.
- [96] H. Peemoeller, R. K. Shenoy, and M. M. Pintar, "Two-dimensional NMR time evolution correlation spectroscopy in wet lysozyme," *J. Magn. Reson.*, vol. 45, pp. 193–204, Nov. 1981.
- [97] L. Venkataramanan, Y.-Q. Song, and M. D. Hurlimann, "Solving Fredholm integrals of the first kind with tensor product structure in 2 and 2.5 dimensions," *IEEE Trans. Signal Process.*, vol. 50, no. 5, pp. 1017–1026, 2002.
- [98] A. Valori, P. J. McDonald, and V. Rodin, "On the interpretation of  $^1\text{H}$  2-dimensional NMR relaxation exchange spectra in cements: is there exchange between pores with two characteristic sizes or  $\text{Fe}^{3+}$  concentrations?," *Cem. Concr. Res.*, vol. 40, pp. 1375–1377, 2010.
- [99] F. Barberon, J.-P. Korb, D. Petit, V. Morin, and E. Bermejo, "Probing the Surface Area of a Cement-Based Material by Nuclear Magnetic Relaxation Dispersion," *Phys. Rev. Lett.*, vol. 90, pp. 116103–1–4, 2003.
- [100] J.-P. Korb, P. J. McDonald, L. Monteilhet, A. G. Kalinichev, and R. J. Kirkpatrick, "Comparison of proton field-cycling relaxometry and molecular dynamics simulations for proton–water surface dynamics in cement-based materials," *Cem. Concr. Res.*, vol. 37, pp. 348–350, 2007.
- [101] S. Bhattacharja, M. Moukwa, F. D’Orazio, J.-Y. Jehn, and W. P. Halperin, "Microstructure Determination of Cement Pastes by NMR and Conventional Techniques," *Adv. Cem. Based Mater.*, vol. 1, pp. 67–76, 1993.
- [102] R. M. E. Valckenborg, "Pore water distribution in mortar during drying as determined by NMR," *Mater. Struct.*, vol. 34, no. 244, pp. 599–604, 2005.
- [103] V. Kocaba, "MC-RTN Procedure for mixing of cement pastes," 2007.
- [104] A. C. A. Muller, "Personal communication - Mixing cement paste with addition of silica fume," 2012.

- [105] R. M. Kowalczyk, A. M. Gajewicz, and P. J. McDonald, "The mechanism of water-isopropanol exchange in cement pastes evidenced by NMR relaxometry," *RSC Adv.*, vol. 4, pp. 20709–20715, 2014.
- [106] Y.-Q. Song, L. Venkataramanan, and L. Burcaw, "Determining the resolution of Laplace inversion spectrum," *J. Chem. Phys.*, vol. 122, pp. 104104–1–8, Mar. 2005.
- [107] S. Godefroy, B. Ryland, and P. T. Callaghan, "2D Laplace Inversion Instruction Manual," Victoria University of Wellington, Wellington, 2008.
- [108] B. Z. Dilnesa, "Application of Thermogravimetric Method in Cement Science," [http://www.empa.ch/plugin/template/empa/\\*/95268/--/l=1](http://www.empa.ch/plugin/template/empa/*/95268/--/l=1). .
- [109] E. Gallucci, X. Zhang, and K. L. Scrivener, "Effect of temperature on the microstructure of calcium silicate hydrate (C-S-H)," *Cem. Concr. Res.*, vol. 53, pp. 185–195, 2013.
- [110] "[http://www.metalpoweranalytical.com/moisture\\_sorption\\_analysis.htm](http://www.metalpoweranalytical.com/moisture_sorption_analysis.htm)," 2014. .
- [111] M. R. Boudry, "A simple conversion formula for type 'T' (copper-constantan) thermocouple readings," *J. Phys. E.*, vol. 9, pp. 1064–1065, 1976.
- [112] A. Valori, "Characterisation of cementitious materials by  $^1\text{H}$  NMR; PhD thesis," University of Surrey, 2009.
- [113] R. F. Feldman, "Assessment of experimental evidence for models of hydrated portland cement," *Highw. Res. Rec.*, vol. 370, pp. 8–24, 1972.
- [114] V. Baroghel-Bouny, "Water vapour sorption experiments on hardened cementitious materials Part I: Essential tool for analysis of hygral behaviour and its relation to pore structure," *Cem. Concr. Res.*, vol. 37, pp. 414–437, 2007.
- [115] H. Chen, M. Wyrzykowski, K. L. Scrivener, and P. Lura, "Modeling of Internal Relative Humidity Evolution in Cement Pastes at Early Age," in *Second International Conference on Microstructural-related Durability of Cementitious Composites*, April 2012, pp. 140–147.
- [116] M. Geiker and T. Knudsen, "Chemical Shrinkage of Portland Cement Pastes," *Cem. Concr. Res.*, vol. 12, pp. 603–610, 1982.
- [117] B. Lothenbach, F. Winnefeld, C. Alder, E. Wieland, and P. Lunk, "Effect of temperature on the pore solution, microstructure and hydration products of Portland cement pastes," *Cem. Concr. Res.*, vol. 37, pp. 483–491, 2007.
- [118] M. Zajac, S. Garrault, and A. Nonat, "Effect of the hydration temperature on mechanical resistance of Portland cement mortar and paste," *Cem. Wapno Bet.*, vol. 2, pp. 68–75, 2007.
- [119] K. O. Kjellsen, R. J. Detwiler, and O. E. Gjorv, "Pore Structure of Plain Cement Pastes Hydrated at Different Temperatures," *Cem. Concr. Res.*, vol. 20, pp. 927–933, 1990.
- [120] K. O. Kjellsen, R. J. Detwiler, and O. E. Gjorv, "Development of microstructures in plain cement pastes hydrated at different temperatures," *Cem. Concr. Res.*, vol. 21, pp. 179–189, 1991.
- [121] L. D. Mitchell and J. C. Margeson, "The effects of solvents on C–S–H as determined by thermal analysis," *J. Therm. Anal. Calorim.*, vol. 86, pp. 591–594, 2006.
- [122] Q. Zhou and F. P. Glasser, "Thermal stability and decomposition mechanisms of ettringite at  $<120^\circ\text{C}$ ," *Cem. Concr. Res.*, vol. 31, pp. 1333–1339, 2001.

- [123] C. Hall, P. Barnes, A. D. Billimore, A. C. Jupe, and X. Turrillas, "Thermal decomposition of ettringite  $\text{Ca}_6[\text{Al}(\text{OH})_6]_2(\text{SO}_4)_3 \cdot 26\text{H}_2\text{O}$ ," *J. Chem. Soc. Faraday Trans.*, vol. 92, pp. 2125–2129, 1996.
- [124] A. N. Christensen, T. R. Jensen, and J. C. Hanson, "Formation of ettringite,  $\text{Ca}_6\text{Al}_2(\text{SO}_4)_3(\text{OH})_{12} \cdot 26\text{H}_2\text{O}$ , AFt, and monosulfate,  $\text{Ca}_4\text{Al}_2\text{O}_6(\text{SO}_4) \cdot 14\text{H}_2\text{O}$ , AFm-14, in hydrothermal hydration of Portland cement and of calcium aluminum oxide-calcium sulfate dihydrate mixtures studied by in situ synchrotron X-ray powder," *J. Solid State Chem.*, vol. 177, pp. 1944–1951, 2004.
- [125] K. Krynicky, "Proton Spin-Lattice Relaxation in Pure Water Between 0°C and 100°C," *Physica*, vol. 32, pp. 167–178, 1966.
- [126] H. J. Busscher, G. A. M. Kip, A. van Silfhout, and J. Arends, "Spreading Pressures of Water and n-Propanol on Polymer Surfaces," *J. Colloid Interface Sci.*, vol. 114, pp. 1–7, 1986.
- [127] J. J. Thomas and H. M. Jennings, "Effects of  $\text{D}_2\text{O}$  and Mixing on the Early Hydration Kinetics of Tricalcium Silicate," *Chem. Mater.*, vol. 11, pp. 1907–1914, 1999.
- [128] A. C. A. Muller, K. L. Scrivener, A. M. Gajewicz, and P. J. McDonald, "Densification of C-S-H measured by  $^1\text{H}$  NMR Relaxometry," *J. Phys. Chem. C*, vol. 117, pp. 403–412, 2013.